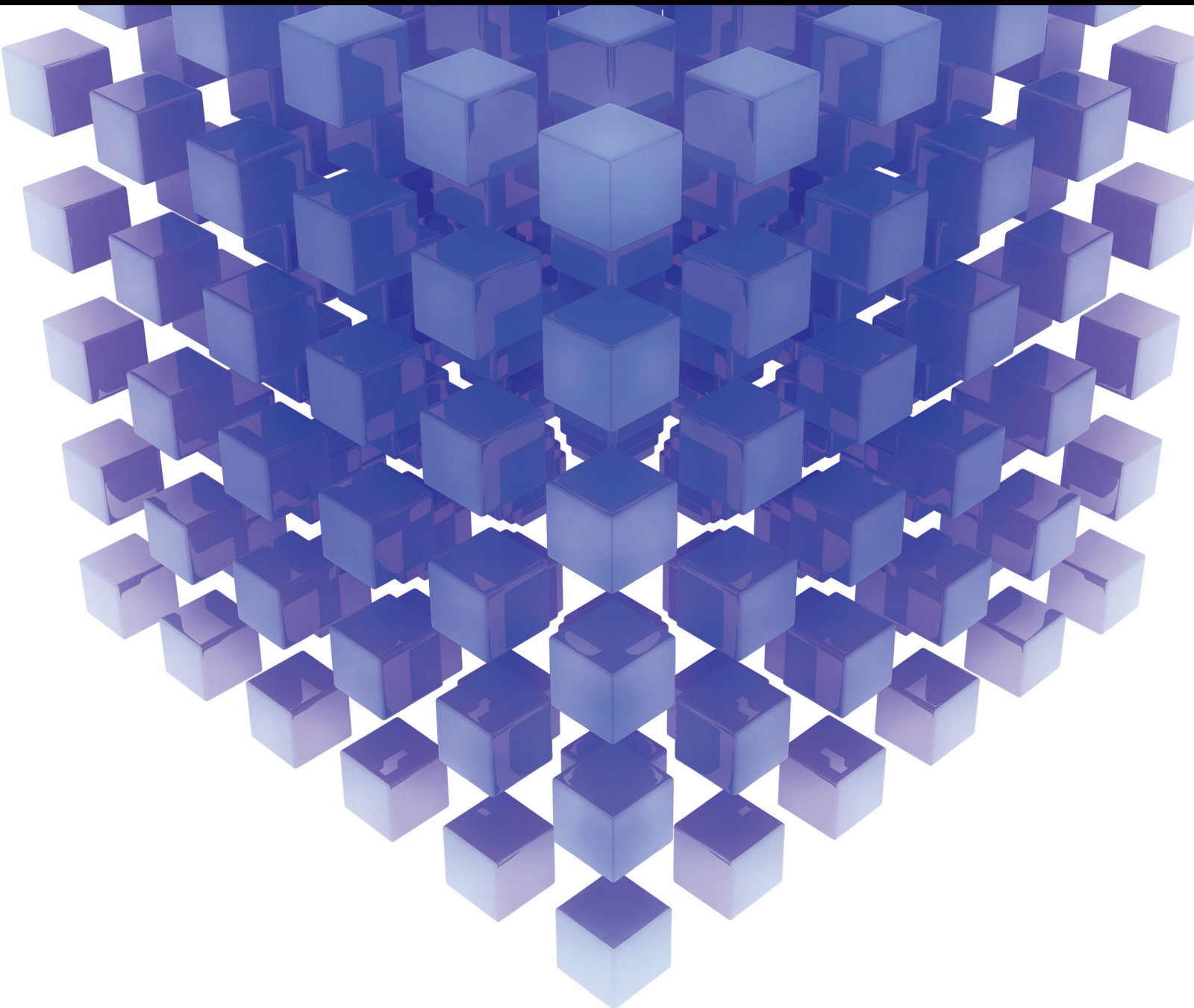


Mathematical Problems in Engineering

Inverse Problems in Structural Engineering

Guest Editors: Sang-Youl Lee, Guillermo Rus, Georgios E. Stavroulakis,
and Woo-Young Jung





Inverse Problems in Structural Engineering

Mathematical Problems in Engineering

Inverse Problems in Structural Engineering

Guest Editors: Sang-Youl Lee, Guillermo Rus,
Georgios E. Stavroulakis, and Woo-Young Jung



Copyright © 2015 Hindawi Publishing Corporation. All rights reserved.

This is a special issue published in “Mathematical Problems in Engineering.” All articles are open access articles distributed under the Creative Commons Attribution License, which permits unrestricted use, distribution, and reproduction in any medium, provided the original work is properly cited.

Editorial Board

Mohamed Abd El Aziz, Egypt
Farid Abed-Meraim, France
Silvia Abrahão, Spain
Paolo Addresso, Italy
Claudia Adduce, Italy
Ramesh Agarwal, USA
Juan C. Agüero, Australia
Ricardo Aguilar-López, Mexico
Tarek Ahmed-Ali, France
Hamid Akbarzadeh, Canada
Muhammad N. Akram, Norway
Mohammad-Reza Alam, USA
Salvatore Alfonzetti, Italy
Francisco Alhama, Spain
Juan A. Almendral, Spain
Saiied Aminossadati, Australia
Lionel Amodeo, France
Igor Andrianov, Germany
Sebastian Anita, Romania
Renata Archetti, Italy
Felice Arena, Italy
Sabri Arik, Turkey
Fumihiko Ashida, Japan
Hassan Askari, Canada
Mohsen Asle Zaeem, USA
Francesco Aymerich, Italy
Seungik Baek, USA
Khaled Bahlali, France
Laurent Bako, France
Stefan Balint, Romania
Alfonso Banos, Spain
Roberto Baratti, Italy
Martino Bardi, Italy
Azeddine Beghdadi, France
Abdel-Hakim Bendada, Canada
Ivano Benedetti, Italy
Elena Benvenuti, Italy
Jamal Berakdar, Germany
Enrique Berjano, Spain
Jean-Charles Beugnot, France
Simone Bianco, Italy
David Bigaud, France
Jonathan N. Blakely, USA
Daniela Boso, Italy
Abdel-Ouahab Boudraa, France
Taha Boukhobza, France
Francesco Braghin, Italy
Michael J. Brennan, UK
Gunther Brenner, Germany
Maurizio Brocchini, Italy
Julien Bruchon, France
Javier Bulduú, Spain
Tito Busani, USA
Pierfrancesco Cacciola, UK
Salvatore Caddemi, Italy
Jose E. Capilla, Spain
Ana Carpio, Spain
Miguel E. Cerrolaza, Spain
Mohammed Chadli, France
Gregory Chagnon, France
Ching-Ter Chang, Taiwan
Michael J. Chappell, UK
Kacem Chehdi, France
Chunlin Chen, China
Xinkai Chen, Japan
Francisco Chicano, Spain
Hung-Yuan Chung, Taiwan
Joaquim Ciurana, Spain
John D. Clayton, USA
Carlo Cosentino, Italy
Paolo Crippa, Italy
Erik Cuevas, Mexico
Peter Dabnichki, Australia
Luca D'Acerno, Italy
Weizhong Dai, USA
Purushothaman Damodaran, USA
Farhang Daneshmand, Canada
Fabio De Angelis, Italy
Stefano de Miranda, Italy
Filippo de Monte, Italy
Xavier Delorme, France
Luca Deseri, USA
Yannis Dimakopoulos, Greece
Zhengtao Ding, UK
Ralph B. Dinwiddie, USA
Mohamed Djemai, France
Alexandre B. Dolgui, France
George S. Dulikravich, USA
Bogdan Dumitrescu, Finland
Horst Ecker, Austria
Karen Egiazarian, Finland
Ahmed El Hajjaji, France
Fouad Erchiqui, Canada
Anders Eriksson, Sweden
Giovanni Falsone, Italy
Hua Fan, China
Yann Favennec, France
Giuseppe Fedele, Italy
Roberto Fedele, Italy
Jacques Ferland, Canada
Jose R. Fernandez, Spain
Simme Douwe Flapper, Netherlands
Thierry Floquet, France
Eric Florentin, France
Francesco Franco, Italy
Tomonari Furukawa, USA
Mohamed Gadala, Canada
Matteo Gaeta, Italy
Zoran Gajic, USA
Ciprian G. Gal, USA
Ugo Galvanetto, Italy
Akemi Gálvez, Spain
Rita Gamberini, Italy
Maria Gandarias, Spain
Arman Ganji, Canada
Xin-Lin Gao, USA
Zhong-Ke Gao, China
Giovanni Garcea, Italy
Fernando Garcia, Spain
Laura Gardini, Italy
Alessandro Gasparetto, Italy
Vincenzo Gattulli, Italy
Jürgen Geiser, Germany
Oleg V. Gendelman, Israel
Mergen H. Ghayesh, Australia
Anna M. Gil-Lafuente, Spain
Hector Gómez, Spain
Rama S. R. Gorla, USA
Oded Gottlieb, Israel
Antoine Grall, France
Jason Gu, Canada
Quang Phuc Ha, Australia
Ofer Hadar, Israel
Masoud Hajarian, Iran
Frédéric Hamelin, France

Zhen-Lai Han, China
Thomas Hanne, Switzerland
Xiao-Qiao He, China
María I. Herreros, Spain
Vincent Hilaire, France
Eckhard Hitzer, Japan
Jaromir Horacek, Czech Republic
Muneo Hori, Japan
Andrs Horvth, Italy
Gordon Huang, Canada
Sajid Hussain, Canada
Asier Ibeas, Spain
Giacomo Innocenti, Italy
Emilio Insfran, Spain
Nazrul Islam, USA
Payman Jalali, Finland
Reza Jazar, Australia
Khalide Jbilou, France
Linni Jian, China
Bin Jiang, China
Zhongping Jiang, USA
Ningde Jin, China
Grand R. Joldes, Australia
Joaquim Joao Judice, Portugal
Tadeusz Kaczorek, Poland
Tamas Kalmar-Nagy, Hungary
Tomasz Kapitaniak, Poland
Haranath Kar, India
Konstantinos Karamanos, Belgium
C. Masood Khaliq, South Africa
Do Wan Kim, Korea
Nam-Il Kim, Korea
Oleg Kirillov, Germany
Manfred Krafczyk, Germany
Frederic Kratz, France
Jurgen Kurths, Germany
Kyandoghere Kyamakya, Austria
Davide La Torre, Italy
Risto Lahdelma, Finland
Hak-Keung Lam, UK
Antonino Laudani, Italy
Aime' Lay-Ekuakille, Italy
Marek Lefik, Poland
Yaguo Lei, China
Thibault Lemaire, France
Stefano Lenci, Italy
Roman Lewandowski, Poland
Qing Q. Liang, Australia

Panos Liatsis, UK
Wanquan Liu, Australia
Yan-Jun Liu, China
Peide Liu, China
Peter Liu, Taiwan
Jean J. Loiseau, France
Paolo Lonetti, Italy
Luis M. López-Ochoa, Spain
Vassilios C. Loukopoulos, Greece
Valentin Lychagin, Norway
F. M. Mahomed, South Africa
Yassir T. Makkawi, UK
Noureddine Manamanni, France
Didier Maquin, France
Paolo Maria Mariano, Italy
Benoit Marx, France
Geérard A. Maugin, France
Driss Mehdi, France
Roderick Melnik, Canada
Pasquale Memmolo, Italy
Xiangyu Meng, Canada
Jose Merodio, Spain
Luciano Mescia, Italy
Laurent Mevel, France
Y. V. Mikhlin, Ukraine
Aki Mikkola, Finland
Hiroyuki Mino, Japan
Pablo Mira, Spain
Vito Mocella, Italy
Roberto Montanini, Italy
Gisele Mophou, France
Rafael Morales, Spain
Aziz Moukrim, France
Emiliano Mucchi, Italy
Domenico Mundo, Italy
Jose J. Muoz, Spain
Giuseppe Muscolino, Italy
Marco Mussetta, Italy
Hakim Naceur, France
Hassane Naji, France
Dong Ngoduy, UK
Tatsushi Nishi, Japan
Ben T. Nohara, Japan
Mohammed Nouari, France
Mustapha Nourelfath, Canada
Sotiris K. Ntouyas, Greece
Roger Ohayon, France
Mitsuhiro Okayasu, Japan

Eva Onaindia, Spain
Javier Ortega-Garcia, Spain
Alejandro Ortega-Moux, Spain
Naohisa Otsuka, Japan
Erika Ottaviano, Italy
Alkiviadis Paipetis, Greece
Alessandro Palmeri, UK
Anna Pandolfi, Italy
Elena Panteley, France
Manuel Pastor, Spain
Pubudu N. Pathirana, Australia
Francesco Pellicano, Italy
Mingshu Peng, China
Haipeng Peng, China
Zhike Peng, China
Marzio Pennisi, Italy
Matjaz Perc, Slovenia
Francesco Pesavento, Italy
M. do Rosário Pinho, Portugal
Antonina Pirrotta, Italy
Vicent Pla, Spain
Javier Plaza, Spain
Jean-Christophe Ponsart, France
Mauro Pontani, Italy
Stanislav Potapenko, Canada
Sergio Preidikman, USA
Christopher Pretty, New Zealand
Carsten Proppe, Germany
Luca Pugi, Italy
Yuming Qin, China
Dane Quinn, USA
Jose Ragot, France
K. Ramamani Rajagopal, USA
Gianluca Ranzi, Australia
Sivaguru Ravindran, USA
Alessandro Reali, Italy
Giuseppe Rega, Italy
Oscar Reinoso, Spain
Nidhal Rezg, France
Ricardo Riaza, Spain
Gerasimos Rigatos, Greece
José Rodellar, Spain
Rosana Rodriguez-Lopez, Spain
Ignacio Rojas, Spain
Carla Roque, Portugal
Aline Roumy, France
Debasish Roy, India
R. Ruiz Garcia, Spain

Antonio Ruiz-Cortes, Spain
Ivan D. Rukhlenko, Australia
Mazen Saad, France
Kishin Sadarangani, Spain
Mehrdad Saif, Canada
Miguel A. Salido, Spain
Roque J. Saltarén, Spain
Francisco J. Salvador, Spain
Alessandro Salvini, Italy
Angel Sánchez, Spain
Maura Sandri, Italy
Miguel A. F. Sanjuan, Spain
Juan F. San-Juan, Spain
Roberta Santoro, Italy
Ilmar Ferreira Santos, Denmark
José A. Sanz-Herrera, Spain
Nickolas S. Sapidis, Greece
E. J. Sapountzakis, Greece
Themistoklis P. Sapsis, USA
Andrey V. Savkin, Australia
Valery Sbitnev, Russia
Thomas Schuster, Germany
Mohammed Seaid, UK
Lotfi Senhadji, France
Joan Serra-Sagrasta, Spain
Leonid Shaikhet, Ukraine
Hassan M. Shanechi, USA
Sanjay K. Sharma, India
Bo Shen, Germany
Babak Shotorban, USA
Zhan Shu, UK
Dan Simon, USA
Luciano Simoni, Italy
Christos H. Skiadas, Greece

Michael Small, Australia
Francesco Soldovieri, Italy
Raffaele Solimene, Italy
Ruben Specogna, Italy
Sri Sridharan, USA
Ivanka Stamova, USA
Yakov Strelniker, Israel
Sergey A. Suslov, Australia
Thomas Svensson, Sweden
Andrzej Swierniak, Poland
Yang Tang, Germany
Sergio Teggi, Italy
Roger Temam, USA
Alexander Timokha, Norway
Rafael Toledo-Moreo, Spain
Gisella Tomasini, Italy
Francesco Tornabene, Italy
Antonio Tornambe, Italy
Fernando Torres, Spain
Fabio Tramontana, Italy
Sébastien Tremblay, Canada
Irina N. Trendafilova, UK
George Tsiatas, Greece
Antonios Tsourdos, UK
Vladimir Turetsky, Israel
Mustafa Tutar, Spain
Efstratios Tzirtzilakis, Greece
Filippo Ubertini, Italy
Francesco Ubertini, Italy
Hassan Ugail, UK
Giuseppe Vairo, Italy
Kuppalapalle Vajravelu, USA
Robertt A. Valente, Portugal
Raoul van Loon, UK

Pandian Vasant, Malaysia
M. E. Vázquez-Méndez, Spain
Josep Vehi, Spain
Kalyana C. Veluvolu, Korea
Fons J. Verbeek, Netherlands
Franck J. Vernerey, USA
Georgios Veronis, USA
Anna Vila, Spain
Rafael J. Villanueva, Spain
U. E. Vincent, UK
Mirko Viroli, Italy
Michael Vynnycky, Sweden
Junwu Wang, China
Shuming Wang, Singapore
Yan-Wu Wang, China
Yongqi Wang, Germany
Jeroen A. S. Witteveen, Netherlands
Yuqiang Wu, China
Dash Desheng Wu, Canada
Guangming Xie, China
Xuejun Xie, China
Gen Qi Xu, China
Hang Xu, China
Xinggang Yan, UK
Luis J. Yebra, Spain
Peng-Yeng Yin, Taiwan
Ibrahim Zeid, USA
Huaguang Zhang, China
Qingling Zhang, China
Jian Guo Zhou, UK
Quanxin Zhu, China
Mustapha Zidi, France
Alessandro Zona, Italy

Contents

Inverse Problems in Structural Engineering, Sang-Youl Lee, Guillermo Rus, Georgios E. Stavroulakis, and Woo-Young Jung

Volume 2015, Article ID 926432, 1 page

Evaluation of Seismic Fragility of Weir Structures in South Korea, Bu Seog Ju and WooYoung Jung

Volume 2015, Article ID 391569, 10 pages

Field Evaluation of the System Identification Approach for Tension Estimation of External Tendons, Myung-Hyun Noh, Taek-Ryong Seong, and Kyu-Sik Park

Volume 2015, Article ID 160271, 10 pages

Probabilistic Risk Assessment: Piping Fragility due to Earthquake Fault Mechanisms, Bu Seog Ju, WooYoung Jung, and Myung-Hyun Noh

Volume 2015, Article ID 525921, 8 pages

Field Application of Cable Tension Estimation Technique Using the h-SI Method,

Myung-Hyun Noh and WooYoung Jung

Volume 2015, Article ID 971023, 13 pages

Mass Change Prediction Model of Concrete Subjected to Sulfate Attack, Kwang-Myong Lee, Su-Ho Bae, Jae-Im Park, and Soon-Oh Kwon

Volume 2015, Article ID 298918, 10 pages

Interring Gas Dynamic Analysis of Piston in a Diesel Engine considering the Thermal Effect, Wanyou Li, Yibin Guo, Tao He, Xiqun Lu, and Dequan Zou

Volume 2015, Article ID 176893, 11 pages

Mathematical Approach in Rheological Characterizing of Asphalt Emulsion Residues,

Seong Hwan Cho and Jeong Hyuk Im

Volume 2015, Article ID 797808, 13 pages

Feasibility Study on Tension Estimation Technique for Hanger Cables Using the FE Model-Based System Identification Method, Kyu-Sik Park, Taek-Ryong Seong, and Myung-Hyun Noh

Volume 2015, Article ID 512858, 12 pages

Derivation Method for the Foundation Boundaries of Hydraulic Numerical Simulation Models Based on the Elastic Boussinesq Solution, Jintao Song, Chongshi Gu, Hao Gu, and Shaowei Wang

Volume 2015, Article ID 262163, 7 pages

An Advanced Coupled Genetic Algorithm for Identifying Unknown Moving Loads on Bridge Decks, Sang-Youl Lee

Volume 2014, Article ID 462341, 11 pages

Editorial

Inverse Problems in Structural Engineering

Sang-Youl Lee,¹ Guillermo Rus,² Georgios E. Stavroulakis,³ and Woo-Young Jung⁴

¹*Department of Civil Engineering, Andong National University, Andong-Si, Gyeongsangbuk-Do 760-749, Republic of Korea*

²*Department of Mecanica de Estructuras, Universidad de Granada Politecnico de Fuentenueva, 18071 Granada, Spain*

³*Department of Production Engineering and Management, Institute of Computational Mechanics and Optimization, Technical University of Crete, University Campus, 73100 Chania, Greece*

⁴*Department of Civil Engineering, Gangneung-Wonju National University, Gangneung 210-702, Republic of Korea*

Correspondence should be addressed to Sang-Youl Lee; lsy@anu.ac.kr

Received 13 May 2015; Accepted 14 May 2015

Copyright © 2015 Sang-Youl Lee et al. This is an open access article distributed under the Creative Commons Attribution License, which permits unrestricted use, distribution, and reproduction in any medium, provided the original work is properly cited.

When it is possible to determine governing equations, shapes and sizes of the domains, boundary and initial conditions, material properties of structures, and internal sources and external forces or inputs, then the analysis determining the unknown field is considered mathematically or numerically solvable. This issue compiles excellent articles, most of which are very meticulously performed reviews of the available current literature.

The availability of cheap electronic monitoring systems and computers makes the structural health monitoring affordable. More and more practical applications will appear in the next years. The need of studying inverse problems in structures becomes higher. Inverse techniques for various structures are studied by a host of investigators using a variety of approaches.

S. H. Cho and J. H. Im deal with mathematical approach in rheological characterizing of asphalt emulsion residues. In their study three different emulsion residues, such as SS-IHP, HFE-90, and SS-IVH (Trackless), and a base asphalt binder (PG 64-22) are compared to characterize rheological properties by using DSR test. J. Song et al. propose a derivation method for the foundation boundaries of the hydraulic numerical simulation model based on the elastic Boussinesq solution. The paper by S.-Y. Lee proposes an advanced coupled genetic algorithm for identifying unknown moving loads on bridge decks.

The tendon force identification method is addressed in three manuscripts. K.-S. Park et al. study feasibilities on tension estimation technique for hanger cables using the FE

model-based system identification method. In their work, the applicability of the tension estimation methods using the system identification approach is investigated using the hanger cables. M.-H. Noh and W.-Y. Jung verify the applicability of tension estimation method based on the finite element model with system identification technique. The proposed method is applied to estimate the tension of benchmark numerical example, model structures, and field structures. M.-H. Noh and W.-Y. Jung present field application of cable tension estimation technique using the h-SI method.

Besides those, there are several interesting topics in the issue. K.-M. Lee et al. suggest a mass change prediction model for sulfate attack of concrete containing mineral admixtures through an immersion test in sulfate solutions. For this, 100% OPC as well as binary and ternary cement concrete specimens are manufactured by changing the types and amount of mineral admixture. W. Li et al. perform interring gas dynamic analysis of piston in a diesel engine considering the thermal effect. B. S. Ju et al. review probabilistic risk assessment in piping fragility due to earthquake fault mechanisms. B. S. Ju and W.-Y. Jung review evaluation of seismic fragility of weir structures in South Korea.

By compiling these papers, we hope to enrich our readers and researchers with respect to various inverse problems and their solutions in structural engineering.

*Sang-Youl Lee
Guillermo Rus
Georgios E. Stavroulakis
Woo-Young Jung*

Research Article

Evaluation of Seismic Fragility of Weir Structures in South Korea

Bu Seog Ju¹ and WooYoung Jung²

¹*Institute for Disaster Prevention, Gangneung-Wonju National University, Gangneung 210-702, Republic of Korea*

²*Department of Civil Engineering, Gangneung-Wonju National University, Gangneung 210-702, Republic of Korea*

Correspondence should be addressed to WooYoung Jung; woojung@gwnu.ac.kr

Received 3 September 2014; Accepted 2 February 2015

Academic Editor: Valder Steffen Jr.

Copyright © 2015 B. S. Ju and W. Jung. This is an open access article distributed under the Creative Commons Attribution License, which permits unrestricted use, distribution, and reproduction in any medium, provided the original work is properly cited.

In order to reduce earthquake damage of multifunctional weir systems similar to a dam structure, this study focused on probabilistic seismic risk assessment of the weir structure using the fragility methodology based on Monte Carlo simulation (MCS), with emphasis on the uncertainties of the seismic ground motions in terms of near field induced pulse-like motions and far field faults. The 2D simple linear elastic plain strain finite element (FE) model including soil structure foundations using tie connection method in ABAQUS was developed to incorporate the uncertainty. In addition, five different limit states as safety criteria were defined for the seismic vulnerability of the weir system. As a consequence, the results obtained from multiple linear time history analyses revealed that the weir structure was more vulnerable to the tensile stress of the mass concrete in both near and far field ground motions specified earthquake hazard levels. In addition, the system subjected to near field motions was primarily more fragile than that under far field ground motions. On the other hand, the probability of failure due to the tensile stress at weir sill and stilling basin showed the similar trend in the overall peak ground acceleration levels.

1. Introduction

Recently 16 multifunctional weir structures were constructed on four major rivers in Korea. Weir structures designed to change river flow characteristics have similar functions like dams such as electric power generation, flooding control, and water supply. While there are many advantages associated with weir structures, they also have weaknesses; few weaknesses were reported in the case of weir structures built in the rivers. In another word, the weir structure is one of the infrastructures that have coexisting pros and cons. The general examples of drawbacks include increase of the oxygen content, accumulating garbage and other debris, and fauna changes in the water (<http://en.wikipedia.org/wiki/Weir>). Furthermore, the weir structures can be exposed to multiple hazards such as earthquakes and flooding caused by serious problems such as flooding due to structural failure, discontinuity between soil foundation and the weir, and strong impulse water wave due to ground motions.

According to Chanson [1], over the past decades, several failures in 20 hydraulic structures (dams and weirs) derived

from foundation failures, concrete cracks, and flood overflow in the world. In addition, the hydraulic structures as an essential energy supply system like the power plant must remain operational and functional safety without hydrodynamic instabilities during an earthquake. However, on September 21st, 1999, Chi-Chi earthquake (M_w 7.6) struck critical facilities such as Taipei 101 building, Shih-Kang dam as a concrete gravity dam, and Shih-Kang Primary School located at central region of Taiwan. Taipei 101 building did not suffer any significant structural damage even though it was under construction during the earthquake. On the other hand, Kung et al. [2] observed that the damage of Shih-Kang dam was caused by three different types of failures: (1) structural failure due to large ground motion greater than allowable deformation of the concrete gravity dam; (2) the cracks to weir body and the piers due to strong contact impact; (3) the fracture failure (i.e., one of the most complicated failure types) to the spillways and the abutment of the dam due to combination impact between strong ground motion and fault rupture energy. Besides, analytical studies of seismic evaluation in terms of hydraulic structures

have been issued in recent years, after the unique failure of Shih-Kang dam as a concrete gravity dam structure.

For example, Yao et al. [3] conducted the safety evaluation using seismic fragility of a concrete arch dam located in the southwestern area of China. The seismic fragility was evaluated by nonlinear time history analyses using 18 realistic seismic ground motions. The results from numerical analyses using ABAQUS 3D Finite Element (FE) model noted that the failure criteria such as opening, slipping, and displacement of the dam were affected by seismic ground motions intensity levels. Tekie and Ellingwood [4] used 4 limit states (material failure-concrete, material failure-foundation, sliding at the dam, and deflection of the top of the dam relative to the heel) to develop seismic fragility of concrete gravity dam located on New River in West Virginia in the USA. In particular, the dam-reservoir hydraulic interaction was considered in dynamic equation of motion and spectral accelerations, especially 12 earthquake records which occurred in the USA as intensity measure of ground motions were applied. The numerical results obtained from 2D FE analyses revealed that the sliding at the dam and tensile cracking at the neck of the dam were more critical than other limit states.

Consequently, the seismic safety evaluation of infrastructure (i.e., weir structures) with increase of earthquake records in Korea has received more attention as a key area of research. This study focused on evaluating Probabilistic Seismic Risk Assessment (PSRA) of the weir structure. More specifically, the 2D FE model of the weir structure including soil-structure foundation was conducted by ABAQUS Finite Element package, in order to develop the seismic fragility of the weirs. Furthermore, 30 near-field and 30 far-field earthquake records scaled to different peak ground acceleration (PGA) levels were considered as intensity measure and ground motions uncertainty. In this study, multiple linear time history analyses were carried out to generate the fragility based on Monte Carlo Simulation (MCS).

2. Description of the Weir Structure

The weir structure, Gangjeong-Goryeong weir, designed in 2009 to 2011 is located on the Nakdong River near Daegu Metropolitan City in Korea. This structure was constructed to control the flood and drought, supply the drinking water, and generate the electric power (3000 kW). The overall length of the multifunctional weir system as a concrete gravity structure is 933.5 m. It consists of two different systems: (1) the weir structure (nonoverflow section) with rising sector gates (120 m); (2) another concrete gravity weir system to allow overflow through their tops (833.5 m). The height of each structure is 11 m and the elevation of the two different systems is 9.47 m and 19.50 m, respectively. The storage volume of the system is 92.3 million m^3 and the design flood is 13,200 m^3/s . Moreover, the structure is designed for the maximum flood elevation at 24.02 m. The maintenance range of upstream and downstream of the structure is 300 m and 700 m, respectively, as shown in Figure 1 (<http://www.kwater.or.kr/>). The soil foundation at the site is classified by three layers: (1) sand layer; (2) gravel-sand mixture layer; (3) rock layer. Figure 2 shows a general design of weirs and the dimensions of overflow



FIGURE 1: The maintenance range of upstream and downstream in the Weir (<http://www.kwater.or.kr/>).

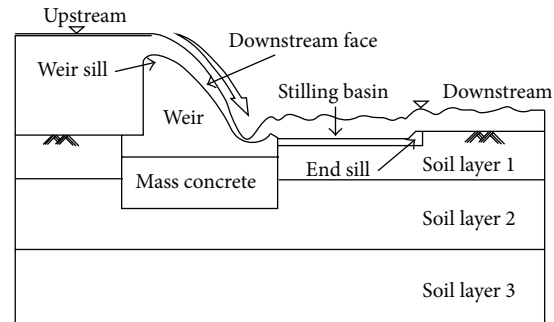


FIGURE 2: Description of the Gangjeong-Goryeong weir.

TABLE 1: Material properties of the weir structure.

Structures	Elastic modulus (MPa)	Poisson's ratio	Density (t/mm^3)
Weir body	26,637	0.167	$2.4E - 9$
Mass concrete	24,579	0.167	$2.4E - 9$
Steel	200,000	0.25	$7.85E - 9$
Soil layer 1	2	0.4	$1.7E - 9$
Soil layer 1	25	0.4	$1.9E - 9$
Soil layer 1	2,000	0.3	$2.4E - 9$

monolith (block number 10) at Gangjeong-Goryeong weir structure which is shown in Figure 3.

3. Finite Element Model of the Weir Structure

3.1. FE Modeling Description. To evaluate the performance of the weir structures, the Finite Element (FE) model was generated by ABAQUS [5], as shown in Figure 4, and a 4-node bilinear plane strain quadrilateral element was applied to the weir body, mass concrete, and soil-structure foundation. The dimension of y direction of the weir system was modeled with 58.114 m and x direction was 83.5 m including upstream and downstream side, in consideration of stress transfer. The material properties for the weir system were listed in Table 1. The design strength of the weir body and mass concrete system designed to peak ground acceleration at 0.154 g was 24 MPa and 18 MPa, respectively, and unit weight was 2350 kg/m^3 . For simplification, the weir body as a master surface and mass concrete as a slave surface were connected by tie condition in ABAQUS.

Block-10

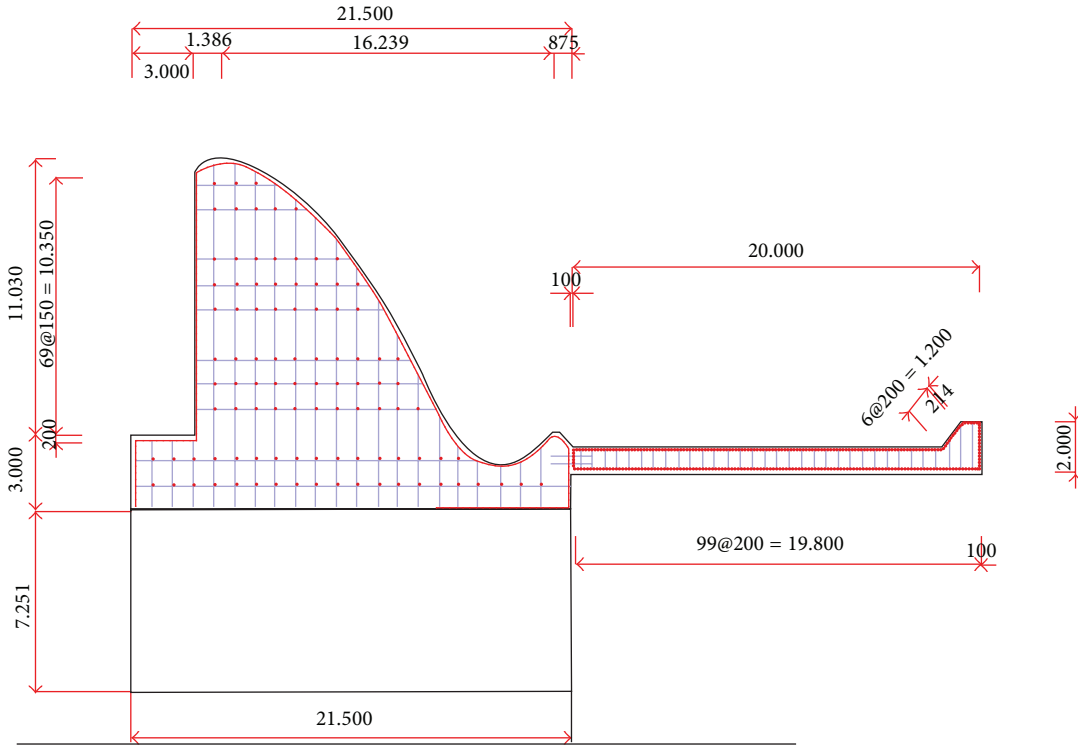


FIGURE 3: Schematic design of the weir structure (block number 10, unit: mm).

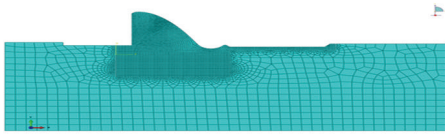


FIGURE 4: FE model of the weir including soil foundations.

3.2. Loading Conditions. In general, the system weight (gravity-weight) was determined by the combination of concrete unit weight and the system volume and 5 different loading conditions (hydrostatic pressure, hydrodynamic pressure, uplift pressure, silt pressure, and earthquake) were considered in this study. The hydrostatic pressure is typically proportional to the depth of water and the equation of hydrostatic pressure can be expressed as

$$P_w = \gamma_w h, \quad (1)$$

where γ_w = unit weight of water and h is the depth of water. Therefore, the total water pressure in the horizontal direction and vertical water pressure by the unit length are $(1/2)\gamma_w h^2$ and $\gamma_w hA$, respectively.

Next, the weir-reservoir interaction as a hydrodynamic effect was obtained from Westergaard [6] hydrodynamic approach. The mathematical description of hydrodynamic

governing equation in two-dimensional system can be derived as follows [6, 7]:

$$\frac{\partial^2 P}{\partial x^2} + \frac{\partial^2 P}{\partial y^2} = \frac{1}{C^2} \frac{\partial^2 P}{\partial t^2}. \quad (2)$$

In this equation, the velocity of sound in water $C = \sqrt{K/\rho_w}$ and $P(x, y, t)$ is the hydrodynamic pressure. ρ_w is the water density and K is the water bulk modulus. In particular, for the structure subjected to an earthquake, the Westergaard hydrodynamic pressure based on added mass method is given as follows:

$$P_d = \frac{7}{8} \rho_w g k \sqrt{H \times h}, \quad (3)$$

where k is $(2/3)(PGA/g)$. H is the total depth of the water and h is the depth from the water surface to the point of hydrodynamic pressure [8].

The uplift pressure of the weir structure is characterized by upward pressure of water as it flows through opening cracks of the foundation or the body connection parts due to the seepage or penetration path [8]. The equation of uplift pressure associated with the hydrostatic pressure may be written as [9]

$$U = \gamma_w \times C \times A \times \left[H_2 + \frac{1}{2} (H_1 - H_2) \times \tau \right], \quad (4)$$

where C is the ratio of area with respect to hydrostatic pressure and A is the bottom area due to uplift pressure. H_1 is

the depth of upstream of the system and H_2 is the depth of downstream of the weir. Also, τ means the ratio of $H_1 - H_2$ in terms of cut-off grouting and drainage curtain.

Besides, earth pressure due to backfill placed against the structure in foundation excavation and silt (horizontal and vertical) pressure due to deposit of silt must be taken into account in the dam or weir design [10]. With dam design criteria in Korea (2011), silt pressure can be calculated by the following:

$$P_s = \gamma_{\text{sub}} K_a H, \quad (5)$$

in which γ_{sub} is the submerged unit weight; K_a defines the coefficient of earth pressure, and H is the depth of silt deposit in the structure.

Lastly, in order to consider the dynamic interaction among the structure, reservoir, and soil-foundation, the dynamic equation of motion of the system subjected to a seismic ground motion can be obtained

$$[m] \{\ddot{u}(t)\} + [c] \{\dot{u}(t)\} + [k] \{u(t)\} = -[m] \{\ddot{u}_g(t)\} + R, \quad (6)$$

where $\ddot{u}(t)$, $\dot{u}(t)$, and $u(t)$ are the acceleration, velocity, and displacement, $\ddot{u}_g(t)$ is the ground motion, and R is the hydropressure and earth pressure mentioned above. In addition, $[m]$, $[c]$, and $[k]$ are the mass, damping, and stiffness matrices of the system. Details of seismic ground motions for analytical fragility functions of the weir structure are described in the next section.

4. Seismic Ground Motions

In order to develop the seismic vulnerability of the system, the uncertainties of the ground motions with respect to frequency range, ground motion intensity, and earthquake fault mechanism were taken into account. According to Billah et al. [11], the ground motion fault mechanisms as an uncertainty characteristic have a significant effect on the seismic fragility of the bridge. In case of near fault mechanisms, a long period velocity pulse (pulse-like motion) and higher input energy on the system were discharged [11, 12]. Hence, 30-near-field set with epicentral distance less than 10 km and 30-far-field set with epicentral distance over 10 km were carried out to generate the seismic fragility for the weir structure. The details of the ground motions selected from PEER-NGA [13] were listed in Tables 2 and 3.

5. Probabilistic Risk Assessment Methodology: Fragility Function

In recent years, seismic probabilistic risk assessment (SPRA) has been applied to identify the performance and limit/damage state of the systems (nuclear power plants (NPP), bridges, buildings, dams, etc.) in hazard and risk management. Kennedy et al. [14] came out with the seismic fragility as a factor of safe method for NPP and the Electric Power Research Institute (EPRI) [15] developed the assessment of NPP seismic margin using conservative deterministic failure

margin methodology to provide in-depth recommendation for the seismic fragility analysis. Moreover, in order to estimate the seismic vulnerability of a bridge structure, various analytical fragility methodologies such as nonlinear time history analyses [16], nonlinear static analyses [17], and Bayesian approach [18] were used. Ellingwood and Tekie [19] and Tekie and Ellingwood [4] presented the safety evaluation of existing concrete gravity dams by reservoir inflow, pool elevation, and spectral acceleration of seismic ground motions. Additionally, Ju et al. [20], Ju and Jung [21], and Ju and Jung [22] carried out Monte Carlo Simulation (MCS) to generate the seismic fragility of piping systems as a nonstructural component in critical facilities. Based on MCS methodology, the conditional probability of failure of the weir structure can be defined as follows:

$$P_f(\text{PGA}) = P[\text{EDPs} > \text{LS} \mid \text{PGA}], \quad (7)$$

in which $P_f(\text{PGA})$ denotes the conditional probability in terms of peak ground acceleration (PGA) as the ground intensity measure. In this study, the displacement and stresses are considered as engineering demand parameters (EDPs) and limit state (LS) is associated with EDPs to construct the fragility. Then, the empirical fragility of the weir structure corresponding to LS given in (8) was obtained from multiple linear time-history analyses using MCS accounting for ground motion uncertainties:

$$P_f(\lambda) = \frac{\sum_{i=1}^N (\text{EDPs} \geq \text{LS} \mid \text{PGA} = \lambda)}{\#\text{EQ}_s}, \quad (8)$$

where EDPs are the maximum stress or displacement from i th linear earthquake time-history analysis at a given PGA level. Therefore, the analytical fragility based on MCS for the weir structure in this study can be derived by log-normal cumulative distribution function (CDF) [23]:

$$P_f(\lambda) = \Phi \left[\frac{\ln(\lambda/m_c)}{\beta_{\text{sd}}} \right]. \quad (9)$$

Also, the analytical fragility of the weir structure corresponding to damage states is conducted by a correlation between the median capacity (m_c) and the logarithmic standard deviation (β_{sd}) of the structural system. Therefore, the damage states or limit states must be achieved prior to evaluation of the probability of failure of the system. This study defined the limit states of the weir structure based on Concrete Design Criteria 2003 [24] and Dam Design Criteria 2011 [9] in Korea and five different limit states for the system were presented in Table 4.

6. Seismic Fragility of the Weir Structure

A straightforward elastic FE model of the weir structure including the soil-structure foundation was dealt with for the fragility analyses. Before the evaluation, the analysis of eigenvalues and eigenvectors was conducted, in order to determine the dynamic properties of the weir structure with 5% damping ratio. The damping matrix in this study was determined by Rayleigh damping method in form of [25]

$$[C] = \alpha [M] + \beta [K], \quad (10)$$

TABLE 2: Selected ground motions: near field.

Number	Events	Year	Station	Mag.	Fault	Epicentral distance (km)	PGA (g)
1	Parkfield	June 28th, 1966	Cholame-Shand on Array number 5	6.19	Strike-slip	9.6	0.1381
2	San Fernando	Feb. 9th, 1971	Pacoima dam	6.61	Reverse	0	1.2259
3	Tabas, Iran	Sep. 16th, 1978	Dayhook	7.35	Reverse	0	0.3279
4	Tabas, Iran	Sep. 16th, 1978	Tabas	7.35	Reverse	1.8	0.8358
5	Imperial Valley	Oct. 15th, 1979	Aeropuerto Mexicali	6.53	Strike-slip	0	0.3267
6	Imperial Valley	Oct. 15th, 1979	El Centro Array number 10	6.53	Strike-slip	6.2	0.1053
7	Imperial Valley	Oct. 15th, 1979	El Centro Array number 4	6.53	Strike-slip	4.9	0.2478
8	Imperial Valley	Oct. 15th, 1979	Sahop Casa Flores	6.53	Strike-slip	9.6	0.2874
9	Victoria, Mexico	June 9th, 1980	Victoria Hospital	6.33	Strike-slip	6.1	0.0446
10	Irpinia, Italy	Nov. 23rd, 1980	Auletta	6.9	Normal	9.5	0.0576
11	Irpinia, Italy	Nov. 23rd, 1980	Bagnoli Irpino	6.9	Normal	8.1	0.1394
12	Irpinia, Italy	Nov. 23rd, 1980	Sturno	6.9	Normal	6.8	0.2506
13	Irpinia, Italy	Nov. 23rd, 1980	Calitri	6.9	Normal	8.8	0.1774
14	Morgan Hill	Apr. 24th, 1984	Anderson Dam	6.19	Strike-slip	3.2	0.4230
15	Morgan Hill	Apr. 24th, 1984	Coyote Lake Dam	6.19	Strike-slip	0.2	0.7109
16	Nahanni, Canada	Dec. 23rd, 1985	Site 2	6.76	Reverse	0	0.4890
17	Nahanni, Canada	Dec. 23rd, 1985	Site 3	6.76	Reverse	4.9	0.1404
18	N. Palm Springs	July 08th, 1986	Desert Hot Springs	6.06	Reverse	1.0	0.3313
19	N. Palm Springs	July 08th, 1986	Morongo Valley	6.06	Reverse	3.7	0.2182
20	N. Palm Springs	July 08th, 1986	North Palm Springs	6.06	Reverse	0	0.5941
21	Superstition Hills	Nov. 24th, 1987	Parachute Test Site	6.54	Strike-slip	0.9	0.4550
22	Loma Prieta	Oct. 18th, 1989	Capitola	6.93	Reverse	8.7	0.5285
23	Loma Prieta	Oct. 18th, 1989	Gilroy Gavilan Coll.	6.93	Reverse	9.2	0.3570
24	Loma Prieta	Oct. 18th, 1989	Gilroy Array number 1	6.93	Reverse	8.8	0.2088
25	Chi-Chi Taiwan	Sep. 20th, 1999	CHY006	7.62	Reverse	9.8	0.1301
26	Chi-Chi Taiwan	Sep. 20th, 1999	TCU076	7.62	Reverse	2.8	0.3029
27	Kobe, Japan	Jan. 16th, 1995	Nishi Akashi	6.9	Strike-slip	7.1	0.5093

TABLE 2: Continued.

Number	Events	Year	Station	Mag.	Fault	Epicentral distance (km)	PGA (g)
28	Kobe, Japan	Jan. 16th, 1995	Takatori	6.9	Strike-slip	1.5	0.6114
29	North Ridge	Jan. 17th, 1994	Newhall	6.69	Reverse	3.2	0.5830
30	North Ridge	Jan. 17th, 1994	Pacoima Kagel Canyon	6.69	Reverse	5.3	0.3011

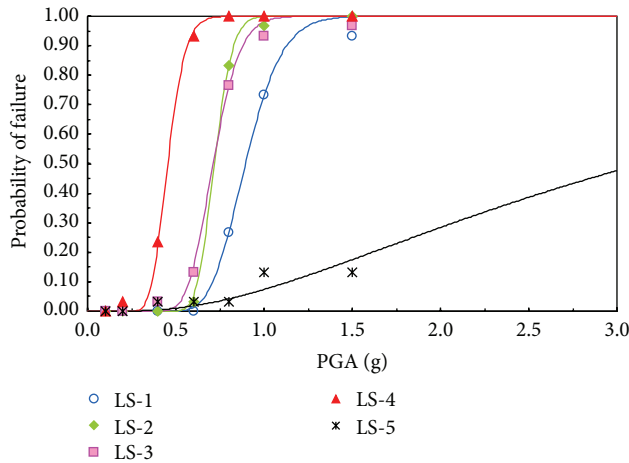


FIGURE 5: The seismic fragility of the weir subjected to near field ground motions.

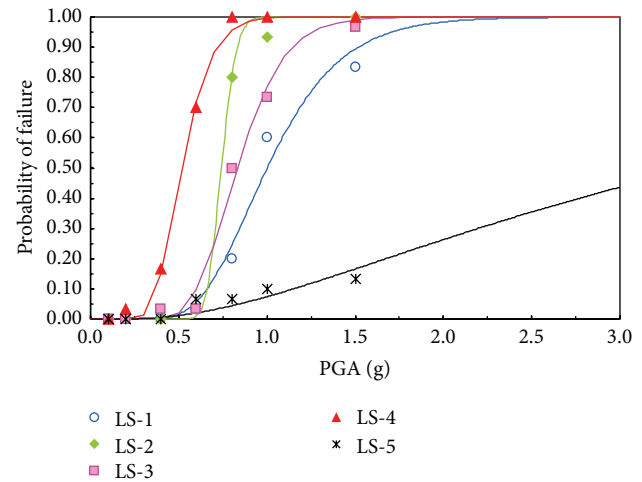


FIGURE 6: The seismic fragility of the weir subjected to far field ground motions.

where α = the mass constant value and β = the stiffness constant value. Then, the fundamental, second, and third frequencies from the eigenvalues were 0.8911, 1.1223, and 1.2622 Hz, respectively, and about 26% effective mass participation was observed at the third mode. It revealed that the third mode was the largest proportion of the total mass in horizontal direction. Consequently, in the estimation of the fragility of the weir structure, 30-near-field and 30-far-field ground motions normalized to the same PGA levels (0.1g, 0.2g, 0.4g, 0.6g, 0.8g, 1.0g, and 1.5g) were applied to the simple linear elastic FE model, respectively. In addition, the seismic fragilities were implemented at each PGA using (8) as the empirical method and the analytical seismic fragilities were established by (9) for the Gangjeong-Goryeong weir system. With the multiple time-history analyses accounting for ground motion uncertainties, seismic fragilities corresponding to the limit states were described in Figures 5 and 6. The fragilities noted that the system subjected to ground motions was more vulnerable to the tensile stress of the mass concrete structure than other damages. The similar manner is also observed in the weir system subjected to near field and far field ground motions. The probability of failure due to tensile stress (LS-2) of the weir body was not significantly different from LS-3 (i.e., compressive stress of the mass concrete) in overall PGA levels, as shown in Figure 5. On the other hand, in case of the far field ground motions (Figure 6), the failure

difference between LS-2 and LS-3 gradually increased as the seismic hazard level increased. Particularly, it showed that the fragility difference between tensile stress of the weir body and compressive stress of the mass concrete was about 27% at PGA 1.0g. Also, the relative displacement (LS-5) showed the lowest probability of failure in comparison to other damage states on both ground motions. The fragility comparison for the weir structure subjected to near field and far field ground motion intensity was described in Figures 7 to 11. In comparison to the fragility at limit state 2, the probability of failure of the system presented the similar trend between near field and far field ground motions. In addition, the system subjected to near field ground motions was more vulnerable than the weir structure subjected to far field ground motions. However, the probability of failure of the system at LS-1 due to far field ground motions was higher than that of the system under near field ground motion intensity up to PGA 0.78g. Therefore, the investigations depicted that the weir structure was sensitive to the ground motion intensity, which was the acceleration-sensitivity structural system.

7. Conclusions

The seismic probabilistic risk assessment, which is the seismic fragility, can be commonly used to identify the performance or characteristic strength of the system at a given seismic

TABLE 3: Selected ground motions: far field.

Number	Events	Year	Station	Mag.	Fault	Epicentral distance (km)	PGA (g)
1	Kocaeli, Turkey	June 28th, 1999	Ambarli	7.51	Strike-slip	68.1	0.2487
2	San Fernando	Feb. 9th, 1971	Carbon Canyon Dam	6.61	Reverse	61.8	0.0695
3	San Fernando	Feb. 9th, 1971	Cedar Spring	6.61	Reverse	92.2	0.0267
4	San Fernando	Feb. 9th, 1971	Colton	6.61	Reverse	96.8	0.0321
5	San Fernando	Feb. 9th, 1971	Fairmont Dam	6.61	Reverse	25.6	0.0712
6	Friuli, Italy	May 6th, 1976	Barcis	6.5	Reverse	49.1	0.0289
7	Friuli, Italy	May 6th, 1976	Conegliano	6.5	Reverse	80.4	0.0491
8	Irpinia Italy-01	Nov. 23rd, 1980	Rionero in Vulture	6.9	Normal	29.8	0.1059
9	Imperial Valley	Oct 15th, 1979	Calipatria Fire STA	6.53	Strike-slip	23.2	0.1282
10	Imperial Valley	Oct. 15th, 1979	Cerro Prieto	6.53	Strike-slip	15.2	0.1691
11	Irpinia Italy-02	Nov. 23rd, 1980	Mercato San Severino	6.2	Normal	43.5	0.0417
12	Imperial Valley	Oct. 15th, 1979	Compuertas	6.53	Strike-slip	13.5	0.1862
13	Imperial Valley	Oct. 15th 1979	Delta	6.53	Strike-slip	22	0.2378
14	Imperial Valley	Oct. 15th, 1979	Parachute Test Site	6.53	Strike-slip	12.7	0.1113
15	Imperial Valley	Oct. 15th, 1979	Superstition MTN Camera	6.53	Strike-slip	24.6	0.1092
16	Irpinia Italy-02	Nov. 23rd, 1980	Rionero in Vulture	6.2	Normal	22.7	0.0988
17	Chi-Chi Taiwan	Sep. 20th, 1999	CHY019	7.62	Reverse	50	0.0637
18	Chi-Chi Taiwan	Sep. 20th, 1999	CHY022	7.62	Reverse	63.2	0.0443
19	Chi-Chi Taiwan	Sep. 20th, 1999	CHY023	7.62	Reverse	81.1	0.0584
20	Chi-Chi Taiwan	Sep. 20th, 1999	CHY025	7.62	Reverse	19.1	0.1592
21	Kocaeli, Turkey	June 28th, 1999	Arcelik	7.51	Strike-slip	10.6	0.2188
22	Kocaeli, Turkey	June 28th, 1999	Atakoy	7.51	Strike-slip	56.5	0.1048
23	Kocaeli, Turkey	June 28th, 1999	Bursa	7.51	Strike-slip	65.5	0.0453
24	New Zealand 02	Mar. 2nd, 1987	Matahina Dam	6.6	Normal	16.1	0.2553
25	Imperial Valley	Oct. 15th, 1979	El Centro Array number 12	6.53	Strike-slip	17.9	0.0658
26	Imperial Valley	Oct. 15th, 1979	El Centro Array number 13	6.53	Strike-slip	22	0.0456

TABLE 3: Continued.

Number	Events	Year	Station	Mag.	Fault	Epicentral distance (km)	PGA (g)
27	Imperial Valley	Oct. 15th, 1979	El Centro Array number 3	6.53	Strike-slip	10.8	0.1267
28	Imperial Valley	Oct. 15th, 1979	El Centro Array number 1	6.53	Strike-slip	21.7	0.0564
29	Imperial Valley	Oct. 15th, 1979	El Centro Array number 11	6.53	Strike-slip	12.4	0.1403
30	Parkfield	June 28th, 1966	Temblor Pre-1969	6.19	Strike-slip	17.6	0.3574

TABLE 4: Limit states of the weir structure.

Limit states	Details	Design criteria
LS-1	Compressive stress at the weir body and stilling basin	$0.25 f_{ck} = 6 \text{ MPa}$
LS-2	Tensile stress at the weir body and stilling basin	$0.42 \sqrt{f_{ck}} = 2.058 \text{ MPa}$
LS-3	Compressive stress at the mass concrete	$0.25 f_{ck} = 4.5 \text{ MPa}$
LS-4	Tensile stress at the mass concrete	$0.42 \sqrt{f_{ck}} = 1.782 \text{ MPa}$
LS-5	The displacement of the weir structure	10 mm

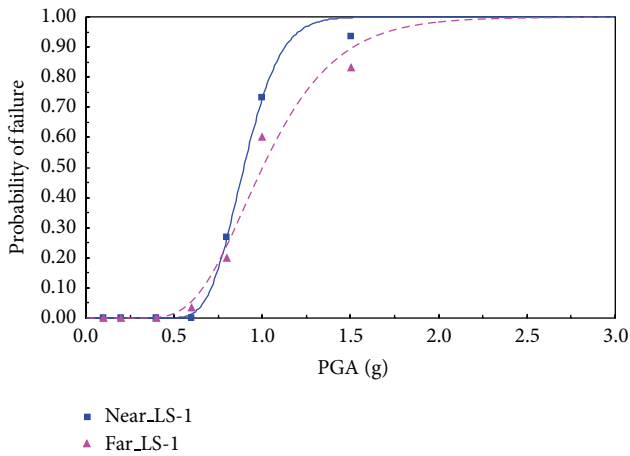


FIGURE 7: Comparison of the fragility corresponding to LS-1.

hazard level in civil engineering structures. In order to develop the safety assessment for the weir structure as a critical structure in Korea, the fragility analysis was carried out in this study. More specifically, this study developed the simple linear elastic FE model including the soil-structure foundation of Gangjeong-Goryeong weir located on the Nakdong River near Daegu Metropolitan City in Korea. To describe the uncertainty in ground motions of the seismic fragility analyses, near field (30 earthquake records) and far

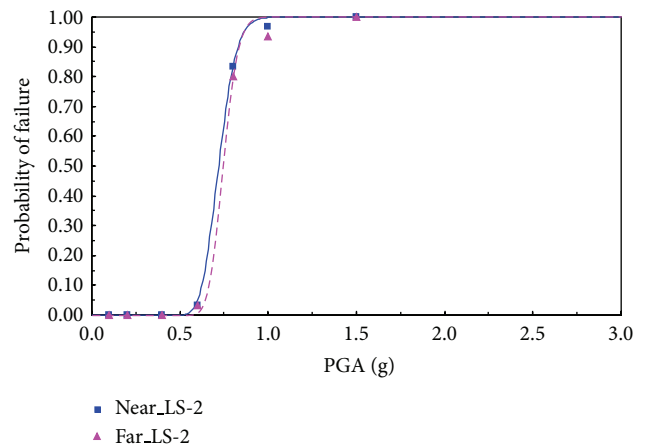


FIGURE 8: Comparison of the fragility corresponding to LS-2.

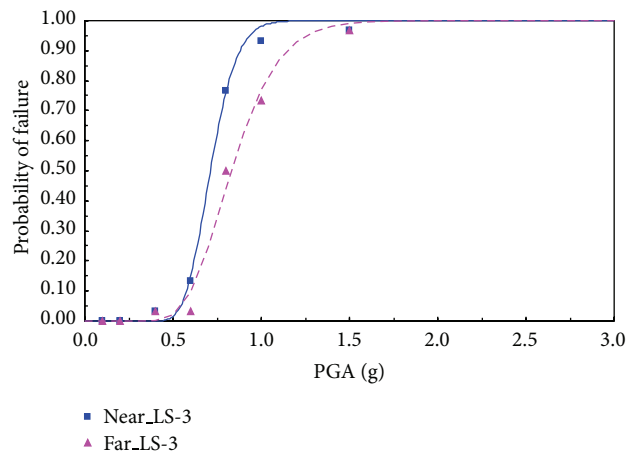


FIGURE 9: Comparison of the fragility corresponding to LS-3.

field (30 earthquake records) earthquakes were accounted for as intensity measures. With the particular emphasis on incorporating uncertainty into the 2D plain FE model, multiple linear time history analyses based on MCS were carried out. Through this preprocess, the vulnerability of the weir structure was estimated. As a result, from the eigenvalue

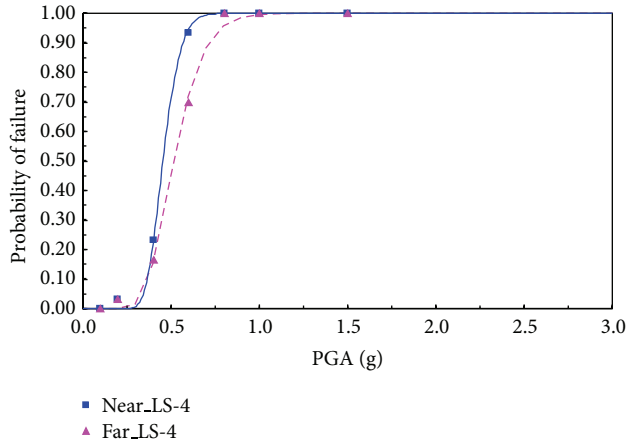


FIGURE 10: Comparison of the fragility corresponding to LS-4.

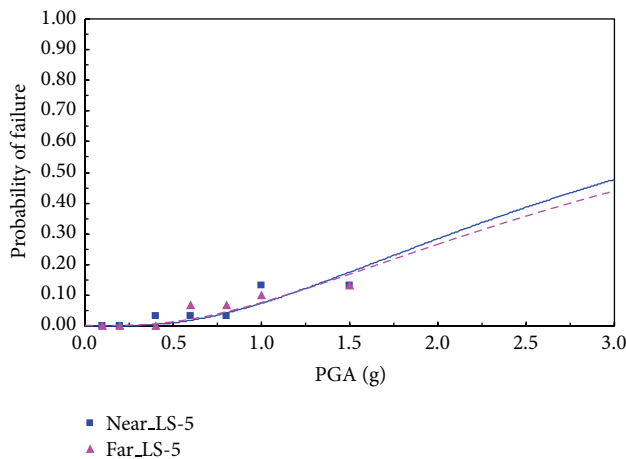


FIGURE 11: Comparison of the fragility corresponding to LS-5.

analysis, the effective mass participation of the third mode in the weir structure was significantly larger than that of the first mode and the second mode in horizontal direction. It was noted that the mode shape and mass participation were very different from the typical building type. The empirical and analytical fragility results in particular revealed that the weir structure was more conservative to the near field fault mechanism in comparison to the far field fault. Furthermore, the weir system including mass concrete and soil foundations was relatively susceptible to limit state 4 (tensile stress at the mass concrete) as compared to other damage states, during an earthquake.

Finally, the seismic fragility accounting for the nonlinearity with respect to the interaction between the weir body and soil-structure foundation must be achieved and for a future safety assessment of the weir system the effect of flooding condition must be also considered.

Conflict of Interests

The authors declare that there is no conflict of interests regarding the publication of this paper.

Acknowledgments

This research was supported by a Grant (14SCIP-B065985-02) from Smart Civil Infrastructure Research Program funded by Ministry of Land, Infrastructure and Transport (MOLIT) of Korea government and Korea Agency for Infrastructure Technology Advancement (KAIA).

References

- [1] H. Chanson, "A review of accidents and failures of stepped spillways and weirs," *Proceedings of the Institution of Civil Engineers: Water and Maritime Engineering*, vol. 142, no. 4, pp. 177–188, 2000.
- [2] C. S. Kung, W. P. Ni, and Y. J. Chiang, "Damage and rehabilitation work of Shih-Kang dam," in *Proceedings of the Seismic Fault-Induced Failures Workshop*, pp. 33–48, 2001, <http://shake.iis.utokyo.ac.jp/seismic-fault/workshops/papers/03.PDF>.
- [3] X. W. Yao, A. S. Elnashai, and J. Q. Jiang, "Analytical seismic fragility analysis of concrete arch dams," in *Proceedings of the 15th World Conference on Earthquake Engineering*, Lisbon, Portugal, September 2012.
- [4] P. B. Tekie and B. R. Ellingwood, "Seismic fragility assessment of concrete gravity dams," *Earthquake Engineering and Structural Dynamics*, vol. 32, no. 14, pp. 2221–2240, 2003.
- [5] ABAQUS, "Ver 6.13, Dassault Systemes".
- [6] H. M. Westergaard, "Water pressure on dams during earthquakes," *Transactions of the ASCE*, vol. 98, pp. 418–433, 1933.
- [7] P. Chakrabarti and K. Chopra, "Earthquake analysis of gravity dams including hydrodynamic interaction," *Earthquake Engineering and Structural Dynamics*, vol. 2, no. 2, pp. 143–160, 1973.
- [8] A. Rasekh, "Hydrodynamic pressure on culvert gates during an earthquake," in *Proceedings of the SIMULA Community Conference*, pp. 1–13, 2012.
- [9] *Dam Design Criteria in Korea*, Ministry of Land, Infrastructure and Transport, 2011.
- [10] R. S. Jansen, *Advanced Dam Engineering for Design, Construction, and Rehabilitation*, Van Nostrand Reinhold, New York, NY, USA, 115th edition, 1988.
- [11] A. H. M. M. Billah, M. S. Alam, and M. A. R. Bhuiyan, "Fragility analysis of retrofitted multicolumn bridge bent subjected to near-fault and far-field ground motion," *Journal of Bridge Engineering*, ASCE, vol. 18, no. 10, pp. 992–1004, 2013.
- [12] P. G. Somerville, "Characterizing near fault ground motion for the design and evaluation of bridges," in *Proceedings of the 3rd National Conference and Workshop on Bridges and Highways*, Portland, Ore, USA, 2002.
- [13] PEER-NGA, Pacific Earthquake Engineering Research Center: NGA Database, <http://peer.berkeley.edu/nga/>.
- [14] R. P. Kennedy, C. A. Cornell, R. D. Campbell, S. Kaplan, and H. F. Perla, "Probabilistic seismic safety study of an existing nuclear power plant," *Nuclear Engineering and Design*, vol. 59, no. 2, pp. 315–338, 1980.
- [15] Electric Power Research Institute (EPRI), "Methodology for developing seismic fragilities," Research Project TR-103959, 1994.
- [16] J. Park and E. Choi, "Fragility analysis of track-on steel-plate-girder railway bridges in Korea," *Engineering Structures*, vol. 33, no. 3, pp. 696–705, 2011.
- [17] M. Shinozuka, M. Q. Feng, H.-K. Kim, and S.-H. Kim, "Nonlinear static procedure for fragility curve development," *Journal of Engineering Mechanics*, vol. 126, no. 12, pp. 1287–1295, 2000.

- [18] J. Li, B. F. Spencer, and A. S. Elnashai, "Bayesian updating of fragility functions using hybrid simulation," *Journal of Structural Engineering*, vol. 139, no. 7, pp. 1160–1171, 2013.
- [19] B. Ellingwood and P. B. Tekie, "Fragility analysis of concrete gravity dams," *Journal of Infrastructure Systems*, vol. 7, no. 2, pp. 41–48, 2001.
- [20] B. S. Ju, S. K. Tadinada, and A. Gupta, "Fragility analysis of threaded T-joint connections in hospital piping systems," in *Proceedings of the Pressure Vessels and Piping Conference (PVP '11)*, pp. 147–155, Baltimore, Md, USA, July 2011.
- [21] B. S. Ju and W. Y. Jung, "Seismic fragility evaluation of multi-branch piping systems installed in critical low-rise buildings," *Disaster Advances*, vol. 6, no. 4, pp. 59–65, 2013.
- [22] B. S. Ju and W. Y. Jung, "Probabilistic risk assessment: piping fragility due to earthquake fault mechanisms," *Mathematical Problems in Engineering*. In press.
- [23] R. P. Kennedy and M. K. Ravindra, "Seismic fragilities for nuclear power plant risk studies," *Nuclear Engineering and Design*, vol. 79, no. 1, pp. 47–68, 1984.
- [24] *Concrete Design Criteria in Korea*, Korea Concrete Institute, 2003.
- [25] A. K. Chopra, *Dynamics of Structures*, Prentice Hall, Upper Saddle River, NJ, USA, 2nd edition, 2007.

Research Article

Field Evaluation of the System Identification Approach for Tension Estimation of External Tendons

Myung-Hyun Noh, Taek-Ryong Seong, and Kyu-Sik Park

Steel Solution Center, POSCO, 100 Songdogwahak-ro, Yeonsu-gu, Incheon 406-840, Republic of Korea

Correspondence should be addressed to Kyu-Sik Park; kyusik.park@posco.com

Received 24 September 2014; Accepted 24 November 2014

Academic Editor: Guillermo Rus

Copyright © 2015 Myung-Hyun Noh et al. This is an open access article distributed under the Creative Commons Attribution License, which permits unrestricted use, distribution, and reproduction in any medium, provided the original work is properly cited.

Various types of external tendons are considered to verify the applicability of tension estimation method based on the finite element model with system identification technique. The proposed method is applied to estimate the tension of benchmark numerical example, model structure, and field structure. The numerical and experimental results show that the existing methods such as taut string theory and linear regression method show large error in the estimated tension when the condition of external tendon is different with the basic assumption used during the derivation of relationship between tension and natural frequency. However, the proposed method gives reasonable results for all of the considered external tendons in this study. Furthermore, the proposed method can evaluate the accuracy of estimated tension indirectly by comparing the measured and calculated natural frequencies. Therefore, the proposed method can be effectively used for field application of various types of external tendons.

1. Introduction

Many structures use external tendons including the main and hanger cables for suspension bridges as well as the main cables for cable-stayed bridges, stranded cables, external reinforcing cables. External tendons use the tensile force applied to the cable, and it is used as the main or sub-members for many structures. The tensile force of the external tendon applied during the construction phase varies over time after completion depending on various factors. Therefore, to estimate the tensile force of the external tendon is of a paramount importance in terms of the stability and maintenance of a structure. The most accurate means to estimate the tension on the cables is to use load cells to collect the data directly. However, this is not an option in many cases due to the conditions in the field and the higher price of the cells and short service lives of these components, which can be a maintenance challenge when malfunctions occur. Therefore, the most commonly used method is to extract the natural frequency from the acceleration signal measures and enter the data into an equation that shows the relationship between the natural frequency and tension, to estimate the tension indirectly.

The two most widely used methods are the taut string theory [1] which does not take the bending stiffness into consideration and the linear regression method [2–4] which regards the cable as a beam under the axial load and considers the bending stiffness. The estimation methods for tension using the existing dynamic method put the natural frequency values to the equation on the natural frequency and tension. Therefore, if the mathematical model used differs significantly from the actual structure, a significant error is unavoidable.

The method of estimating the tensile force of external tendons we introduce in this paper has the following two outstanding characteristics. First, since it uses the finite element model, it can be applied to any form of external tendon because when the structure is geometrically complex and difficult to determine the value of a mathematical model, the finite element model is the most effective alternative. That is, the natural frequencies of the structure can be calculated using the finite element model but not analytical methods. Second, when the number of variables to be identified is large, the methods to minimize the error between the calculated natural frequency and the measured natural frequency involve a lot of computation. For this reason, we applied

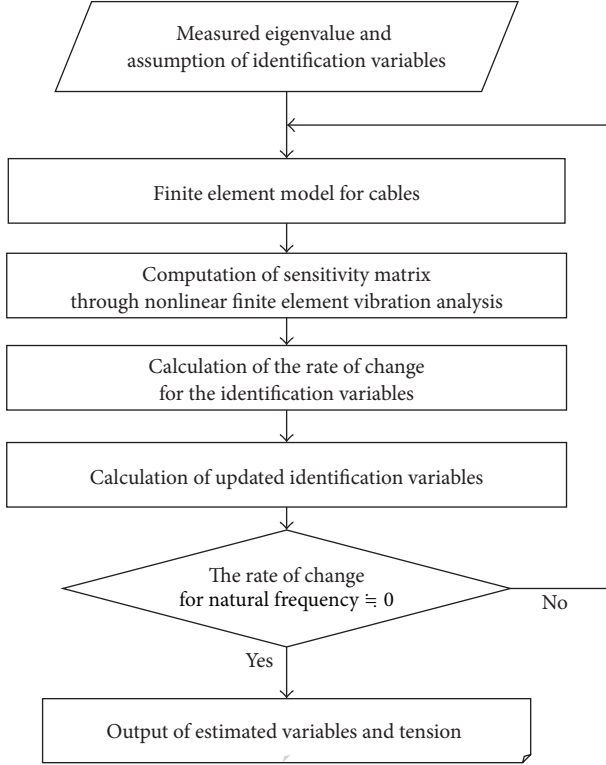


FIGURE 1: The process of estimating the tensile force using the system identification method [5].

the system identification method that uses the sensitivity analysis, which is garnering greater attention these days. The overall diagram for the process of estimating the tensile force using the system identification method is shown in Figure 1, and further details can be found in the studies by Park and Kim [5] and Park et al. [6]. In this study, the theoretical formulation of tension estimation is carried out through the system identification technique that uses the sensitivity updating algorithm, which is then applied to the benchmark numerical examples, laboratory test samples, and the field structures to verify the effectiveness of our method.

2. Theoretical Formulation

In the process of estimating the tension using the system identification approach based on the finite element model, the tension of external tendons is illustrated by the identification vector which is composed of several unknown parameters. The identification vector containing unknown parameters x^p ($p = 1, \dots, m$) used for identifying the tensile force in the system identification procedure can be defined as

$$\mathbf{x} = [x^1 \ x^2 \ \dots \ x^k]^T, \quad (1)$$

where x^1, x^2, \dots, x^k denote the identification variables for estimating tensile force. For example, the x^k could be set to the tension or other physical property for external tendons, that is, need to identify.

The identification vector for the r th iteration in the sensitivity-based updating algorithm can be assumed as

$${}^r \mathbf{x} = [{}^r x^1 \ {}^r x^2 \ \dots \ {}^r x^k]^T, \quad (2)$$

where ${}^r x^1, {}^r x^2, \dots, {}^r x^k$ mean the identification variables for the r th iteration.

Then, the static displacement and tendon force distribution can be produced for the identification vector. In the next step, the natural frequency ω_j ($j = 1, \dots, q$) is determined from the finite element vibration analysis using the static displacement curve and tendon force distribution. Using the change in natural frequencies for different identification variables, the sensitivity matrix (\mathbf{S}) with $(q \times p)$ size can be determined approximately as follows:

$${}^r \mathbf{S} = \begin{bmatrix} \frac{\partial^r \omega_1}{\partial^r x^1} & \frac{\partial^r \omega_1}{\partial^r \omega_1} & \dots & \frac{\partial^r \omega_1}{\partial^r x^p} & \frac{\partial^r \omega_1}{\partial^r \omega_1} \\ \vdots & \ddots & \ddots & \vdots & \vdots \\ \frac{\partial^r \omega_q}{\partial^r x^1} & \frac{\partial^r \omega_q}{\partial^r \omega_q} & \dots & \frac{\partial^r \omega_q}{\partial^r x^p} & \frac{\partial^r \omega_q}{\partial^r \omega_q} \end{bmatrix}. \quad (3)$$

Then, from the produced natural frequency data, the rate of change ($d^r \omega$) for the eigenvalue can be obtained as

$$d^r \omega = \left[\frac{\omega_1^m - {}^r \omega_1^c}{{}^r \omega_1^c} \ \dots \ \frac{\omega_q^m - {}^r \omega_q^c}{{}^r \omega_q^c} \right]^T, \quad (4)$$

where ω_q^m and ${}^r \omega_q^c$ denote the q th mode's natural frequency measured from experiment or field test and the q th mode's frequency calculated from nonlinear finite element vibration analysis using ${}^r x^p$ in the r th iteration, respectively. Equation (4) can be rewritten in the vector form as

$$d^r \omega_{(q \times 1)} = {}^r \mathbf{S}_{(q \times p)} d^r \mathbf{x}_{(p \times 1)}. \quad (5)$$

Equation (5) is referred to as a linear sensitivity equation, and the rate of change for the identification vector by using (5) can be expressed as

$$d^r \mathbf{x} = {}^r \mathbf{S}^{-1} d^r \omega, \quad (6)$$

where ${}^r \mathbf{S}^{-1}$ means the pseudoinverse matrix for ${}^r \mathbf{S}$ and can be determined as

$${}^r \mathbf{S}^{-1} = ({}^r \mathbf{S}^T {}^r \mathbf{S})^{-1} {}^r \mathbf{S}^T. \quad (7)$$

Finally, the p th identification variable in the $(r + 1)$ th iteration can be recalculated as

$${}^{r+1} x^p = (1 + d^r x^p) {}^r x^p, \quad (8)$$

$${}^{r+1} \mathbf{x} = [{}^{r+1} x^1 \ {}^{r+1} x^2 \ \dots \ {}^{r+1} x^k]^T.$$

From (2) to (8), the loop is repeated until the termination condition is satisfied. The convergence condition for

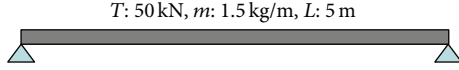


FIGURE 2: Benchmark numerical examples.

the repetition analysis uses the square roots of the sum of square (SRSS) in the following:

$$\left| \sqrt{\left(\sum_{q=1}^n \left| \frac{\omega_q^m - \omega_q^c}{\omega_q^m} \right| \times 100 \right)^2} \right|_{\text{step } r} - \left| \sqrt{\left(\sum_{q=1}^n \left| \frac{\omega_q^m - \omega_q^c}{\omega_q^m} \right| \times 100 \right)^2} \right|_{\text{step } r+1} < 0.01. \quad (9)$$

Finally, tensile force is determined from the identification variables holding at the termination stage and relevant natural frequencies can be determined through the finite element vibration analysis with the identification variables.

To identify the mode shape number of measured natural frequency, a number of sensors are required in the system identification approach based on the finite element model.

However, few sensors (e.g., less than 4 sensors) are enough to get the required number of natural frequency with mode shape (e.g., 2 or 3 modes) in this approach. Furthermore, the sensor location can be varied when there are a limited number of sensors.

The tension estimation results will be compared with existing methods, that is, taut string theory and linear regression method and the governing equations of these two methods are shown as

$$T = 4mL_e^2 \left(\frac{\omega_n}{n} \right)^2, \quad (10)$$

$$\left(\frac{\omega_n}{n} \right)^2 = \frac{T}{4mL_e^2} + \left(\frac{EI\pi^2}{4mL_e^4} \right) n^2,$$

where m , L_e , and EI are mass per unit length, effective length, and flexural rigidity, respectively.

3. Benchmark Numerical Examples

Before the field application of the tension estimation method using the system identification technique, we developed the benchmark example shown in Figure 2 to verify the development theory. In this case, the bending stiffness and boundary conditions of the cable were changed as shown in Table 1 to validate the advantages of the newly developed theory compared to existing ones.

The purpose of C1 and C2 in Table 1 is to check the influence of the bending stiffness, while C2 and C3 are to see the influence of the boundary conditions. For each of the cables, the theoretical first through third natural frequencies are shown in Table 2.

Table 3 shows the results of the tensile force estimations for the three benchmark cables using the taut string theory,



(a) No shielding



(b) Shielding

FIGURE 3: Seven-strand cables.

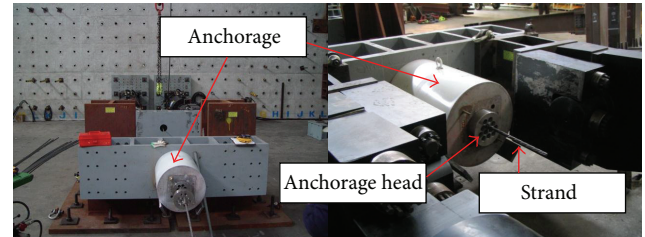


FIGURE 4: Test set-up.

TABLE 1: Variation of parameter for benchmark numerical examples.

Cable ID	Bending stiffness (N-m ²)	Boundary condition
C1	100	Hinged-Hinged
C2	1000	Hinged-Hinged
C3	1000	Fixed-Fixed

TABLE 2: Natural frequencies calculated from benchmark numerical examples (Hz).

Cable ID	1st	2nd	3rd
C1	18.26	36.57	54.79
C2	18.33	37.09	56.69
C3	19.44	39.33	60.12

the linear regression method, and the newly developed method. As shown in Table 3, the taut string theory, which is in capable of considering the bending stiffness, shows the

TABLE 3: Tension estimations error (%) of the benchmark examples.

Cable ID	Taut string theory		Linear regression method	System identification method (this study)
C1	1st	0.08	0.00	0.00
	2nd	0.32		
	3rd	0.71		
C2	1st	0.08	0.00	0.00
	2nd	3.16		
	3rd	7.11		
C3	1st	13.32	12.43	0.00
	2nd	16.01		
	3rd	20.47		

TABLE 4: Estimation error (%) of multiple variables for the cable C2.

Identification variable	Estimation error
T, L	$T = 0.02, L = 0.01$
T, m	$T = 0.13, m = 0.13$
m, L	$m = 0.04, L = 0.02$
T, m, L	$T = 0.77, m = 0.00, L = 0.36$

TABLE 5: Applied tension and extracted natural frequencies.

Test ID	Applied tension (ton)	Extracted natural frequencies (Hz)
Test 1	4.05	21.36, 42.94
Test 2	8.73	30.88, 61.87, 93.41
Test 3	13.46	38.07, 76.35, 114.80
Test 4	18.35	44.31, 88.68

errors in the estimated tensile forces as the bending stiffness increases (C1 to C2.) For tension estimations through the taut string theory and linear regression method, the boundary conditions cannot be considered, which resulted in a significant error in the C3 cable. Also, as the string theory has only one natural frequency, it can estimate the tensile force differently depending on the mode of natural frequency used even under the same tensile force. Therefore, when there is a difference in the natural frequency used in the field without the identification of the natural vibration mode, a big error is inevitable. On the other hand, the method of system identification considers the physical properties and boundary conditions, including bending stiffness. Therefore, the numerical example demonstrated that it is able to estimate the tensile force with precision. In addition, we used the SRSS (square root of sum of square) of the converged errors of the natural frequencies during the field application, which allowed us to indirectly verify the reliability of the estimated tensile force.

Since the tension estimation method using the system identification technique is based on the finite element model, it is possible to estimate not only the tensile force but also the effective length, unit mass, and bending stiffness. It is also capable of estimating single and multiple variables simultaneously. Table 4 shows the results of estimation of multiple variables for the cable C2 in Table 1.

Estimation of the multiple variables can reduce errors in the estimation of tensile force, as it can indirectly determine

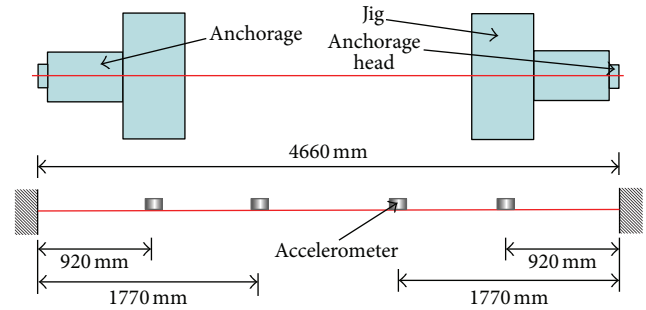


FIGURE 5: Vibration measurement set-up.

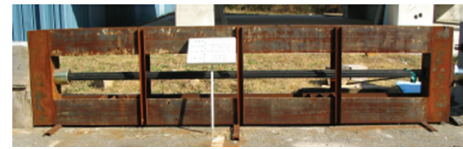


FIGURE 6: Laboratory-scale cable-stayed bridge test sample.

the variable that significantly affects the errors in estimating the tensile force (effective length, boundary conditions, and equivalent unit mass)

4. Application to Laboratory Test Samples

Before we applied the newly developed method that was verified by means of the benchmark numerical example, we applied this new method to two test samples to identify possible problems that might occur during field applications and complement them as necessary.

4.1. Strand Cable Test Sample. Strand cables are composed of 7 smaller wires and are usually the basic element to make PC steel strands or cables for cable stayed bridges and suspended cables. Depending on the application, some strands use additional fillers or shielding to prevent them from being corroded, as shown in Figure 3. The steel strand cable used in this study was a seven-strand cable used for PC steel strand cables, and it had no fillers or shielding.

To check the estimation effect of the tension due to the changes in tension as shown in Figure 4, we used a 3000-kN



FIGURE 7: Vibration test with a laboratory-scale test sample of a cable-stayed bridge.

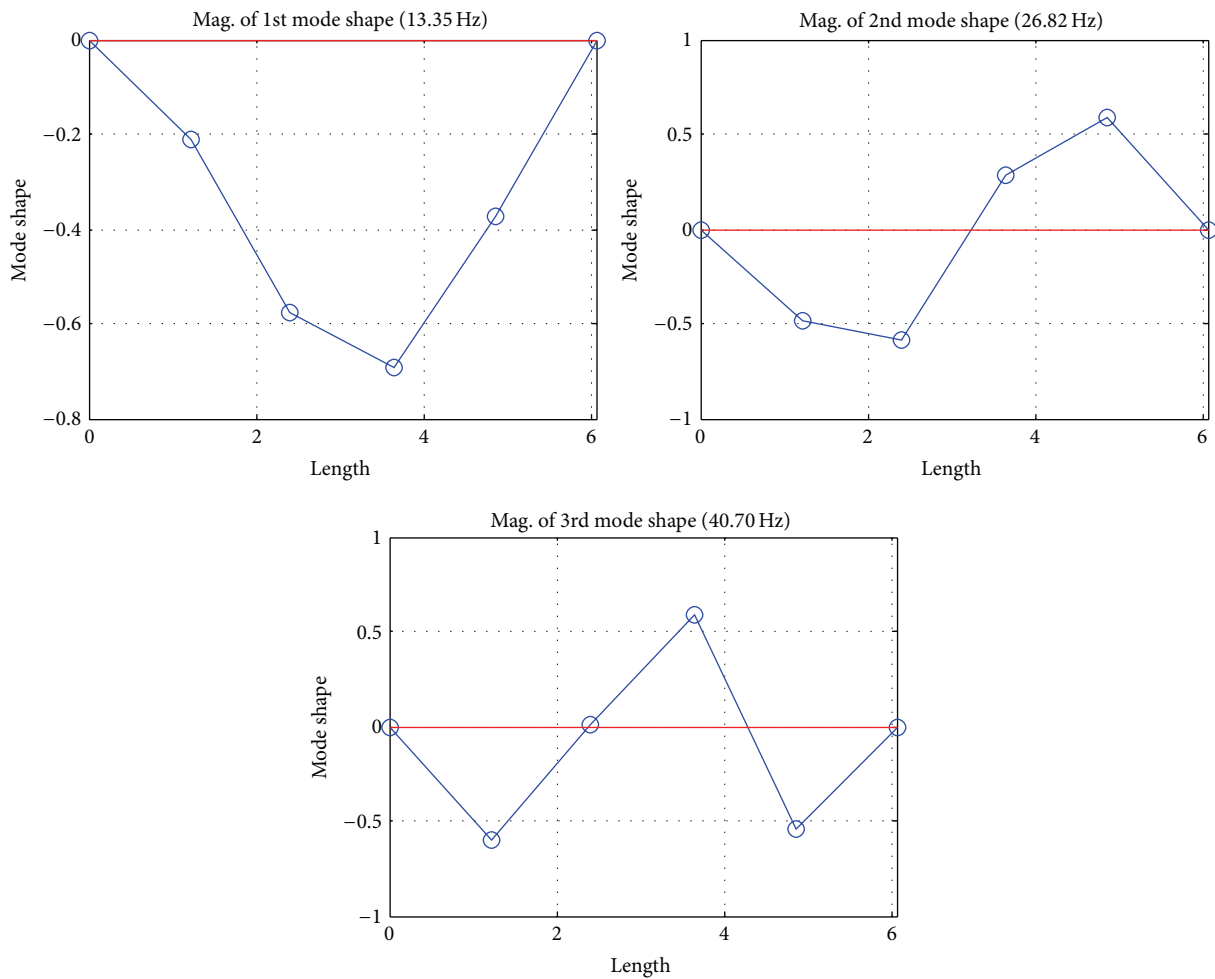


FIGURE 8: Extraction of natural vibration mode for test 1.

actuator that was located in the POSCO steel structure testing center. To measure the signals of acceleration, as shown in Figure 5, we added four accelerometers to the strand cable. The acceleration signal was transmitted to the computer through a wireless logger.

The load was applied in 4 steps. The natural frequency based on the natural vibration mode extracted from the

acceleration signals are shown in Table 5. Here, tests 1 and 4 failed to identify the third natural vibration mode.

As shown in Table 6, the technique of estimating the tensile force using the system identification method turned out to have less errors in terms of tensile force estimation compared to the taut string theory or linear regression method. This is because the existing theories could not

TABLE 6: Applied tension estimation error (%) of strand cables.

Test ID	Taut string theory		Linear regression method	System identification method (this study)
Test 1	1st	11.68	11.29	0.70
	2nd	12.83		
Test 2	1st	8.09	7.74	0.05
	2nd	8.48		
	3rd	9.90		
Test 3	1st	6.61	6.56	0.35
	2nd	7.20		
	3rd	7.72		
Test 4	1st	5.92	5.87	0.62
	2nd	6.07		

TABLE 7: Tension estimation error (%) of a laboratory-scale test sample of a cable-stayed bridge.

Test ID	Taut string theory		Linear regression method	System identification method (this study)
Test 1	1st	12.95	12.35	1.49
	2nd	13.98		
	3rd	16.59		
Test 2	1st	12.95	12.36	1.60
	2nd	14.24		
	3rd	16.94		
Test 3 (Test 4)	1st	14.24	13.44	2.19
	2nd	14.24		
	3rd	17.03		

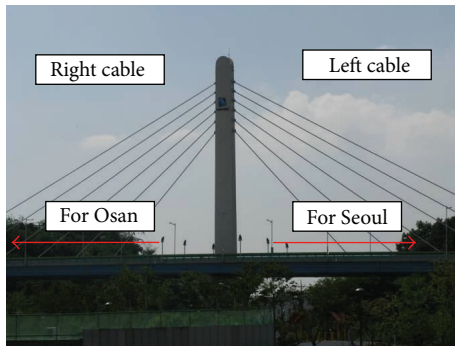


FIGURE 9: Yeongdeok number 1 cable-stayed bridge.

TABLE 8: Mean and standard deviation (%) of tension estimation errors for stay-cable.

Method	Mean	Standard deviation
Taut string theory	4.42	4.59
Linear regression method	4.14	4.29
System identification method (this study)	1.95	1.59

consider the boundary conditions of the strand cable or the bending stiffness.

4.2. Laboratory-Scale Cable-Stayed Bridge Test Sample. In addition to the strand cable test sample, we conducted the tensile force estimation experiment with a laboratory-scale

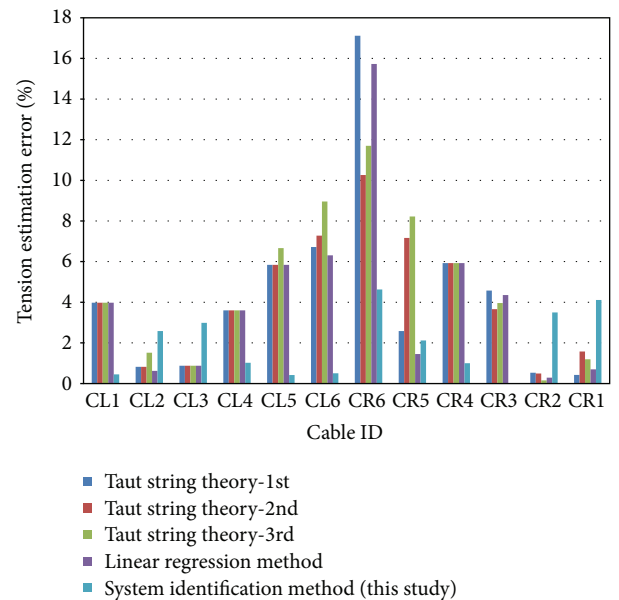


FIGURE 10: Tension estimation error (%) of Yeongdeok number 1 stay-cable.

test sample of a cable-stayed bridge as shown in Figures 6 and 7. In this case, the cable used was shielded steel strand cable, with a tensile force of 30 kN.

To examine the influence on the estimation of the tensile force by the setup of the vibration measurement, we altered the positions of the accelerometers, the hitting point of the impact hammer, and the time of measuring the vibration, in four separate test scenarios.

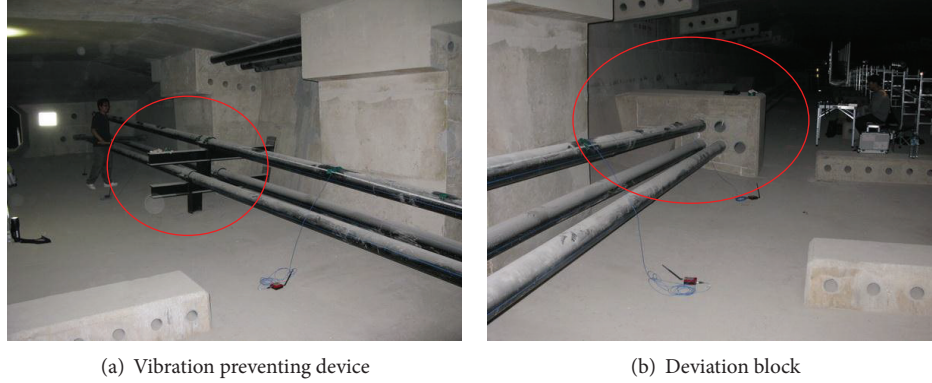


FIGURE 11: External tendon of the approach bridge of Incheon Grand Bridge.

As carried out in the case of the strand cable test, we extracted three natural frequencies for each test. Figure 8 shows the extracted natural vibration modes for test 1. Based on these frequencies, we estimated the tensile force as shown in Table 7, which also shows the technique for estimating the tensile force using the system identification method. This turned out to have fewer errors in terms of tensile force estimation compared to the taut string theory or the linear regression method, as with the case of steel strand cables.

5. Field Application

We verified the feasibility of the system identification method, which was verified by the tests with laboratory-scale test samples, by estimating the tensile forces in the field.

5.1. Stay-Cable of Yeongdeok Number 1 Bridge. The first test in the field was conducted with the cables in a cable-stayed bridge, for which the tension estimations in the field were being performed using existing theories (string theory, linear regression). Yeongdeok number 1 Bridge is a cable-stayed bridge located in Giheung district, Youngin-si, Gyeonggi-do. This bridge uses PPWS (prefabricated parallel wire strands) cables.

We estimated the tensile forces of 12 cables on both sides of the bridge as shown in Figure 9 and compared the estimation results from the existing methods and new method. Figure 10 shows that the force estimation made by the system identification method has errors not exceeding 5%. However, the existing methods, in some cases, showed a high level of errors. However, the methods of estimating the tensile force using the existing theories also yielded relatively desirable outcomes. This is because the length of cable stays of the bridge is within a range from 44 m to 95 m, which is relatively long and similar to the assumptions used in the existing theories.

The tension estimation method using the system identification shown in Table 8 has a relatively smaller standard deviation for the estimation errors compared to those of the existing theories. Therefore, the tensile forces are able to be estimated with more reliability.

TABLE 9: Mean and standard deviation (%) of tension estimation errors for external tendon.

Method	Mean	Standard deviation
Taut string theory	18.60	7.61
Linear regression method	11.13	4.19
System identification method (this study)	3.11	2.21

5.2. External Tendon for the Approach Bridge Section of Incheon Grand Bridge. The external tendon for normal bridges is applied during the construction phase or afterwards for reinforcing the structure. To check the applicability of the system identification method for such external tendons, we applied this method to the external tendons of the approach bridge section of the Incheon Grand Bridge. The external tendons, unlike cables in cable-stayed or suspension bridges, installed deviation blocks, or vibration preventing device between the external tendons, as shown in Figure 11. Also, the external tendon was shielded in HDPE pipes and the interior was filled with mortar to prevent corrosion. Therefore, it was difficult to apply the existing theories, and there is no other way used in the field to examine the tension except load cells.

Figure 12 and Table 9 show that existing theories show significant errors with the external tendon, which is unlike the cases in the cable stays in the Yeongdeok Bridge number 1. This is because the external tendon differs significantly in many aspects of the assumptions. The tension estimation technique using the system identification method showed increased errors from the level in Yeongdeok Bridge. Still, however, the range of errors did not exceed 5%.

5.3. Extradosed Cable for Aam Bridge. Aam Bridge of Figure 13 constructed in the approach sector of the Incheon Grand Bridge. It was built as an extradosed bridge, which is similar to a cable stayed bridge and uses MS (multistrand) cables that are shielded in HDPE pipes. There is no separate grouting inside the cable. Figure 14 shows the vibration measurement set-up of an extradosed cable.

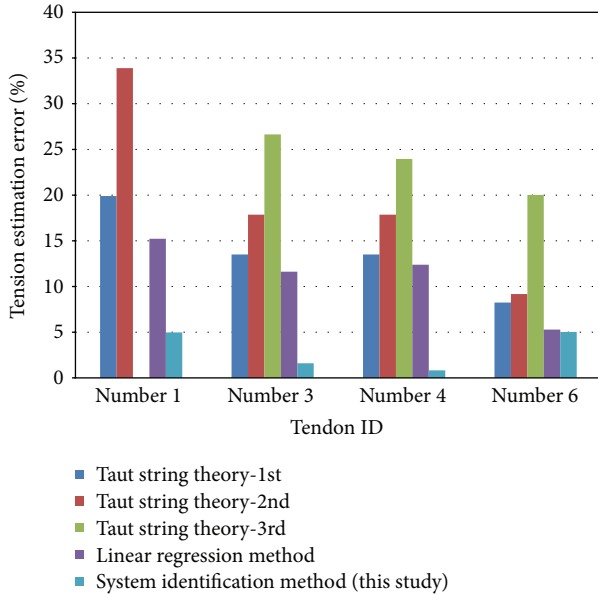


FIGURE 12: Tension estimation error (%) of external tendon of Incheon Grand Bridge.



FIGURE 13: An overall view of Aam Bridge.

TABLE 10: Mean and standard deviation (%) of tension estimation errors for extradosed cables.

Method	Mean	Standard deviation
Taut string theory	1.93	1.24
Linear regression method	1.08	0.54
System identification method (this study)	2.27	1.34

The cables used in Aam Bridge are relatively long in length, and the estimation results of their tension using the existing theories, as shown in Figure 15 and Table 10, show somewhat improved results compared to those of the system identification method. However, all methods showed tensile force estimation errors within a range of 5%. Therefore, the system identification method is thought to be applicable to the field operations if field engineers assume a $\pm 5\%$ error when estimating tensile force due to errors in the acceleration signal measurements, material properties, and geometrical variable errors, and other environmental errors that cannot be excluded theoretically, such as thermal influence.

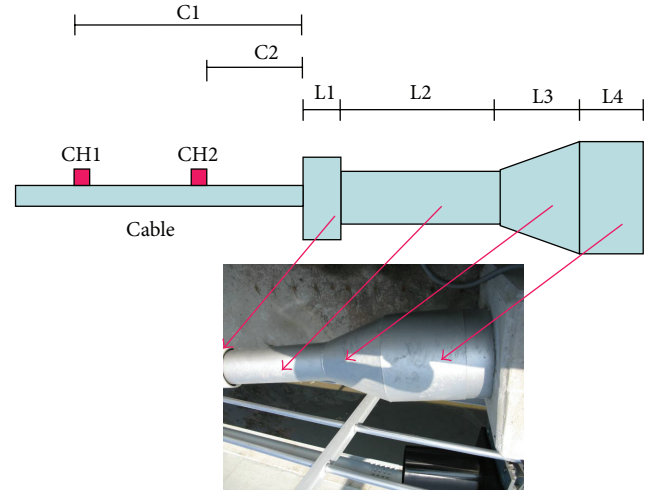


FIGURE 14: Vibration measurement set-up.

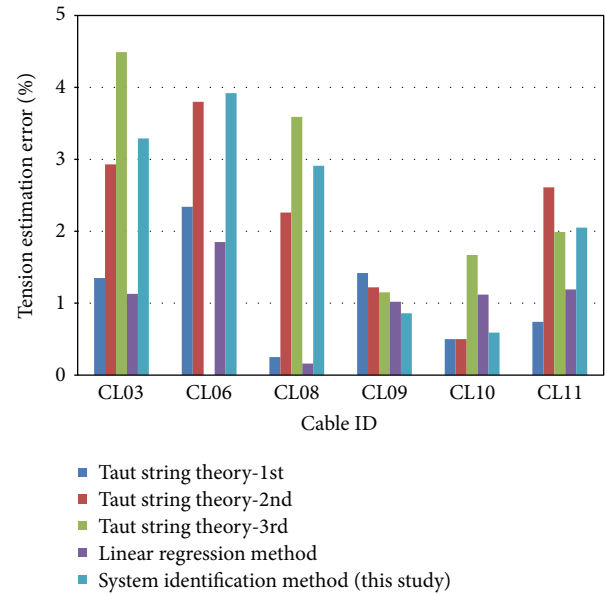


FIGURE 15: Tension estimation error (%) of Aam Bridge.

5.4. The Sigma Level Calculation of the Field Application Results. The statistical information (i.e., error of estimation method) is very important to field engineers. Therefore, as shown in Figures 16, 17, and 18, we performed sigma-level calculations for three field application results based on each tensile force estimation method to verify their reliabilities and applicability. In this case, the string theory and the linear regression methods differed in terms of their error level depending on the site, which did not satisfy the requirements for regularity. Therefore, the DPMO (Defect Per Million Opportunities) method was used for a short-term sigma-level calculation. As for the system identification method, it satisfied the regularity requirement, and the Z-bench value was used to calculate the short-term sigma level. In all methods, a tensile force estimation error of 5% was set as the upper limit.

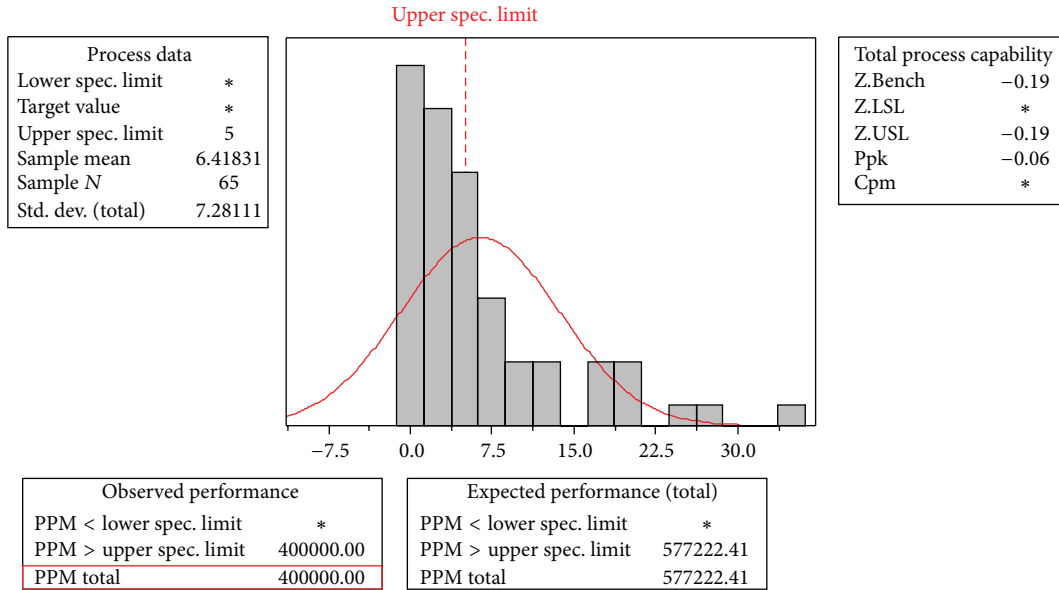


FIGURE 16: Process capability of field application error for the taut string theory.

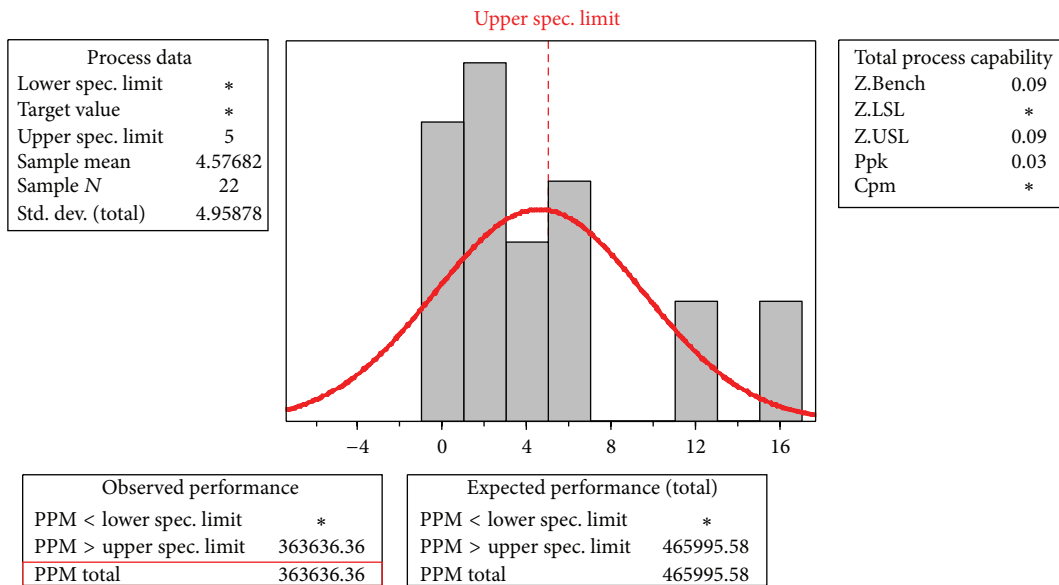


FIGURE 17: Process capability of field application error for the linear regression method.

As with Table 11, the system identification method was shown to be a better method than existing theories in terms of field applicability for external tendons of various types if the yield and short-term sigma level are compared.

6. Conclusion

This study used the system identification method for estimating the tensile force of external tendons to benchmark numerical examples, laboratory test samples, and field structure to get the following conclusion.

The string theory and the linear regression method are based on theoretical closed-form equations. For this reason, they showed an allowable level of errors in terms of estimating the tensile force for the field applications with the external tendons that had similar characteristics with the assumptions used in deriving the relationship equations between the natural frequencies and tensile forces (for Yeongdeok number 1 Bridge and Aam Bridge). However, they were not applicable for field applications as the errors were too large for the external tendons with different properties from those assumed, whereas the tension estimation method using the system

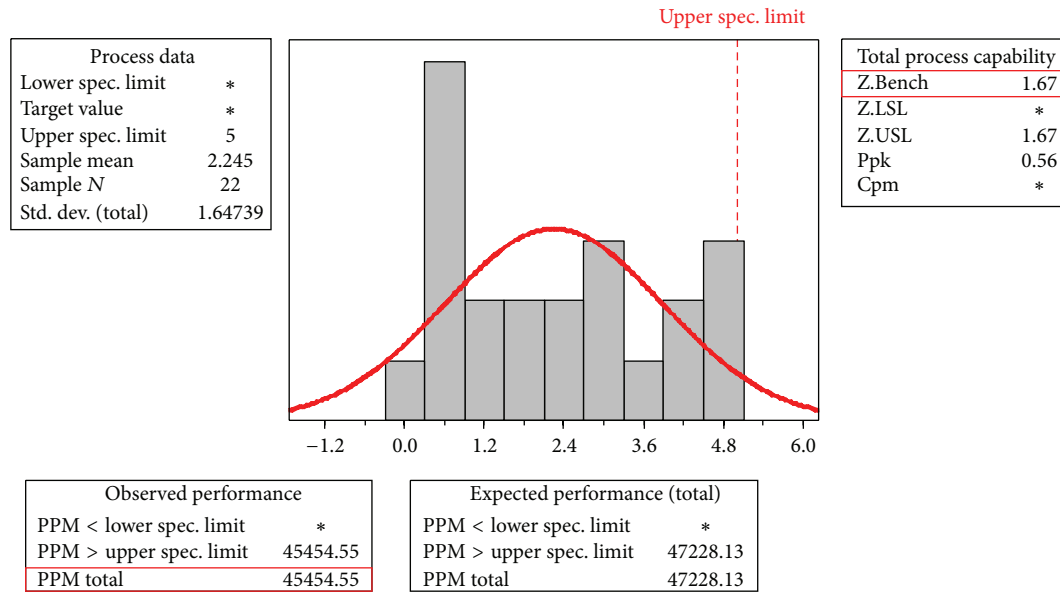


FIGURE 18: Process capability of field application error for the system identification method.

TABLE 11: Final yield and short-term sigma level.

Method	DPMO/Z-bench	Yield (%)	Short-term sigma level
Taut string theory	400,000	60.0	1.75
Linear regression method	363,636	63.6	1.85
System identification method (this study)	1.67	95.3	3.17

identification technique was applicable not only to the external tendons to which the existing theories could be applied (Yeongdeok number 1 Bridge and Aam Bridge) but also to the external tendons to which they could not be applied (approach bridge section of Incheon Grand Bridge). This is because the development method was based on the finite element model. Also, the newly developed method could use the SRSS errors between the measurements of natural frequencies and their calculated results to determine the reliability of the estimated tensile force. Therefore, the tensile force estimation method using the system identification technique could be used efficiently to estimate the tensile forces of various types of external tendons.

Conflict of Interests

The authors declare that there is no conflict of interests regarding the publication of this paper.

Acknowledgments

This research was supported by the Construction Core Technology Program funded by the Ministry of Construction & Transportation of the Korean government (Grant no. 2006-D20). The financial support is gratefully acknowledged.

References

- [1] H. M. Irvine, *Cable Structures*, The MIT Press, Cambridge, Mass, USA, 1981.
- [2] H. Zui, T. Shinke, and Y. Namita, "Practical formulas for estimation of cable tension by vibration method," *Journal of Structural Engineering*, vol. 122, no. 6, pp. 651–656, 1996.
- [3] W.-H. P. Yen, A. B. Mehrabi, and H. Tabatabai, "Evaluation of stay cable tension using a non-destructive vibration technique," in *Proceedings of the 15th Structures Congress*, pp. 503–507, ASCE, New York, NY, USA, April 1997.
- [4] A. B. Mehrabi and H. Tabatabai, "Unified finite difference formulation for free vibration of cables," *Journal of Structural Engineering*, vol. 124, no. 11, pp. 1313–1322, 1998.
- [5] T. Park and B. H. Kim, "Estimation of cable tension using system identification technique: I. theory," *Journal of the Korean Society of Civil Engineers*, vol. 25, no. 4A, pp. 661–668, 2005.
- [6] T. Park, S. Moon, H. J. Joo, and B. H. Kim, "Estimating tensile force of hangers in suspension bridges using frequency based SI technique: I. Theory," *Journal of the Korean Society of Civil Engineers*, vol. 27, no. 2, pp. 165–172, 2007.

Research Article

Probabilistic Risk Assessment: Piping Fragility due to Earthquake Fault Mechanisms

Bu Seog Ju,¹ WooYoung Jung,² and Myung-Hyun Noh³

¹ Department of Civil Engineering, North Carolina State University, Raleigh, NC 27695, USA

² Department of Civil Engineering, Gangneung-Wonju National University, Gangneung 210-702, Republic of Korea

³ Steel Solution Center, POSCO, 100 Songdo Gwahak-ro, Yeonsu-gu, Incheon 406-840, Republic of Korea

Correspondence should be addressed to Myung-Hyun Noh; mnoh@posco.com

Received 28 July 2014; Accepted 15 September 2014

Academic Editor: Sang-Youl Lee

Copyright © 2015 Bu Seog Ju et al. This is an open access article distributed under the Creative Commons Attribution License, which permits unrestricted use, distribution, and reproduction in any medium, provided the original work is properly cited.

A lifeline system, serving as an energy-supply system, is an essential component of urban infrastructure. In a hospital, for example, the piping system supplies elements essential for hospital operations, such as water and fire-suppression foam. Such nonstructural components, especially piping systems and their subcomponents, must remain operational and functional during earthquake-induced fires. But the behavior of piping systems as subjected to seismic ground motions is very complex, owing particularly to the nonlinearity affected by the existence of many connections such as T-joints and elbows. The present study carried out a probabilistic risk assessment on a hospital fire-protection piping system's acceleration-sensitive 2-inch T-joint sprinkler components under seismic ground motions. Specifically, the system's seismic capacity, using an experimental-test-based nonlinear finite element (FE) model, was evaluated for the probability of failure under different earthquake-fault mechanisms including normal fault, reverse fault, strike-slip fault, and near-source ground motions. It was observed that the probabilistic failure of the T-joint of the fire-protection piping system varied significantly according to the fault mechanisms. The normal-fault mechanism led to a higher probability of system failure at locations 1 and 2. The strike-slip fault mechanism, contrastingly, affected the lowest fragility of the piping system at a higher PGA.

1. Introduction

In the event of earthquake, the fire-protection piping system (sprinkler piping system), as an essential nonstructural component in critical facilities such as hospitals, emergency clinics, and high-tech factories, must remain secure and operational in order to prevent the damage from fire. Interestingly, many previous reports have attributed the most serious earthquake damage to the poor performance of nonstructural components such as HVAC, ceiling system, and fire-protection piping system [1] rather than to structural components. The Olive View Hospital, for example, seismically retrofitted after the 1971 San Fernando earthquake, did not incur any structural damage from the 1994 Northridge event. However, due to leakages from the fire-protection piping system and the chilled water distribution system, the hospital had to be shut down, further necessitating the evacuation of 377 patients [2]. During the 1995 Kobe

earthquake in Japan, 40.8% of fire-suppression systems such as sprinkler piping systems were damaged [3], due to the acute seismic vulnerability of sprinkler piping systems (as part of fire-protection piping systems) relative to other fire-suppression systems such as indoor fire hydrants, foam-based extinguishing systems, and fire doors.

In order to prevent or minimize damage from fire, hospitals' nonstructural components including automatic fire alarm systems, HVAC systems, and fire-protection piping systems (sprinkler piping systems) must remain operational and functional both during and after earthquakes. In recent years, significant research has been conducted to evaluate the seismic performance and vulnerability of fire-protection piping systems in hospitals according to earthquake engineering principles. Antaki and Guzy [4] performed a seismic performance analysis of a fire-protection piping system incorporating grooved and threaded connections. Also, the University of Buffalo [5, 6] conducted experimental tests on

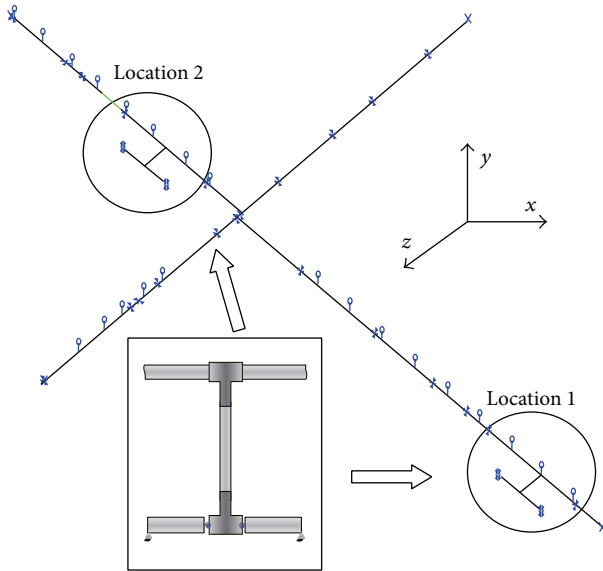


FIGURE 1: Sprinkler piping system configuration with multibranch systems [7].

a sprinkler piping system under monotonic and cyclic loading conditions, with respect to two connection types (threaded T-joint and grooved T-joint) and two materials (black iron and chlorinated polyvinyl chloride (CPVC)).

Based on the outcomes of relevant previous investigations [7, 8, 11], the present study, in order to reduce seismic-induced fire risk and develop a probabilistic risk assessment protocol for sprinkler piping systems in hospitals, (1) incorporated an analytical and numerical nonlinear T-joint model specified by experimental-test-derived moment-rotation relationships, (2) considered various seismic ground-motion intensities and various fault mechanisms as a function of uncertainties, (3) conducted multiple nonlinear time-history analyses for a Monte Carlo simulation, and (4) estimated the system's change of probabilistic failure and acceleration sensitivity according to various earthquake-fault mechanisms.

2. Fire-Protection Piping System

Taking the lead of Ju and Jung [7], a hospital's top-floor main piping system (designed according to the NFPA-13 [12] and SMACNA [13] seismic guidelines), with two nonlinear T-joint branch systems supported by unbraced single hangers, transverse braced hangers, and longitudinal braced hangers, was selected for the purposes of the present study. The particular locations of the multibranch piping systems were determined, by linear time-history analysis of the complete piping system, to be the first and second maximum displacements and rotations. Figure 1 illustrates the piping system configuration considered in this study. The natural frequencies of the piping system in the fundamental and second modes were 1.82 (Hz) and 3.28 (Hz), respectively.

2.1. Finite Element (FE) Model of T-Joint System [7]. The existence of many connections and linkages in a sprinkler

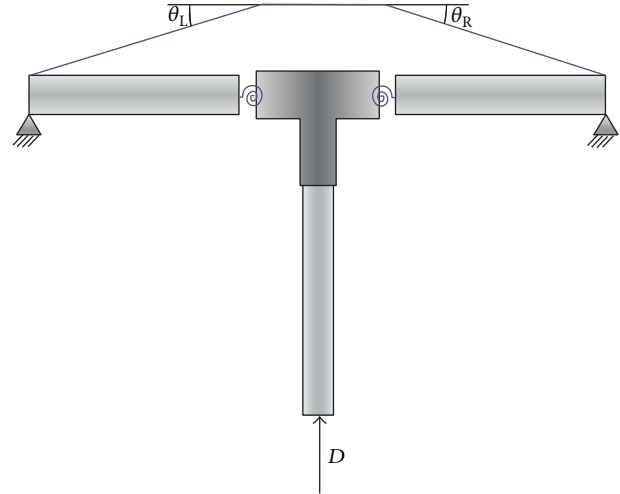


FIGURE 2: FE model of T-joint system [8].

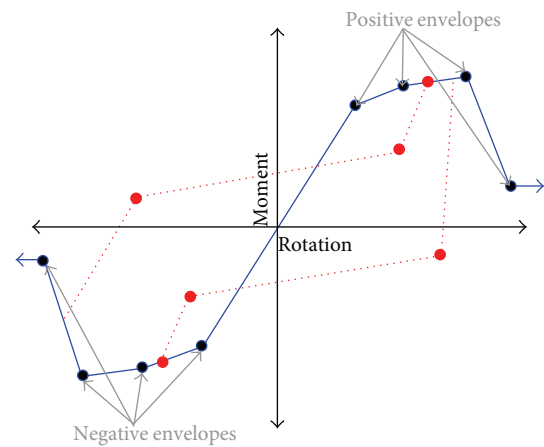


FIGURE 3: *Pinching4* material in *OpenSees* [9].

piping system causes complex nonlinear behavior. In the study of nonlinear behavior by FE analysis, dense mesh and special contact elements often are required; however, considering these factors in fragility estimation can be computationally inefficient. Therefore, in the present study, a nonlinear moment-rotation relationship obtained from University of Buffalo (UB) cyclic-experimental data [5, 6] was used to generate the nonlinear FE model of a threaded T-joint in a 2-inch black iron branch piping system. Figure 2 provides a schematic of the FE model, which represents the system's nonlinear behavior by two nonlinear rotational springs. Smaller rotations were allowed by means of a hinge supporting the branch pipes. The load was applied at the bottom along the perpendicular axis. The *Pinching4* uniaxial material was applied on the *OpenSees* platform [14]. The *Pinching4* material shown in Figure 3 used various parameters such as positive and negative response envelopes, the ratio of deformation, force, and strength under unloading conditions, and the ratio of deformation, force, and strength under reloading conditions. Furthermore, the *Pinching4* material model was able to represent the stiffness degradation, the strength

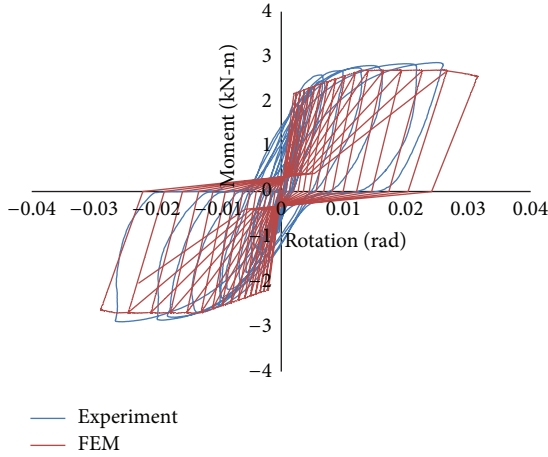


FIGURE 4: Validation of FE model for 2-inch threaded T-joint system [8].

degradation, and the unloading/reloading conditions under cyclic loading [9]. Figure 4 plots the validation data on the FE model for the threaded T-joint system. The moment-rotation relationship obtained in the FE analysis was in good agreement with the experimental values.

3. Seismic Ground Motions

Damage to a nonstructural fire-protection piping system subjected to seismic ground motions is a function of the strength and deformation capacity of each component. Damage to structural and nonstructural components, meanwhile, correlates with both input and dissipated energy [15]. In the present study, various ground motions, namely, normal-fault, reverse-fault, strike-slip fault, and near-source ground motions, were applied in order to investigate the effect of input and dissipated energy on the piping system. Ground motions over the Richter magnitude M_w 6.0 were selected from PEER-NGA [16], and near-source ground motions influenced by a few pulses were borrowed from Sasani et al. [15]. Each earthquake dataset was normalized to the same peak ground acceleration (PGA) (1.0 g). Figures 5(a) to 5(d) provide the response spectra for a 5% damping ratio. The thick solid curve indicates the mean value of the response spectra.

The dynamic equation of motion for this piping system subjected to earthquakes can be expressed as

$$[M] \{\ddot{u}(t)\} + [C] \{\dot{u}(t)\} + [K] \{u(t)\} = -[M] \{\ddot{u}_g(t)\}, \quad (1)$$

where M , C , K , and $\ddot{u}_g(t)$ are mass, damping, stiffness, and ground acceleration, respectively. In particular, Rayleigh classical damping known as mass and stiffness proportional damping was used in order to generate damping matrix. The damping equation is as follows:

$$[C] = \alpha [M] + \beta [K]. \quad (2)$$

The mass and stiffness coefficients (α and β) can be described as follows:

$$\frac{1}{2} \begin{bmatrix} \frac{1}{\omega_i} & \omega_i \\ \frac{1}{\omega_j} & \omega_j \end{bmatrix} \begin{Bmatrix} \alpha \\ \beta \end{Bmatrix} = \begin{Bmatrix} \xi_i \\ \xi_j \end{Bmatrix}, \quad (3)$$

in which ω_i and ω_j are the natural frequency for the i th and j th modes. Also, ξ_i and ξ_j are the specified damping ratios for the i th and j th modes [17]. Specifically, in this study, 2% damping ratio was applied for the black iron piping system.

4. Probabilistic Risk Assessment of Piping System

Probabilistic risk assessment and performance-based design are practical approaches to the mitigation of potential fire, hurricane, or earthquake damage to structural systems [18]. Additionally, the Electric Power Research Institute (EPRI) recently formulated a fragility analysis methodology for use in probabilistic risk assessment (PRA) of nuclear power plants [19]. According to Shinozuka et al. [20], the empirical fragilities based on lognormal distribution function were classified into two different methods: (1) Parameter Estimation (Method 1) by means of the maximum likelihood procedure and (2) Parameter Estimation (Method 2) by log-standard deviation along with the medians of the lognormal distribution in terms of the aid of maximum likelihood method. The maximum likelihood function for Method 1 can be expressed as

$$L = \prod_{i=1}^N [F(a_i)]^{x_i} [1 - F(a_i)]^{1-x_i}, \quad (4)$$

where $F(a_i)$ indicates the probability of failure with respect to the specified damage level and the analytical solution for the fragility curve was given by

$$F(\cdot) = \Phi \left[\frac{\ln(a/c)}{\varsigma} \right], \quad (5)$$

where parameter “ a ” is peak ground acceleration (PGA).

Furthermore, the fragility (Method 2) corresponding to four damage states (E_1 , E_2 , E_3 , and E_4) is described by two parameters: median (m_c) and lognormal standard deviation (β_{sd}) given in

$$F(\cdot) = \Phi \left[\frac{\ln(a_i/m_c)}{\beta_{sd}} \right]. \quad (6)$$

The probability of failure for each damage state (no damage, minor, moderate, and major damage) at given PGA levels was also described as follows:

$$\begin{aligned} P_1 &= P(a_i, E_1) = 1 - F_1(\cdot), \\ P_2 &= P(a_i, E_2) = F_1(\cdot) - F_2(\cdot), \\ P_3 &= P(a_i, E_3) = F_2(\cdot) - F_3(\cdot), \\ P_4 &= P(a_i, E_4) = F_3(\cdot). \end{aligned} \quad (7)$$

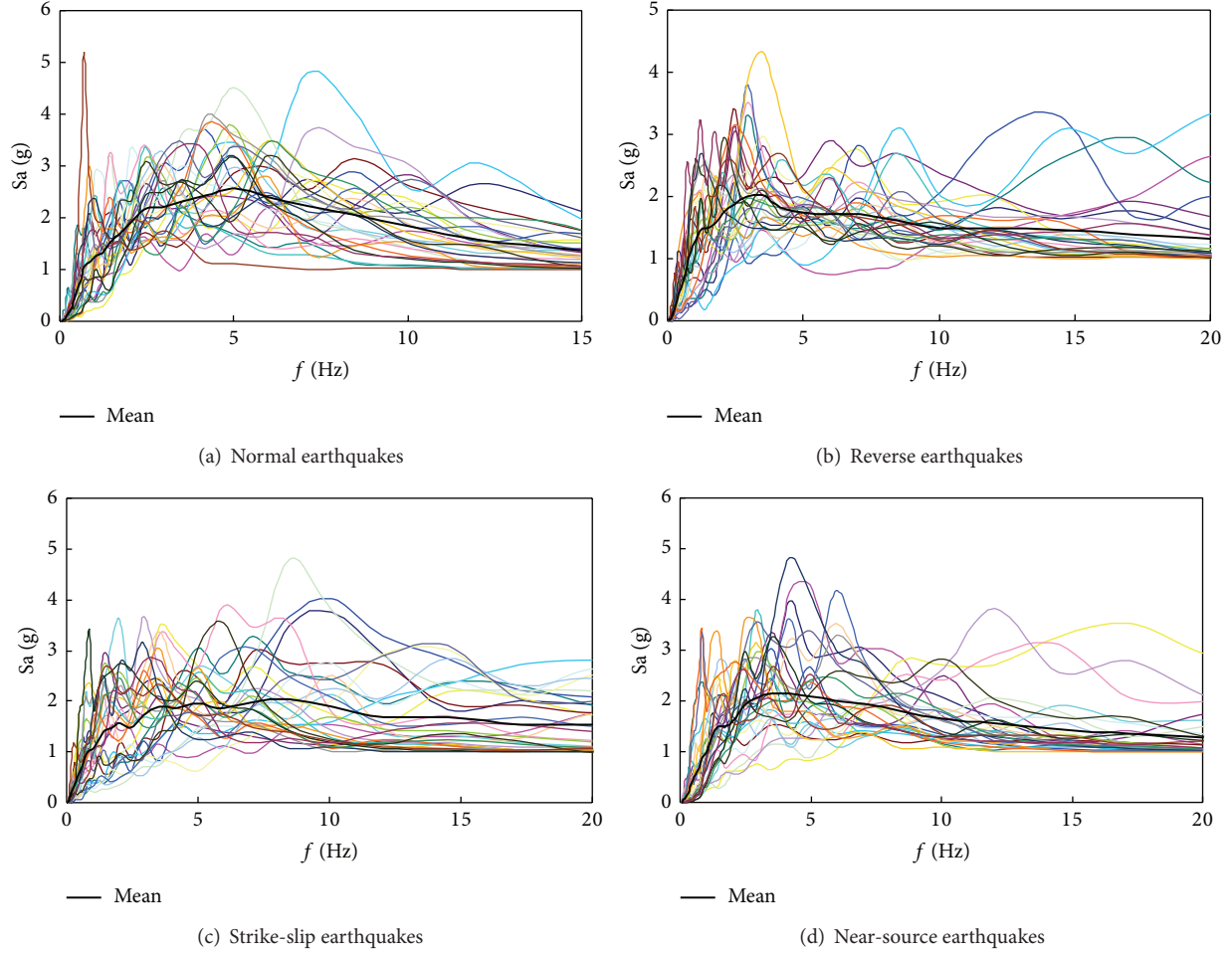


FIGURE 5: Seismic ground motions: response spectra based on fault mechanisms.

In this case, the likelihood function can be generalized as

$$L(\cdot) = \prod_{i=1}^N \prod_{j=1}^4 P_j(a_i; E_j)^{x_{ij}}. \quad (8)$$

Further details for the analytical fragility methodology can be found in the study by Shinozuka et al. [20].

Based on this fragility analysis (Parameter Estimation: Method 2), Ju et al. [8] defined the probability of failure of a fire-protection piping system as follows:

$$P_f(\lambda) = P[G(\cdot) < 0 \mid \text{Earthquake Intensity} = \lambda], \quad (9)$$

$$P_f(\lambda) = P[C < D \mid \text{PGA} = \lambda],$$

in which $G(\cdot)$ represents failure limit state, C is the capacity or strength of the system, and D is the load or demand.

Nonstructural fragilities, which are engineering demand parameter (EDP) functions, indicate the probabilities that certain nonstructural components will exceed a certain level of damage [18]. Equation (9) above formulates fragility for a peak ground acceleration (PGA) level of λ .

Structural fragilities, meanwhile, are estimated empirically by conducting multiple nonlinear time-history analyses of a structure for various ground motions:

$$P_f(\lambda) = \frac{\sum_{i=1}^N 1(\theta_{i,\lambda} \geq \theta_{\text{lim}} \mid \text{PGA} = \lambda)}{N}. \quad (10)$$

In (10), $\theta_{i,\lambda}$ is the maximum rotation from the i th earthquake time-history analysis at a PGA level of λ , and $1(\cdot)$ is the indicator function.

5. Limit State of 2-Inch T-Joint System

As (9) and (10) reflect, it was necessary to characterize the limit state criteria corresponding to fire-protection piping system damage. Failure due to leakage generally predominated over support system failure in this study. Therefore, the American Society of Mechanical Engineers (ASME) BPVP code (Section 3) defined rotation corresponding to plastic collapse of piping components using the “twice the elastic slope” (TES) criteria [8]. Based on these criteria, the rotation corresponding to plastic collapse θ_φ can be determined by the abscissa of the point at which a line with twice the elastic

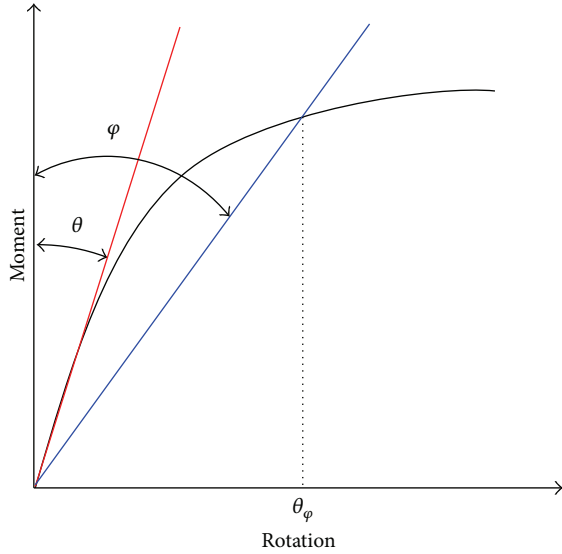


FIGURE 6: Twice elastic slope (TES) criteria [8].

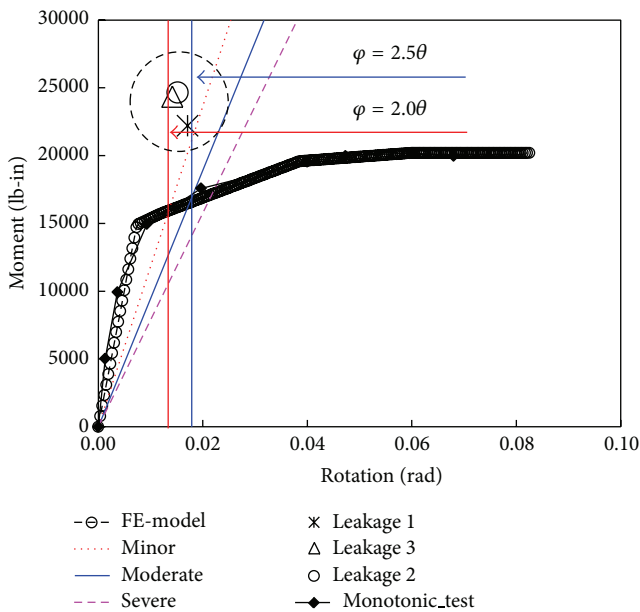


FIGURE 7: Damage states of 2-inch threaded T-joint piping system [8].

slope intersects the moment-rotation curve. This condition is exemplified in Figure 6, where $\varphi = 2\theta$. In Figure 7, the rotations of the left spring corresponding to the “First-Leak” damage state during three cyclic tests are plotted along with the moment-rotation relationship obtained from the experimental data. It can be seen that all three failure rotations lay between the lines $\varphi = 2\theta$ and $\varphi = 2.5\theta$, where θ is the elastic slope. It can be concluded that the TES ($\varphi = 2\theta$) criteria can be conservatively assumed as the limit state corresponding to the “First Leak” (0.0135 radians) [8]. Hence, three damage states are defined by minor (0.0135 rad), moderate (0.0175 rad), and severe damage (0.0217 rad), respectively.

6. Seismic Fragility of Fire-Protection Piping Systems Subjected to Various Fault Mechanisms

The piping-system seismic fragility evaluation presented in this paper was based on analyses of multiple nonlinear time-histories as functions of uncertainties such as magnitude, soil types, and fault mechanisms. The evaluation proceeds as follows.

- (1) Select seismic ground motions of each fault mechanism (normal, reverse, and strike-slip) and near-source ground motions as functions of uncertainties.
- (2) Incorporate the nonlinear T-joint FE model into the main piping system based on the experimental result.
- (3) Perform multiple nonlinear time-history analyses by means of a Monte Carlo simulation (MCS) of the fire-protection piping system on the *OpenSees* platform.

Finally, from the numerical analyses, the absolute maximum inelastic rotations were obtained, and the numerical fragility curves for the three different fault mechanisms and near-source ground motions were evaluated by (10). Figure 8 showed the procedure of system fragility analysis based on Monte Carlo simulation [10]. The nonlinear time-history analyses were conducted at many PGA levels ranging from 0.2 g to 4.0 g increments.

The fragility estimates (i.e., probabilities of failure) corresponding to the piping system’s limit state of inelastic rotation (0.0135 radians) for each fault mechanism case are compared in Figure 9. The fragility of a fire-protection piping system subjected to 50 seismic ground motions (50 EQs) was determined by Ju and Jung [7]. As shown in the figure, the probability of failure at location 1 significantly differed among the four earthquake types. The piping system subjected to 50 EQs was most fragile under the normal-fault mechanism and yielded greatly. The fragility values according to the reverse and near-source ground motions tended to show similar probabilities of failure. The maximum probability difference, between the normal- and strike-slip fault mechanisms, was approximately 40% at the PGA of 1.8 g.

Figure 10 plots the probabilities of failure at location 2. Overall, the fragility values there were lower than at location 1. The fragility as subjected to the normal-fault mechanism was highly conservative, showing a similar pattern to that indicated in Figure 9. However, the values with respect to the probability of failure at location 2 under the reverse-fault mechanism were significantly lower than the other values up to the PGA of 2.5 g. The maximum fragility difference, this time between the normal- and reverse-fault mechanisms, was approximately 41% at the PGA of 2.2 g. Also, analytical fragility curves (solid lines) for each case are evaluated by (6) and median and lognormal standard deviation (Table 1) is obtained from numerical fragility analyses (MCS). Based on (7), Figure 11 illustrates the damage-state (minor, moderate, and severe damage) probabilities of the piping system subjected to normal earthquake-fault mechanism at locations 1 and 2.

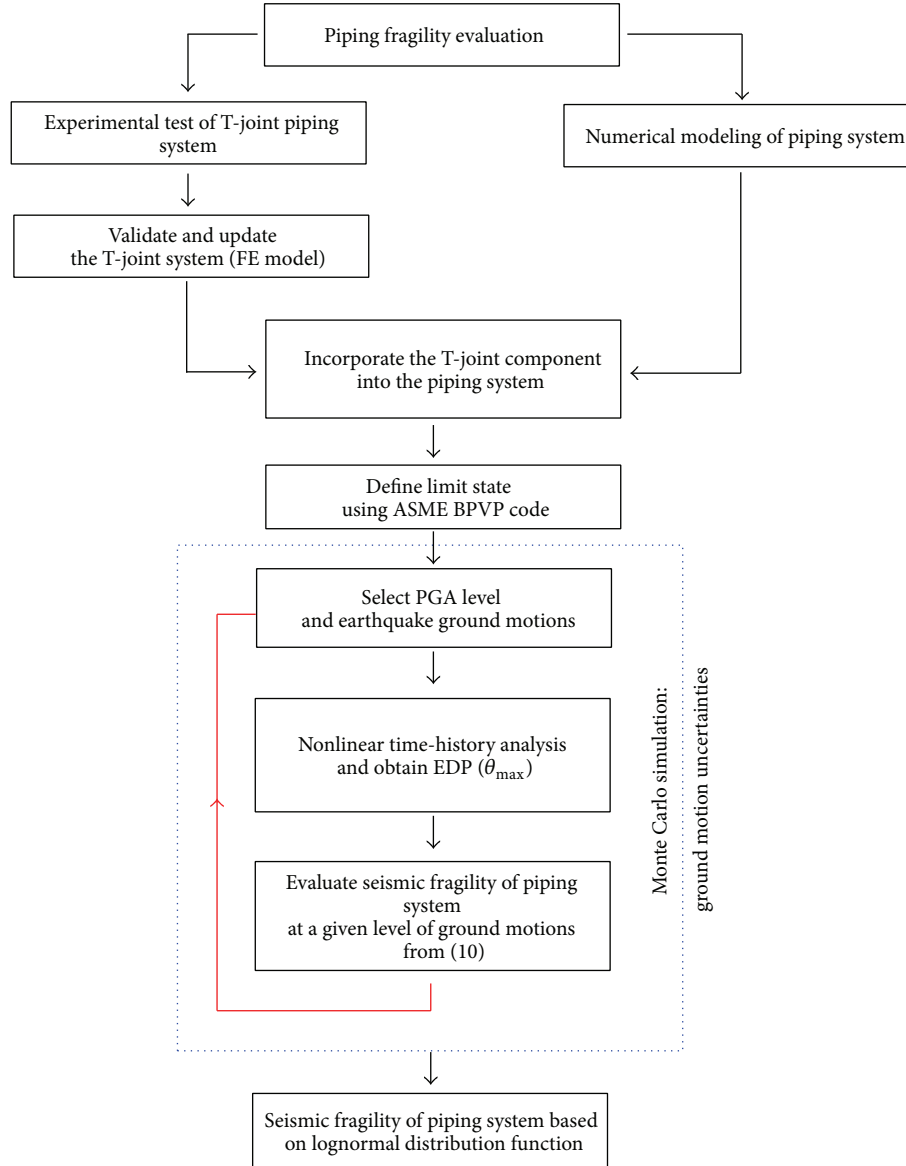


FIGURE 8: Flowchart of seismic fragility of piping system [10].

TABLE 1: Median and lognormal standard deviation variables.

Fault mechanisms	Location 1		Location 2	
	m_c	β_{sd}	m_c	β_{sd}
Normal	0.4835	0.2534	0.6264	0.3594
Reverse	0.6679	0.3945	0.9095	0.2598
Strike-slip	0.8144	0.5210	0.9270	0.5167
Near-source	0.6752	0.2948	0.7792	0.3963
50 EQs	0.4144	0.3741	0.6771	0.3398

In addition, in order to generate entire fragility corresponding to particular damage state, the ground acceleration capacity (A) related to median ground acceleration capacity (a_m) and lognormal random variables ($\epsilon_R \epsilon_U$) in terms of the

median and uncertainty in the median value must be defined by [21]

$$A = a_m \epsilon_R \epsilon_U. \quad (11)$$

Therefore, the median PGA capacities (50% probability of failure) at locations 1 and 2 are listed in Table 2. The primary reason for the differences among the fragility values was the sensitive response of the piping system to the seismic ground-motion frequency and acceleration.

7. Conclusions

This study developed a framework for probabilistic risk assessment of fire-protection piping systems (sprinkler piping systems) subjected to various earthquake-fault mechanisms in order to improve their seismic performance and reduce

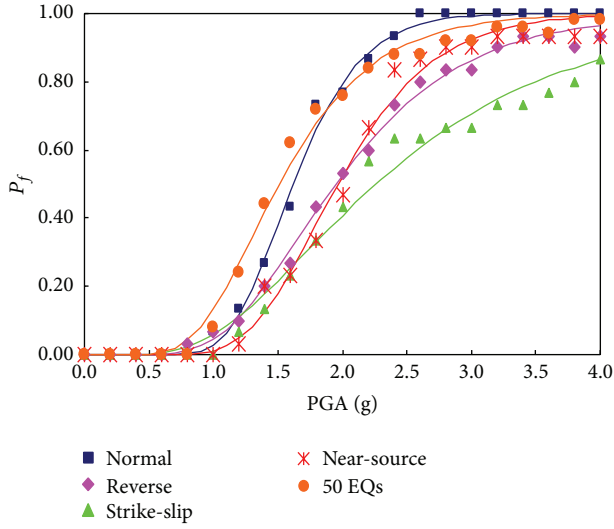


FIGURE 9: Probabilities of failure of fire-protection piping system at location 1.

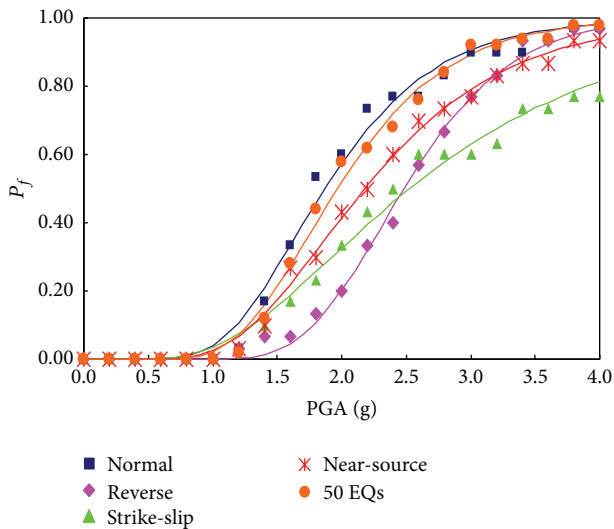
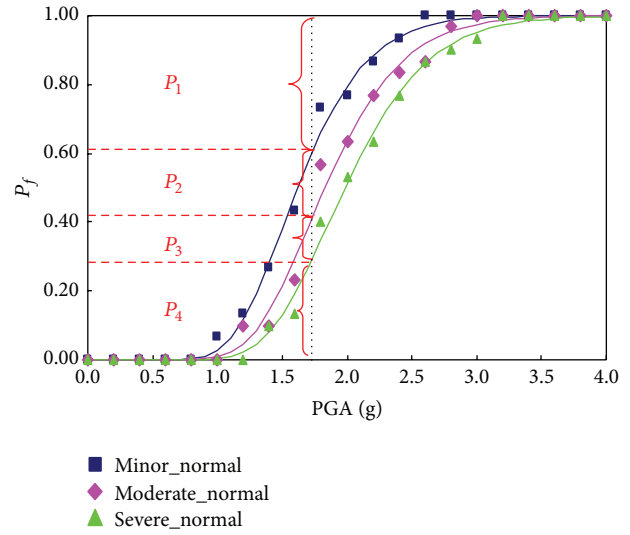


FIGURE 10: Probabilities of failure of fire-protection piping system at location 2.

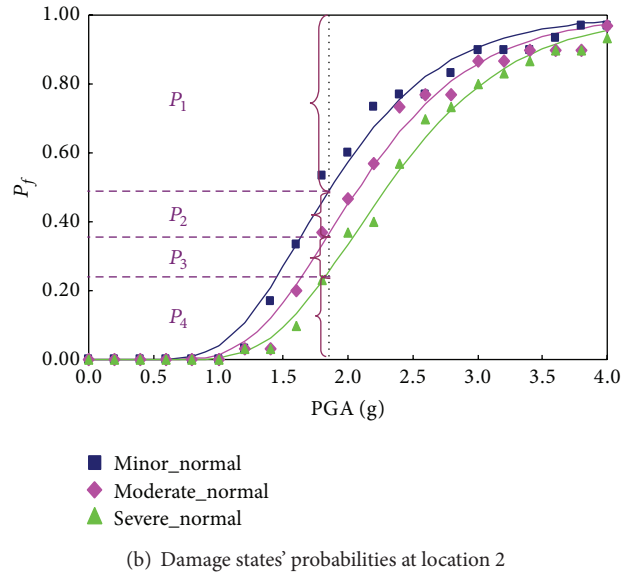
TABLE 2: Median PGA capacities.

Fault mechanisms	Location 1 (g)	Location 2 (g)
Normal	1.624	1.872
Reverse	1.960	2.484
Strike-slip	2.260	2.548
Near-source	1.968	2.184
50 EQs	1.524	1.972

seismic-induced fire damage during and after an earthquake. A stochastic seismic analysis was performed on a 2-inch black iron multibranch piping system represented by a nonlinear FE model. A Monte Carlo simulation was conducted in order to evaluate the system-level fragility of T-joint piping system. Based on the finding from simulation, the fragility curves



(a) Damage states' probabilities at location 1



(b) Damage states' probabilities at location 2

FIGURE 11: Probabilities of failure corresponding to the damage states.

properly fitted into a lognormal cumulative distribution. The overall study results showed that the failure probabilities at locations 1 and 2 differ significantly by fault mechanism. The fragility according to the normal-fault mechanism was similar to the fragility of the piping system as subjected to 50 EQs at locations 1 and 2. This normal-fault fragility was extremely conservative or, in other words, exceedingly fragile. The maximum difference between the different fault types was approximately 40% at both locations 1 and 2. This suggests that seismic ground-motion acceleration and frequency in piping systems that include acceleration-sensitive components can have a considerable effect on fragility. Indeed, this was the rationale for the present study's evaluation of the seismic capacities of the T-joint sprinkler piping components. Further evaluation of the interaction between buildings and their fire-protection piping systems and of the dynamic

impact influence between ceiling systems and sprinkler heads remains for future work.

Conflict of Interests

The authors declare that there is no conflict of interests regarding the publication of this paper.

Acknowledgment

This research was supported by a Grant (13SCIPA01) from Smart Civil Infrastructure Research Program funded by the Ministry of Land, Infrastructure and Transport (MOLIT) of Korea Government and Korea Agency for Infrastructure Technology Advancement (KAIA) and supported by a National Research Foundation of Korea (NRF) grant funded by the Korean government (MEST) (no. 2012-0008762).

References

- [1] N. C. Gould and M. J. Griffin, "The value of seismically installing and strengthening non-structural equipment and systems to significantly reduce business interruption losses," in *Proceedings of the Seminar on Seismic Design, Performance, and Retrofit of Nonstructural Components in Critical Facilities*, ATC-29-2, Newport Beach, Calif, USA, 2003.
- [2] M. Shinozuka and S. Masri, "Seismic risk assessment of non-structural components in hospitals," in *Proceedings of Seminar on Seismic Design, Performance, and Retrofit of Nonstructural Components in Critical Facilities*, Newport Beach, Calif, USA, 2003.
- [3] A. I. Sekizawa, M. Ebihara, and H. Notake, "Development of seismic-induced fire risk assessment method for a building," in *Proceedings of the 7th International Symposium on Fire Safety Science*, pp. 309–320, June 2003.
- [4] G. Antaki and D. Guzy, "Seismic testing of grooved and threaded fire protection joints and correlation with nfpa seismic design provisions," in *Proceedings of the ASME Pressure Vessels & Piping Conference*, vol. 364, pp. 69–75, 1998.
- [5] J. Dow, "Testing and analysis of iron and plastic T-joint in sprinkler systems," NEESR–GC: "Simulation of the Seismic Performance of Nonstructural Systems", 2010, https://nees.org/site/resources/pdfs/REU2009_Dow_Paper.pdf.
- [6] Y. Tian, J. Fuchs, G. Mosqueda, and A. Filiatrault, "NEESR Nonstructural: progress report on tests of Tee Joint component of sprinkler piping system," Progress Report, NEESR-GC: Simulation of the Seismic Performance of Nonstructural Systems, 2010.
- [7] B. S. Ju and W. Y. Jung, "Seismic fragility evaluation of multi-branch piping systems installed in critical low-rise buildings," *Disaster Advances*, vol. 6, no. 4, pp. 59–65, 2013.
- [8] B. S. Ju, S. K. Tadinada, and A. Gupta, "Fragility analysis of threaded T-joint connections in hospital piping systems," in *Proceedings of the ASME Pressure Vessels and Piping Conference (PVP '11)*, vol. 8, pp. 147–155, Baltimore, Md, USA, July 2011.
- [9] S. Mazzoni, F. McKenna, M. H. Scoot, and G. L. Fenves, *OpenSees Command Language Manual*, 2006, <http://opensees.berkeley.edu/>.
- [10] B. S. Ju and W. Y. Jung, "Framework for fragility evaluation of piping system," in *Proceedings of the 22nd Conference on Structural Mechanics in Reactor Technology (SMiRT '22)*, San Francisco, Calif, USA, August 2013.
- [11] B. S. Ju, W. Y. Jung, and Y. H. Ryu, "Seismic fragility evaluation of piping system installed in critical structures," *Structural Engineering and Mechanics*, vol. 46, no. 3, pp. 337–352, 2013.
- [12] NFPA-13, *Standard for the Installation of Sprinkler System*, National Fire Protection Association, Quincy, Mass, USA, 2007.
- [13] SMACNA, *Seismic Restraint Manual Guidelines for Mechanical Systems*, Sheet Metal and Air Conditioning Contractors' National Association, Inc., 2003.
- [14] OpenSees, *Open System for Earthquake Engineering Simulation*, <http://opensees.berkeley.edu/>.
- [15] M. Sasani, A. der Kiureghian, and V. V. Bertero, "Seismic fragility of short period reinforced concrete structural walls under near-source ground motions," *Structural Safety*, vol. 24, no. 2-4, pp. 123–138, 2002.
- [16] PEER-NRG, Pacific Earthquake Engineering Research Center: NGA Database, <http://peer.berkeley.edu/nga/>.
- [17] A. K. Chopra, *Dynamics of Structures*, Prentice Hall, New York, NY, USA, 2nd edition, 2007.
- [18] K. Porter and R. Bachman, "Developing fragility functions for building components for ATC-58," ATC-58 Nonstructural Products Team, 2006, <http://www.sparisk.com/pubs/Porter-2006-deriving-fragility.pdf>.
- [19] Electric Power Research Institute (EPRI), "Methodology for developing seismic fragilities," TR-103959 Research Project, Electric Power Research Institute (EPRI), 1994.
- [20] M. Shinozuka, M. Q. Feng, H. Kim, T. Uzawa, and T. Ueda, "Statistical analysis of fragility curves," Technical Report MCEER, FHWA Contract Number: DTFH61-92-C-00106, 2001.
- [21] M. K. Ravindra, *Probabilistic Structural Mechanics Handbook: Seismic Risk Assessment*, Chapman & Hall, Springer, New York, NY, USA, 1995.

Research Article

Field Application of Cable Tension Estimation Technique Using the h-SI Method

Myung-Hyun Noh¹ and WooYoung Jung²

¹Steel Solution Center, POSCO, 100 Songdogwahak-ro, Yeonsu-gu, Incheon 406-840, Republic of Korea

²Department of Civil Engineering, Gangneung-Wonju National University, Gangneung 210-702, Republic of Korea

Correspondence should be addressed to WooYoung Jung; woojung@gwnu.ac.kr

Received 31 July 2014; Accepted 13 August 2014

Academic Editor: Sang-Youl Lee

Copyright © 2015 M.-H. Noh and W. Jung. This is an open access article distributed under the Creative Commons Attribution License, which permits unrestricted use, distribution, and reproduction in any medium, provided the original work is properly cited.

This paper investigates field applicability of a new system identification technique of estimating tensile force for a cable of long span bridges. The newly proposed h-SI method using the combination of the sensitivity updating algorithm and the advanced hybrid microgenetic algorithm can allow not only avoiding the trap of local minimum at initial searching stage but also finding the optimal solution in terms of better numerical efficiency than existing methods. First, this paper overviews the procedure of tension estimation through a theoretical formulation. Secondly, the validity of the proposed technique is numerically examined using a set of dynamic data obtained from benchmark numerical samples considering the effect of sag extensibility and bending stiffness of a sag-cable system. Finally, the feasibility of the proposed method is investigated through actual field data extracted from a cable-stayed Seohae Bridge. The test results show that the existing methods require precise initial data in advance but the proposed method is not affected by such initial information. In particular, the proposed method can improve accuracy and convergence rate toward final values. Consequently, the proposed method can be more effective than existing methods in terms of characterizing the tensile force variation for cable structures.

1. Introduction

Recently, the number of cable-stayed structures built in countries around the world is increasing. The cable-stayed structures deteriorate due to a variety of reasons such as overloading, aging, manufacturing imperfection, and climate conditions. Localized damage in materials may make deleterious contributions to the tensile force of the cable system. Therefore, it is necessary to estimate the tension of the cables to ensure structural safety during the construction phase and maintenance work after completion.

The tensile force of the cable system can be characterized by means of a condition assessment technology based on a variety of disciplines. Among the many nondestructive evaluation (NDE) methods, this study is focused on the use of dynamic response in detecting tensile forces in the cable structure system. Of the many condition assessment techniques for cable-stayed structures available today, system identification methods are based on detecting the changes in

static or dynamic behavior of a cable [1–3]. The tensile force of cables could be inversely determined by using mathematical models based on the taut string theory or axially loaded beam theory from natural frequency data. These works, based on simplified analytical approaches, have limited capabilities in dealing with complex problems, primarily due to their limitations in handling real cable shapes in the analysis. The differences between the real structural system and mathematical model for various cables make deleterious contributions to the accurate detection of the tensile force [4]. In addition, Bati and Toniatti [5] presented the significance of the flexural rigidity of cables in determining tensile forces. They reported that the tensile force induced from the simplified string model, which does not consider flexural rigidity, is not reliable for most cases. The difference becomes more dramatic for cases of the geometrical shape of cables, construction tolerances, or support conditions. Blasi and Sorace [6] proposed a method for detecting tensile forces by combining static and dynamic identification techniques, which reflect

the characteristics of the tie-rod structural system. Park et al. [7] carried out the identification of the tensile force in high-tension bars using modal sensitivities. Park et al. [8] developed a system identification technique to determine the tensile force and various rigidities of cables simultaneously by using the finite element method and sensitivity equation. They proved the proposed method through lab-scale and field test.

These works, based on the local optimization algorithm (LOA), have limited capabilities in dealing with complex problems, primarily due to their limitations in handling assumed initial conditions in the analysis. They have several limitations, such as divergence and instability problems, during numerical calculations. In particular, the trap problem of false minimum is frequently observed for large and complicated structures. In recent years, global optimization algorithms (GOA), such as neural networks, genetic algorithms (GAs), and simulated annealing methods have been developed and promisingly applied to the field of structural identification. Among them, GAs attracted our attention because not a great deal of data was needed in advance. This is an advantage over natural frequency-based neural network methods that require priori-knowledge of both the modal frequencies and the modal shapes to train the neural network and to detect the structural damage. Lee and Wooh [9] presented a microgenetic algorithm that is able to identify the location and extent of damage in plate-type structures using only the frequency information. Noh et al. [10] suggested a differential evolutionary algorithm to determine external tension forces and Rayleigh damping coefficients.

Despite the broad spectrum of applications, the conventional GAs usually require a large number of iterations and thus high computational cost. To solve an inverse problem using a GA, it is necessary to carry out iterative forward computations for each individual. Noh and Lee [11] developed a hybrid genetic algorithm (h-GA) to reduce the iterations by using the organic-hybridization technique. For a cable-stayed structure, global optimization algorithms such as GAs and an efficient sensitivity method could serve a dominant role in improving the convergence. Noh and Hu [12] developed a new algorithm using the advantages of both the LOA and GOA. They adopted the posthybridization method where the GOA provides the initial values for the LOA. The most significant characteristic of this method is that the hybrid microgenetic algorithm (h-GA), which is a GOA, helps solve the local convergence problem due to incorrect initial value settings, by using the sensitivity-updating algorithm (SUA), which is a LOA, to improve the precision and convergence to the final value. However, the validity of the new method has been restrictively verified through numerical and laboratory-scale studies from computation efficiency point of view. Therefore, it will be also necessary to prove the concept from further experimental studies for real cable-stayed long-span bridges.

In this paper, we will focus on the practical applications of the proposed method to cable-stayed long-span bridge suggested in the study of Noh and Hu [12]. First, the process of tension estimation using the h-SI method is reformulated in a general form theoretically. Secondly, the validity of

the technique is numerically verified using a set of dynamic data obtained from a simulation of benchmark numerical samples considering the effect of sag-extensibility and bending stiffness of a sag-cable system. Finally, the feasibility of the proposed method is investigated through field data extracted from a cable-stayed Seohae Bridge, and its applicability is verified.

2. Theoretical Background for Tension Estimation Method Using the h-SI

Noh and Hu [12] developed the hybrid system identification method using the combined effects of the hybrid microgenetic algorithms (h-GA) and the sensitivity equation for the tension estimation of cable structures. Figure 1 illustrates the hybrid procedure used in this study. The hybrid system identification (h-SI) algorithm consists of h-GA in GOA and the sensitivity-updating algorithm in LOA. It also uses the posthybridization procedure to avoid the local convergence, in which the GOA provides the initial value to LOA.

In the process of tension estimation using the h-SI method based on the finite element model, the tensile force to be identified is a component of an identification vector of the following form:

$$\mathbf{x} = [x^1 \ x^2 \ \dots \ x^j \ \dots \ x^p]^T, \quad (1)$$

where x^j ($j = 1, \dots, p$) denotes the component of the identification vector and p denotes the number of identification parameters. The tension of a cable should be a major component of the identification vector, and material and/or geometrical properties of the cable can also be other components.

First, to explain a new reproduction process of the h-GA in GOA different compared to the existing GA algorithm, the reproduction process for mating pools is formulated, assuming the k th generation ${}^k\mathbf{P}$ consisting of N members. Consider

$${}^k\mathbf{P} = [{}^k\chi_1 \ {}^k\chi_2 \ \dots \ {}^k\chi_i \ \dots \ {}^k\chi_N]^T, \quad (2)$$

where ${}^k\chi_i$ ($i = 1, \dots, N$) denotes the i th individual for every k th generation, is composed of a binary combination of identification parameters for the estimation of the tension, and can be expressed as

$${}^k\chi_i = ({}^k\chi_i^1 \ {}^k\chi_i^2 \ \dots \ {}^k\chi_i^j \ \dots \ {}^k\chi_i^m), \quad (3)$$

where ${}^k\chi_i^j$ ($j = 1, \dots, m$) denotes a component of the binary string vector for the i th individual of the k th generation, which consists of either 0 or 1, and m denotes the number of total bits assigned to the string vector composed of the combination of identification.

Next, for the reproduction process, the string vector of (3) can be decoded as

$${}^k\mathbf{x}_i = [{}^kx_i^1 \ {}^kx_i^2 \ \dots \ {}^kx_i^j \ \dots \ {}^kx_i^p]^T, \quad (4)$$

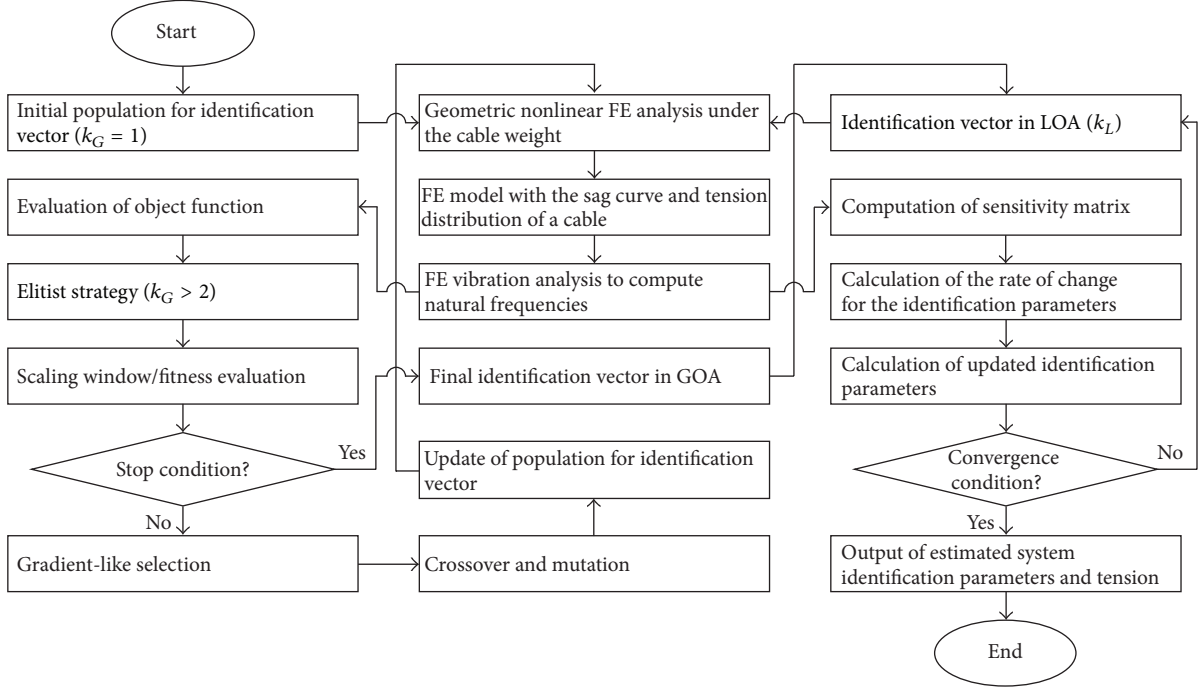


FIGURE 1: A schematic representation of the h-SI method.

where ${}^k x_i^j$ denotes the j th identification parameter for i th individual in the k th generation. The components of the row vectors are real numbers. Using those row vectors, an identification matrix with $(N \times p)$ size can be defined as

$${}^k \mathbf{X} = \begin{bmatrix} {}^k x_1^1 & {}^k x_1^2 & \dots & {}^k x_1^j & \dots & {}^k x_1^p \\ {}^k x_2^1 & {}^k x_2^2 & \dots & {}^k x_2^j & \dots & {}^k x_2^p \\ \vdots & \vdots & & \vdots & & \vdots \\ {}^k x_i^1 & {}^k x_i^2 & \dots & {}^k x_i^j & \dots & {}^k x_i^p \\ \vdots & \vdots & & \vdots & & \vdots \\ {}^k x_N^1 & {}^k x_N^2 & \dots & {}^k x_N^j & \dots & {}^k x_N^p \end{bmatrix}. \quad (5)$$

To identify the tension of cables accurately, h-GA should be combined with the nonlinear finite element model that can reflect the properties of cables in the present state. That is, the finite element model parameters that can be sensitive to changes in tension should be determined as the identification parameters in the system identification procedure. In this study, natural frequencies are produced from the finite element model, which are considered the deflection curve and tensile force distribution of cables. The produced frequencies are used for determining the object function (${}^k \Xi_i$) and fitness values (${}^k f_i$) as follows:

$${}^k \Xi_i({}^k \mathbf{x}_i) = \sum_{j=1}^q \|\omega_j^* - {}^k \omega_j({}^k \mathbf{x}_i)\| \quad (6)$$

$${}^k f_i({}^k \mathbf{x}_i) = -{}^k \Xi_i({}^k \mathbf{x}_i) - {}^{k-1} \gamma (> 0),$$

where ω_j^* denotes the natural frequency data measured from real cable structures and ${}^k \omega_j$ denotes the produced natural

frequency data calculated from the finite element vibration model. Then, the best fitness function can be prescribed by finding the minimum of the ${}^k f_i({}^k \mathbf{x}_i)$ among the total individuals in a loop. Consider

$${}^k \mathbf{x}_b = {}^k \mathbf{x}_{\text{best}} \quad (7)$$

$${}^k f_b = \min_{1 \leq i \leq N} [{}^k f_i({}^k \mathbf{x}_i)],$$

where $\text{best} = \text{argmin}_{1 \leq i \leq N} [{}^k f_i({}^k \mathbf{x}_i)]$ and $\text{argmin}[\cdot]$ is the function to transfer a number of the individuals, which minimizes the value of the fitness function.

In the next step, new identification parameters including the tension of a cable are investigated using (7). The new search point is defined as

$${}^{k+1} \bar{\mathbf{x}}_i = [1 - {}^k \xi_i] {}^k \mathbf{x}_i + {}^k \xi_i {}^k \mathbf{x}_b, \quad (8)$$

where ${}^{k+1} \bar{\mathbf{x}}_i (= [{}^k \bar{x}_i^1 \quad {}^k \bar{x}_i^2 \quad \dots \quad {}^k \bar{x}_i^j \quad \dots \quad {}^k \bar{x}_i^p]^T \in \mathbb{R}^p)$ that is the i th real number row vector provided newly is used to form the $(k+1)$ th mating pool and ${}^k \xi_i (= \eta_i [{}^k f_b - {}^k f_i] / ({}^k f_b))$ denotes the coefficient of linear combination in which η_i applies a positive constant between 0 and 2.

It may be noted that the next search point ${}^{k+1} \bar{\mathbf{x}}_i$, selected sequentially by the linear combination of ${}^k \mathbf{x}_i$ and ${}^k \mathbf{x}_b$, can be the best gene to have survived from the previous iteration. Then, the identification parameters can be encoded in binary digits to form a gene for each individual as shown in the following expressions:

$${}^{k+1} \bar{\mathbf{P}} = [{}^{k+1} \bar{\chi}_1 \quad {}^{k+1} \bar{\chi}_2 \quad \dots \quad {}^{k+1} \bar{\chi}_i \quad \dots \quad {}^{k+1} \bar{\chi}_N]^T. \quad (9)$$

Once the parent genes are selected by a new h-GA reproduction process through (1) to (9), matings take place using the existing crossover scheme and then a temporary offspring matrix is produced as

$${}^{k+1}\tilde{\mathbf{P}} = \left[{}^{k+1}\tilde{\chi}_1 \quad {}^{k+1}\tilde{\chi}_2 \quad \dots \quad {}^{k+1}\tilde{\chi}_i \quad \dots \quad {}^{k+1}\tilde{\chi}_N \right]^T. \quad (10)$$

Then, the purpose of the final loop of the h-GA operation is to introduce diversity by mutation, in order to explore other areas in the search space. It is suggested that the mutation probability should be lowered adaptively as the process converges. Finally, through the mutation process, the following group matrix for the $(k + 1)$ th generation can be obtained:

$${}^{k+1}\mathbf{P} = \left[{}^{k+1}\chi_1 \quad {}^{k+1}\chi_2 \quad \dots \quad {}^{k+1}\chi_i \quad \dots \quad {}^{k+1}\chi_N \right]^T. \quad (11)$$

The group matrix ${}^{k+1}\mathbf{P}$ for the $(k + 1)$ th generation is used as initial information of LOA in the system updating algorithm (SUA) after performing the repeated operation up to the preassigned number for h-GA of GOA. In the case of applying methods to detect the tensile forces using LOA, the proposed h-GA provides initial values for better efficiency, especially for insufficient information at the initial stage.

In order to decide a proper bifurcation between GOA and LOA, the number of generations in h-GA and iterations in SUA should be assigned in advance. In this study, the relationship between the number of generations (k_G) in h-GA and the number of identification parameters (p) is assumed

to be linear, and the number of iterations (k_L) in SUA also can be preassigned for computational efficiency using the k_G as

$$\begin{aligned} k_G &= N_a p \\ k_L &= \text{Ceil} \left[\frac{k_G}{2p} \right], \end{aligned} \quad (12)$$

where N_a denotes the preassigned arbitrary integer and $\text{Ceil}[\cdot]$ is the function to transfer the smallest following integer.

After iterative calculations for k_G , the final identification vector can be obtained as

$${}^{k_G+1}\mathbf{x}_b = \left[{}^{k_G+1}x_b^1 \quad {}^{k_G+1}x_b^2 \quad \dots \quad {}^{k_G+1}x_b^j \quad \dots \quad {}^{k_G+1}x_b^p \right]^T, \quad (13)$$

where $(k_G + 1)$ means the first iteration step of SUA in LOA. After the termination of the h-GA procedure, the identification vector for the r th ($1 \leq r \leq k_L$) iteration in SUA can be assumed as

$${}^r\mathbf{x} = \left[{}^r x^1 \quad {}^r x^2 \quad \dots \quad {}^r x^j \quad \dots \quad {}^r x^p \right]^T. \quad (14)$$

Then, the static displacement and tensile force distribution can be produced for the identification vector, which is similar to the h-GA process. In the next step, the natural frequencies are determined from the finite element vibration model using the static displacement curve and tensile force distribution. Using the change in natural frequencies for different identification parameters, the sensitivity matrix (${}^r\mathbf{S}$) with $(q \times p)$ size can be determined approximately as follows:

$${}^r\mathbf{S} = \begin{bmatrix} \frac{\partial^r \omega_1}{\partial^r x^1} \frac{\partial^r x^1}{\partial^r \omega_1} & \frac{\partial^r \omega_1}{\partial^r x^2} \frac{\partial^r x^2}{\partial^r \omega_1} & \dots & \frac{\partial^r \omega_1}{\partial^r x^j} \frac{\partial^r x^j}{\partial^r \omega_1} & \dots & \frac{\partial^r \omega_1}{\partial^r x^p} \frac{\partial^r x^p}{\partial^r \omega_1} \\ \frac{\partial^r \omega_2}{\partial^r x^1} \frac{\partial^r x^1}{\partial^r \omega_2} & \frac{\partial^r \omega_2}{\partial^r x^2} \frac{\partial^r x^2}{\partial^r \omega_2} & \dots & \frac{\partial^r \omega_2}{\partial^r x^j} \frac{\partial^r x^j}{\partial^r \omega_2} & \dots & \frac{\partial^r \omega_2}{\partial^r x^p} \frac{\partial^r x^p}{\partial^r \omega_2} \\ \vdots & \vdots & & \vdots & & \vdots \\ \frac{\partial^r \omega_i}{\partial^r x^1} \frac{\partial^r x^1}{\partial^r \omega_i} & \frac{\partial^r \omega_i}{\partial^r x^2} \frac{\partial^r x^2}{\partial^r \omega_i} & \dots & \frac{\partial^r \omega_i}{\partial^r x^j} \frac{\partial^r x^j}{\partial^r \omega_i} & \dots & \frac{\partial^r \omega_i}{\partial^r x^p} \frac{\partial^r x^p}{\partial^r \omega_i} \\ \vdots & \vdots & & \vdots & & \vdots \\ \frac{\partial^r \omega_q}{\partial^r x^1} \frac{\partial^r x^1}{\partial^r \omega_q} & \frac{\partial^r \omega_q}{\partial^r x^2} \frac{\partial^r x^2}{\partial^r \omega_q} & \dots & \frac{\partial^r \omega_q}{\partial^r x^j} \frac{\partial^r x^j}{\partial^r \omega_q} & \dots & \frac{\partial^r \omega_q}{\partial^r x^p} \frac{\partial^r x^p}{\partial^r \omega_q} \end{bmatrix}, \quad (15)$$

where ${}^r x^j$ ($j = 1, \dots, p$) and ${}^r \omega_i$ ($i = 1, \dots, q$) denote the j th component of the identification vector and the i th mode natural frequency for the r th iteration in SUA, respectively.

Then, from the produced natural frequency data, the rate of change ($d^r \boldsymbol{\omega}$) for the eigenvalue can be obtained as

$$\begin{aligned} d^r \boldsymbol{\omega} &= \left[\frac{\omega_1^* - {}^r \omega_1}{{}^r \omega_1} \quad \frac{\omega_2^* - {}^r \omega_2}{{}^r \omega_2} \quad \dots \quad \frac{\omega_i^* - {}^r \omega_i}{{}^r \omega_i} \quad \dots \quad \frac{\omega_q^* - {}^r \omega_q}{{}^r \omega_q} \right]^T, \\ & \quad (16) \end{aligned}$$

where ω_i^* and ${}^r \omega_i$ denote natural frequencies measured from experiment or field test and produced from nonlinear finite element vibration analysis using ${}^r \mathbf{x}$ in the r th iteration, respectively. Equation (16) can be rewritten in vector form using (15) as

$$d^r \boldsymbol{\omega}_{(q \times 1)} = {}^r \mathbf{S}_{(q \times p)} d^r \mathbf{x}_{(p \times 1)}. \quad (17)$$

Equation (17) is referred to as a linear sensitivity equation, and the rate of change for the identification vector by using (17) can be expressed as

$$d^r \mathbf{x} = {}^r \mathbf{S}^{-1} d^r \boldsymbol{\omega}, \quad (18)$$

where ${}^r \mathbf{S}^{-1}$ means the pseudoinverse matrix for ${}^r \mathbf{S}$ and can be determined as

$${}^r \mathbf{S}^{-1} = ({}^r \mathbf{S}^T {}^r \mathbf{S})^{-1} {}^r \mathbf{S}^T. \quad (19)$$

Finally, the j th identification parameter in the $(r + 1)$ th iteration can be recalculated as

$${}^{r+1} x^j = (1 + d^r x^j) {}^r x^j \quad (20)$$

$${}^{r+1} \mathbf{x} = [{}^{r+1} x^1 \quad {}^{r+1} x^2 \quad \dots \quad {}^{r+1} x^j \quad \dots \quad {}^{r+1} x^p]^T.$$

From (13) to (20), the loop is repeated until the termination condition is satisfied. In the case of not preassigning the number of iterations (k_L) in SUA, the convergence condition for termination of SUA process can be determined by the predefined object function that is the square roots of the sum of square (SRSS) in the following:

$$\left| \sqrt{\left(\sum_{i=1}^q \left| \frac{\omega_i^* - {}^r \omega_i}{\omega_i^*} \right| \times 100 \right)^2} - \sqrt{\left(\sum_{i=1}^q \left| \frac{\omega_i^* - {}^{r+1} \omega_i}{\omega_i^*} \right| \times 100 \right)^2} \right| < 0.01. \quad (21)$$

Finally, the tension of a cable is determined from the identification parameters holding at the termination stage and relevant natural frequencies can also be determined through the finite element vibration analysis using the identification parameters.

3. Benchmark Numerical Tests

Before the field application of the tension estimation method using the h-SI method, the benchmark numerical tests are carried out to verify the development theory. In addition, the results of the estimations of the tension force using the characteristic equation of the mathematical model, the system identification method based on the LOA and GOA, and the proposed h-SI method are compared to investigate the accuracy and applicability of the proposed h-SI method.

Figure 2 shows a sagged cable model for benchmark numerical tests, and the mechanical and material properties of four types (B1~B4) of cables used in this study are summarized in Table 1. In the table, λ^2 and ξ represent characteristics of cables that mean dimensionless sag-extensibility and bending-stiffness parameters, respectively. When we consider the calculated values shown in Table 1, B1 is a slope cable with a very small sag and high bending stiffness and B2 is a slope cable with large sag and a moderate bending stiffness. Also, B3 means a slope cable with moderate sag and

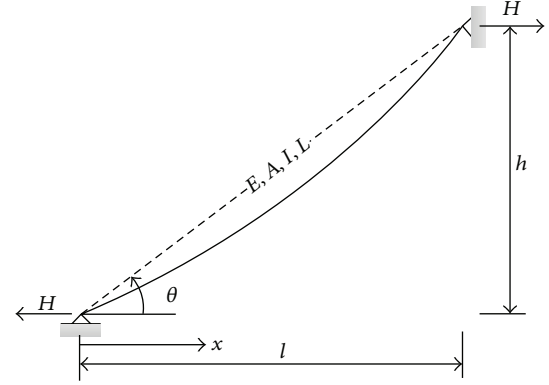


FIGURE 2: The sagged cable mode for benchmark numerical tests.

an intermediate bending stiffness, while B4 means a slope cable with intermediate sag and high bending stiffness.

The finite element models of the cables used in the benchmark numerical tests were modeled with 60 linear beam elements of the same length. Also, in the repetitive calculation phase of the h-SI method, the finite element model used for vibration analysis is renewed at the time when the system identification parameters are updated. The process of renewal can be summarized as follows. First, for the identification parameters that are updated at each repetition, a geometric nonlinear finite element analysis under the weight of the cable is performed to calculate the static sag and distribution of the tension force. Then, a finite element model that has a static sag curve and a calculated distribution of tension force is constructed. After that, the vibration analysis is performed to calculate the natural frequency.

To estimate the tension force of benchmark numerical examples for a slope cable including sags using the h-SI method, the first thing that should be done is to select the system identification parameters. In this benchmark numerical study, the tension of cables is characterized by three independent identification parameters of horizontal force (H), effective diameter (d_e), and effective mass per unit length (m_e) of the cable. Here, the reason why the effective nominal diameter and the mass per unit length in addition to the horizontal force of the cable are included as the identification parameters is that a real cable is not of a full-section, and therefore it is necessary to calculate the precise nominal diameter to estimate the accurate tension of cables. For the tension force estimation method using the existing mathematical characteristic, errors were created as they assumed the cables to be of a full-section. Table 2 shows the search range of the identification parameters used in h-GA, which is a GOA of the h-SI method.

Since we set the value of N_a at 25 in this numerical study, the maximum number (k_C) of generations of GOA that applies h-GA is 75, while the maximum number (k_L) of calculations of LOA that applies SUA is 38, making a total of 113 repetitions. Table 3 shows the results of the 113 repetitive calculations using the h-SI method. Except for the B1 cable with a very small sag and high bending stiffness, all cases show an error of 1% or less. This is evidence that they were

TABLE 1: Material and geometrical properties for four numerical inclined cable models.

Items	Material and geometrical properties			
	B1	B2	B3	B4
λ^2	0.079	5075.8	1.41	0.508
ξ	1923.5	3.0295	50.459	505.113
θ (°)	30	30	30	30
L (m)	100	100	100	100
m (kg/m)	400	400	400	400
H (MN)	2.9036	0.7259	26.1325	0.7259
E (GPa)	1.5988	17.186	20826.0	0.00478
A (10^{-3} m ²)	7.8507	7.6110	7.8633	273.45
d (m)	0.1	0.984	0.1001	0.5901
I (10^{-6} m ⁴)	4.9535	4.6097	4.9204	5950.6

TABLE 2: The search range of identification variable.

Parameters	Search range
H (MN)	[0 30]
d_e (m)	[10^{-3} 1.0]
m_e (kg/m)	[10^{-3} 500]

TABLE 3: Estimated identification parameters (total number of iterative computation: 113).

Parameters	Estimated results			
	B1	B2	B3	B4
H (MN)	2.749 (-5.324)	0.726 (-0.041)	26.058 (-0.285)	0.730 (0.620)
d_e (m)	0.097 (-3.000)	0.984 (-0.010)	0.100 (-0.100)	0.592 (0.305)
m_e (kg/m)	378.735 (-5.316)	399.800 (-0.050)	398.856 (-0.286)	402.530 (0.632)
Elapsed time (sec)	0.65	0.56	0.57	0.58

(): identification error (%).

capable of precisely estimating the tension force. For B1, it was not possible to guarantee the convergence of the final value with 113 repetitive calculations. Therefore, it was necessary to increase the number of calculations of the SUA of LOA so after more than 300 repetitive calculations, the H value was calculated as 2.9035 MN, which reduced the errors to approximately 0.001%.

Figure 3 shows the convergence tendency of the lateral force of B1~B4 cables. The cases of B2~4, other than B1, converge to the final value after 113 repetitive calculations. The B1 case shows a change in the value of the lateral force during being identified after the 98th repetitive calculation, hinting that it is following a track of continuous convergence process. Therefore, in the case of B1, the number of LOA's repetitive calculations should be increased to reduce identification errors. As shown in the figure, the GOA, which is operated to provide initial value information for LOA, converges at relatively early generations. It needs to be noticed that the GOA's h-GA provides information on the initial value of the LOA's SUA very effectively.

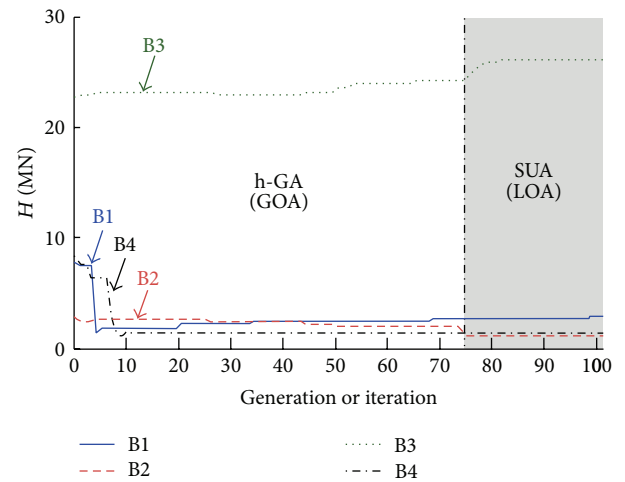


FIGURE 3: The convergence processes to find the horizontal force for B1~4.

The proposed method using the h-SI is compared with those of various existing approaches as listed in Table 4. The table reveals that these works, based on analytical approaches, have limited capabilities in dealing with the tension detection of cables, primarily due to their limitations in handling different geometries of cables and bending stiffness effects in the analysis. It should be also noted that the approach using the characteristic equation of beams could result in model error, especially for cables with large sag.

In the case of applying SUA and h-SI, it shows excellent detectability as errors were within 0.63%, except for B1, because it uses the FE model which reflects the geometrical characteristics of cables such as the sag. For the same iteration (113 times), the detectability for the case of B1 is lower than others because of their complexity due to small sagged geometry and large flexural stiffness. It means that, for B1, it is not possible to guarantee the convergence of the final value with 113 repetitive calculations. Therefore, it is necessary to increase the number of calculations of SUA of LOA in order to obtain an optimal solution.

Table 5 shows the results of estimations of the identification parameters using the SUA methods with and 90%

TABLE 4: Estimation results of cable tension using various existing approaches.

Methods	Estimated cable tension (MN)			
	B1	B2	B3	B4
Taut string theory	3.325 (-0.048)	112.346 (>100)	44.789 (48.430)	0.838 (-0.522)
Triantafyllou and Grinfogel [16]	3.352 (-0.057)	0.815 (-3.287)	31.330 (3.828)	0.841 (-0.202)
Linear regression method	3.352 (-0.069)	0.690 (-18.073)	30.160 (-0.049)	0.835 (-0.973)
Zui et al. [1]	3.354 (-0.012)	2.940 (>100)	29.031 (-3.791)	0.685 (-18.696)
Sensitivity updating algorithm	3.106 (-7.391)	0.838 (-0.558)	30.089 (-0.285)	0.848 (0.629)
Microgenetic algorithm (μ -GA)	3.362 (0.242)	1.398 (65.895)	27.736 (-8.083)	0.723 (-14.204)
This study (h-GA + SUA)	3.174 (-5.634)	0.838 (-0.558)	30.089 (-0.285)	0.843 (0.036)
True cable tension (T_{true})	3.354	0.843	30.175	0.843

(): identification error (%).

TABLE 5: Influence of initial information of identification parameters on the estimated results.

Case	Initial value	Identification parameters		
		H (MN)	d (m)	m (kg/m)
B1	$^0x^j$ (Max)	5.547	0.139	764.340
	$^0x^j$ (90% of True)	2.690	0.096	370.587
	$^0x^j$ (Min)	*	*	*
B2	$^0x^j$ (Max)	*	*	*
	$^0x^j$ (90% of True)	0.726	0.984	399.800
	$^0x^j$ (Min)	*	*	*
B3	$^0x^j$ (Max)	*	*	*
	$^0x^j$ (90% of True)	26.058	0.100	398.856
	$^0x^j$ (Min)	*	*	*
B4	$^0x^j$ (Max)	5.126	0.997	2828.500
	$^0x^j$ (90% of True)	0.734	0.592	402.530
	$^0x^j$ (Min)	*	*	*

*: numerical divergence or local minimum.

of actual values of Table 1 and maximum and minimum values of Table 2. All numerical tests confirm the possibility that the wrong selection of initial information may result in numerical divergence or local minimum. This emphasizes the significance of the information at the initial stage when applying SUA, which is one of the drawbacks of the LOA method. If the initial value is set similar to the actual value, the estimated errors can be reduced and the calculation time for LOA can be reduced. However, in actual field, the information on the initial values is very limited, and a repetitive process of trial and error is inevitable.

Since the μ -GA is dealing with small populations, it is unlikely that the process converges into the true value in the first iteration loop. In this case, we need more iteration to converge into the accurate value. Note that the tension force detection of cables in this case is heavily dependent on the number of iterations and initial information. On the other

hand, the h-SI method using a combination of GOA and LOA shows the excellent detectability for all cases. This shows that the tension estimation technique using the proposed h-SI can provide good initial information for SUA. Table 6 shows elapsed times of each system identification method after 113 iterative generations or computing. We may conclude from the table that the computational performance of the h-SI is equal to or greater improvement than the μ -GA and SUA while maintaining the same level of accuracy.

4. Field Applicability Tests

To investigate field applicability of the proposed h-SI method, we considered the time series data measured by the four accelerometers that were installed by 2 on each side of an actual cable-stayed bridge (cables number 1 and number 44, Seohae Bridge). As shown in Figure 4, the cross-section

TABLE 6: Comparison of elapsed time of each system identification method after 113 iterative generations or computing.

System identification methods	Elapsed time (sec)			
	B1	B2	B3	B4
SUA [$^0x^j$ (Max)]	0.62	*	*	1.48
SUA [$^0x^j$ (90% of True)]	1.12	1.29	1.18	1.31
SUA [$^0x^j$ (Min)]	*	*	*	*
μ -GA	0.72	0.69	0.61	0.72
h-SI (This study)	0.65	0.56	0.57	0.58

*: numerical divergence or local minimum.

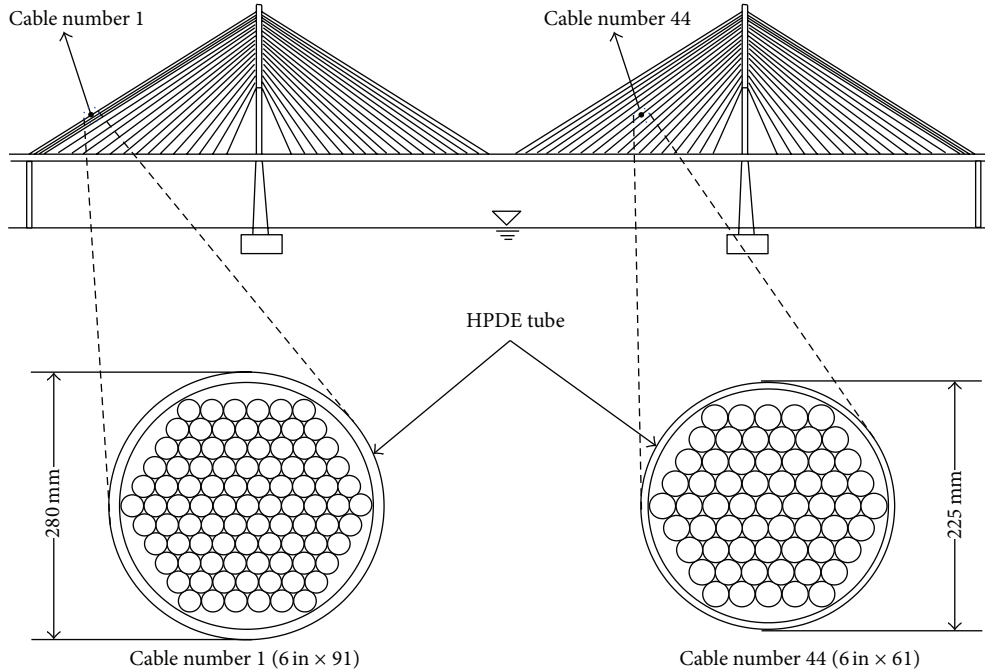


FIGURE 4: The locations, number, and section of measured cables.

of cable number 1 is composed of 91 strands of which the nominal diameter (ϕ) is 0.0157 m (0.6 in). The cable is shielded in HPDE pipes. Cable number 1 is the longest and vulnerable to vibration. The weight of cable number 1 is 125 kgf/m, which is also the heaviest. The cross-section of cable number 44 is composed of 61 strand wires with the same diameter as those in cable number 1. The cable is also shielded by HPDE tubes. The weight of cable number 44 is 84 kgf/m. Here, to build a necessary finite element model for the system identification, an ideal sloped cable as shown in Figure 5 is constructed.

Using a Piezoelectric type accelerometer, time series acceleration data perpendicular to the longitudinal direction of the cables on both sides were obtained. Here, the sampling frequency was 0.01 sec, while the average wind velocity during the measurement was 4.23 m/s. The ambient temperature was -1.76°C . The time series data of the acceleration measurement was examined using Welch's method (NFFT = 2048, Hanning window) to identify the acceleration spectrum. Also, by using the ERADC [13] method, the natural frequency was also extracted. Tables 7 and 8 show the natural

frequencies extracted by the finite element model with 100 elements and the natural frequencies measured from cables number 1 and number 44 on each side of the bridge. The material and geometrical properties of the cables for the finite element analysis are shown in Table 9.

The result of cable tension force estimation using the existing methods and the proposed h-SI method based on the natural frequency obtained through the field measurement is shown in Table 10. In addition, using the SUA, μ -GA, and h-SI methods, the results of estimating the lateral forces and effective nominal diameters, which are two identification parameters, are shown in Table 11.

The estimation of the tension force using the taut string theory yields average tension forces of 5.586 MN and 5.532 MN for cable number 1 on each side of the bridge, while cable number 44 yields 5.226 MN and 5.253 MN, respectively. Here, the effective lengths of the cable applied were 228.86 m and 165.33 m, while the mass per unit length was as per the reported actual physical properties of the actual cables. The method of Triantafyllou and Gingsfogel, which estimates the average tension force from nonlinear

TABLE 7: Extracted natural frequencies from measured data and calculated natural frequencies from FE models for cable number 1 (Hz).

Mode number	Upward-bound			Downward-bound		
	Test	FEM	Error (%)	Test	FEM	Error (%)
1	0.47	0.46	-1.71	—	0.46	—
2	0.94	0.92	-1.87	0.92	0.92	0.48
3	—	1.14	—	—	0.94	—
4	1.38	1.38	-0.28	1.38	1.38	0.25
5	1.84	1.85	0.42	1.84	1.84	0.25
6	—	2.28	—	—	1.87	—
7	2.30	2.31	0.30	2.29	2.29	-0.20
8	2.76	2.77	0.19	2.75	2.75	-0.11
9	3.23	3.23	0.06	—	2.80	—
10	—	3.42	—	3.21	3.21	0.06
11	3.69	3.69	-0.01	3.67	3.67	-0.07
12	4.15	4.16	0.24	—	3.74	—
13	—	4.56	—	4.13	4.13	0.04
14	4.61	4.62	0.25	4.59	4.59	0.07
15	5.08	5.08	0.09	—	4.68	—
16	5.54	5.54	0.03	5.05	5.05	0.07
17	—	5.70	—	5.51	5.51	-0.02
18	6.00	6.00	0.08	—	5.61	—
19	6.46	6.46	-0.01	5.98	5.97	-0.15
20	—	6.84	—	6.44	6.43	-0.10

—: not extracted.

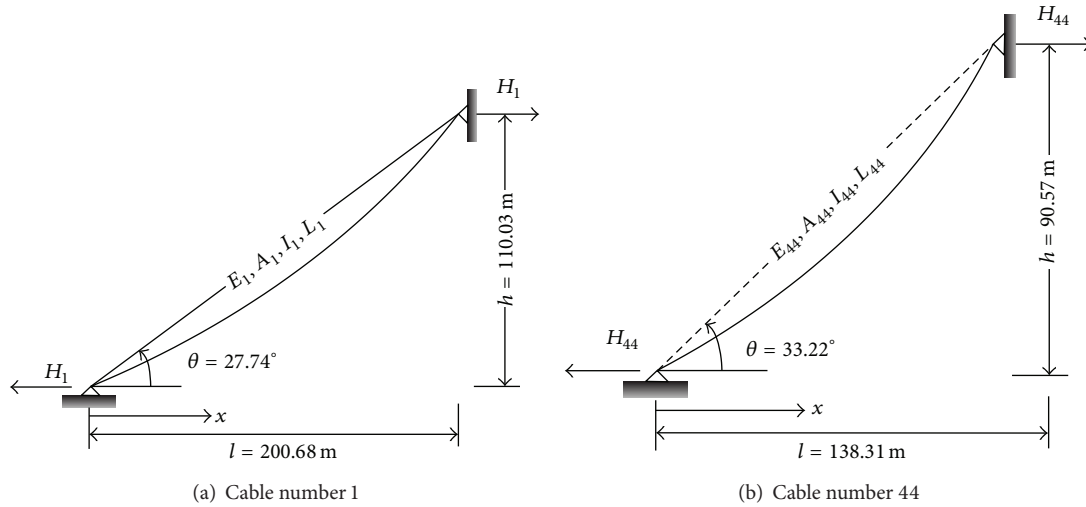


FIGURE 5: Idealized cable for FE model.

characteristics equations of the sloped cables and takes sags into consideration, shows errors within 1.4% in all cases, indicating a moderate level of precision in estimation. The mass per unit length of the cable and data on the axial stiffness of the cable were assumed to be known in advance. The estimated tension force using the linear regression method, which considers bending, ignores the sag, and uses the relationships between the natural frequency, bending stiffness, and average tension forces, shows errors within 1.8% for a relatively higher level of precision. However, when

the bending stiffness was estimated, F4 case showed a negative value of bending stiffness, which was $-2.545e + 05$ MN, rendering the results physically irrelevant. This shows the limitations in estimating the tension force using the linear regression method. The estimation of the tension force using the high mode method suggested by Shimada [2] shows an error range within 2.3%. This is the least precise of all estimation methods. Still, the error is relatively small.

The estimation results by the SUA, μ -GA, and h-SI methods, which are system identification methods, show

TABLE 8: Extracted natural frequencies from measured data and calculated natural frequencies from FE models for cable number 44 (Hz).

Mode number	Upward-bound			Downward-bound		
	Test	FEM	Error (%)	Test	FEM	Error (%)
1	—	0.75	—	—	0.76	—
2	—	1.33	—	—	1.33	—
3	1.50	1.51	0.50	1.51	1.51	0.33
4	2.26	2.26	0.06	2.27	2.27	0.05
5	—	2.66	—	—	2.67	—
6	3.01	3.02	0.24	3.02	3.02	0.00
7	3.77	3.77	-0.03	3.78	3.78	-0.12
8	—	3.99	—	—	4.00	—
9	4.52	4.52	-0.02	4.55	4.54	-0.13
10	5.29	5.28	-0.18	5.31	5.29	-0.38
11	—	5.32	—	—	5.34	—
12	6.03	6.03	-0.05	6.05	6.05	0.02
13	—	6.65	—	—	6.67	—
14	6.79	6.79	-0.03	6.82	6.81	-0.21
15	7.55	7.54	-0.19	7.58	7.56	-0.27
16	—	7.99	—	—	8.01	—
17	8.31	8.3	-0.09	8.33	8.32	-0.17
18	9.06	9.05	-0.09	9.09	9.07	-0.25
19	—	9.32	—	—	9.35	—
20	9.81	9.81	-0.03	9.83	9.83	-0.02

—: not extracted.

TABLE 9: The material and geometrical properties of each cable.

Condition	Tests			
	F1	F2	F3	F4
λ^2	0.0147	0.0093	0.0021	0.0017
ξ	1455.3	873.1	800.5	4313.9
Horizontal load (MN)	4.8940	4.8341	4.3652	4.3938
Effective diameter (m)	0.280	0.280	0.225	0.225
Elasticity (GPa)	2.1	2.1	2.1	2.1
Remark	Number 1 (up)	Number 1 (down)	Number 44 (up)	Number 44 (down)

TABLE 10: Cable tension force estimated from existing methods and the h-SI method.

Methods	Estimated cable tension (MN)			
	F1	F2	F3	F4
Taut string theory	5.586 (-1.000)	5.532 (-1.401)	5.226 (-1.547)	5.253 (1.152)
Triantafyllou and Grinfogel [16]	5.578 (-1.147)	5.534 (-1.372)	5.226 (-1.545)	5.253 (1.152)
Linear regression method	5.571 (-1.276)	5.518 (-1.650)	5.214 (-1.773)	5.267 (1.419)
Shimada [2]	5.549 (-1.653)	5.486 (-2.233)	5.196 (-2.110)	5.204 (0.206)
Sensitivity updating algorithm	5.583 (-1.058)	5.525 (-1.533)	5.233 (-1.413)	5.275 (1.579)
Microgenetic algorithm (μ -GA)	5.592 (-0.899)	5.514 (-1.729)	5.250 (-1.093)	5.287 (1.810)
This study (h-GA + SUA)	5.583 (-1.058)	5.525 (-1.533)	5.233 (-1.413)	5.272 (1.521)
Static jacking force (T_{true})	5.643	5.611	5.308	5.193

(:) : identification error (%).

TABLE 11: Estimation results of identification parameters through various system identification methods.

Case	$final_{x^j}$	Methods		
		SUA (LOA)	μ -GA (GOA)	h-SI (GOA + LOA)
F1	H (MN)	4.892	4.887	4.892
	d (m)	0.184	0.210	0.188
	EI (Nm ²)	1.182e + 05	2.005e + 05	1.288e + 05
	EA (MN)	55.840	73.736	58.294
	λ^2	0.033	0.043	0.034
	ξ	1,473	1,130	1,411
F2	H (MN)	4.841	4.832	4.841
	d (m)	0.208	0.224	0.208
	EI (Nm ²)	1.929e + 05	2.595e + 05	1.929e + 05
	EA (MN)	71.357	82.757	71.357
	λ^2	0.043	0.051	0.043
	ξ	1,147	988	1,147
F3	H (MN)	4.362	4.887	4.892
	d (m)	0.212	0.210	0.188
	EI (Nm ²)	2.082e + 05	2.005e + 05	1.288e + 05
	EA (MN)	55.840	73.736	58.294
	λ^2	0.014	0.010	0.014
	ξ	757	1,087	750
F4	H (MN)	4.892	4.887	4.892
	d (m)	0.184	0.210	0.188
	EI (Nm ²)	1.182e + 05	2.005e + 05	1.288e + 05
	EA (MN)	55.840	73.736	58.294
	λ^2	0.014	0.013	0.012
	ξ	760	813	871

errors within 1.6%, 1.9%, and 1.6%, respectively. These errors do not differ significantly from those of existing methods using the mathematical equations. The reason for this is that the cables of the cable-stayed bridges used in field study are part of systems that are less influenced by sags and bending compared to those of the benchmark numerical models. In fact, the values of the dimensionless sag-extensibility (λ^2) for the numerical model are of a range of 0.079~5,076. However, as shown in Table 9, they are less than 0.015 in all field experiment cases, which signifies that the cables used in field study are less influenced by sags and bending.

When compared to the tension forces measured using a hydraulic jack before completion [14] all methods show errors by less than 2.3%. Such errors can be regarded as the loss of cable tension force. When considering the fact that the bridge undergoes the tension loss by continuous changes of tension forces, with an accumulation of damage due to the environmental cyclic loadings such as thermal, traffic, and wind loads, the reduction rate in tension force mentioned above is insignificant. Unlike cables used in the benchmark numerical tests, the actual cables of cable-stayed bridges used in field study are systems that are less influenced by sags and bending. Therefore, the existing estimation methods and the proposed h-SI method do not differ significantly in terms of the estimation result. However, while the existing mathematical models and SUA, which are LOA, require

accurate data in advance, it should be noted that the μ -GA, which was GOA, and the h-SI method are not affected by such initial information. Also, compared to the μ -GA, it should be noted that h-SI could improve the converging tendency toward the final value and the precision by being combined with SUA.

5. Summary and Conclusions

In this paper, the characteristics of the h-SI methods that could be applied to the estimation of the tension forces effectively are examined and the theoretical formulation process of the h-SI method is suggested. Also, to verify the efficiency of the h-SI tension force estimation method, benchmark numerical tests for various cases are conducted and the applicability of the h-SI method through field tests is verified. During the benchmark numerical and field studies, comparative studies with the existing characteristics equation methods and system identification methods are also carried out. The key findings from this study are summarized as follows.

The h-SI method is a new algorithm combined to use the advantages of both the LOA and GOA and adopts the posthybridization method where the GOA provides the initial values for the LOA. The most significant characteristic of this method is that the h-GA, which is a GOA, helps solve

the local convergence problem due to incorrect initial value settings, by using the sensitivity based system identification method, which is a LOA, to improve the precision and convergence to the final value.

The benchmark numerical tests that consider sag and bending stiffness showed that, in the case of string theory, it was more appropriate for the estimation of tension force for a simple cable system where the influence of sag and bending stiffness is not significant. Also, the method suggested by Triantafyllou and Grinfolgel, which considers sags, showed errors within 4% in all cases, proving to be a relatively precise method. However, as the method uses a trial and error method, it is time consuming to find the tension compared to the string theory and initial information on the mass per unit length and axial stiffness of the cable is required to estimate the tension force properly. For estimating the tension force using the linear regression method, in which bending is considered but sags are not, except for the cable with large sags, the tension force can be estimated precisely within 1% errors. However, when applying the characteristic equation of the beam under axial loading for cables with large sags, model errors were confirmed in the results of tension estimation. For the low mode method suggested by Zui et al. [1] and Yen et al. [15], which considers both bending and sag, the bending stiffness, axial stiffness, and sag ratio are required in advance to estimate cable tension accurately. For cables with larger sags or higher bending stiffness, the accuracy of the estimation of the tension force was confirmed to be undermined significantly. On the other hand, when applying SUA, which is a LOA, all showed an estimation error lower within 1.2% except for B1, signifying that the estimation method using SUA is effective. All benchmark numerical tests showed the possibility that the wrong selection of initial information may result in numerical divergence or local minimum. In the case of applying μ -GA, which is a GOA, when exploring the solution space, it could not have a direction, and it resulted in slow convergence to the final value. Therefore, with 113 generations in total, it still did not converge to the final value showing the errors in all cases. Therefore, after 113 generations, it still did not converge to the final value and showed significant errors in all cases. The proposed h-SI technique that combined the h-GA and SUA was the most effective in estimation. In particular, in the h-SI method of estimating the tension force, the h-GA can play an important role in the initial operation of the SUA.

In the field test that used cables applied to an actual cable-stayed bridge, all methods showed errors smaller than 2.3%. When considering the fact that the bridge undergoes the tension loss by continuous changes of tension forces, with an accumulation of damage due to the environmental cyclic loadings such as thermal, traffic, and wind loads, the reduction rate in tension force mentioned above is insignificant. Unlike cables used in the benchmark numerical tests, the actual cables of cable-stayed bridges used in field study are systems that are less influenced by sags and bending. Therefore, the existing estimation methods and the proposed h-SI method do not differ significantly in terms of the estimation result. However, while the existing mathematical models and the SUA, which is LOA, require precise data in

advance, it should be noted that the μ -GA, which is GOA, and the h-SI method are not affected by such information. Also, compared to the μ -GA, it should be noted that h-SI could improve the converging tendency toward the final value and precision by being combined with SUA.

Conclusively, the proposed h-SI method could be effectively applied to estimate the tension force variation without initial information in actual cable bridges with inclined cables including sag.

Conflict of Interests

The authors declare that there is no conflict of interests regarding the publication of this paper.

Acknowledgment

This work was supported by a National Research Foundation of Korea (NRF) Grant funded by the Korean government (MEST) (no. 2012-0008762).

References

- [1] H. Zui, T. Shinke, and Y. Namita, "Practical formulas for estimation of cable tension by vibration method," *Journal of Structural Engineering*, vol. 122, no. 6, pp. 651–656, 1996.
- [2] T. Shimada, "Estimating method of cable tension from natural frequency of high mode," *Proceedings of the Japan Society of Civil Engineers*, vol. 501, no. 29, pp. 163–171, 1994.
- [3] H. Tang, S. Xue, and C. Fan, "Differential evolution strategy for structural system identification," *Computers and Structures*, vol. 86, no. 21-22, pp. 2004–2012, 2008.
- [4] T. Park, S. Moon, H. J. Joo, and B. H. Kim, "Estimating tensile force of hangers in suspension bridges using frequency based SI technique: I. theory," *Journal of the Korean Society of Civil Engineers*, vol. 27, no. 2A, pp. 165–172, 2007.
- [5] S. B. Bati and U. Tonietti, "Experimental methods for estimating in situ tensile force in tie-rods," *Journal of Engineering Mechanics*, vol. 127, no. 12, pp. 1275–1283, 2001.
- [6] C. Blasi and S. Sorace, "Determining the axial force in metallic rods," *Structural Engineering International (IABSE)*, vol. 4, pp. 241–246, 1994.
- [7] S. Park, S. Choi, S.-T. Oh, N. Stubbs, and H.-C. Song, "Identification of the tensile force in high-tension bars using modal sensitivities," *International Journal of Solids and Structures*, vol. 43, no. 10, pp. 3185–3196, 2006.
- [8] T. Park, H. T. Jang, M. H. Noh, and K. S. Park, "Evaluation on the lost prestressing force of an external tendon using the combination of FEM and HGA: I. theory," *Journal of the Korean Institute for Structural Maintenance Inspection*, vol. 13, no. 5, pp. 109–120, 2009.
- [9] S.-Y. Lee and S.-C. Wooh, "Waveform-based identification of structural damage using the combined finite element method and microgenetic algorithms," *Journal of Structural Engineering*, vol. 131, no. 9, pp. 1464–1472, 2005.
- [10] M. H. Noh, H. T. Jang, S. Y. Lee, and T. Park, "Tensile force estimation of externally prestressed tendon using SI technique based on differential evolutionary algorithm," *Journal of the Korean Society of Civil Engineers*, vol. 29, no. 1, pp. 9–18, 2009.

- [11] M. H. Noh and S. Y. Lee, "Moving load identification in time domain using a coupled genetic algorithm," in *Green and Smart Technology with Sensor Applications*, vol. 338 of *Communications in Computer and Information Science*, pp. 136–143, Springer, Berlin, Germany, 2012.
- [12] M.-H. Noh and J. W. Hu, "Tensile force identification in cable-stayed structures: hybrid system identification algorithm and experimental verification," *Journal of Mechanical Science and Technology*, vol. 28, no. 11, pp. 4563–4572, 2014.
- [13] J.-N. Juang, *Applied System Identification*, Prentice-Hall, Englewood Cliffs, NJ, USA, 1974.
- [14] J. C. Park, C. M. Park, and P. Y. Song, "Evaluation of structural behaviors using full scale measurements on the Seo Hae cable-stayed bridge," *KSCE Journal of Civil Engineering*, vol. 24, no. 2A, pp. 249–257, 2004.
- [15] W. H. Yen, A. B. Mehrabi, and H. Tabatabai, "Evaluation of stay cable tension using a non-destructive vibration technique," in *Building to Last Structures Congress: Proceedings of the 15th Structures Congress*, L. Kempner Jr. and C. B. Brown, Eds., vol. 1, pp. 503–507, ASCE, New York, NY, USA, 1997.
- [16] M. S. Triantafyllou and L. Grinfogel, "Natural frequencies and modes of inclined cables," *Journal of Structural Engineering*, vol. 112, no. 1, pp. 139–148, 1986.

Research Article

Mass Change Prediction Model of Concrete Subjected to Sulfate Attack

Kwang-Myong Lee,¹ Su-Ho Bae,² Jae-Im Park,³ and Soon-Oh Kwon²

¹ Department of Civil and Environmental Engineering, Sungkyunkwan University, Suwon 440-746, Republic of Korea

² Department of Civil Engineering, Andong National University, Andong 760-749, Republic of Korea

³ Metropolitan Transit System Research Division, Korea Railroad Research Institute, Uiwang 437-757, Republic of Korea

Correspondence should be addressed to Su-Ho Bae; shbae@andong.ac.kr

Received 5 September 2014; Accepted 5 October 2014

Academic Editor: Sang-Youl Lee

Copyright © 2015 Kwang-Myong Lee et al. This is an open access article distributed under the Creative Commons Attribution License, which permits unrestricted use, distribution, and reproduction in any medium, provided the original work is properly cited.

The present study suggested a mass change prediction model for sulfate attack of concrete containing mineral admixtures through an immersion test in sulfate solutions. For this, 100% OPC as well as binary and ternary blended cement concrete specimens were manufactured by changing the types and amount of mineral admixture. The concrete specimens were immersed in fresh water, 10% sodium sulfate solution, and 10% magnesium sulfate solution, respectively, and mass change of the specimens was measured at 28, 56, 91, 182, and 365 days. The experimental results indicated that resistance of concrete containing mineral admixture against sodium sulfate attack was far greater than that of 100% OPC concrete. However, in terms of resistance against magnesium sulfate attack, concrete containing mineral admixture was lower than 100% OPC concrete due to the formation of magnesium silicate hydrate (M-S-H), the noncementitious material. Ultimately, based on the experimental results, a mass change prediction model was suggested and it was found that the prediction values using the model corresponded relatively well with the experimental results.

1. Introduction

Concrete structures exposed to soil, groundwater, and sea-water environments are subject to performance degradation due to sulfate attack. The harmful ions including sulfate ion penetrate into concrete and react with calcium hydroxide and calcium aluminate hydrate to form expansion hydration products such as gypsum and ettringite. This may lead to cracking and softening action and eventually lower durability of concrete structures [1–4]. In case of sodium sulfate (Na_2SO_4) attack, the reaction of sulfate ion (SO_4^{2-}) and calcium hydroxide generated by cement hydration forms gypsum, which results in softening and loss of strength of cement paste. In this case, the gypsum reacts with calcium aluminate hydrate (C_4AH_{13}), monosulfate ($\text{C}_4\text{A}\bar{\text{S}}\text{H}_{12}$), and tricalcium aluminate (C_3A) to produce secondary ettringite, which accompanies volume increase, and therefore results in expansion and cracking [5–7]. In case of magnesium sulfate (MgSO_4) attack, magnesium sulfate and calcium hydroxide

react first to form gypsum and brucite ($\text{Mg}(\text{OH})_2$). Brucite is low in pH and thus destabilizes C-S-H (calcium silicate hydrate) and ettringite. As a result, magnesium sulfate reacts easily with C-S-H to form gypsum, brucite, and silica gel (S_2H). The lime freed by this reaction reacts further with magnesium sulfate instead of reestablishing the pH and forms more brucite; accordingly the concentration of gypsum and brucite in the paste matrix will increase. As the increased brucite reacts with S_2H , C-S-H gradually loses lime and becomes converted to noncementitious M-S-H [6, 8, 9].

The chemical reaction mechanism by sulfate is influenced by the numerous controlling parameters, such as concentration of sulfate ions, ambient temperature, types and proportions of cementitious materials, water-binder ratio (W/B), and curing period [2, 10]. This is a complex and time-dependent phenomenon that takes place over a long time due to the relatively lower diffusivities of sulfate ions that penetrate into concrete. Accordingly, although studies have been conducted for long on the chemical erosion of concrete,

TABLE 1: Physical properties and chemical composition of cement and mineral admixtures.

Type of binder	Physical properties		Chemical composition (%)						
	Specific gravity	Blaine (m ² /kg)	SiO ₂	Al ₂ O ₃	Fe ₂ O ₃	CaO	MgO	SO ₃	R ₂ O
OPC	3.15	329.0	21.1	4.6	3.5	61.8	3.2	2.1	0.9
GGBFS	2.89	489.3	34.1	16.1	0.4	42.3	4.1	2.5	0.7
FA	2.23	375.0	56.5	27.1	4.4	3.8	0.8	0.2	1.3
SF	2.20	20,000	88.7	1.8	1.8	1.5	0.8	0.1	1.0

TABLE 2: C₃A content of concretes containing mineral admixtures.

Type of concrete	100% OPC	BBC*	TBC1**	TBC2***
C ₃ A content (%)	6.58	3.18	2.87	2.70

*OPC : GGBFS = 50% : 50%.

**OPC : GGBFS : FA = 40% : 40% : 20%.

***OPC : GGBFS : SF = 50% : 45% : 5%.

TABLE 3: Physical properties of fine aggregate.

Specimen	Density (g/cm ³)	Absorption (%)	Unit mass (kg/m ³)	Amount of passing No. 200 sieve (%)	Fineness modulus
River sand	2.60	1.47	1,597	2.2	2.43

TABLE 4: Physical properties of coarse aggregate.

Specimen	G _{max} (mm)	Density (g/cm ³)	Absorption (%)	Unit mass (kg/m ³)	Fineness modulus
Crushed rock	20	2.65	0.58	1,648	7.27

TABLE 5: Properties of superplasticizer.

Main composition	Specific gravity	pH	Solid content (%)	Quantity (%) (by mass of cement)
Polycarbonic acid	1.05	9	38	0.5~2.5

complete verification of the mechanism and establishment of prevention measures are yet to be done.

Meanwhile, a study has been conducted to improve sulfate attack resistance of concrete by utilizing mineral admixture such as fly ash (FA), ground granulated blast furnace slag (GGBFS), and silica fume (SF). Mineral admixtures react with the portlandite (Ca(OH)₂) liberated during the hydration of cement to form secondary C-S-H gel, which is relatively denser than the primary C-S-H gel, thus resulting in pore refinement. The other beneficial effect of incorporating mineral admixtures into the concrete mixture is the reduction of portlandite and alumina contents in the cementitious material that are essential for the formation of gypsum and ettringite [2, 6, 11–13].

Thus, the purpose of this research is to investigate the influence of mineral admixture on sulfate attack resistance of concrete through an immersion test in sulfate solutions and to suggest a mass change prediction model of concrete subjected to sulfate attack. For this, concrete test specimens with W/Bs of 32% and 43% were manufactured using 100% ordinary portland cement (OPC) concrete as well as binary blended cement (BBC) and ternary blended cement (TBC) concrete mixed with OPC and mineral admixture. Then, according to the JSTM C 7401 [14] sulfate attack resistance was assessed by

investigating mass change as per immersion age. Ultimately, based on the experimental results, a mass change prediction model for sulfate attack of concrete was suggested.

2. Experimental Work

2.1. Materials Used and Mix Proportions. To manufacture concrete specimens for sulfate resistance test, OPC, FA, GGBFS, and SF were used. The physical properties and chemical compositions of cement and mineral admixtures are given in Table 1. To use C₃A content in concrete, which exerts significant influence on the sulfate attack mechanism, as a key parameter of sulfate attack prediction model, C₃A contents of concrete containing a number of mineral admixtures as shown in Table 2 were analyzed. For fine aggregate and coarse aggregate, river sand and crushed rock were used, respectively. Their physical properties are given in Tables 3 and 4. To control fluidity of concrete mixture, air entraining (AE) and high-range water reducing agent of polycarbonic acid were used as a kind of superplasticizer. The properties are as shown in Table 5.

To manufacture concrete specimens for sulfate resistance test, mix proportions for BBC concrete and two types of

TABLE 6: Mix proportions of concrete mixtures.

G_{\max} (mm)	W/B (%)	S/a (%)	Cement type	Unit mass (kg/m ³)							
				W	OPC	Binder (B)			S	G	Superplasticizer (B × %)
						GGBFS	FA	SF			
20	32	42	OPC	160	500	0	0	0	691	966	1.10
			BBC	160	250	250	0	0	684	955	0.85
			TBC1	160	200	200	100	0	707	910	1.30
			TBC2	160	250	225	0	25	681	951	1.36
20	43	47	OPC	165	388	0	0	0	811	925	1.00
			BBC	165	194	194	0	0	805	918	0.80
			TBC1	165	155.2	155.2	77.6	0	798	910	1.03
			TBC2	165	194	174.6	0	19.4	802	915	1.23

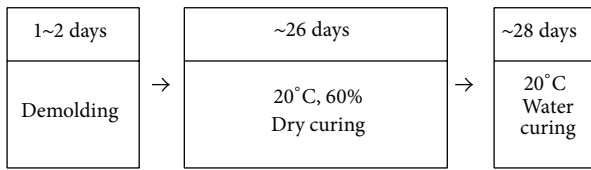


FIGURE 1: Pretreatment process of concrete in case of no incrustation.

ternary blended cement (TBC1, TBC2) concrete were determined as shown in Table 6 in addition to 100% OPC concrete. OPC and GGBFS were used for BBC concrete and FA and SF were additionally used, respectively, for TBC concrete. W/B was 32% and 43% and target slumps and air contents of all of the concrete mixtures were 180 ± 25 mm and $5.0 \pm 0.5\%$, respectively.

2.2. Specimen Preparation. Concrete cylinders ($\varnothing 100 \times 200$ mm) were prepared for compressive strength test and sulfate attack test. After cylinders were molded, they were kept inside a constant temperature and humidity chamber over 24 hours. Then, the molds were removed and test specimens for standard curing were cured in a water bath with temperature of $20 \pm 2^\circ\text{C}$ until test began. As for test specimens for sulfate solution immersion, pretreatment was conducted as illustrated in Figure 1. In this study, no incrustation specimens were used. Therefore, test specimens were left inside a constant temperature and humidity chamber with temperature of $20 \pm 2^\circ\text{C}$ and relative humidity of $60 \pm 5\%$ until 26 days and then the specimens were cured underwater at $20 \pm 2^\circ\text{C}$ until 28 days.

2.3. Test Method for Sulfate Attack Resistance. The test method for chemical resistance of concrete is also specified in the ASTM C 1012 [15]. However, this method is for mortar and therefore, in this study, sulfate attack resistance of concrete was tested according to the “test method for chemical resistance by concrete immersion in solution” of JSTM C 7401 [14]. This method is to assess chemical resistance by immersing test specimens into acid or alkaline solutions for a prescribed period of time and by comparing changes in the measurements against those of standard curing specimens.

Of chemicals proposed for this method, 10% sodium sulfate and 10% magnesium sulfate solutions were selected for the test.

In this test, sulfate attack resistance of concrete is assessed in terms of compressive strength ratio as well as mass and length change ratios. For this study, sulfate attack resistance was assessed by mass change ratio as follows:

$$\text{mass change ratio (\%)} = \frac{W_i - W_{ci}}{W_{ci}} \times 100, \quad (1)$$

where W_i is mass of concrete immersed in test solution at the measuring age (g) and W_{ci} is mass of concrete before immersion in test solution (g).

In addition, to investigate microstructure of the concrete degraded by sulfate ion, powder samples were extracted from the sulfate reaction areas of concrete specimens immersed in each solution for 365 days and XRD analysis was conducted on the samples using JCPDS (joint committee on powder diffraction standards) card method.

3. Results and Discussion

3.1. Fundamental Properties. Table 7 shows slumps and air contents of fresh concrete as well as compressive strengths of standard cured concrete at 28 days per mix proportions of concrete used in the sulfate attack resistance test. Compressive strengths and slumps of concrete are the mean value for 3 and 2 times, respectively, and air contents are one measured value. Slumps and air contents of all of the concrete mixtures satisfied the target values of 180 ± 25 mm and $5.0 \pm 0.5\%$, respectively. In case of W/B = 32%, compressive strength of BBC concrete and TBC concrete containing mineral admixture was higher than 100% OPC concrete. On the other hand, in case of W/B = 43%, compressive strength of BBC concrete and TBC concrete was found to be generally lower than 100% OPC concrete. This is because, in concrete containing GGBFS, compressive strength increases regardless of GGBFS replacement ratio in case of high strength concrete with unit binder content of 500 kg/m^3 , but, in normal strength concrete with unit binder content of approximately 400 kg/m^3 , compressive strength becomes lower than that of OPC concrete when GGBFS replacement ratio exceeds approximately 30% [16].

TABLE 7: Compressive strength, slump, and air content for concrete.

W/B (%)	Cement type	Compressive strength at 28 days (MPa)	Slump (mm)	Air content (%)
32	OPC	49.5	196	5.2
	BBC	57.4	197	4.9
	TBC1	54.0	205	5.2
	TBC2	54.6	196	5.1
43	OPC	36.6	197	5.0
	BBC	26.5	203	5.2
	TBC1	29.5	205	5.1
	TBC2	36.7	194	5.0

3.2. *Mass Change.* Table 8 shows changes in the appearance of concrete specimens immersed in 10% sodium sulfate and 10% magnesium sulfate solutions for 28, 182, and 365 days. Figures 2 and 3 show mass change ratios of concrete specimens immersed in sulfate solution for 28, 56, 91, 182, and 365 days according to W/B.

In case of W/B = 32%, all of the concrete specimens immersed in 10% sodium sulfate solution displayed almost no mass change. This is because the low W/B increased density of the microstructure of concrete and therefore slowed down the process of deterioration by sodium sulfate attack. This result indicated that the use of low W/B was very effective in suppressing sodium sulfate attack. In case of W/B = 43%, the rate of mass decrease in 100% OPC concrete and BBC concrete was found to increase as the age increased. On the other hand, rate of mass decrease was almost not observed in TBC1 concrete and TBC2 concrete. This result proves that resistance against sodium sulfate of mineral admixture is more effective in TBC concrete additionally containing silica fume or fly ash than in OPC concrete and BBC concrete (Table 8).

In case of specimens immersed in 10% magnesium sulfate solution, the rate of mass decrease in concrete containing mineral admixture was larger than that in 100% OPC concrete regardless of W/B. The reason that the rate of mass decrease is higher by magnesium sulfate attack than sodium sulfate attack is because magnesium hydroxide reacts with silica gel and, as a result, C-S-H gradually loses calcium and becomes converted into magnesium silicate hydrates, the nonbinding material [8, 9]. In this case, resistance against magnesium sulfate attack was found to be higher in the order of OPC, TBC2, TBC1, and BBC concrete indicating that use of mineral admixture is disadvantageous. Therefore, caution is required in using mineral admixture when concrete is exposed to magnesium sulfates, such as soil and groundwater.

3.3. *XRD Analysis.* Figure 4 shows the result of XRD analysis on the sulfate reaction parts of concrete specimens with W/B = 43% immersed in sulfate solution for 365 days. As illustrated by the figure, gypsum and ettringite peaks were formed when specimens were immersed in sodium sulfate solution indicating that these two types of hydrates are the main products of reaction against sodium sulfate attack

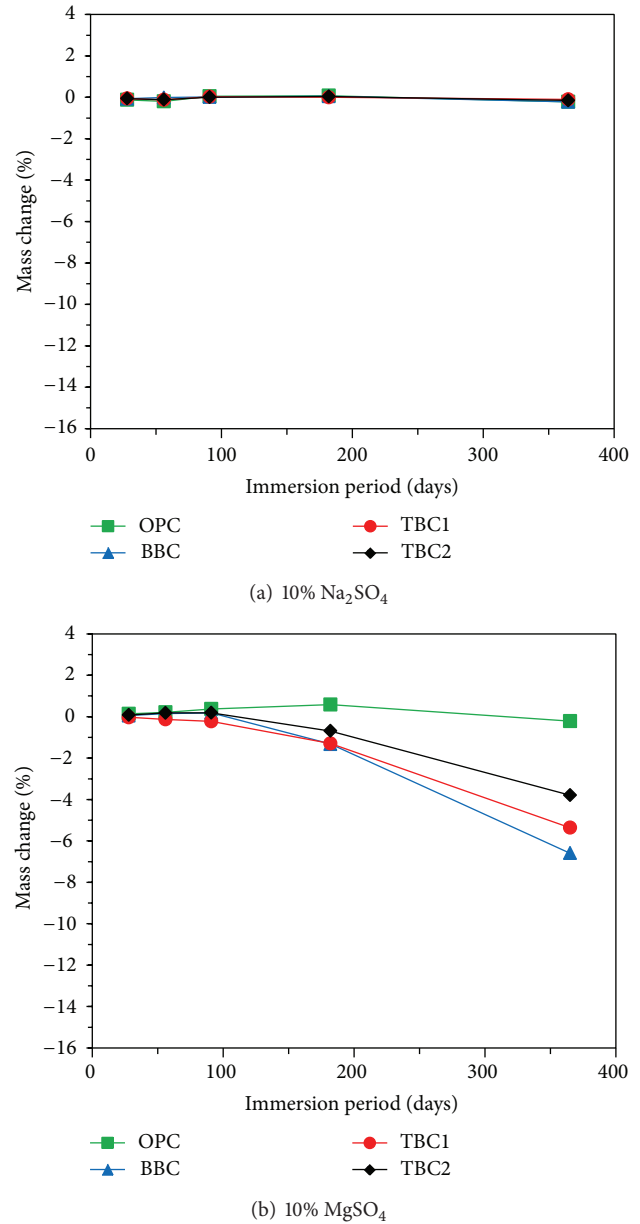


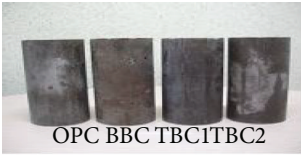
FIGURE 2: Mass change of concrete (W/B = 32%).

causing expansion and cracking. In case of immersion in magnesium sulfate solution, brucite of a relatively lower peak was observed in addition to gypsum and ettringite. Brucite is generated by the reaction of hydration products of cement and cation (Mg^{2+}) which combines with sulfate ions. It plays a determinant role in magnesium sulfate attack mechanism. Therefore, it was indicated that cation (Mg^{2+}) bound with sulfate ions affected the mechanism of magnesium sulfate attack.

3.4. Mass Change Prediction Model for Sulfate Attack

3.4.1. *Suggestion of Mass Change Prediction Model for Sulfate Attack.* As sulfate attack prediction models of concrete,

TABLE 8: Visual appearance changes with immersion ages.

W/B (%)	Immersion period (days)	10% Na ₂ SO ₄	10% MgSO ₄
32	28	 OPC BBC TBC1TBC2	 OPC BBCTBC1TBC2
	182	 OPC BBC TBC1TBC2	 OPC BBC TBC1TBC2
	365	 OPC BBC TBC1TBC2	 OPC BBC TBC1TBC2
43	28	 OPC BBCTBC1TBC2	 OPC BBC TBC1TBC2
	182	 OPC BBCTBC1TBC2	 OPC BBCTBC1TBC2
	365	 OPC BBC TBC1TBC2	 OPC BBC TBC1TBC2

empirical model, mechanistic model, and numerical model are available. However, since the mechanism of sulfate attack is yet to be completely verified, empirical model based on test results is mainly used. Equations (2) and (3) are an empirical model suggested by Kurtis et al. [17]. This is a result of regression analysis on concrete specimens immersed in 2.1% sodium sulfate solution for 40 years to predict concrete expansion by sulfate attack with W/C, immersion period, and C₃A content as independent variables and concrete expansion amount as a dependent variable. In case C₃A content is low, this equation can also be applied to concrete with wide W/C range. However, if C₃A content is high, the W/C-related variables are statistically insignificant and therefore W/C was not included in the prediction model. Consider

$$\text{Exp} = 0.0246 + [0.0180 (T) (W/C)] + [0.00016 (T) (C_3A)] : C_3A < 8\%, \quad (2)$$

$$\text{In (Exp)} = -3.753 + [0.930 (T)] + [0.0998 \text{In} (T) (C_3A)] : C_3A > 10\%, \quad (3)$$

where Exp is percentage of expansion by sulfate attack (%), T is immersion period (year), W/C is water-cement ratio, and C₃A is C₃A content of cement (%).

Equation (4) is an empirical model suggested by Jambor [18] of which W/B is 60% and the purpose is to verify behavior of mortar immersed in sodium sulfate solution. In this test, C₃A content was 9~13%. Also, 10~70% GGBFS and 10~50% volcanic tuff were used. As the test solution, sodium sulfate solution with SO₄ content of 500~33,800 mg/L was used. Using results of measuring amount of sulfates bound by the mortar specimens, mass change, volume change, dynamic modulus of elasticity, compressive strength, and bending strength change of mortar specimens over 4 years, a prediction model for the degree of sulfate-induced corrosion was suggested. In this model, SO₄ concentration, immersion period, C₃A content, and replacement ratio of

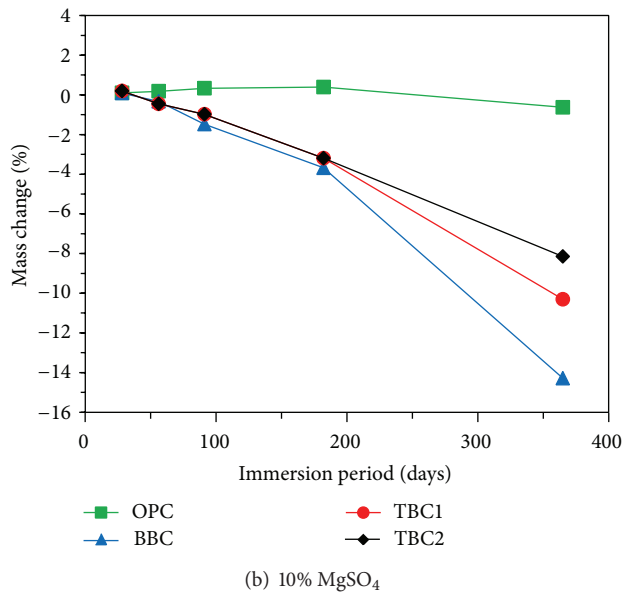
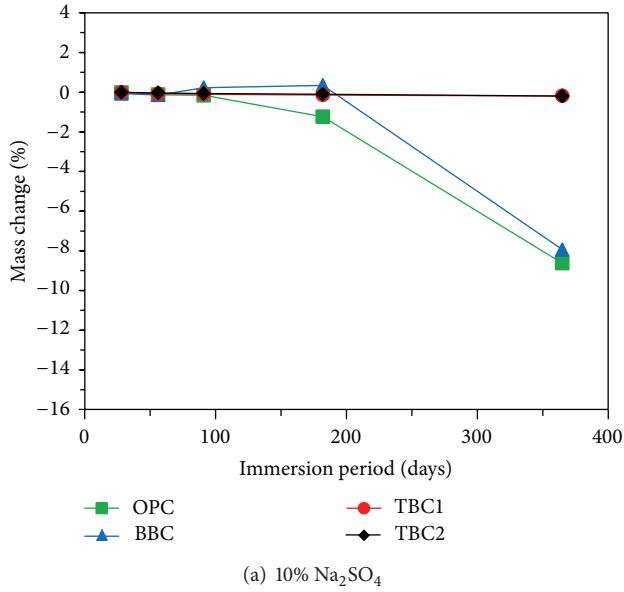


FIGURE 3: Mass change of concrete (W/B = 43%).

mineral admixture were used as independent variables and degree of sulfate-induced corrosion of mortar was used as a dependent variable. Consider

$$DC = e^{-0.016A} \cdot [0.11S^{0.45}] [0.143T^{0.33}] [0.204e^{0.145C_3A}], \quad (4)$$

where DC is degree of sulfate-induced corrosion, S is SO₄ concentration (mg/L) of sulfate solution, T is immersion period (day), C₃A is C₃A content of cement (%), and A is replacement ratio of mineral admixture (binder mass %).

In this study, mass changes of concrete specimens immersed in 10% sodium sulfate solution and 10% magnesium sulfate solution for 1 year were measured per age of immersion and, based on the existing empirical model of (2), a prediction model for mass change by sulfate attack was suggested as of (5)~(8). To determine coefficients of

this model, regression analysis was conducted using SAS (statistical analysis system) [19], a general statistical program, with immersion period, W/B, and C₃A content of concrete as independent variables and mass change as a dependent variable.

- (i) Concrete immersed in sodium sulfate solution for 100% OPC concrete is

$$MC = -\exp[-5.997 + 1.455(T^{0.5})(W/B) - 0.00165(T)(C_3A)] \quad (R^2 = 0.98); \quad (5)$$

for BBC concrete and TBC concrete:

$$MC = -\exp[-3.131 + 0.088(T)\ln(W/B) + 0.076(T)\ln(C_3A)] \quad (R^2 = 0.77). \quad (6)$$

- (ii) Concrete immersed in magnesium sulfate solution for 100% OPC concrete is

$$MC = [0.586 - 0.00525(T)(W/B) - 0.078\ln(T)(C_3A)] \quad (R^2 = 0.50); \quad (7)$$

for BBC concrete and TBC concrete:

$$MC = -\exp[-0.466 + 0.007(T)\ln(W/B) + 0.0046(T)(C_3A)] \quad (R^2 = 0.83), \quad (8)$$

where MC is mass change of concrete by sulfate attack (%), T is immersion period (day), W/B is water-binder ratio, and C₃A is C₃A content of concrete (%).

3.4.2. Verification of Mass Change Prediction Model.

Figures 5 and 6 summarize comparison of the test results of mass change of concrete specimens immersed in sulfate solution with mass change prediction values using the model suggested in this study. As illustrated by the figures, the test results and mass change prediction values of the model suggested in this study correspond relatively well, indicating that prediction of mass change by sulfate attack with a relatively high reliability can be achieved using the model suggested in this study.

Figure 7 compares mass change prediction result using the model suggested in this study with result of the existing model of (4) to predict the degree of sulfate-induced corrosion, in case of concrete immersed in 10% sodium sulfate solution per immersion period. Despite following a similar trend as a whole, the results have slight differences. This is because while the existing model of (4) predicts a general degradation of mortar according to mass and volume change, strength, and dynamic modulus of elasticity, the suggested model predicts only the mass change of concrete by sulfate attack and therefore test conditions and variables are different.

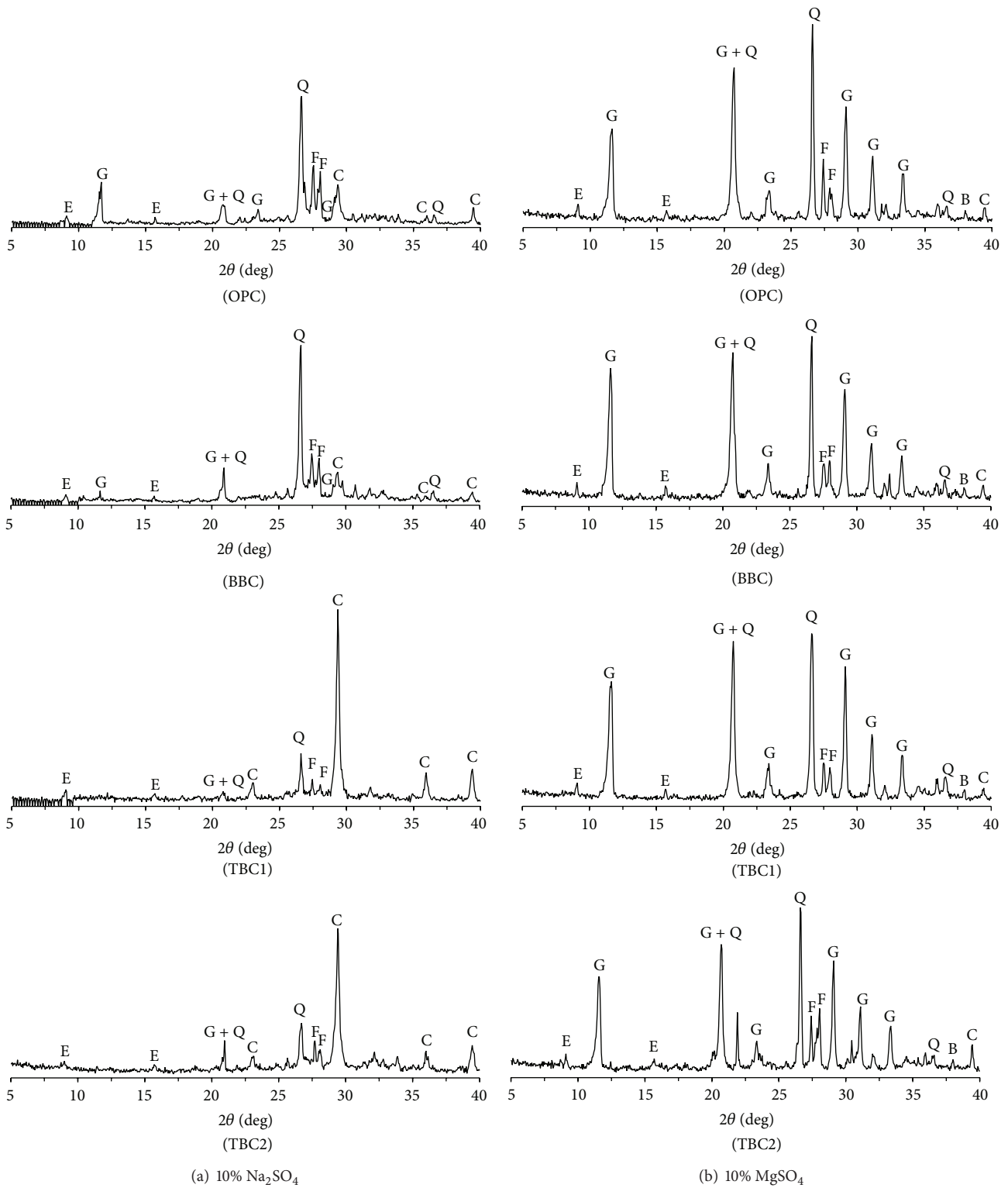


FIGURE 4: XRD analysis results of concrete specimens (G: gypsum, E: ettringite, B: brucite Q: quartz, C: calcite, and F: feldspar).

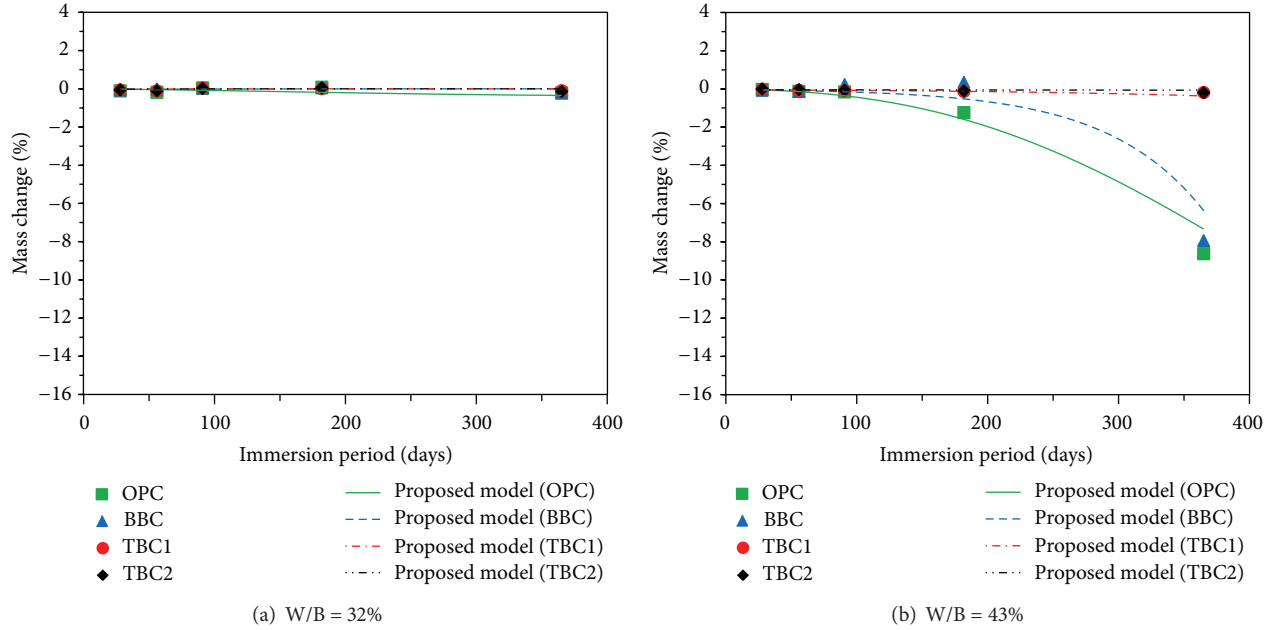


FIGURE 5: Comparison of the measurements and predictions (10% Na_2SO_4).

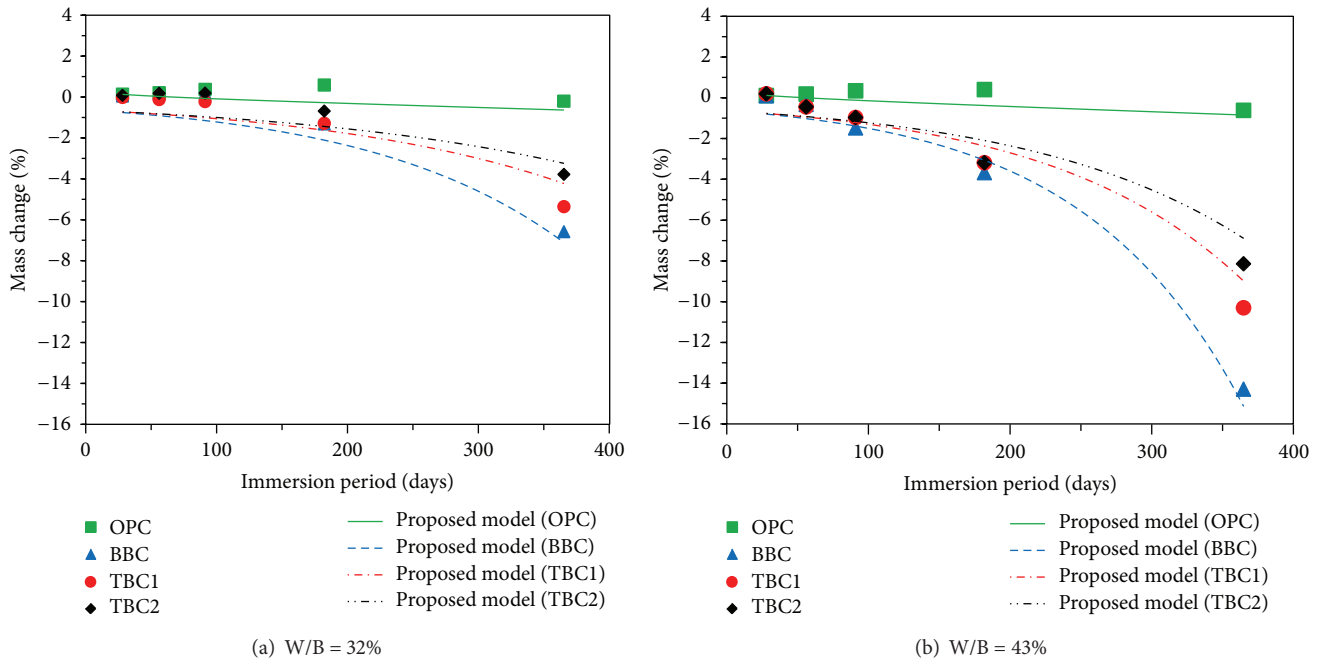


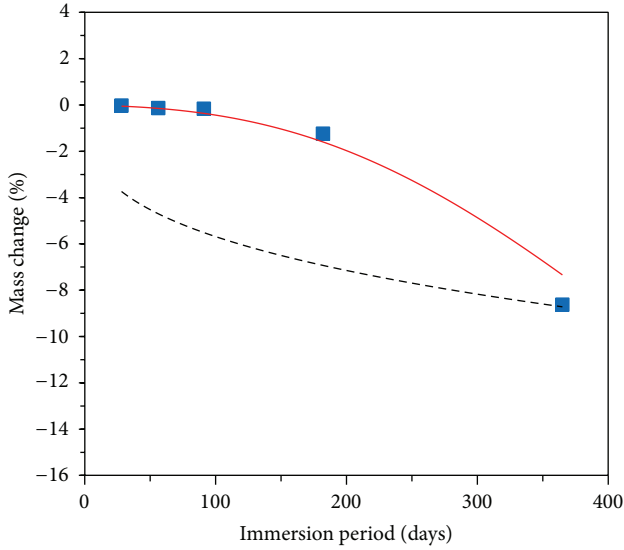
FIGURE 6: Comparison of the measurements and predictions (10% MgSO_4).

4. Conclusions

The following conclusions were drawn from the experimental study on the mass change of concrete subjected to sulfate attack.

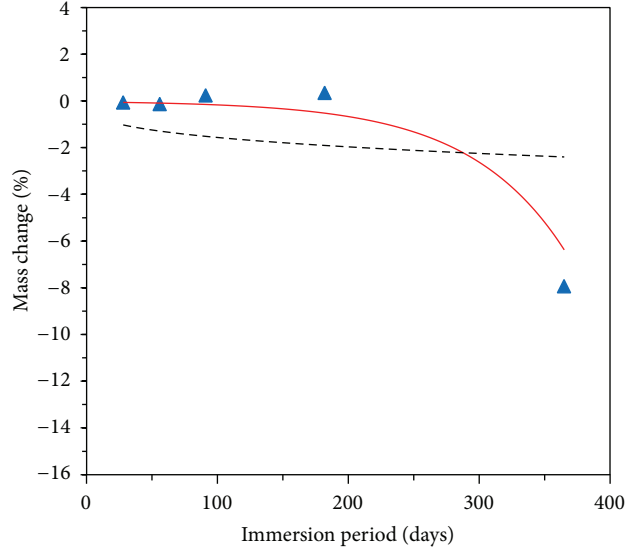
- (1) In case of immersion in 10% sodium sulfate solution, almost no mass change was observed in all of the concrete specimens regardless of the use of mineral

admixture when W/B was 32%. This is because the low W/B increased density of concrete microstructure and therefore slowed down degradation by sodium sulfate attack. When W/B was 43%, the rate of mass decrease in 100% OPC concrete and BBC concrete specimens was found to be higher as the age of immersion increased. However, there was almost no mass decrease of TBC1 concrete and TBC2 concrete.



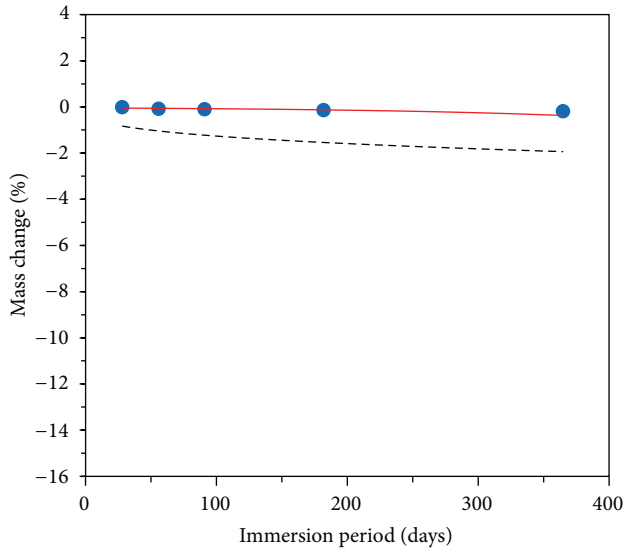
■ Experimental results
 — Proposed model (Eq. (5))
 - - - Jambor's model (Eq. (4))

(a) OPC concrete



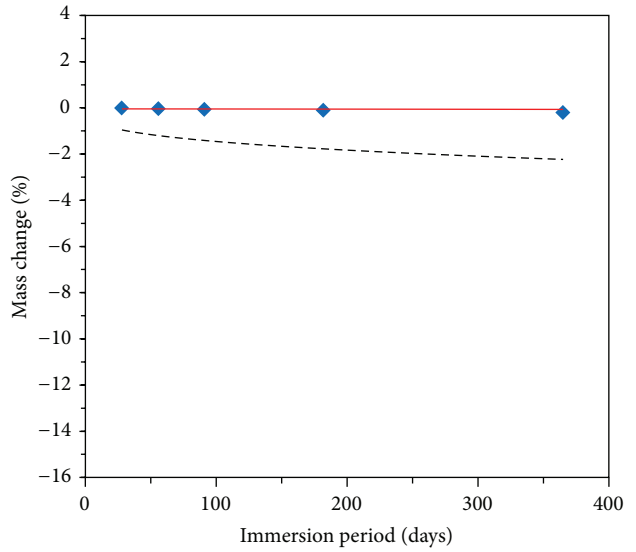
▲ Experimental results
 — Proposed model (Eq. (6))
 - - - Jambor's model (Eq. (4))

(b) BBC concrete



● Experimental results
 — Proposed model (Eq. (6))
 - - - Jambor's model (Eq. (4))

(c) TBC1 concrete



◆ Experimental results
 — Proposed model (Eq. (6))
 - - - Jambor's model (Eq. (4))

(d) TBC2 concrete

FIGURE 7: Comparison of results predicted by proposed model and Jambor's model ($W/B = 43\%$, $10\% Na_2SO_4$).

This proves that the resistance of mineral admixture against sodium sulfate was greater in TBC than in BBC.

- (2) In case of immersion in 10% magnesium sulfate solution, the rate of mass decrease of concrete containing mineral admixture was found to be higher than OPC concrete regardless of W/B. This is because pozzolanic reaction of mineral admixture consumes

calcium hydroxide and resultantly lowers the C-S-H protection effect of calcium hydroxide at magnesium sulfate attack. Therefore, it is necessary to take caution in using mineral admixture when concrete is exposed to the magnesium sulfate environment, such as soil and groundwater.

- (3) Based on the test results, a prediction model for mass change of concrete by sulfate attack was suggested and

it was found that the test results and predictions by the suggested model corresponded relatively well. To further generalize sulfate attack prediction model, it will be necessary to pursue studies on sulfate resistance test and mechanistic and numerical methods by considering a variety of influential factors.

Conflict of Interests

The authors declare that there is no conflict of interests regarding the publication of this paper.

Acknowledgments

This research was supported by “the Center for Concrete Korea” and “04KIBANKUCHOOKA02” sponsored by Ministry of Land, Infrastructure, and Transport of Korea. This support is gratefully acknowledged.

References

- [1] P. K. Mehta, “Mechanism of sulfate attack on portland cement concrete—another look,” *Cement and Concrete Research*, vol. 13, no. 3, pp. 401–406, 1983.
- [2] T. H. Wee, A. K. Suryavanshi, S. F. Wong, and A. K. M. Anisur Rahman, “Sulfate resistance of concrete containing mineral admixtures,” *ACI Materials Journal*, vol. 97, no. 5, pp. 536–549, 2000.
- [3] M. A. Shazali, M. H. Baluch, and A. H. Al-Gadhib, “Predicting residual strength in unsaturated concrete exposed to sulfate attack,” *Journal of Materials in Civil Engineering*, vol. 18, no. 3, pp. 343–354, 2006.
- [4] A. Cavdar and S. Yetgin, “Investigation of mechanical and mineralogical properties of mortars subjected to sulfate,” *Construction and Building Materials*, vol. 24, no. 11, pp. 2231–2242, 2010.
- [5] P. S. Mangat and J. M. Khatib, “Influence of fly ash, silica fume, and slag on sulfate resistance of concrete,” *ACI Materials Journal*, vol. 92, no. 5, pp. 542–552, 1995.
- [6] O. S. B. Al-Amoudi, “Mechanisms of sulfate attack in plain and blended cements: a review,” in *Proceedings of the Conference Extending Performance of Concrete Structures. International Congress “Creating with Concrete”*, pp. 247–260, Dundee, UK, 1999.
- [7] N. Shanahan and A. Zayed, “Cement composition and sulfate attack: part I,” *Cement and Concrete Research*, vol. 37, no. 4, pp. 618–623, 2007.
- [8] M. Santhanam, M. D. Cohen, and J. Olek, “Mechanism of sulfate attack: a fresh look: part 1: summary of experimental results,” *Cement and Concrete Research*, vol. 32, no. 6, pp. 915–921, 2002.
- [9] M. Santhanam, M. D. Cohen, and J. Olek, “Mechanism of sulfate attack: a fresh look part 2 : proposed mechanisms,” *Cement and Concrete Research*, vol. 33, no. 3, pp. 341–346, 2003.
- [10] N. Yoshida, Y. Matsunami, M. Nagayama, and E. Sakai, “Salt weathering in residential concrete foundations exposed to sulfate-bearing ground,” *Journal of Advanced Concrete Technology*, vol. 8, no. 2, pp. 121–134, 2010.
- [11] S. U. Al-Dulajjan, “Sulfate resistance of plain and blended cements exposed to magnesium sulfate solutions,” *Construction and Building Materials*, vol. 21, no. 8, pp. 1792–1802, 2007.
- [12] S. Goyal, M. Kumar, D. S. Sidhu, and B. Bhattacharjee, “Resistance of mineral admixture concrete to acid attack,” *Journal of Advanced Concrete Technology*, vol. 7, no. 2, pp. 273–283, 2009.
- [13] H. N. Atahan and D. Dikme, “Use of mineral admixtures for enhanced resistance against sulfate attack,” *Construction and Building Materials*, vol. 25, no. 8, pp. 3450–3457, 2011.
- [14] JSTMC 7401, *Method of Test for Chemical Resistance of Concrete in Aggressive Solution*, Japanese Industrial Standard, Tokyo, Japan, 1999.
- [15] ASTM, “Standard test method for length change of hydraulic-cement mortars exposed to sulfate solution,” ASTM C 1012, American Society for Testing and Materials, 2007.
- [16] S. H. Bae, Y. S. Chung, K. S. Park, and J. G. Lee, “An experimental study on the properties of admixtures for concrete,” *Journal of Korea Concrete Institute*, vol. 11, no. 2, pp. 115–125, 1999.
- [17] K. E. Kurtis, P. J. M. Monteiro, and S. M. Madanat, “Empirical models to predict concrete expansion caused by sulfate attack,” *ACI Structural Journal*, vol. 97, no. 2, pp. 156–161, 2000.
- [18] J. Skalny, J. Marchand, and I. Odler, *Sulfate Attack on Concrete*, pp. 153–160, Spon Press, 2002.
- [19] SAS Institute, *Statistical Analysis Systems (SAS)*, Version 9.1.3, SAS Institute, Cary, NC, USA, 2002.

Research Article

Interring Gas Dynamic Analysis of Piston in a Diesel Engine considering the Thermal Effect

Wanyou Li,¹ Yibin Guo,¹ Tao He,^{1,2} Xiqun Lu,¹ and Dequan Zou^{1,2}

¹College of Power and Energy Engineering, Harbin Engineering University, Harbin, Heilongjiang 150001, China

²Washington University in St. Louis, St. Louis, MO 63108, USA

Correspondence should be addressed to Wanyou Li; hrbeu_rivet.lwy@163.com

Received 28 August 2014; Accepted 10 November 2014

Academic Editor: Woo-Young Jung

Copyright © 2015 Wanyou Li et al. This is an open access article distributed under the Creative Commons Attribution License, which permits unrestricted use, distribution, and reproduction in any medium, provided the original work is properly cited.

Understanding the interaction between ring dynamics and gas transport in ring pack systems is crucial and needs to be imperatively studied. The present work features detailed interring gas dynamics of piston ring pack behavior in internal combustion engines. The model is developed for a ring pack with four rings. The dynamics of ring pack are simulated. Due to the fact that small changes in geometry of the grooves and lands would have a significant impact on the interring gas dynamics, the thermal deformation of piston has been considered during the ring pack motion analysis in this study. In order to get the temperature distribution of piston head more quickly and accurately, an efficient method utilizing the concept of inverse heat conduction is presented. Moreover, a sensitive analysis based on the analysis of partial regression coefficients is presented to investigate the effect of groove parameters on blowby.

1. Introduction

The piston ring performs its function as a seal of high and low pressure sides in a cylinder and a medium of heat transfer from piston to cylinder walls. The operation of piston ring packs influences the performance, efficiency, durability, and emissions of engines in terms of friction, wear, oil consumption, and gas blowby. For those reasons, the performance of piston rings in combustion engines has been a topic of research for many years. Ting and Mayer [1, 2] developed early models of ring lubrication and blowby. Their models were aimed at the eventual prediction of cylinder wear. The work of Dowson et al. [3] and Ruddy et al. [4, 5] has resulted in the development of more integrated simulations, which include effects of ring dynamics. Rhode [6] has incorporated into ring lubrication calculations a model of mixed lubrication, which allows more realistic calculation of ring friction; it has been so since adopted by a number of other investigators. The effort toward further integration of various submodels into what has become an established scheme of two-dimensional axisymmetric analysis of ring packs has continued in the eighties [7], with more studies involving various design parameters as well as comparison to data [8, 9].

Classical theory of lubrication is based on the Reynolds equation, which can be derived from control volume analysis under certain simplifying assumptions. This equation calculates the oil film pressure given the film thickness, squeeze velocity, and the pressure at the boundaries (typically ambient pressure). Then attention had been shifting from ring dynamics and blowby, which can be predicted with reasonable accuracy, to the modeling of oil consumption, the accuracy of the current oil consumption models [9–11]. Keribar et al. [12] developed an integrated model of piston ring pack including ring-liner hydrodynamic and boundary lubrication, ring axial, radial, and twist dynamics, interring gas dynamics, and blowby. Blow-by gas flow refers to the undesired gas flow from combustion chamber to the crankcase. It reduces the efficiency of the engine and contaminates oil with the combustion products present in the gases; the ring pack system serves as a channel for blow-by gases. As a result, it is important for engine manufacturers and lubricant suppliers to optimize ring pack system to take it into account in controlling oil consumption resulting from blow-by gases. Such research pursues to decrease the amount of blow-by gas flow while upholding sufficient lubrication and minimum friction.

Most of the existing models above are based on the axisymmetric assumption, called 2D models. With the help of these 2D models, a great deal of detailed analysis of ring lubrication has been performed and some conclusions have been used successfully in guiding the practical application [13]. The efforts to model the ring dynamics in 3D manner can also be found in the publications. Tian et al. [14] presented ring dynamics and gas flow model to study ring/groove contact, blowby, and the influence of ring static twist, keystone ring/groove configurations, and other piston ring parameters. Ejakov et al. [15] simulated the dynamic twist angle of the piston ring pack along the circumference by using finite element analysis. In [16], a combination of a detailed elastic analysis and a complementarity method was used to evaluate the ring/bore conformability in an accurate way. Ma [17, 18] implemented a flow-continuity algorithm in the hydrodynamic lubrication submodel, which ensured an accurate oil transport simulation. Liu [19] developed a piston ring pack model considering nonaxisymmetric characteristics of power cylinder system considering oil transport along the liner. The oil transport along the ring pack system is driven by the motion of the piston rings [20]. Sometimes, oil is entrained in blow-by gases, transported within the ring pack. The demonstration of the interaction between ring performance and gas transport can help to understand oil transport mechanism and lead to effective ways of reducing the oil consumption. Li [21] took the ring geometry, assembly load, and mechanical and thermal properties into consideration in their simulation of piston ring behavior.

In order to know the ring pack motion, the most important part is to analyse the interring gas dynamic. Due to the fact that small changes in geometry of the grooves, lands, and bore would have a significant impact on the interring gas dynamics, the thermal deformation should be taken into consideration during ring pack motion analysis. In order to determine the thermal deformation of bore and piston, a 2D finite element (FE) model is used in this study. In the thermal analysis part, an efficient method utilizing the concept of inverse heat conduction is presented to get the temperature distribution of piston. After getting the temperature distribution of piston, a thermostructure analysis is presented to get the deformation of piston lands and grooves and bore, as the input data for ring pack dynamics and tribological analysis. The second part of this study focuses on the interring gas dynamics of piston ring pack behavior in internal combustion engines. The model is developed for a ring pack with four rings. The dynamics of the top three rings and the gas pressure in the regions about the oil control ring are simulated.

2. Modeling of Piston Ring Pack Dynamics

The motion of piston ring within the piston groove can be described by the axial rotational (toroidal twist) and radial motions in the three respective degrees of freedom. The ring motion in the circumference direction is neglected in this study. As shown in Figure 1, a small section for the ring at a

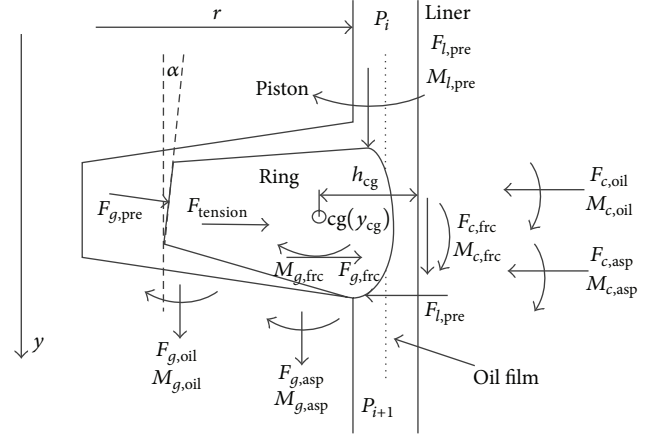


FIGURE 1: Free body diagram of ring cross-section.

circumferential location is considered. The governing equations for the ring motion are written as

$$\begin{aligned}
 m_r \frac{d^2 y_{cg}}{dt^2} &= F_{g,oil} + F_{g,asp} + F_{c,fric} - F_{l,pre} - m_r g, \\
 I_r \frac{d^2 \alpha}{dt^2} &= M_{g,oil} + M_{g,asp} + M_{c,fric} \\
 &\quad + M_{l,pre} + M_{c,oil} + M_{c,asp} - K_{rt} \alpha, \\
 m_r \frac{d^2 h_{cg}}{dt^2} &= F_{g,pre} + F_{g,fric} + F_{c,oil} \\
 &\quad - F_{c,asp} - F'_{l,pre} + K_{rr} (h' + h_0),
 \end{aligned} \tag{1}$$

where y_{cg} and h_{cg} are the axial and radial position of the center of gravity of the ring and α is the twist angle. m_r , I_r , and K_{rt} are ring mass, moment of inertia for toroidal rotation, and cross-sectional torsional stiffness. K_{rr} is the radial tension stiffness, h' the reduction in ring radius at installation, and h_0 the minimum ring-bore oil film thickness ($F_{tension} = K_{rr}(h' + h_0)$). F 's and M 's are forces and moments acting on the ring cross-section, as shown in the free body diagrams of Figures 1 and 2. In terms of forces and moments in (1) the first subscript indicates location on the ring (g = groove, c = cylinder, and l = land) and the second subscript describes the source of the force or moment (oil = oil pressure, asp = normal pressure due to asperity contact, pre = gas pressure, and fric = hydrodynamic or boundary friction). The torsional moment M_{rt} is calculated as

$$M_{rt} = K_{rt} \alpha. \tag{2}$$

For a complete ring with rectangular cross-section, the cross-sectional torsional stiffness (K_{rt}) is given by

$$K_{rt} = \frac{Eb^3 \ln(D/d)}{3(D+d)}, \tag{3}$$

where E is the modulus of elasticity of piston ring, b is the axial height of piston ring section, d is the inner diameter,

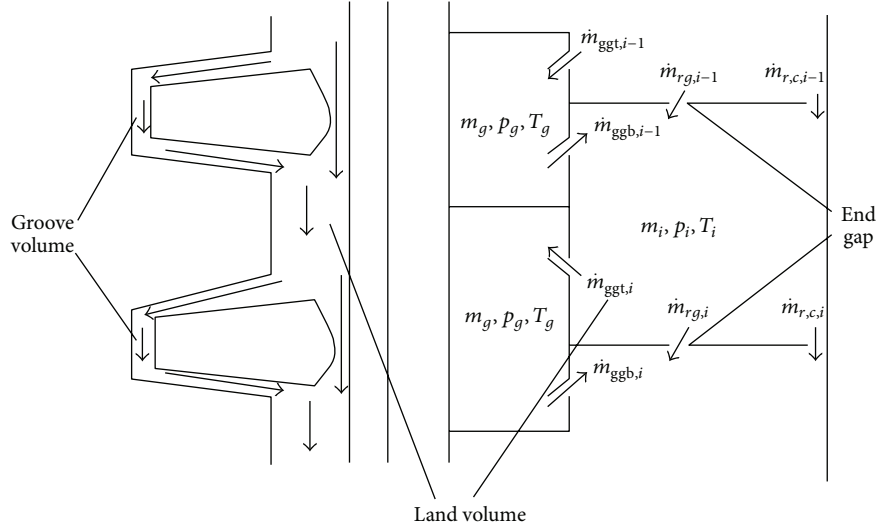


FIGURE 2: Gas volumes and gas flow paths in ring pack.

and D is the outer diameter of piston ring. The axial motion of a ring relative to piston can be expressed as

$$\begin{aligned} y_{cg} &= y_p + y_{rp}, \\ \frac{dy_{cg}}{dt} &= \frac{dy_p}{dt} + \frac{dy_{rp}}{dt}, \\ \frac{d^2 y_{cg}}{dt^2} &= \frac{d^2 y_p}{dt^2} + \frac{d^2 y_{rp}}{dt^2}, \end{aligned} \quad (4)$$

where y_p is the axial position of the piston and y_{rp} is the axial position of the ring related to the piston.

Forces and moment associated with land and groove gas pressure are calculated using pressure solutions from gas dynamics submodel. Those associated with oil pressure are obtained from the lubrication submodel, and those associated with local asperity contact pressure are calculated by asperity deformation model. Ring axial position and twist influence gas flow paths and the forces at the ring groove interface. Ring twist also affects the effective profile presented by the ring face to the cylinder bore and thus oil film thickness and ring friction. The lubrication model, asperity deformation model, and oil film squeezing model at ring side and groove interface have specific introduction in [12, 14].

3. Interring Gas Dynamics

The gas flow between the rings and groove flanks and the flow behind the ring are calculated based on the actual interring volumes due to actual clearances and ring positions. The real mass flow rate is determined from the ideal flow by use of discharge coefficients. The purpose of the interring gas dynamics model is the calculation of the rate of gas blowby through the leakage paths between series of gas volumes. The gas volumes in ring grooves as well as ring-lands are considered and calculated from the piston, groove, and ring geometries and positions, as shown in Figure 2. The leakage

paths are the gaps between rings and grooves (due to areas that become available during ring motions in grooves), the gaps between the ring face and cylinder bore (due to ring lift), and the ring-end gaps. The blowby is assumed to be an unsteady adiabatic flow satisfying the perfect gas law. It is also assumed that the combustion chamber pressure versus crank angle relation remains unaffected despite the gas leakage. The continuity equations for the land and groove gas volumes are written as

$$\begin{aligned} \frac{dm_{l,i}}{dt} &= \dot{m}_{leg,i-1} + \dot{m}_{ggb,i-1} + \dot{m}_{rlg,i-1} - \dot{m}_{geg,i} \\ &\quad - \dot{m}_{ggt,i} - \dot{m}_{rlg,i}, \quad (i = 2, \dots, N), \\ \frac{dm_{g,i}}{dt} &= \dot{m}_{ggt,i} + \dot{m}_{geg,i} - \dot{m}_{ggb,i} - \dot{m}_{leg,i}, \quad (i = 1, \dots, N), \end{aligned} \quad (5)$$

where m is the mass of gas in volume and \dot{m} denotes the mass flow rate through the various flow paths identified by subscripts “leg”/“geg” (ring-end gaps connected to groove volume and connected to land volume), “ggt”/“ggb” (ring groove gaps above and below ring), and “rlg” (ring-left gaps). For the first land volume, the continuity equation is

$$\frac{dm_{l,1}}{dt} = \dot{m}_{lin,1} - \dot{m}_{geg,1} - \dot{m}_{ggt,1} - \dot{m}_{rlg,1}, \quad (6)$$

where $\dot{m}_{lin,1}$ is the mass flow rate through the gap between piston and bore at the piston top position. The gas flow rates through the flow paths are calculated by the following relationship.

$$\text{If } p_d/p_u > (2/(\gamma + 1))^{\gamma/(\gamma-1)},$$

$$\begin{aligned} \dot{m} &= C_f A \left(\frac{2\gamma}{R(\gamma + 1)T_u} \right)^{1/2} \\ &\quad \cdot p_u \left(\frac{p_d}{p_u} \right)^{1/\gamma} \left[1 - \left(\frac{p_d}{p_u} \right)^{(\gamma-1)/\gamma} \right]^{1/2}. \end{aligned} \quad (7)$$

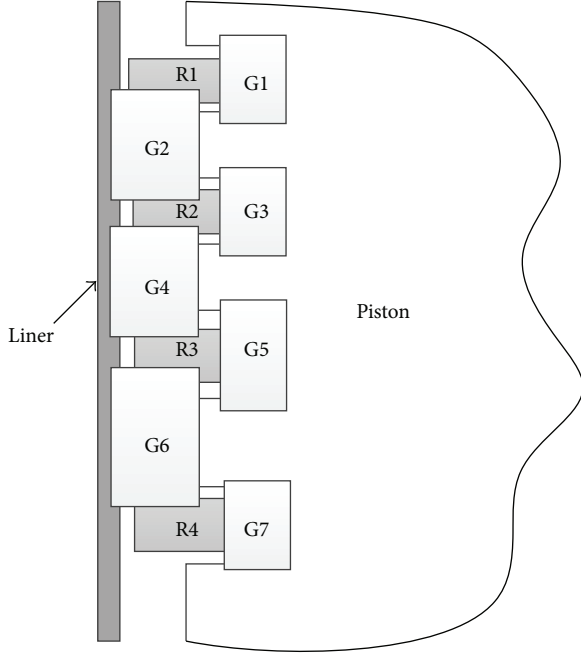


FIGURE 3: Gas zones during piston ring pack dynamic.

If $p_d/p_u \leq (2/(\gamma + 1))^{\gamma/(\gamma-1)}$,

$$\dot{m} = C_f A \left(\frac{2\gamma}{R(\gamma + 1)T_u} \right)^{1/2} \cdot p_u \left(\frac{2}{\gamma + 1} \right)^{1/(\gamma-1)} \left[1 - \left(\frac{2}{\gamma + 1} \right) \right]^{1/2}. \quad (8)$$

In (7) and (8), C_f is the orifice flow coefficient, A is the orifice area, R and γ are the gas constant and polytropic exponent, p_u and p_d are pressure upstream and downstream of the orifice, and T_u is the upstream temperature.

The gas equation of state is applied to land volumes and the groove volumes:

$$\begin{aligned} p_{l,i} V_{l,i} &= m_{l,i} R T_{l,i}, \quad (i = 1, \dots, N), \\ p_{g,i} V_{g,i} &= m_{g,i} R T_{g,i}, \quad (i = 1, \dots, N). \end{aligned} \quad (9)$$

In this paper, the whole system includes three piston rings and five gas zones that are formed by rings, piston, and liner as sketched in Figure 3. Gas temperatures in the land volumes and groove volumes are assumed to be equal to the instantaneous area-weighted average of the temperature of surfaces surrounding each volume. And those temperatures and volumes would be gotten by the thermomechanical analysis of piston. In this study, an efficient method utilizing the concept of inverse heat conduction based on the FEA is presented for the thermal analysis of piston.

4. Thermomechanical Analysis of Piston Based on Using the Inverse Heat Conduction Method

According to the structure of piston head and bore, shown in Figure 3, in order to get the gas temperatures in land volumes and groove volumes, it is important to know the temperature distribution of piston head and bore. In recent years, finite element method has been used to calculate piston temperature [21–29]. It should be noticed that after having identified one correlation for one engine, we acknowledge that those correlation parameters are not valid for another engine with similar characteristics. This is because the convection heat transfer coefficient has many influence factors, and it is hard to give an accurate correlation to describe the distribution of HTC. In this paper, an efficient method utilizing the concept of inverse heat conduction based on the FEA is presented for the thermal analysis of pistons [27]. And using the inverse heat conduction method, the HTC can be effectively determined without giving the correlation.

4.1. Inverse Heat Conduction Method. The relationship between temperature and HTC (h_c) can be given by

$$T = T(h_c). \quad (10)$$

Thus, the inverse heat conduction problem can be described to find

$$\sum_{i=1}^n |[T' - T(h_c)]| \rightarrow \min, \quad (11)$$

where T' is the real temperature (testing temperature), related to $T(h_c)$ (predicted temperature) and n is the number of conduction segments. Due to the specific piston, the structure of this piston is known, and the HTC is the only unknown parameter. According to (11), if the error between calculated temperature and test temperature can be satisfied, the calculation requirement, the HTC h_c can be tried as the real HTC during conduction in real situation. The governing equation of the steady state thermal conduction in the piston can be expressed as [27]

$$k \frac{\partial T}{\partial n} \Big|_{\Gamma} = h_c (t - T_f) \Big|_{\Gamma}, \quad (12)$$

where T and k represent the temperature and thermal conductivity, respectively. Similar to earlier studies on the thermal analysis of the piston [30], the convection boundary condition can be applied to the piston surface according to the equation as follows:

$$q = h(T - T_{\infty}), \quad (13)$$

where q , h , and T_{∞} represent the outward normal heat flux, the HTC, and the surrounding temperature at the surface, respectively. The surrounding temperature T_{∞} can be defined as the combustion gas temperature T_{gas} at the combustion-side top surface of the piston head, the cooling

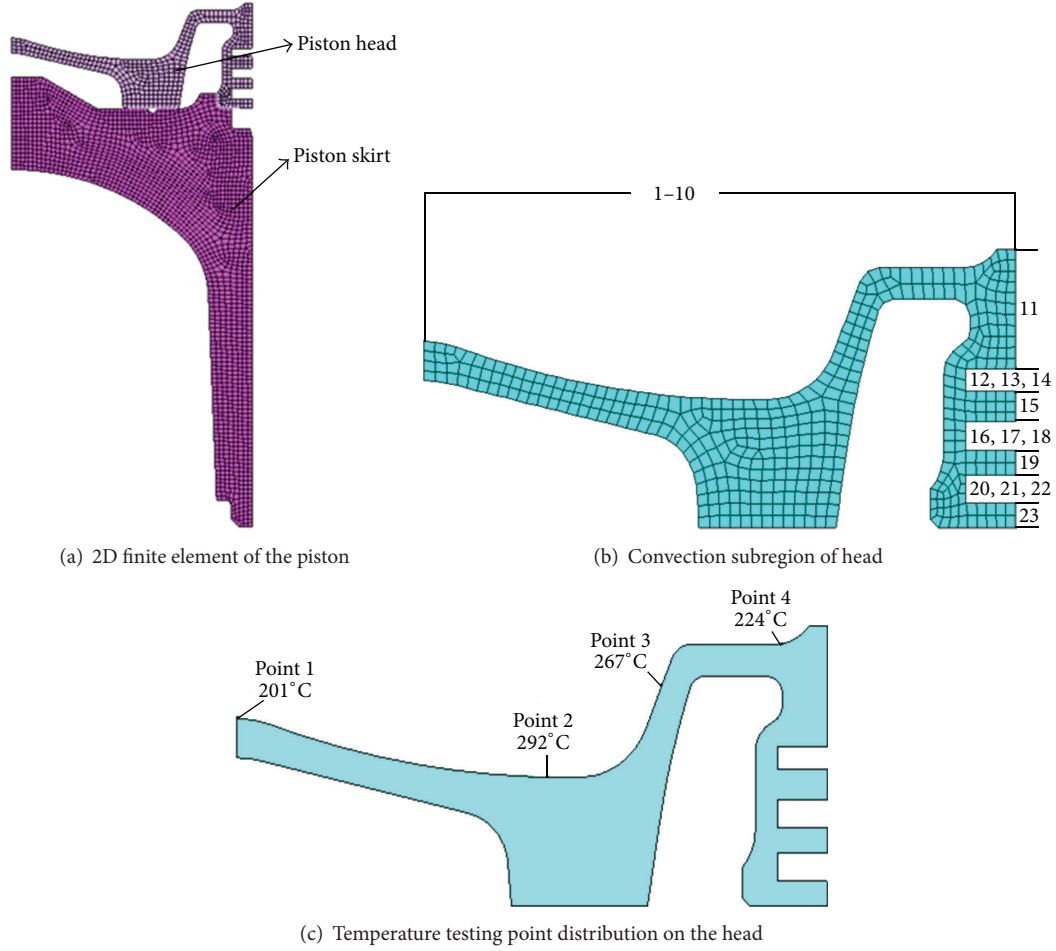


FIGURE 4: 2D model of piston.

water temperature T_c at the side, and the oil temperature T_{oil} at the underside and cooling gallery [31].

In order to find an accurate solution to the inverse heat conduction problem, the finite element (FE) method is employed in this study. The 2D FE model of piston is built by quadratic solid 55 elements in order to analyze the axisymmetric problem (as shown in Figure 4(a)). And the head of piston is divided into numerous boundary segments ($n = 23$) of which HTC's are a piecewise constant (as shown in Figure 4(b)). The distribution of testing point is shown in Figure 4(c). Assume the temperature of node i is $T_i(h_c)$, and the initial magnitude is $h_{c0} = (h_{c10}, h_{c20}, \dots, h_{cn0})$. Thus using Taylor's formula, $T_i(h_c)$ can be expressed as

$$T_i(h_c) = T_i(h_{c0}) + \sum_{j=1}^n \frac{\partial T_i}{\partial h_{cj}} h_{cj} (h_{cj} - h_{cj0}), \quad (14)$$

$$(i = 1, 2, \dots, n).$$

If $T_i(h_c) = T_i$, (14) can be written as

$$\sum_{j=1}^n \frac{\partial T_i}{\partial h_{cj}} h_{cj} = T_i' - T_i(h_{c0}) + \sum \frac{\partial T_i}{\partial h_{cj}} h_{cj0}. \quad (15)$$

Thus, those equations can compose a linear equation system relating to $(h_{c1}, h_{c2}, \dots, h_{cn})$, and it can be written as

$$\mathbf{W} \mathbf{h}_c = \mathbf{P}, \quad (16)$$

where the HTC matrix $\mathbf{h}_c = (h_{c1}, h_{c2}, \dots, h_{cn})^T$, the equation coefficient matrix $\mathbf{W} = \begin{bmatrix} w_{11} & \dots & w_{1n} \\ \vdots & & \vdots \\ w_{m1} & \dots & w_{mn} \end{bmatrix}$, and each element can be calculated by

$$w_{jk} = \left. \frac{\partial T_i}{\partial h_{ck}} \right|_{h_{ck}=h_{ck0}}. \quad (17)$$

And $\mathbf{P} = \{P_1, P_2, \dots, P_n\}$; vector element in this matrix can be given by

$$P_k = T_i' - T_i + W h_{c0}. \quad (18)$$

If the partial derivative of each HTC is known, the solution is the optimum solution. However, it is hard to know the linear correlation between HTC and temperature and the following equation can be used to get the better approximate solution:

$$[K]\{T\} = \{P\}, \quad (19)$$

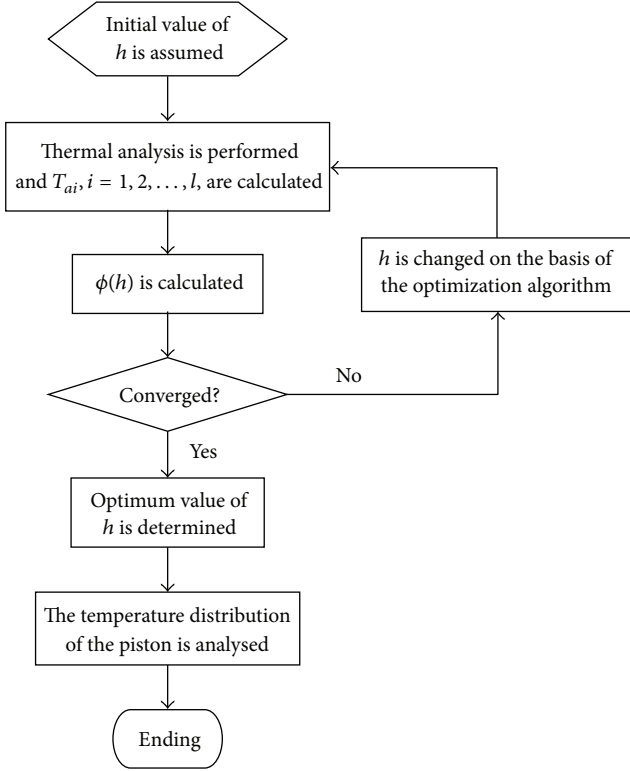


FIGURE 5: Procedure to solve the inverse heat conduction problem.

where $\{T\}$ is the predicted temperature which is unknown and $[K]$ is the function of HTC and heat conductivity coefficient (HCC); it can be given as $K = f(k, h_c)$. There are a number of partial derivatives in (19). In order to improve the solving accuracy, the first-order method of the ANSYS design optimization module is used in this study.

4.2. Numerical Simulation Procedure. The inverse heat conduction problem of the equation above can be solved using the optimization technique; the procedure to solve the problem is described in Figure 5. The HTC varies depending on the location of the piston surface. The HTC at the surface of head, excluding the piston head, is determined by Lu et al. [31], and the initial value of all design variables, that is, the HTC, is set uniformly as $100 \text{ W/m}^2\text{K}$. An inverse heat conduction problem to determine h_i can be formulated as an optimization problem as finding [32]

$$h \equiv \{h_1, \dots, h_n\} \quad (20)$$

to minimize

$$\phi(h) \equiv \sum_{i=1}^l (T_{ai} - T_{mi})^2. \quad (21)$$

The numerical implementation to solve the optimization problem is performed by ANSYS. The first-order method of the ANSYS design optimization module is used, the gradients being calculated with a design variable increment of 0.05 percent of the difference between the upper and lower

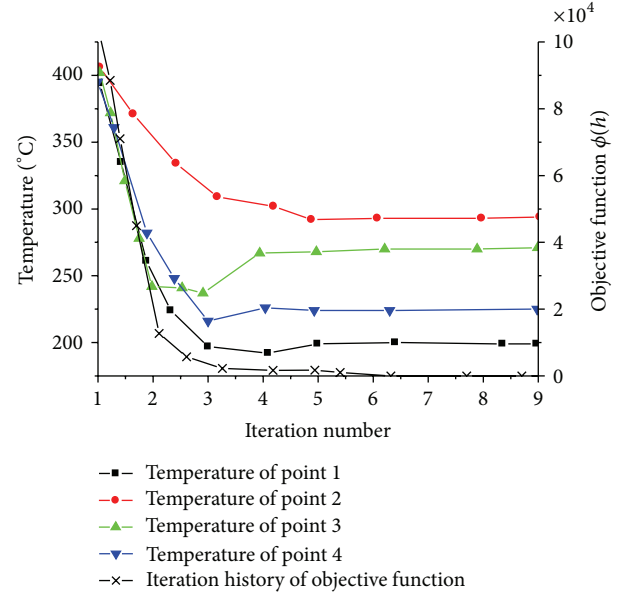


FIGURE 6: Iteration history of the objective function and temperatures of testing point.

TABLE 1: Comparison of the measured temperatures and the predicted temperatures with the optimum HTC.

Measurement points	Predicted temperature T_{mi} °C	Measured temperature T_{ai} °C	$ (T_{mi} - T_{ai})/T_{ai} $ (%)
Point 1	197.25	201	1.9
Point 2	291.31	292	0.23
Point 3	268.15	267	0.43
Point 4	222.68	224	0.59

bounds. The acceptable change in the design variables between iterations for convergence is set as $0.01 \times \text{current value}$.

5. Results and Discussion

5.1. Temperature Distribution and Thermal Deformation of Piston Lands and Grooves. The optimization problem for the piston is analyzed. Less than 9 iterations are taken to obtain the optimum solutions; the history of the objective function and testing points' temperature during iterations is shown in Figure 6. The initial optimum value of the objective function is very large and the optimum value of objective function is very close to zero. As an inverse problem, the temperatures of testing points become close to the test value (shown in Figure 6) very fast. And the temperature distributions calculated by initial and optimum value of the HTC are shown in Figure 7. The analyzed temperature using the optimum HTC is compared with the measured temperature in Table 1. Note that the maximum error is less than 1.9%.

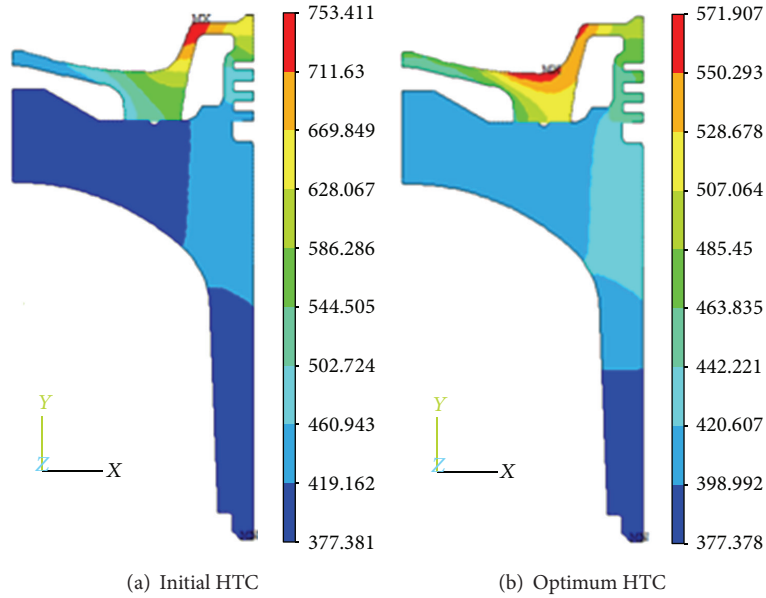


FIGURE 7: Temperature distribution of the piston head.

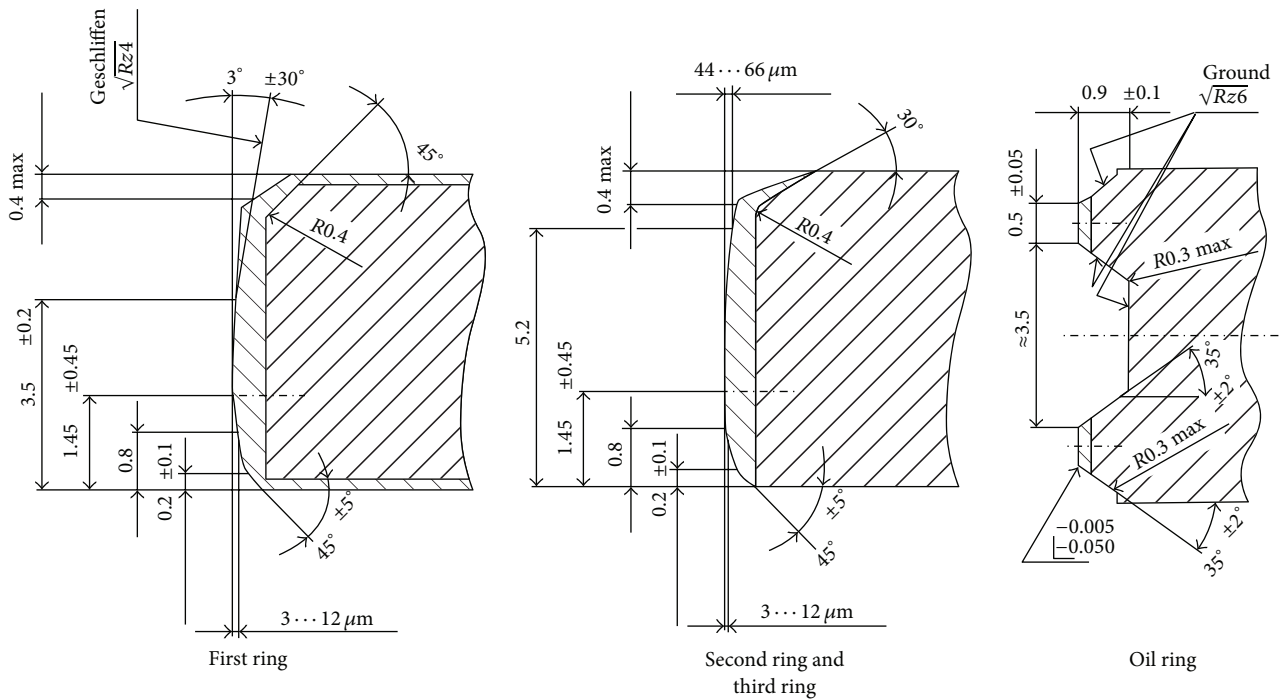


FIGURE 8: The geometry of the piston rings.

5.2. Performance of Ring Pack. The geometry of the piston rings and structure of piston head used in this study are shown in Figures 8 and 9. Each ring is modeled as a single mass; twisting (including pretwist angles) is considered. The equations of motion, which consider equilibrium condition of moments and forces for each ring, are solved. The dynamic components of the ring motion are calculated by means of

time integration methods of explicit type. The mechanism of piston ring sealing is equivalent to a labyrinth seal, where the gap clearances are determined by the actual position of the rings in the groove in consideration of the global movement and tilting of the piston [33]. The law for isotropic flow of ideal gas is used for the calculation of the gas flows, as (9) showed. The calculation of the updated gas pressures due

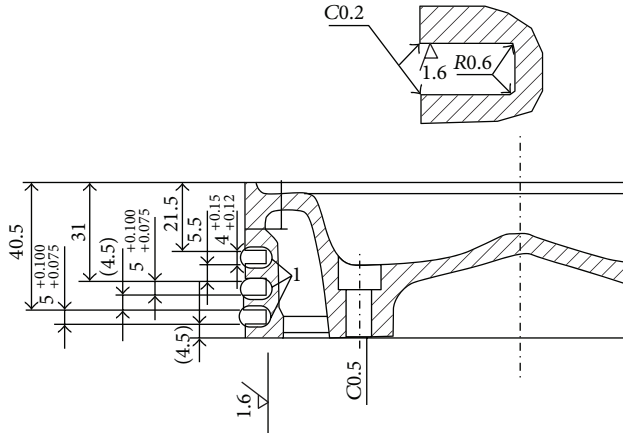


FIGURE 9: The structure of piston head.

TABLE 2: The temperature distribution of piston grooves and lands.

Parameters	Location	Temperature/°C
	1st ring groove (A)	201.6
	1st ring groove (B)	167.1
	1st ring groove (C)	158.7
	1st ring groove (D)	153.5
	2nd ring groove (A)	152.8
	2nd ring groove (B)	147.2
	2nd ring groove (C)	136.5
	2nd ring groove (D)	136.0
	3rd ring groove (A)	135.8
	3rd ring groove (B)	135.7
	3rd ring groove (C)	135.2
	3rd ring groove (D)	135.2

to changes in mass and vessel volume is described by the isotherm equation of state. The particular piston temperature and thermal deformation are given by FEA, listed in Tables 2 and 3. The Reynolds equations are solved iteratively in each time step to determine the hydrodynamic pressure distribution between ring running surface and liner. The last part of the simulation procedure deals with the evaluation of oil consumption to the combustion gas [34] and the friction loss [35, 36]. All relevant mechanisms are considered; the calculation is done quasistatically per time step, and the program code is designed by Fortran.

5.2.1. The Pressure Distribution in Ring Grooves and Piston Lands. The calculated axial position of rings in grooves is

TABLE 3: Deformation of grooves and lands.

Parameters	Value (μm)
1st ring groove	
Δh_1	-35
Δh_2	-2
Δr_1	267
Δr_2	255
2nd ring groove	
Δh_1	-19
Δh_2	1
Δr_1	247
Δr_2	240
3rd ring groove	
Δh_1	4
Δh_2	7
Δr_1	243
Δr_2	259

Positive = increase; negative = decrease.

TABLE 4: The friction loss, blowby, and oil consumption considering thermal effect.

Friction loss (kW)			Total loss (kW)	Oil consumption (g/h)
First ring	Second ring	Third ring		
3.4191	1.3196	1.2451	5.9837	257.5
Inverse blowby* (g/s)			Average blowby (g/s)	
First ring	Second ring	Third ring		
-7.6367	-0.2203	0.00000	0.9675	

*The average blowby is the average of the flow ring downland to upland, and the “-” is the inverse.

shown in Figure 10. Wear of the parallel surfaces in piston ring grooves, commonly called ring groove wear, occurs mainly in the top groove. The main reason for the wear is the combined effect of gas forces and radial motion of the ring, and the wear process is accelerated by poor lubrication and a high temperature. The reasons for the radial motion of the ring are the cylinder distortion, the secondary movement of the piston, and piston tilt allowed by the piston/cylinder clearance. Mass forces, friction forces, axial ring movement, and ring rotation increase the ring groove wear. Instationary gas pressure and gas blowby may cause radial vibrations in the ring, which accelerates the ring groove wear at the ring groove contact areas [37]. And the friction loss and gas blowby at the piston rings are summarized in Table 4. It is clear that the ratios of the first ring in friction loss and inverse blowby are majority (57.14% and 97.44%, resp.), and this means the design of the first ring groove is significant for the piston design.

5.2.2. Piston Groove Parameters Sensitive Analysis. Blow-by gas flow refers to the undesired gas flow from the combustion chamber to the crankcase. It reduces the efficiency of engine and contaminates oil with the combustion products present

TABLE 5: An analysis of variance table for the simple linear regression model.

Source	SS (sums of squares)	df (degrees of freedom)	MS (mean squares)	F-statistic	Significance F
Regression	SS_R	$df_R = m$	MS_R	$F = MS_R/MS_r$	$F_\alpha(m, n - m - 1)$
Residual	SS_r	$df_r = n - m - 1$	MS_r		
Total	SS_T	$df_T = n - 1$			

TABLE 6: Analysis of variance table for the multiple linear regression ($\Delta h1$).

Source	SS	df	MS	F	Significance F
Regression	$2.75E - 03$	3	$9.18E - 04$	$3.00E + 07$	$F_{0.05}(3, 1) = 216$
$\Delta h1(1)$	$4.00E - 08$	1	$4.00E - 08$	$1.31E + 03$	$F_{0.01}(3, 1) = 540$
$\Delta h1(2)$	0	1	0	~ 0	$F_{0.05}(1, 1) = 161$
$\Delta h1(3)$	0	1	0	~ 0	$F_{0.01}(1, 1) = 405$
Residual	$3.06E - 11$	1	1.1867		
Total	$2.75E - 03$	2			

TABLE 7: Analysis of variance table for the multiple linear regression ($\Delta h2$).

Source	SS	df	MS	F	Significance F
Regression	$2.65E - 03$	3	$9.12E - 04$	$2.92E + 07$	$F_{0.05}(3, 1) = 216$
$\Delta h2(1)$	$3.82E - 08$	1	$3.82E - 08$	$1.21E + 03$	$F_{0.01}(3, 1) = 540$
$\Delta h2(2)$	0	1	0	~ 0	$F_{0.05}(1, 1) = 161$
$\Delta h2(3)$	0	1	0	~ 0	$F_{0.01}(1, 1) = 405$
Residual	$3.00E - 11$	1	1.1277		
Total	$2.75E - 03$	2			

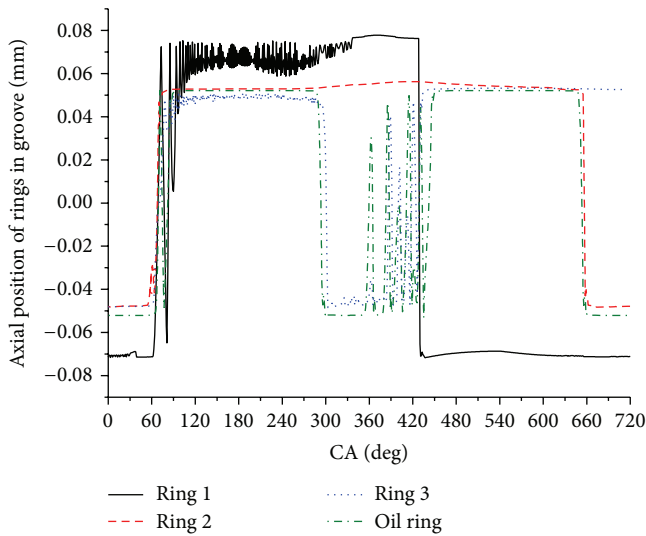


FIGURE 10: The axial position of rings in grooves.

in the gases. The ring pack system serves as a channel for blow-by gases. As a result, it is important for engine manufacturers and lubricant suppliers to optimize ring pack system to take it into account in controlling oil consumption resulting from blow-by gases. In order to investigate the effect of groove parameters on blowby, a sensitive analysis based on the analysis of partial regression coefficients and an analysis of variance (ANOVA) table for the simple linear

regression model can be given in Table 5 [38]. During the multiple linear regression (MLR) analysis, the blowby of first ring is the dependent variable (DV), and the parameters of groove, such as $\Delta h1(i)$, $\Delta h2(i)$, $\Delta r1(i)$, and $\Delta r2(i)$ (i is the number of grooves) shown in Table 2, are the independent variables (IVs). In this study, when one IV increased by one unit (1 mm), all the other IVs are held constant (as shown in Table 3). The analysis results of multiple linear regression related to the groove parameters are listed in Tables 6–9, respectively. Based on those tables, it is obvious that $\Delta h1(1)$ and $\Delta h2(1)$ have significant influence on blow-by gas flow and other parameters without any obvious impact on it. Due to the thermal effect on $\Delta h1(1)$ and $\Delta h2(1)$, the interring gas dynamic analysis should consider the thermal effect.

6. Conclusions

The present work features detailed interring gas dynamics of piston ring pack behavior in internal combustion engines. The model is developed for a ring pack with four rings. The dynamics of ring pack are simulated. Due to the fact that small changes in geometry of the grooves and lands would have a significant impact on the interring gas dynamics, the thermal deformation of piston and bore has been considered during the ring pack motion analysis in this study. In order to get the temperature distribution of piston head more quickly and accurately, an efficient method utilizing the concept of inverse heat conduction is presented. The result of the temperature analyzed using the optimum HTC is compared

TABLE 8: Analysis of variance table for the multiple linear regression ($r1$).

Source	SS	df	MS	F	Significance F
Regression	$2.75E - 03$	3	$9.17E - 04$	$3.06E + 02$	$F_{0.05}(3, 1) = 216$
$r1(1)$	$-2.21E - 12$	1	$-2.21E - 12$	~ 0	$F_{0.01}(3, 1) = 540$
$r1(2)$	0	1	0	~ 0	$F_{0.05}(1, 1) = 161$
$r1(3)$	0	1	0	~ 0	$F_{0.01}(1, 1) = 405$
Residual	$2.99E - 06$	1	$2.99E - 06$		
Total	$2.75E - 03$	2			

TABLE 9: Analysis of variance table for the multiple linear regression ($r2$).

Source	SS	df	MS	F	Significance F
Regression	$2.66E - 03$	3	$8.86E - 04$	$9.30E + 00$	$F_{0.05}(3, 1) = 216$
$r2(1)$	$-5.50E - 18$	1	$-5.50E - 18$	~ 0	$F_{0.01}(3, 1) = 540$
$r2(2)$	$1.44E - 18$	1	$1.44E - 18$	~ 0	$F_{0.05}(1, 1) = 161$
$r2(3)$	$3.77E - 18$	1	$3.77E - 18$	~ 0	$F_{0.01}(1, 1) = 405$
Residual	$9.53E - 05$	1	$9.53E - 05$		
Total	$2.75E - 03$	2			

with the measured temperature, and reasonable agreement is obtained. Moreover, a sensitive analysis based on the analysis of partial regression coefficients is presented to investigate the effect of groove parameters on blowby. And the result shows that $\Delta h1(1)$ and $\Delta h2(1)$ (shown in Table 2) have significant influence on blow-by gas flow, while other parameters have no obvious impact on it. As the thermal effect on $\Delta h1(1)$ and $\Delta h2(1)$, the interring gas dynamic analysis should consider the thermal effect.

Conflict of Interests

The authors declare that they have no conflict of interests regarding this work.

Acknowledgments

The present research has been funded by National Natural Science Foundation of China (Grant no. 51375104) and Fundamental Research Funds for the Central Universities (Code HEUCFZ1117). The authors would like to sincerely express their appreciation.

References

- [1] L. L. Ting and J. E. Mayer, "Piston ring lubrication and cylinder bore wear analysis, part I—theory," *Journal of Lubrication Technology*, vol. 96, pp. 305–314, 1974.
- [2] L. L. Ting and J. E. Mayer, "Piston ring lubrication and cylinder bore wear analysis, part II—theory verification," *Journal of Tribology*, vol. 96, no. 2, pp. 258–266, 1974.
- [3] D. Dowson, P. N. Economou, and B. L. Ruddy, "Piston ring lubrication-part II: theoretical analysis of a single ring and complete ring pack," in *Energy Conservation Through Fluid Film Lubrication Technology: Frontiers in Research and Design—Winter Annual Meeting of the ASME*, pp. 23–52, 1979.
- [4] B. L. Ruddy, D. Dowson, and P. N. Economou, "Piston ring lubrication, Part III: the influence of ring dynamics and ring twist," in *Proceedings of the Winter Annual Meeting of ASME: Energy Conservation Through Fluid Film Lubrication Technology: Frontiers in Research and Design*, pp. 191–215, 1979.
- [5] B. L. Ruddy, D. Dowson, and P. N. Economou, "A theoretical analysis of the twin-land type of oil-control piston ring," *Journal of Mechanical Engineering Science*, vol. 23, no. 2, pp. 51–62, 1981.
- [6] S. M. Rhode, "A mixed friction model for dynamically loaded contacts with application to piston ring lubrication," in *Proceedings of the 7th Leeds-Lyon Symposium on Tribology*, p. 262, Westbury House, September 1980.
- [7] R. Truscott, T. J. Reid, and B. L. Ruddy, "Ring dynamics in a diesel engine and its effects on oil consumption and blowby," SAE Paper 831282, SAE, 1983.
- [8] B. L. Ruddy, T. J. Reid, and A. Veshagh, "Ring pack performance predictions," in *Proceedings of the AE Symposium*, Paper No. 30, 1986.
- [9] T. J. Banks and D. J. Lacy, "The application of analysis to piston ring performance," IMechE paper No. C375/003, 1989.
- [10] K. Maekawa, S. Mitsutake, and S. Morohoshi, "A study of engine lubricating oil consumption by computer simulation," SAE Paper 860546, 1986.
- [11] R. Munro, "Emissions impossible—the piston and ring support system," SAE Paper 900590, 1990.
- [12] R. Keribar, Z. Dursunkaya, and M. F. Flemming, "Integrated model of ring pack performance," *Journal of Engineering for Gas Turbines and Power*, vol. 113, no. 3, pp. 382–389, 1991.
- [13] R. Rabuté and T. Tian, "Challenges involved in piston top ring designs for modern SI engines," *Journal of Engineering for Gas Turbines and Power*, vol. 123, no. 2, pp. 448–459, 2001.
- [14] T. Tian, L. B. Noordzij, V. W. Wong, and J. B. Heywood, "Modeling piston-ring dynamics, blowby, and ring-twist effects," *Journal of Engineering for Gas Turbines and Power*, vol. 120, no. 4, pp. 843–854, 1998.
- [15] M. A. Ejakov, H. J. Shock, and L. J. Brombolich, "Modeling of ring twist for an IC engine," SAE Paper 982693, SAE, 1998.
- [16] Y. Hu, H. S. Cheng, T. Arai, Y. Kobayashi, and S. Aoyama, "Numeric simulation of piston ring in mixed lubrication—a

- nonaxisymmetrical analysis,” *Journal of Tribology*, vol. 116, no. 3, pp. 470–478, 1994.
- [17] M.-T. Ma, I. Sherrington, and E. H. Smith, “Analysis of lubrication and friction for a complete piston-ring pack with an improved oil availability model part 1: circumferentially uniform film,” *Proceedings of the Institution of Mechanical Engineers Part J: Journal of Engineering Tribology*, vol. 211, no. 1, pp. 1–15, 1997.
- [18] M.-T. Ma, I. Sherrington, and E. H. Smith, “Analysis of lubrication and friction for a complete piston-ring pack with an improved oil availability model. Part II: circumferentially variable film,” *Proceedings of the Institution of Mechanical Engineers Part J: Journal of Engineering Tribology*, vol. 211, no. 1, pp. 17–27, 1997.
- [19] L. Liu, *Modeling the performance of the piston ring-pack with consideration of non-axisymmetric characteristics of the power cylinder system in internal combustion engines* [Ph.D. thesis], Massachusetts Institute of Technology, 2005.
- [20] B. Thirouard, *Characterization and modeling of the fundamental aspects of oil transport in the piston ring pack of internal combustion engines* [Ph.D. thesis], MIT, 2001.
- [21] C. H. Li, “Piston thermal deformation and friction considerations,” SAE paper 820086, 1982.
- [22] M. T. Abbes, P. Maspeyrot, A. Bounif, and J. Frene, “A thermo-mechanical model of a direct injection diesel engine piston,” *Proceedings of the Institution of Mechanical Engineers Part D: Journal of Automobile Engineering*, vol. 218, no. 4, pp. 395–409, 2004.
- [23] Y. Liu and R. D. Reitz, “Multidimensional modeling of combustion chamber surface temperatures,” SAE Paper 971539, 1997.
- [24] R. J. Jcnkin, E. H. James, and W. Malalascckra, “Modelling the effects of combustion and turbulence on near-wall temperature gradients in the cylinders of spark ignition engines,” *Proceedings of the Institution of Mechanical Engineers, Part D: Journal of Automobile Engineering*, vol. 212, no. 6, pp. 533–546, 1998.
- [25] S. V. Bohac, D. M. Baker, and D. N. Assanis, “A global model for steady state and transient SI engine heat transfer studies,” SAE Paper 960073, SAE, 1996.
- [26] V. Esfahanian, A. Javaheri, and M. Ghaffarpour, “Thermal analysis of an SI engine piston using different combustion boundary condition treatments,” *Applied Thermal Engineering*, vol. 26, no. 2-3, pp. 277–287, 2006.
- [27] B. Y. Lee and W. J. Kim, “Thermal analysis of a liquid-petroleum-liquid injection engine piston using the inverse heat conduction method,” *Proceedings of the Institution of Mechanical Engineers Part D: Journal of Automobile Engineering*, vol. 222, no. 6, pp. 1033–1045, 2008.
- [28] G. Li, *3D steady thermal analysis and intensity calculation for piston* [M.S. thesis], Harbin Engineering University, Harbin, China, 2006.
- [29] D.-M. Lou, Z.-Y. Zhang, and L.-L. Wang, “Heat transfer boundary condition and thermal load of combined-piston for locomotive diesel engines,” *Journal of Tongji University*, vol. 33, no. 5, pp. 664–667, 2005 (Chinese).
- [30] X.-Q. Lu, T. He, D.-Q. Zou, Y.-B. Guo, and W.-Y. Li, “Thermal analysis of composite piston in marine diesel engine based on inverse evaluation method of heat transfer coefficient,” *Chinese Internal Combustion Engine Engineering*, vol. 33, no. 4, pp. 71–76, 2012.
- [31] X. Lu, Q. Li, W. Zhang, Y. Guo, T. He, and D. Zou, “Thermal analysis on piston of marine diesel engine,” *Applied Thermal Engineering*, vol. 50, no. 1, pp. 168–176, 2013.
- [32] T. He, X. Q. Lu, and Y. B. Guo, “Analysis of the heat transfer coefficients on the top of a marine diesel piston using the inverse heat conduction method,” *Advanced Materials Research*, vol. 291–294, pp. 1657–1661, 2011.
- [33] R. J. Gamble, M. Priest, R. J. Chittenden, and C. M. Taylor, “Preliminary study of the influence of piston secondary motion on piston ring tribology,” *Tribology Series*, vol. 38, pp. 679–691, 2000.
- [34] S. M. Chun, “Simulation of engine life time related with abnormal oil consumption,” *Tribology International*, vol. 44, no. 4, pp. 426–436, 2011.
- [35] S.-W. Cho, S.-M. Choi, and C.-S. Bae, “Frictional modes of barrel shaped piston rings under flooded lubrication,” *Tribology International*, vol. 33, no. 8, pp. 545–551, 2000.
- [36] G. A. Livanos and N. P. Kyrtatos, “Friction model of a marine diesel engine piston assembly,” *Tribology International*, vol. 40, no. 10–12, pp. 1441–1453, 2007.
- [37] K. Mollenhauer, *Diesel Engine*, Springer, Berlin, Germany, 1997, (German).
- [38] <http://wenku.baidu.com/view/857487d5360cbalaa811da03.html>.

Research Article

Mathematical Approach in Rheological Characterizing of Asphalt Emulsion Residues

Seong Hwan Cho¹ and Jeong Hyuk Im²

¹Department of Civil, Construction, and Environmental Engineering, North Carolina State University, Campus Box 7908, 2501 Stinson Drive, Raleigh, NC 27695, USA

²Highway Pavement Research Division, Korea Institute of Civil Engineering and Building Technology (KICT), Daehwa-Dong 283, Goyangdae-ro, Ilsanseo-gu, Goyang-si, Gyeonggi-do 411-712, Republic of Korea

Correspondence should be addressed to Jeong Hyuk Im; jhim5572@gmail.com

Received 3 October 2014; Accepted 24 December 2014

Academic Editor: Woo-Young Jung

Copyright © 2015 S. H. Cho and J. H. Im. This is an open access article distributed under the Creative Commons Attribution License, which permits unrestricted use, distribution, and reproduction in any medium, provided the original work is properly cited.

Three different emulsion residues, such as SSIHP, HFE90, and SS-1VH (trackless), and a base asphalt binder (PG 64-22) are compared to characterize rheological properties by using DSR test. In order to capture the emulsion properties, different frequencies (from 1 to 100 rad/sec at a 10% constant shear rate) and temperatures (from -45°C to 75°C with 15°C increments) were applied. Then, a master curve for shear modulus was plotted for each emulsion. The transition of the HFE90 emulsion from viscous to elastic behavior occurs at lower temperatures, compared to the other materials. This emulsion is known for performing in a wider temperature range as shown in the results. The trackless emulsion presents an elastic behavior at intermediate temperatures. This product is known as having very fast setting and high resistance to shear stresses. The trackless emulsion presents the highest viscous and elastic modulus, followed by the PG 64-22 binder, SSIHP, and HFE90 emulsion. Shear strength test results show a behavior between trackless emulsion and SSIHP similar to the frequency sweep test results performed by DSR.

1. Introduction

As the need for new construction for asphalt pavement has been decreased over time, an increased interest in preventive maintenance and rehabilitation has come to the fore. The asphalt emulsion is one of the most effective materials for the preventive maintenance of asphalt pavement. Also, the asphalt emulsion is an ecofriendly material because its construction system does not include heating equipment. For example, chip seals, which are among the most efficient and cost-effective methods utilized by state highway agencies to preserve and rejuvenate existing pavements, are constructed by application of asphalt emulsion and aggregate. The asphalt emulsion is applied as a liquid condition, and then it becomes a residue condition by curing procedure. Therefore, the properties of asphalt residue play a vital role in the performance.

Diverse laboratory tests are usually performed on the asphalt emulsions and their residue. In order to obtain

appropriate properties that can be related to field performance, it is critical to obtain an emulsion residue that is representative of the emulsion used in the field.

Takamura [1] proved that high temperatures of distillation procedure, which are 177°C or 260°C , can significantly alter or damage the microscopic structure of the emulsion and thus the residues recovered by these processes do not represent the field conditions where construction is done in ambient temperatures. Also, he proposed a new residue recovery procedure that uses airflow under ambient temperatures to simulate field conditions. The forced air-drying procedure, in which the emulsion was dried under ambient temperatures for 5-6 hours, was found to preserve the microscopic polymer network in the residue.

King et al. [2] showed some early indications about the performance of emulsions made using polymer-modified asphalts. The tests were limited to HF emulsions and a CRS emulsion for both neat and polymer-modified asphalts.

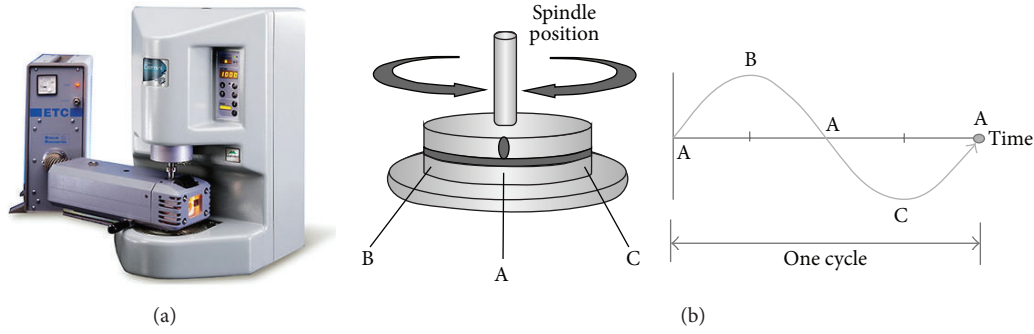


FIGURE 1: (a) DSR equipment and (b) schematic of cylindrical specimen.

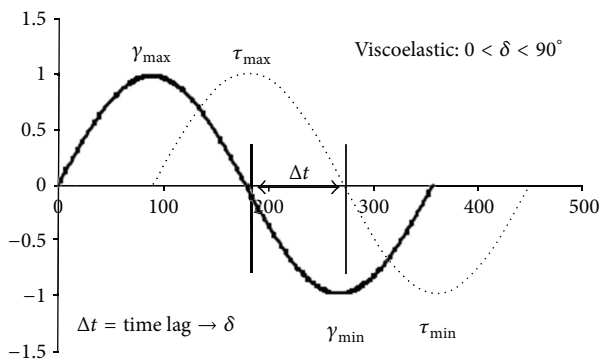


FIGURE 2: Definition of phase angle.

The asphalts were recovered from the respective emulsions by distillation at 204°C . It was found that the use of polymer-modified binder with an HF (high float) emulsifier could decrease the limiting stiffness temperature by 3°C .

Also, Barcena et al. [3] proposed asphalt emulsion used for surface treatments from an extension of King's study. This surface performance grading system follows the PG system with certain changes in the dynamic shear rheometer (DSR) high temperature test and the bending beam rheometer (BBR) test specification limits. They proposed that emulsion residues could be efficiently obtained without degrading polymer morphology by a stirred-can procedure performed under a nitrogen blanket at 163°C for 170 minutes. A survey by TxDOT found that aggregate loss due to flow and brittle fracture at high and low temperatures, respectively, were the principle modes of distress for surface treatments.

Deneuvillers and Samanos [4] conducted a series of emulsions with different particle size diameters and correlated the various rheological properties like viscosity, breaking index, and cohesion build-up with respect to parameters like median diameter of the emulsion gel particles and their standard deviation and also arrived at characterizing grading curves.

Bec et al. [5] studied an accelerated curing mechanism for cold mixes in laboratory conditions, with the idea of

being able to predict final mechanical properties. The study indicates that conditioning of the test pieces at 50°C and 10% RH gives the same level of resistance after five days that would be obtained in 30 days for test pieces conditioned at 18°C and 50% RH. The results also show that, regardless of the temperature and RH conditions, it is almost impossible to completely eliminate the water.

2. Objective

The objective of this study is to characterize rheological properties of three different asphalt emulsion residues and a base binder by using DSR. The results also will be related to the emulsions performance as a tack coat material.

3. Methodology

Three different emulsions SS1HP, HFE90, and SS-1VH (track-less) are used in this study. For the sake of time, the RTFO method has been selected to recover emulsion residues. In addition, a base binder with PG 64-22 is also tested. The samples are characterized by using dynamic shear rheometer (DSR) to find their rheological properties such as shear modulus (G^*) and phase angle (δ). The proposed test procedure is to run a frequency sweep test from 1 to 100 rad/sec at a 10% constant shear rate. The test is conducted at a temperature range of -45°C to 75°C with 15°C increments (9 temperatures in total) to capture the emulsion properties through its glassy behavior to viscous behavior. Then, a master curve for shear modulus is plotted for each emulsion.

3.1. Dynamic Shear Rheometer Test. The dynamic shear rheometer (DSR) is a common device to characterize the elastic and viscoelastic behaviors of asphalt binders as well as asphalt emulsions at high and intermediate temperature. Figure 1(a) presents the DSR equipment used in this study.

The emulsion residues are obtained using the Superpave binder test procedures by Marasteanu and Clyne [6]. For

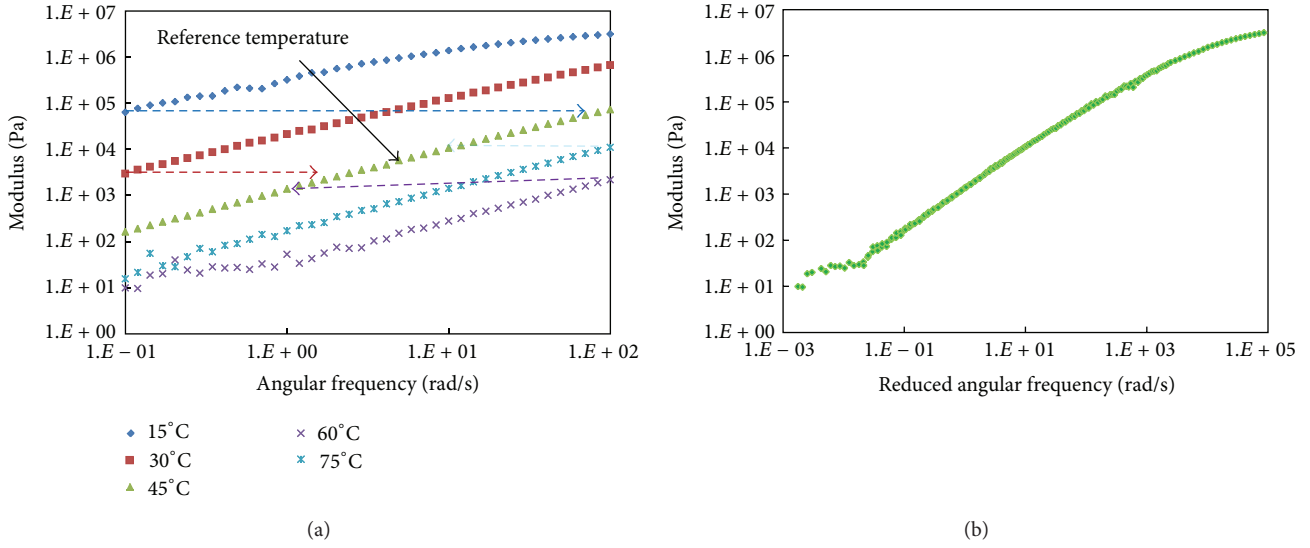


FIGURE 3: (a) Original frequency sweep data at multiple temperatures and (b) shifted frequency data to a reference temperature.

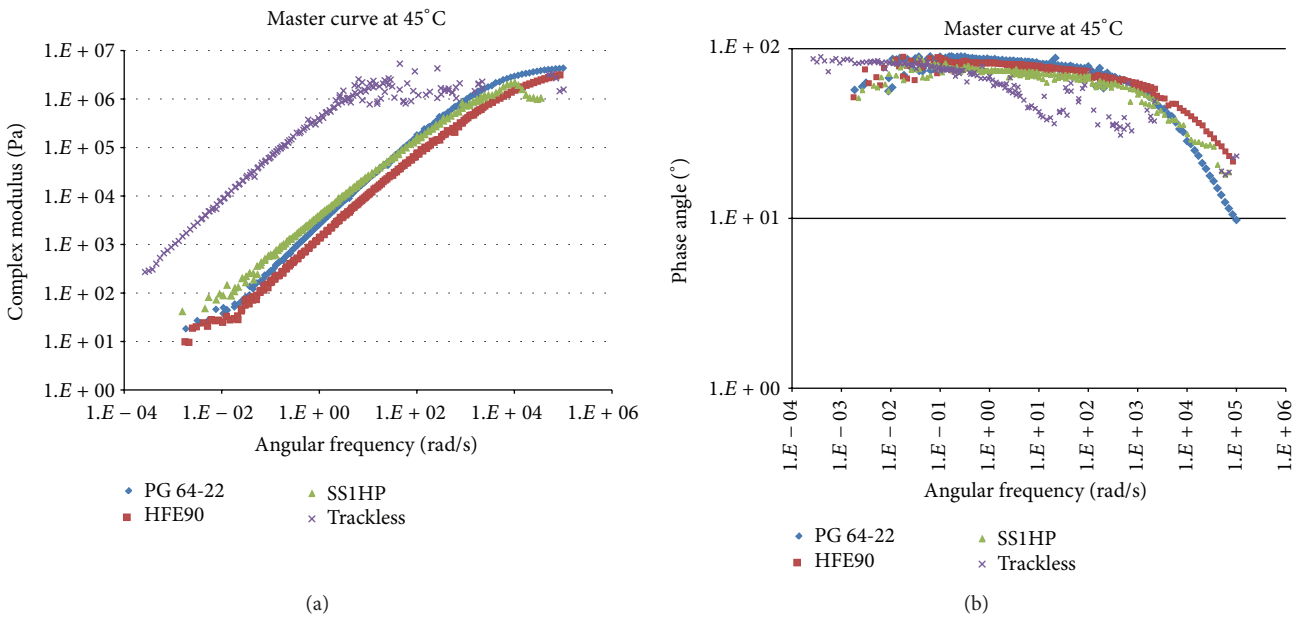


FIGURE 4: (a) G^* master curve and (b) phase angle results at 45°C.

the air cured and RTFOT cured specimens tests are performed on the small plate (8 mm) at intermediate temperatures from 10°C to 40°C and on the large plate (25 mm) at high temperatures from 40°C to 64°C. The specimens are 1 mm thick for the large plate and 2 mm thick for the small plate. Frequency sweeps are performed from 1 to 100 rad/sec.

This test system consists of parallel metal plates, an environmental chamber, a loading device, and a control and data acquisition and measures the rheological properties of asphalt binder. The test is performed by sandwiching the binder specimen between a fixed plate and a rotated plate on which the torque is applied. The DSR is able to directly apply and measure torque (T) and deflection angle (φ). Shear

stresses (τ) and shear strains (γ) are calculated and reported by the instrument using the following equations:

$$\begin{aligned} \gamma_{\max} &= \frac{\varphi \cdot r}{h}, \\ \tau_{\max} &= \frac{2 \cdot T}{\pi \cdot r^3}, \end{aligned} \tag{1}$$

where r is sample radius and h is sample height.

Note that the shear stress and shear strain are not uniform in DSR testing. Rather, stress and strain are maximum at the sample periphery and zero at the sample center. The maximum stress and strain at the edge of the sample are

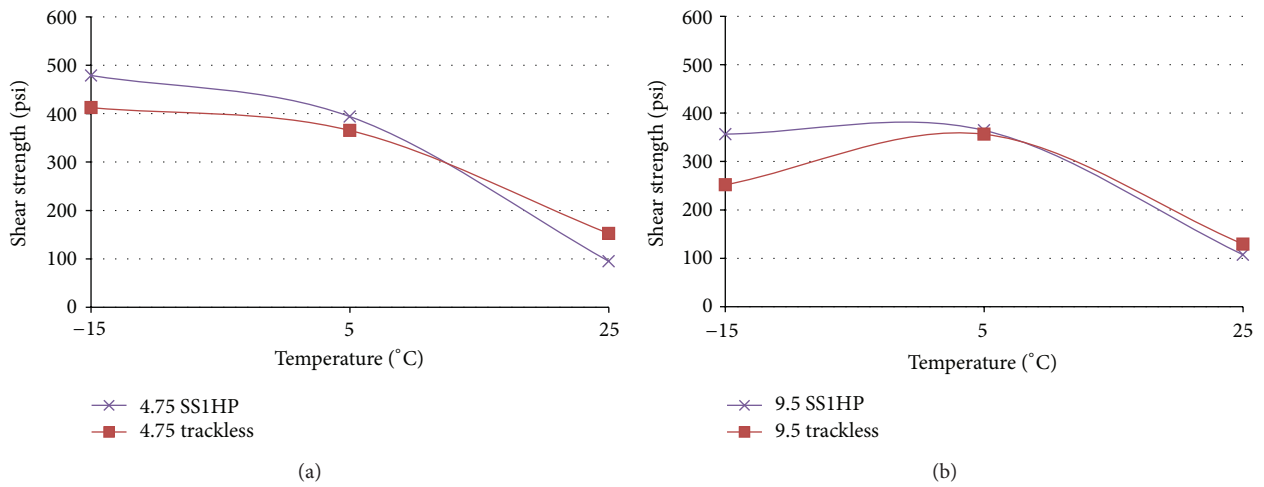


FIGURE 5: Tack coat shear test results.

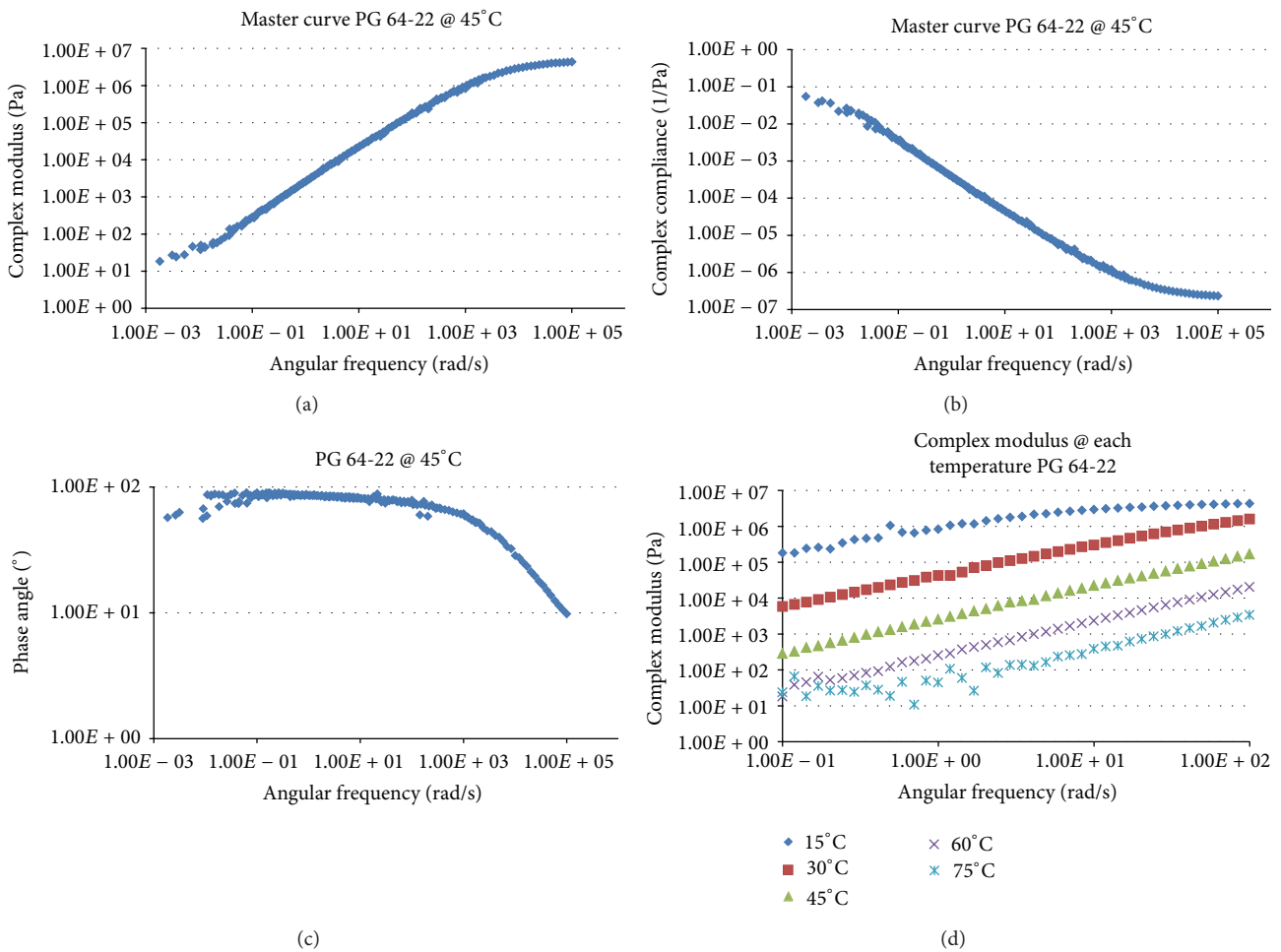
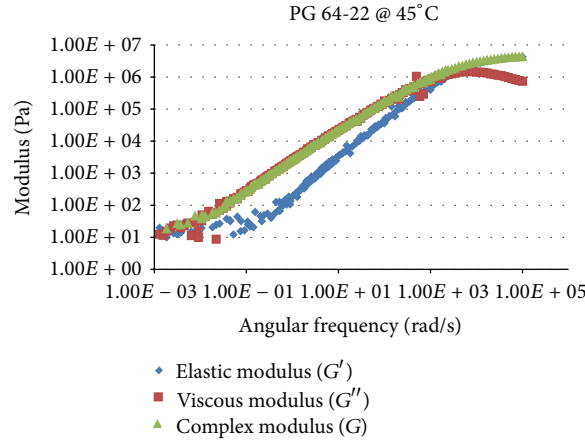
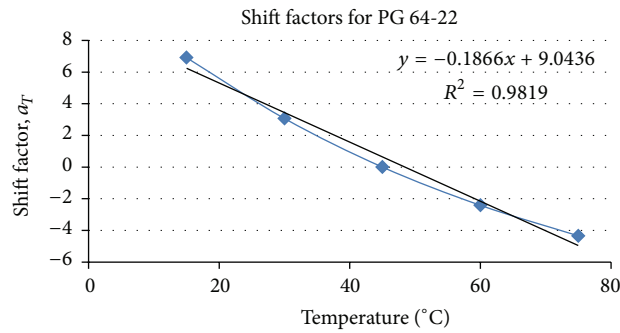


FIGURE 6: (a) Complex modulus, (b) complex compliance master curves, (c) phase angle at 45°C, and (d) complex modulus at each temperature.



(a)

Shift factors for PG 64-22 @ 45 °C		
Temperature (°C)	Log a_T	
15	6.912	
30	3.07	
45	0	
60	-2.4141	
75	-4.344	
WLF	C1	C2
	23.633	132.23
Arrhenius	B1	
	44540	



(b)

FIGURE 7: (a) Elastic and viscous modulus at 45°C and (b) shift factors at reference temperature (45°C).

normally reported in DSR testing, assuming a fixed sample radius and height.

Two important parameters are obtained from the dynamic shear rheometer test on asphalt: $|G^*|$ the complex modulus and δ the phase angle. These parameters can be used to characterize both viscous and elastic behavior of the material. The complex modulus can be defined as a ratio between the maximum and minimum strain and stress as shown in Figure 2 and (2), respectively:

$$G^* = \frac{\tau_{\max} - \tau_{\min}}{\gamma_{\max} - \gamma_{\min}} \quad (2)$$

The complex modulus is a measurement of a binder's total resistance to deformation and can be divided into two components, such as a real part and imaginary part. The simple relation is shown below:

$$\begin{aligned} G^*(\omega) &= G'(\omega) + iG''(\omega), \\ |G^*(\omega)| &= \sqrt{G'(\omega)^2 + G''(\omega)^2}, \\ G'(\omega) &= G^*(\omega) \cos(\delta(\omega)), \\ G''(\omega) &= G^*(\omega) \sin(\delta(\omega)), \end{aligned} \quad (3)$$

where $G^*(\omega)$ is complex shear modulus at frequency ω , $G''(\omega)$ is dynamic storage modulus at frequency ω , $G'(\omega)$ is dynamic loss modulus at frequency ω , $\delta(\omega)$ is phase angle at frequency ω , and i is complex number (equal to $\sqrt{-1}$).

Additionally, the phase angle can be represented by the following equation:

$$\delta = \tan^{-1} \left(\frac{G''(\omega)}{G'(\omega)} \right). \quad (4)$$

The shape of the load, which is used in this test, is sinusoidal, and the loading is controlled by two types, such as constant stress and constant strain mode. The complex shear modulus and phase angle are automatically calculated by proprietary computer software. The more detailed procedures for DSR test can be found in ASTM D7175-05 [7].

Marasteanu and Clyne [6] utilized dynamic shear rheometer (DSR) data to construct master curves for each of the residues. Tests were performed at 6°C temperature increments from 10°C to 64°C using frequency sweeps from 1 to 100 radians/sec. The master curves were constructed by fitting the Christensen-Anderson-Marasteanu (CAM) model to the $|G^*|$ data obtained with the DSR.

Salomon and Zhai [8] conducted dynamic shear rheometer (DSR) test to evaluate the rheological properties of several types of emulsified asphalts. In their study, rheological

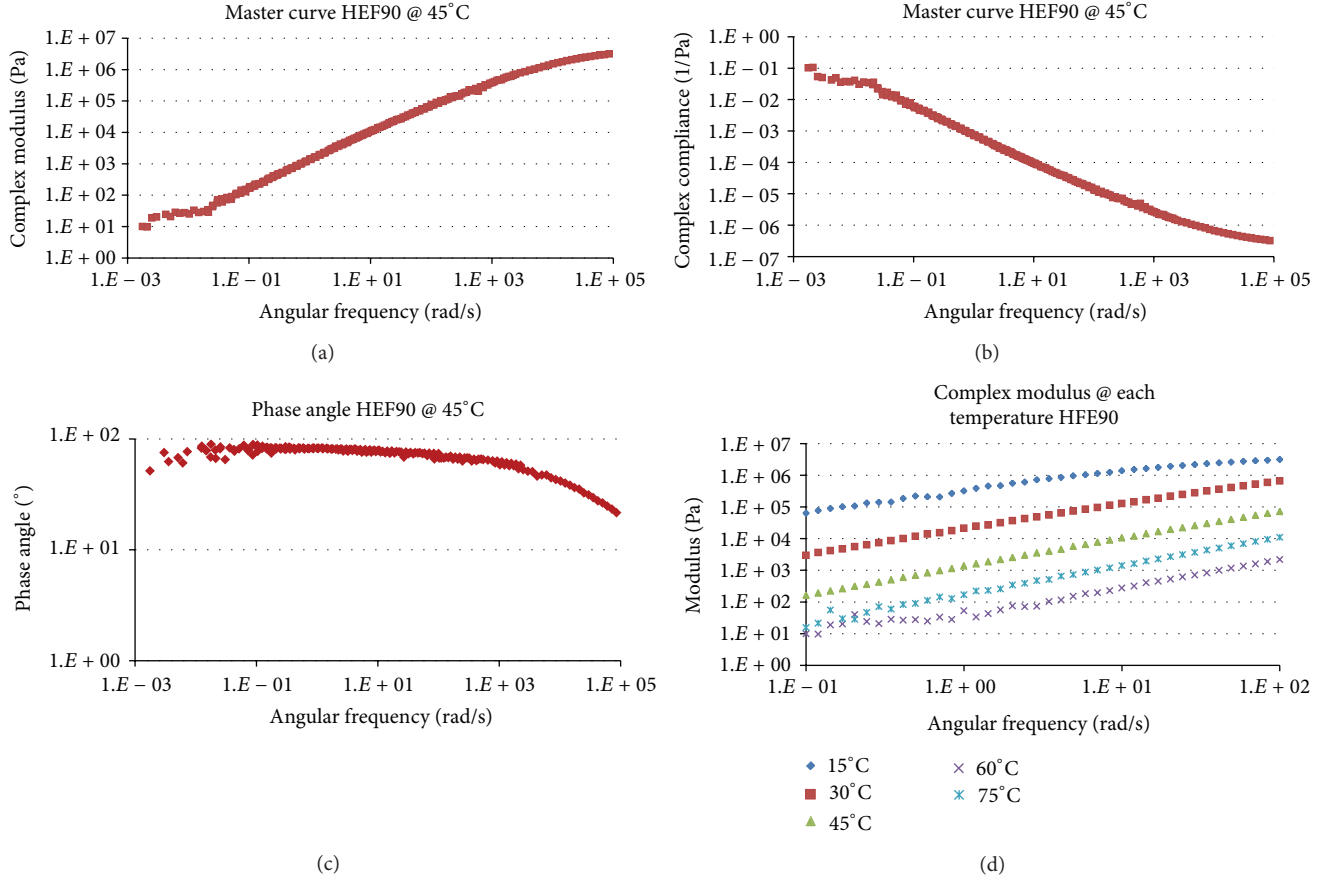


FIGURE 8: (a) Complex modulus, (b) complex compliance master curves, (c) phase angle at 45°C, and (d) complex modulus at each temperature.

properties were obtained by testing emulsified asphalts with test protocols developed for asphalt testing, such as stress sweep, frequency sweep, creep, and recovery. The results demonstrated that rheological measurements can be used to predict the field applications of emulsified asphalts.

Zhai et al. [9] developed several new tests to simulate application conditions of emulsified asphalts by using Bohlin CVO DSR with controlled stress mode. Stress sweeps, time sweep, and temperature sweep tests were all conducted on this DSR. A three-step (low shear rate, high shear rate, and low shear rate) test was developed to simulate spraying and setting characteristics for different emulsions. In this study, they concluded gel point determined by temperature sweep test can be used to study storage stability and setting time for different emulsions and spraying of an emulsion can be simulated using a high shear rate test.

3.2. Time-Temperature Superposition (TTS). Asphalt binder is well-known for *thermorheologically simple* (TRS) material by most researchers in asphalt pavement field if it is constrained to the so-called linear viscoelastic range. The time-temperature superposition principle (*t*-TS) is a renowned characteristic of *thermorheologically simple* (TRS) materials. Viscoelastic properties (i.e., the complex modulus $|G^*|$ values and time-temperature (*t*-*T*) shift factors) obtained in

the linear viscoelastic range at different loading rates and temperatures can be superposed to develop a single master curve by shifting them horizontally to a certain reference temperature. The horizontal distance necessary to superpose a curve to a reference curve, in order to develop a continuous curve, is termed the time-temperature shift factor (a_T), and it is unique to a given temperature.

The effects of time and temperature on viscoelastic material behavior can be combined into a single parameter, called *reduced time*, through the time-temperature superposition principle. Equation (5) represents a definition of reduced time (ξ) in common form. In terms of frequency domain, the reduced frequency is computed using (6):

$$\xi = \frac{t}{a_T}, \quad (5)$$

$$f_R = f \times a_T, \quad (6)$$

$$\log(a_T) = \alpha_1 T^2 + \alpha_2 T + \alpha_3, \quad (7)$$

where f is frequency in Hz, a_T is the time-temperature shift factor, α_1 , α_2 , α_3 are coefficients, and T is temperature.

The principle of time-temperature superposition states that the change in a material property (e.g., $|G^*|$) with respect

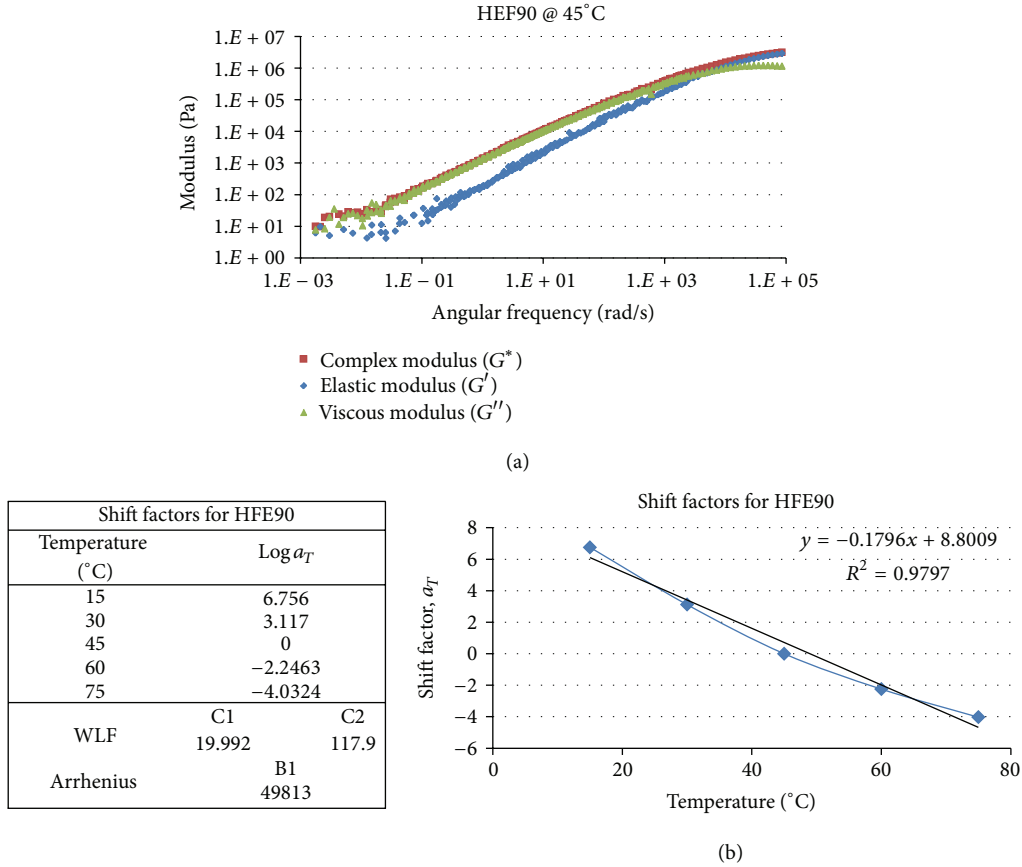


FIGURE 9: (a) Elastic and viscous modulus at 45°C and (b) shift factors at reference temperature (45°C).

to temperature is equivalent to a horizontal shift on the log time or log frequency scale [10]. This principle implies that increasing temperature is equivalent to increasing loading time (or decreasing loading frequency). Similarly, decreasing temperature is equivalent to decreasing loading time (or increasing loading frequency).

The data at various temperatures are shifted with respect to time until the curves merge into a single smooth function. This behavior allows for the horizontal shifting of the data onto an arbitrarily selected reference temperature curve to form a single curve, the master curve, which is used to describe the constitutive behavior of asphalt binder over a wide range of temperatures and frequencies. The concept of a master curve is illustrated in Figure 3.

3.3. Shift Factor Laws. The t - T shift factor (a_T) is the amount of horizontal shift in log scale that is required to create the continuous curve. The amount of shifting is dependent on the temperature chosen as the reference temperature and, therefore, varies by temperature. The amount of shifting along the horizontal x -axis in a typical time-temperature superposition (TTS) plot required to align the individual experimental data points into the master curve is generally described using one of two common theoretical models. The first of these models is the Williams-Landel-Ferry (WLF) equation. The Williams-Landel-Ferry equation can be used to determine

the time-temperature shift factors at any temperature for a given reference temperature by the following equation:

$$\log(a_T) = \frac{-C_1(T - T_0)}{C_2 + (T - T_0)}, \quad (8)$$

where C_1 and C_2 are constant, T_0 is reference temperature (in K), T is measurement temperature (in K), and a_T is shift factor.

The WLF equation is typically used to describe the time-temperature behavior of polymers in the glass transition region. The equation is based on the assumption that, above the glass transition temperature, the fractional free volume increases linearly with respect to temperature. The model also assumes that as the free volume of the material increases, its viscosity rapidly decreases.

The other model commonly used is the Arrhenius equation (9). The Arrhenius equation is typically used to describe behavior outside the glass transition region but has also been used to obtain the activation energy associated with the glass transition:

$$\log(a_T) = C \left(\frac{1}{T} - \frac{1}{T_0} \right) = \frac{0.4347B_1}{R} \left(\frac{1}{T} - \frac{1}{T_0} \right), \quad (9)$$

where C is constant, B_1 is activation energy (J/mol) associated with the relaxation, R is ideal gas constant (8.314 J/mol), T is

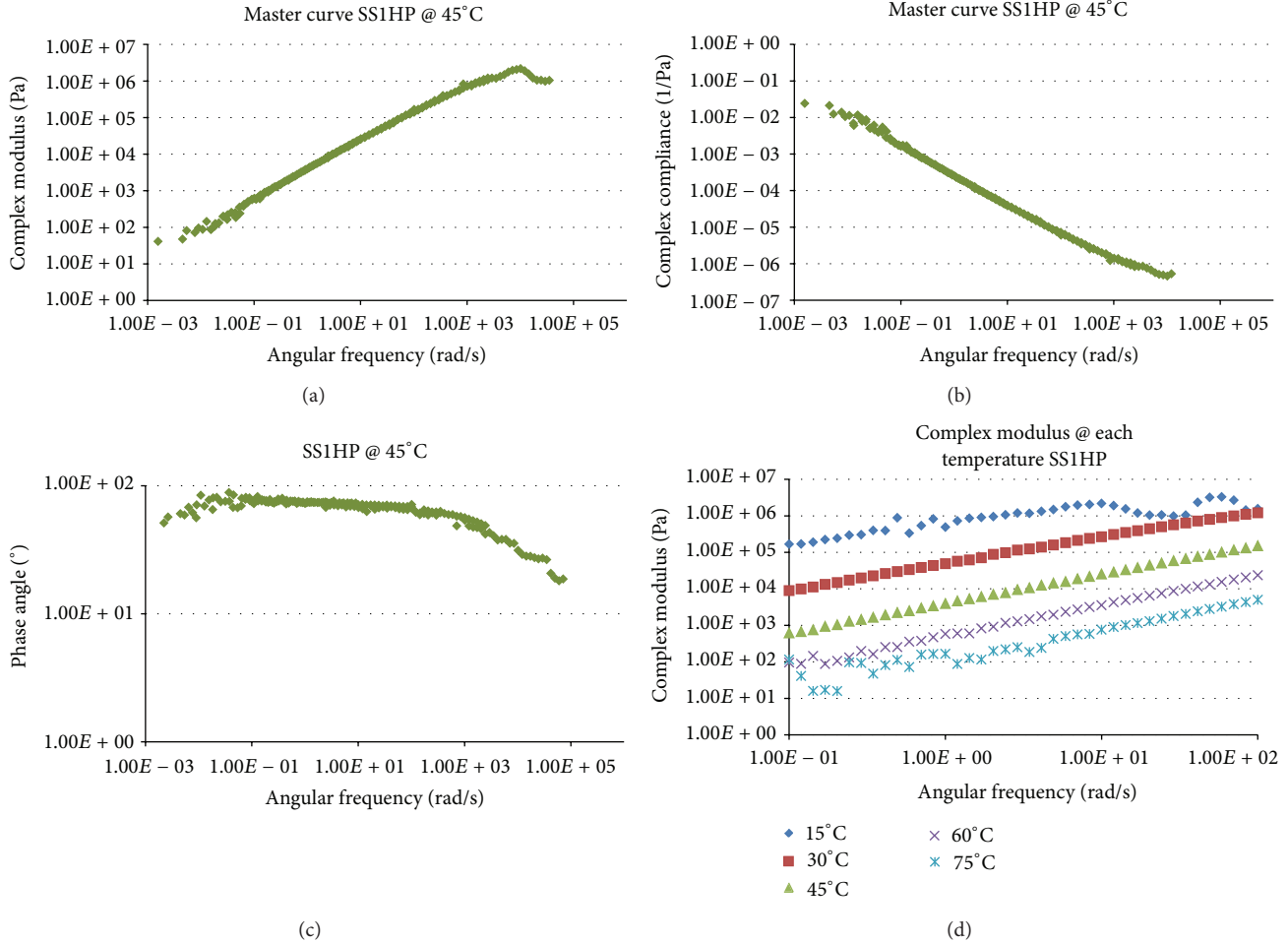


FIGURE 10: (a) Complex modulus, (b) complex compliance master curves, (c) phase angle at 45°C, and (d) complex modulus at each temperature.

measurement temperature, T_0 is reference temperature, and a_T is time-based shift factor.

4. Analysis of Test Results

Several trial tests are performed on the sealant samples. Based on these tests the testing frequency is selected to cover a range from 0.1 rad/sec to 100 rad/sec to cover both high and low loading speeds. The applied strain is changed to 0.1% to make sure that the sample does not damage at either low temperature or high frequency. Because of the testing time and instrument limitation, the temperature range also shortened from 15°C to 75°C.

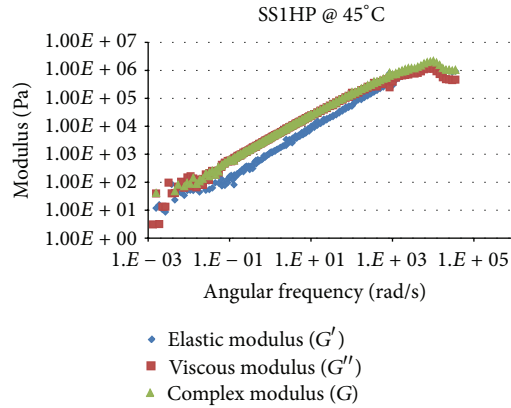
Totally 40 points are measured during each test. For some of the samples, it was hard to capture data at low temperature because of brittleness of the samples which may lead to damage or at high temperature because the sample was so soft to bear a shear load.

Figure 4 shows complex modulus master curve and phase angle result for each material. As shown in Figure 4(a), trackless emulsion is stiffer than other materials on the whole, but it is too brittle at high frequency or low temperature, and

thus scattered results were obtained. Considering the reasons for this phenomenon, the property of trackless emulsion at these conditions is close to solid phase so that some damage might happen. In addition, the loss of contact surface between material and parallel plate can be another factor. Most commonly used emulsion, SS1HP, as a tack coat material is stiffer than HFE90. Also, it is stiffer than PG 64-22 binder at low frequency and high temperature, but if the condition of frequency and temperature are changed inversely, PG 64-22 binder is stiffer than SS1HP. Figure 4(b) shows phase angle results for each material. The result of phase angle for the trackless emulsion shows that the inflection point appears at a lower frequency, as compared with that of other materials.

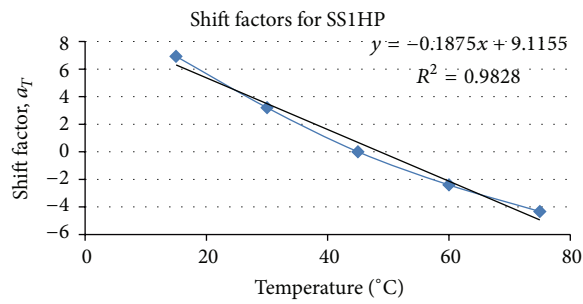
As shown in Figure 5, trackless emulsion at low temperature shows lower shear strength than SS1HP for mixture of both 4.75 mm and 9.5 mm. However, the opposite pattern is shown at the temperature of more than 5°C.

4.1. Asphalt Binder PG 64-22. For PG 64-22 binder, it can be seen that the complex modulus increases as the frequency increases or temperature decreases. For the complex compliance, the behavior is inverted. In other words, it decreases as



(a)

Shift factors for SS1HP		
Temperature (°C)	Log a_T	
15	6.926	
30	3.203	
45	0	
60	-2.404	
75	-4.332	
WLF	C1	C2
	23.143	129.43
Arrhenius	B1	
	47303	



(b)

FIGURE 11: (a) Elastic and viscous modulus at 45°C and (b) shift factors at reference temperature (45°C).

frequency increases or temperature decreases. The maximum complex modulus obtained for this material was 4,318,000 Pa. Regarding the phase angle, it starts decreasing at a higher rate when the reduced frequency reaches an approximate value of 3,000 rad/s. It occurs at 2.9 rad/s and 15°C for the real frequency.

Similarly, it can be noticed from the shear modulus chart that at low frequencies or high temperatures the material presents a viscous-like behavior since the viscous modulus (G'') are higher than the elastic modulus (G'). However, after the crossover point, where $G' = G''$, the material changes to an elastic behavior. Here, the temperature has reduced and frequency has increased. In addition, it is important to notice that the crossover point ($G' = G''$) occurs when the phase angle is 45° (degree). At this same point the frequency is approximately 3,000 rad/s which is the same point discussed above where the phase angle starts to decrease at higher rate.

Considering the prediction of rutting resistance, it is necessary to know the locations where $G'' > G'$ and $G'' < G'$, since these two zones dictate the recoverable and nonrecoverable deformations. Additionally, fatigue cracking can be estimated by analyzing the complex modulus and phase angle for long-term aged materials.

Figure 6 also shows how the shear modulus is higher at low temperatures. Also, for each temperature, the modulus increases as frequency increases. Finally, Figure 7 illustrates the shift factors at each temperature at which the material was tested. The William-Landel-Ferry (WLF) coefficients as

well as the Arrhenius coefficient are presented. However, Arrhenius coefficient is not suitable for this case since the temperatures used are above the glassy transition temperature (T_g).

4.2. HFE90 Emulsion. For HFE90 emulsion, the complex modulus increases as the frequency increases or temperature decreases as can be seen in Figure 8. This behavior is common for viscoelastic materials as presented previously for the PG 64-22 asphalt binder. The maximum complex modulus obtained for this material was 3,131,000 Pa. In Figure 9, the phase angle starts decreasing at a higher rate when the reduced frequency reaches an approximate value of 4,000 rad/s. The crossover point ($G' = G''$) occurs at this same frequency where the phase angle approximates 45°C. It occurs at 4.9 rad/s and 15°C for the real frequency.

For this material, it can be seen again that for each temperature the modulus increases as temperature decreases and frequency increases. The shift factors for each temperature as well as the WLF coefficients and Arrhenius coefficient are also shown.

4.3. SS1HP Emulsion. For SS1-HP emulsion as for the two previous materials, the complex modulus increases as the frequency increases or temperature decreases as can be seen in Figure 10. The maximum complex modulus obtained for this material was 3,281,000 Pa. In Figure 11, the phase angle starts decreasing at a higher rate when the reduced frequency

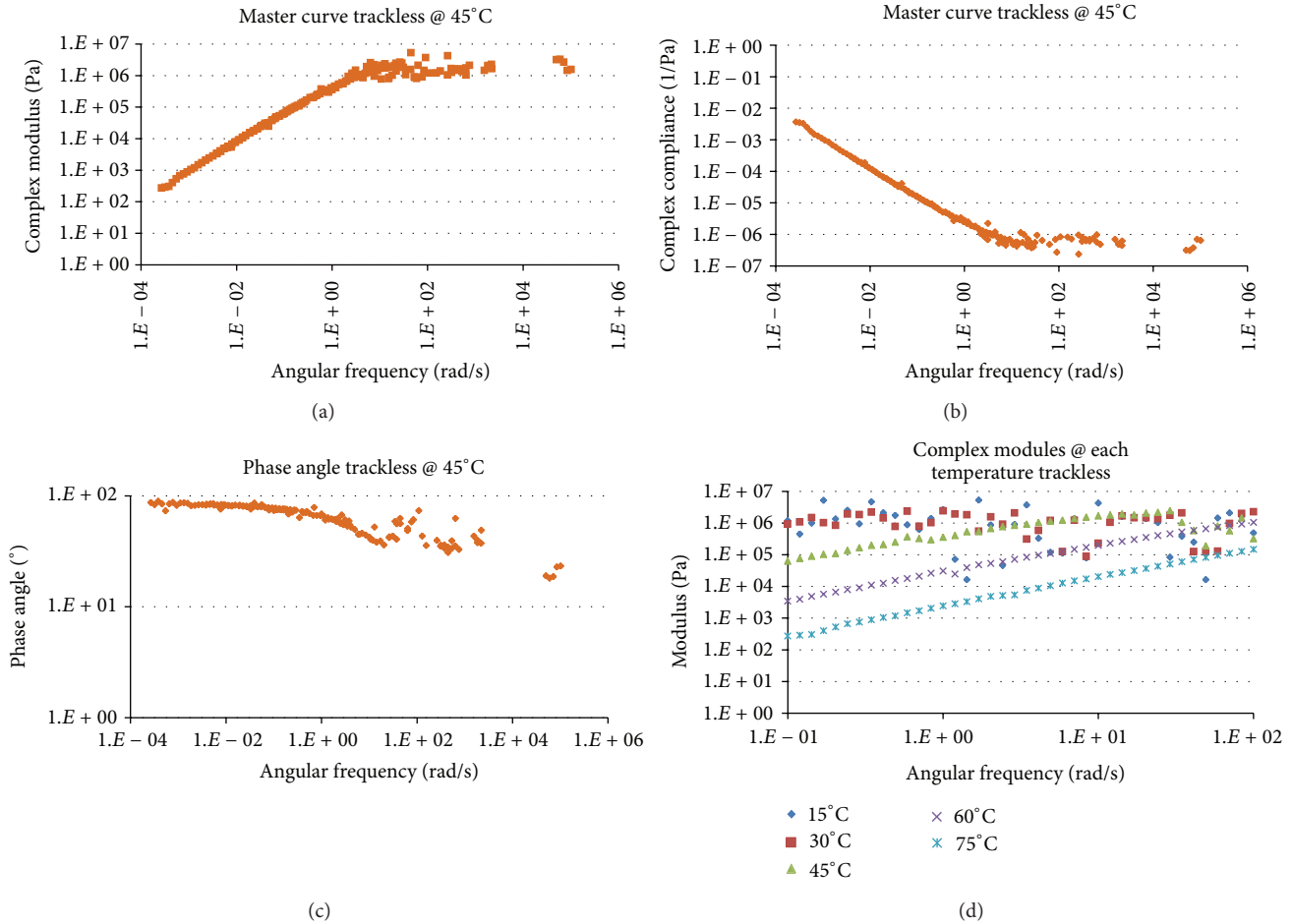


FIGURE 12: (a) Complex modulus, (b) complex compliance master curves, (c) phase angle at 45°C, and (d) complex modulus at each temperature.

reaches an approximate value of 2,100 rad/s. The crossover point ($G' = G''$) occurs at this same frequency where the phase angle approximates 45°C. It occurs at 2.0 rad/s and 15°C for the real frequency.

For this material, it can be seen again that for each temperature the modulus increases as temperature decreases and frequency increases. The shift factors for each temperature as well as the WLF coefficients and Arrhenius coefficient are also shown.

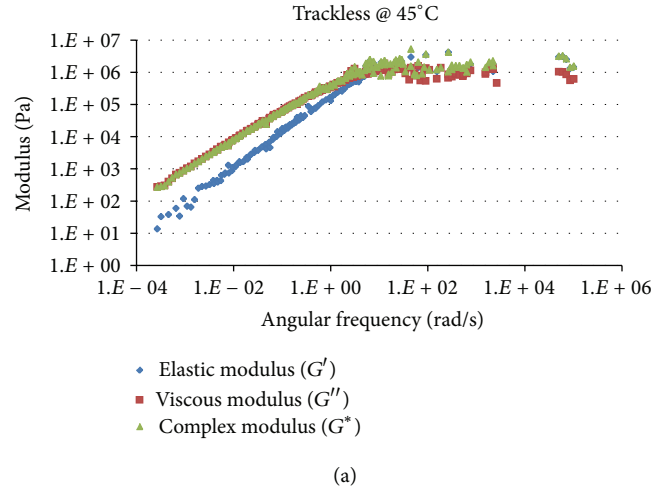
4.4. Trackless Emulsion. For trackless emulsion as for the three previous materials, the complex modulus increases as the frequency increases or temperature decreases as can be seen in Figure 12. However, it became stiffer and is started to show a brittle behavior at low temperatures and high frequencies. As it becomes solid-like, it loses contact with the parallel plates during test causing difficulties to obtain a good data. In Figure 13, it can be seen that the data is scattered at high frequencies. The maximum complex modulus obtained for this material was 5,326,000 Pa. From the data obtained for this material, it is hard to predict at what frequency the phase angle starts decreasing at a higher rate. However, it was estimated to happen at a frequency less than 100 rad/s.

It occurs at 2.9 rad/s and 30°C for the real frequency. The crossover point ($G' = G''$) was also estimated to happen at this same point with phase angle close to 45°C.

Additionally, it can be seen in Figure 13 that the result of shear modulus at 15°C and 30°C behaves in an odd manner. However, as temperature increases, the data starts to stabilize. Regarding the shift factors, it can be seen that the WLF coefficients and Arrhenius coefficient are not similar to the other three materials.

4.5. Comparison of Viscous Modulus. After the results for all the material were shown, it is important to compare at what frequency the crossover point takes place for each material. It was found that for the HFE90 emulsion the crossover point occurred approximately at 4,000 rad/s, which means that for this product the transition from viscous to elastic behavior takes place at lower temperatures comparing to the other three materials. On the other hand, it can be seen from Figure 14 that HFE90 has one of the lowest viscous shear moduli.

Conversely, crossover point of the trackless emulsion was estimated to happen at less than 100 rad/s, which means that this material will become elastic at intermediate



Shift factors for trackless emulsion		
Temperature (°C)	Log a_T	
15	3.276	
30	3.089	
45	0	
60	-3.232	
75	-5.923	
WLF	C1	C2
	-19.31	123.32
Arrhenius	B1	
	-37917	

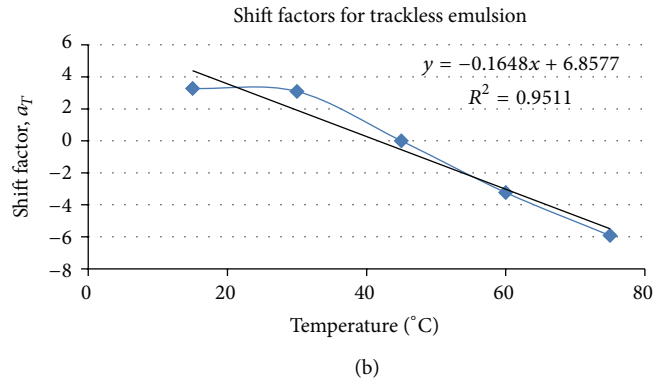


FIGURE 13: (a) Elastic and viscous modulus at 45°C and (b) shift factors at reference temperature (45°C).

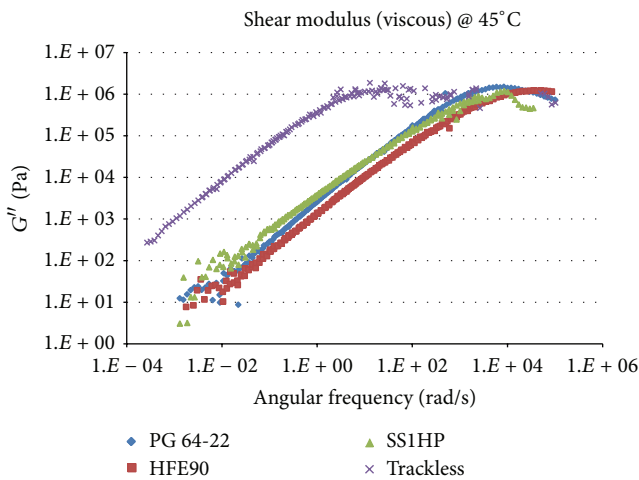


FIGURE 14: Viscous modulus for each material at 45°C.

temperatures. Also, this product has the highest viscous modulus compared to the other three materials.

4.6. *Stiffness Ratio (SR)*. Stiffness ratio (SR) is used to have a better comparison between different emulsions. This stiffness ratio is the modulus (G^* , G' , or G'') of an emulsion divided

by the modulus of SS1HP product at a certain frequency and temperature:

$$SR = \frac{\text{Emulsion Modules}}{\text{SS1HP Modules}} \tag{10}$$

The SR results for viscous modulus are presented in Figure 15 at low (0.1 rad/sec), intermediate (1 and 10 rad/sec), and high (100 rad/s) frequencies. Viscous modulus is an important parameter for emulsions used as a tack coat material. Having a high viscous modulus, tack coat material can perform better at high deformations between the pavement layers and provide proper and long-lasting bonding between them.

Figure 15 shows that SR depends on both temperature and loading frequency. At low frequencies, trackless emulsion has the highest modulus. At high frequencies below a certain temperature trackless emulsion turns to show the lowest modulus. We can call this point turning point for trackless emulsion product behavior. This turning point temperature depends on the frequency. As the frequency increases, the higher temperature will be obtained for the turning point. For example, at 10 rad/sec the turning point temperature is 30°C and at 100 rad/sec it is 20°C.

The results from the shear testing on tack coat also show a similar behavior. For a certain shearing speed at low

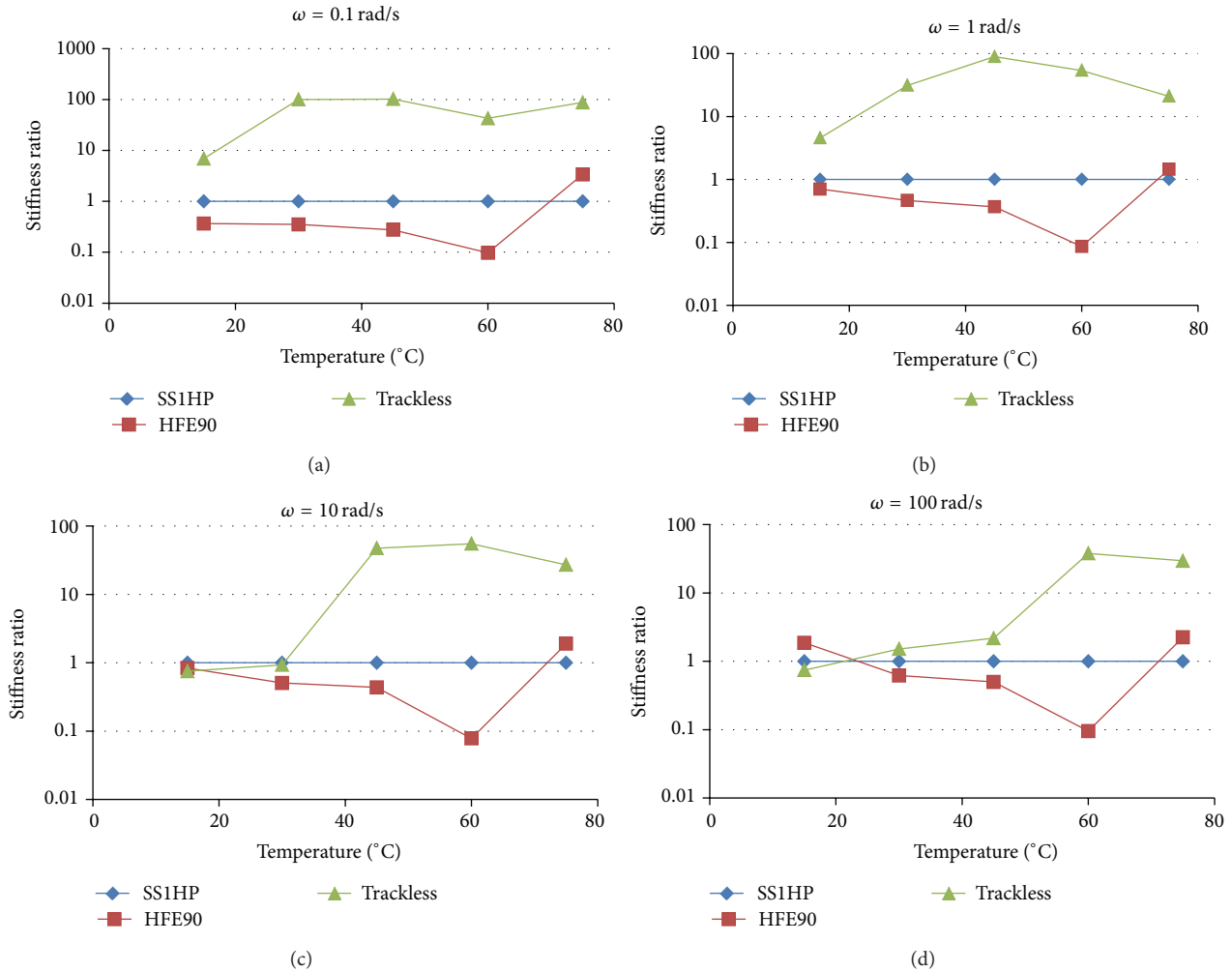


FIGURE 15: SR based on viscous modulus at different frequencies: (a) 0.1, (b) 1, (c) 10, and (d) 100 rad/sec.

temperatures, trackless emulsion has lower shear strength than SS1HP product and at high temperature tack coat has higher shear strength than SS1HP.

5. Conclusion

In this study three different emulsion residues, such as SS1HP, HFE90, and SS-1VH (trackless), and a base asphalt binder (PG 64-22) were compared to characterize rheological properties by using DSR test. In order to capture the emulsion properties, different frequencies and temperatures were applied. Then, a master curve for shear modulus was plotted for each emulsion. The results of this study are as follows.

- (i) The HFE90 emulsion presents the crossover point ($G' = G''$) at the highest frequency. Therefore, the transition from viscous to elastic behavior occurs at lower temperatures, compared to the other materials. This emulsion is known for performing in a wider temperature range as shown in the results.
- (ii) The trackless emulsion has the crossover point at reduced frequency lower than 100 rad/s. It indicates

that the material presents an elastic behavior at intermediate temperatures. This product is known as having very fast setting and high resistance to shear stresses.

- (iii) The trackless emulsion presents the highest viscous and elastic modulus, followed by the PG 64-22 binder, SS1HP, and HFE90 emulsion.
- (iv) At high temperatures trackless emulsion has the highest modulus.
- (v) Depending on the frequency below a certain temperature, trackless material has the lowest modulus. This temperature gets lower as the frequency decreases.
- (vi) Shear strength test results show a behavior between trackless emulsion and SS1HP similar to the frequency sweep test results performed by DSR.

Conflict of Interests

The authors declare that there is no conflict of interests regarding the publication of this paper.

Acknowledgment

The authors would like to acknowledge the financial support from the Korea Institute of Civil Engineering and Building Technology (KICT) under research project “Support for Commercialization of Warm Mix Asphalt.”

References

- [1] K. Takamura, “Comparison of emulsion residues recovered by forced airflow and RTFO drying,” in *Proceedings of the ISSA/AEMA Annual Meeting*, pp. 1–17, March 2000.
- [2] G. N. King, D. Lesueur, H. King, and J. Planche, *SHRP Test Evaluation of High Float and Polymer Modified Bitumen Emulsion Residues*, Koch Materials Laboratory, Terre Haute, Ind, USA, 1996.
- [3] R. Barcena, A. Epps, and D. Hazlett, “A performance-graded binder specification for surface treatments,” in *Proceedings of the 81st Annual Meeting of the Transportation Research Board*, Washington, DC, USA, 2002.
- [4] C. Deneuwillers and J. Samanos, “Contribution to the study of the relationship between characteristics and performances of bitumen emulsions,” in *Proceedings of the 2nd Euraspalt & Eurobitume Congress*, Book 1, pp. 195–202, Barcelona, Spain, 2000.
- [5] S. Le Bec, M. Mazé, B. Brûlé, and J. Lefévre, “Formulation of cold mixes: accelerated curing in the laboratory,” in *Proceedings of the 2nd Euraspalt & Eurobitume Congress*, Book 1, pp. 416–423, Barcelona, Spain, 2000.
- [6] M. O. Marasteanu and T. R. Clyne, “Rheological characterization of asphalt emulsions residues,” *Journal of Materials in Civil Engineering*, vol. 18, no. 3, pp. 398–407, 2006.
- [7] ASTM D7175, *Standard Test Method for Determining the Rheological Properties of Asphalt Binder Using a Dynamic Shear Rheometer*, Annual Book of ASTM Standards, ASTM International, West Conshohocken, Pa, USA, 2005.
- [8] D. Salomon and H. Zhai, “Rheological measurements of asphalt road emulsions,” in *Proceedings of the 3rd World Congress on Emulsions*, Lyon, France, September 2002.
- [9] H. Zhai, D. Salomon, and E. Milliron, *Using Rheological Properties to Evaluate Storage Stability and Setting Behaviors of Emulsified Asphalts*, Idaho Asphalt Supply, Inc., White Paper, Idaho, USA, 2006.
- [10] L. Roderic, *Viscoelastic Materials*, Cambridge University Press, New York, NY, USA, 2009.

Research Article

Feasibility Study on Tension Estimation Technique for Hanger Cables Using the FE Model-Based System Identification Method

Kyu-Sik Park, Taek-Ryong Seong, and Myung-Hyun Noh

Steel Solution Center, POSCO, 100 Songdogwahak-ro, Yeonsu-gu, Incheon 406-840, Republic of Korea

Correspondence should be addressed to Myung-Hyun Noh; mnoh@posco.com

Received 8 September 2014; Accepted 13 October 2014

Academic Editor: Sang-Youl Lee

Copyright © 2015 Kyu-Sik Park et al. This is an open access article distributed under the Creative Commons Attribution License, which permits unrestricted use, distribution, and reproduction in any medium, provided the original work is properly cited.

Hanger cables in suspension bridges are partly constrained by horizontal clamps. So, existing tension estimation methods based on a single cable model are prone to higher errors as the cable gets shorter, making it more sensitive to flexural rigidity. Therefore, inverse analysis and system identification methods based on finite element models are suggested recently. In this paper, the applicability of system identification methods is investigated using the hanger cables of Gwang-An bridge. The test results show that the inverse analysis and systemic identification methods based on finite element models are more reliable than the existing string theory and linear regression method for calculating the tension in terms of natural frequency errors. However, the estimation error of tension can be varied according to the accuracy of finite element model in model based methods. In particular, the boundary conditions affect the results more profoundly when the cable gets shorter. Therefore, it is important to identify the boundary conditions through experiment if it is possible. The FE model-based tension estimation method using system identification method can take various boundary conditions into account. Also, since it is not sensitive to the number of natural frequency inputs, the availability of this system is high.

1. Introduction

Recently, the number of long-span bridges built in countries around the world is increasing. Of these long-span bridges, the suspension bridge uses stiffening girders that are attached to the main cables to support the load. In Korea, starting from the completion of the Nam-Hae Bridge in 1973, Yeongjong, Gwang-An, Yi Sun-Sin, and many other suspension bridges have been constructed, and Ulsan Bridge is also under construction as a suspension bridge. Most long-span bridges, such as suspension bridges, support their loads by means of cables. Therefore, it is necessary to estimate the tension of the cables to ensure structural safety during the construction phase and maintenance work after completion.

The most accurate means to estimate the tension on the cables is to use the load cells to collect the data directly. However, this is not an option in many cases due to the conditions in the field. Therefore, the most commonly used method is to extract the natural frequency from the measurements of acceleration signal and enter the extracted data into

an equation that shows the relationship between the natural frequency and tension, and thus the cable tension can be estimated indirectly. The two most widely used methods are the taut string theory [1], which does not take the flexural rigidity into consideration, and the linear regression method [2], which regards the cable as a beam under the axial load and considers the flexural rigidity. Yun et al. [3] analyzed the influence of the effective length in the linear regression method, while Ahn et al. [4] used the static method, which requires the minimal amount of measurements compared to the dynamic methods, to calculate the tension on the hanger cables.

The estimation methods for tension using the existing dynamic method put the natural frequency values to the equation on the natural frequency and tension. Therefore, if the mathematical model used differs significantly from the actual structure, a significant error is unavoidable. In particular, in the case of hanger cables that transfer the load applied to the stiffening girder to the main cable, they are, in most cases, short cables with higher flexural rigidity. Also,

due to the influence from the clamps and boundary conditions, errors are significant when the tension is estimated using the existing methods [5–7].

Therefore, to estimate the tension of shorter cables that are greatly influenced by flexural rigidity, like the hanger cables in a suspension bridge, some new methods are proposed that are based on the finite element model of the hanger cable. Kim et al. [6, 7] suggested formula-based inverse analysis method, which defines the errors between the calculated frequency using the analysis models and the frequency actually measured as the objective functions, and uses an optimized algorithm, the univariate search method and modal participation factor. Park et al. [5] suggested a vibration-based system identification technique. This method uses the measured frequency as the input variable and the sensitivity equation to estimate the tension force through repeated calculations. Here, for a precise system identification of the hanger cables, a 3D finite element model is created, in which the physical properties including the tension force and the rigidities of hanger cable and clamp are set as the identification variables. The tension estimation technique for the hanger cable using the formula-based inverse analysis method was applied to the Gwang-An Bridge [6, 7] while the tension estimation technique for the hanger cables based on the FE model-based system identification method was applied to the theoretical development [5], Yeongjong Bridge [6, 7], and the test sample [8].

In this paper, through the hanger cables of Gwang-An Bridge, the reliability of the system identification method based on the finite element model, which has higher applicability in tensile force estimation for short cables that are more sensitive to the flexural rigidity, is compared with that of the existing tension estimation methods, and its applicability is verified.

2. Tension Estimation Methods

2.1. Methods Using Mathematical Equation on the Natural Frequency and Tension. Many dynamic methods to estimate tensile force for cables have been developed considering dynamic characteristics and physical properties of cables. Among them, the flat taut string theory for cables that neglect both sag-extensibility and flexural rigidity is as follows:

$$T = 4mL^2 \left(\frac{f_n}{n} \right)^2, \quad (1)$$

where f_n denotes the n th natural frequency in Hz. The terms T , m , and L denote tension force, mass density, and length of cable, respectively. The computation of tension force is straightforward with given measured frequency and mode

number. However, the application of this formula is strictly limited to a flat long slender cable because it can not consider both sag-extensibility and bending stiffness of cables.

The modern cable theory [9] that takes account of the sag-extensibility without flexural rigidity requires additional information of the unstrained length of cable and involves solving a nonlinear characteristic equation by trial-and-error [10]. However, such additional information is often not available in practice, therefore the linear regression method [11] that considers cables as an axial load beam had been developed. This method considers the flexural rigidity but neglects the sag-extensibility as follows:

$$\left(\frac{f_n}{n} \right)^2 = \left(\frac{1}{4mL^2} \right) T + \left(\frac{n^2 \pi^2}{4mL^4} \right) EI, \quad (2)$$

where EI denotes the flexural rigidity of a cable. The unknown tension force and flexural rigidity can be identified through linear regression procedures with given measured frequency and mode number. This method is widely used by the field engineers because of its simplicity and speediness. To consider both sag-extensibility and bending stiffness, the practical formula [12] had been developed. But a priori data of the axial and flexural rigidities of the target cable system is required for the proper use of this practical method. However, the flexural rigidity of cable is often neither available nor valid because the shear and bending mechanisms of a cross section of cable could be different from those of beam.

2.2. Methods Using System Identification Approach Based on FE Model. In the process of estimating the tension using the finite element model based system identification method, the tensile force of cables is illustrated by the identification vector which is composed of several unknown parameters. In this study, the nine unknown parameters x^p ($p = 1, \dots, 9$) are used for identifying the tensile force in the system identification procedure and the identification vector is defined as

$$\begin{aligned} \mathbf{x} &= [x^1 \ x^2 \ \dots \ x^9]^T \\ &= [T \ EA \ EI_y \ EI_z \ GJ \ EA_c \ EI_{yc} \ EI_{zc} \ GJ_c]^T, \end{aligned} \quad (3)$$

where T denotes the tensile force of a cable; EA , EI_y (EI_z), and GJ denote axial, flexural, and torsional rigidities for a cable, respectively; and EA_c , EI_{yc} (EI_{zc}), and GJ_c denote axial, flexural, and torsional rigidities for a clamp, respectively.

The identification vector for the r th iteration in the sensitivity-based updating algorithm can be assumed as

$$\begin{aligned} {}^r \mathbf{x} &= [{}^r x^1 \ {}^r x^2 \ \dots \ {}^r x^9]^T \\ &= [{}^r T \ {}^r EA \ {}^r EI_y \ {}^r EI_z \ {}^r GJ \ {}^r EA_c \ {}^r EI_{yc} \ {}^r EI_{zc} \ {}^r GJ_c]^T, \end{aligned} \quad (4)$$

where ${}^r \mathbf{x}$ mean the identification vector for the r th iteration.

Then, the static displacement and tensile force distribution can be produced for the identification vector. In

the next step, the natural frequency ω_j ($j = 1, \dots, q$) is determined from the finite element vibration analysis using the static displacement curve and tension distribution. Using the change in natural frequencies for different identification variables, the sensitivity matrix (\mathbf{S}) with $(q \times p)$ size can be determined approximately as follows:

$${}^r \mathbf{S} = \begin{bmatrix} \frac{\partial^r \omega_1}{\partial^r x_1} & \frac{\partial^r \omega_1}{\partial^r \omega_1} & \dots & \frac{\partial^r \omega_1}{\partial^r x_p} & \frac{\partial^r \omega_1}{\partial^r \omega_1} \\ \vdots & \vdots & \ddots & \vdots & \vdots \\ \frac{\partial^r \omega_q}{\partial^r x_1} & \frac{\partial^r \omega_q}{\partial^r \omega_1} & \dots & \frac{\partial^r \omega_q}{\partial^r x_p} & \frac{\partial^r \omega_q}{\partial^r \omega_1} \end{bmatrix}. \quad (5)$$

Then, from the produced natural frequency data, the rate of change ($d^r \omega$) for the eigenvalue can be obtained as

$$d^r \omega = \begin{bmatrix} \frac{\omega_1^m - {}^r \omega_1^c}{{}^r \omega_1^c} & \dots & \frac{\omega_q^m - {}^r \omega_q^c}{{}^r \omega_q^c} \end{bmatrix}^T, \quad (6)$$

where ω_q^m and ${}^r \omega_q^c$ denote the q th mode's natural frequency measured from experiment or field test and the q th mode's

frequency calculated from nonlinear finite element vibration analysis using ${}^r x^p$ in the r th iteration, respectively. Equation (6) can be rewritten in the vector form as

$$d^r \omega_{(q \times 1)} = {}^r \mathbf{S}_{(q \times p)} d^r \mathbf{x}_{(p \times 1)}. \quad (7)$$

Equation (7) is referred to as a linear sensitivity equation, and the rate of change for the identification vector by using (7) can be expressed as

$$d^r \mathbf{x} = {}^r \mathbf{S}^{-1} d^r \omega, \quad (8)$$

where ${}^r \mathbf{S}^{-1}$ means the pseudoinverse matrix for ${}^r \mathbf{S}$ and can be determined as

$${}^r \mathbf{S}^{-1} = ({}^r \mathbf{S}^T {}^r \mathbf{S})^{-1} {}^r \mathbf{S}^T. \quad (9)$$

Finally, the p th identification variable in the $(r + 1)$ th iteration can be recalculated as

$${}^{r+1} x^p = (1 + d^r x^p)^r x^p, \quad (10)$$

$${}^{r+1} \mathbf{x} = \begin{bmatrix} {}^{r+1} T & {}^{r+1} EA & {}^{r+1} EI_y & {}^{r+1} EI_z & {}^{r+1} GJ & {}^{r+1} EA_c & {}^{r+1} EI_{yc} & {}^{r+1} EI_{zc} & {}^{r+1} GJ_c \end{bmatrix}^T.$$

From (4) to (10), the loop is repeated until the convergence condition is satisfied. The convergence condition for the repetition analysis uses the square roots of the sum of square (SRSS) in the following:

$$\left| \sqrt{\left(\sum_{q=1}^n \left| \frac{\omega_q^m - \omega_q^c}{\omega_q^m} \right| \times 100 \right)^2}_{\text{step } r} - \sqrt{\left(\sum_{q=1}^n \left| \frac{\omega_q^m - \omega_q^c}{\omega_q^m} \right| \times 100 \right)^2}_{\text{step } r+1} \right| < 0.01. \quad (11)$$

Finally, tensile force is determined from the identification variables holding at the termination stage and relevant natural frequencies can be determined through the finite element vibration analysis with the identification variables.

3. Field Application: Hanger Cables of Gwang-An Bridge

3.1. Measurement of the Vibration Signal. Located in Busan, Gwang-An Bridge is 900 m in total length (center span = 500 m; 3 spans and 2 hinges with each side span = 200 m) and a width of 24 m. The height of the main tower (from sea level) is 116.5 m. The hanger cables of Gwang-An Bridge

become shorter as they approach the center of the span from the location of the main tower. In this paper, we examined the two hanger cables located on the beach side, as shown in Figure 1. At each sector, one hanger cable band holds two groups of hanger cables as shown in Figure 2. Of these, the acceleration signals of the hanger cable installed on the bridge side were measured.

On June 6, 2008, acceleration sensors were installed in a direction perpendicular to the hanger cables as shown in Figure 3, to measure the acceleration vibration signals of the hanger cables. Here, the acceleration sensors were installed at the height of the guardrail on the bridge to avoid missing the low vibration mode and to install them easily. The measurements were taken on holidays, which resulted in smaller amounts of traffic. Therefore, to get more reliable acceleration signals, vibration signals that lasted about 5 minutes over two measurement attempts were measured. Figure 4 shows how the field measurements scene.

For the four hanger cables, the sampling rates at ambient vibration were 1000 Hz. To efficiently obtain vibration measurements, we used a 1CH AnyLogger, a dynamic wireless logger manufactured by Korea Maintenance Co., Ltd. Figure 5 shows the acceleration response signals obtained from the ambient vibrations in a direction perpendicular to the hanger cables and the PSD (power spectral density) of the response signal. When estimating the tensile force using the FE model-based system identification method, the order and natural

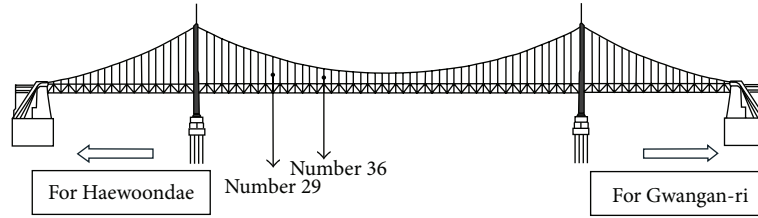


FIGURE 1: The locations of two hanger cables for measurement [6, 7].

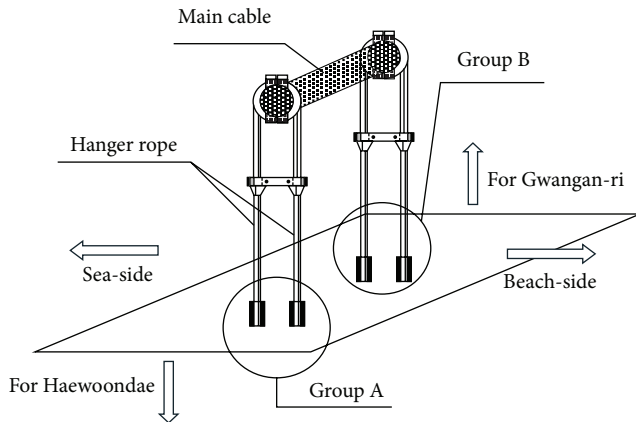


FIGURE 2: The groups of hanger cables [6, 7].

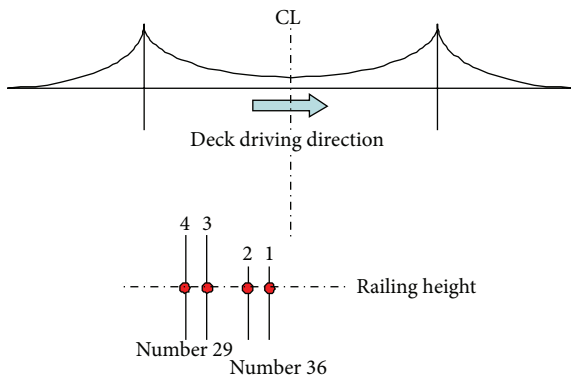


FIGURE 3: The locations for accelerometers attached on hanger cables.

frequency value of each vibration mode are important, while the absolute magnitude of acceleration signal and PSD do not significantly affect the results of tension estimation.

3.2. Finite Element Model. For the tensile force estimation method using the system identification technique, the hanger cables were modeled using three-dimensional linear elements that support the axial load to analyze the changes in natural frequency due to changes in tensile force. Here, the mass matrix was that of the frame elements, while the stiffness matrix is the sum of the stiffness matrix (Euler beam) of the normal frame elements and the geometric stiffness matrix in consideration of the influence of the tension.



FIGURE 4: Acceleration measurements for hanger cables.

The lengths and physical properties of the hanger cables of Gwang-An Bridge assuming hinges at both ends are as shown in Table 1. Here, the diameter of the cable is the effective diameter equivalent to the effective cross-sectional area. The design tension was the tensile force mentioned in the design specifications of the hanger cable for the bridge and was assumed to be the initial tension when estimating the tension force using the FE model-based system identification method.

As for the clamps, the rectangular part other than the lower fixed sockets was modeled. Also, the length of the cable at the upper part of the clamp in the hanger cables was set at 1 m without variation. The cable at the bottom of the clamp was assumed to be the length minus the height (0.5 m) of the fixed socket at the bottom of the clamp to consider that some part of the cable is fixed by the clamps.

Figure 6 shows the finite element model of cable 29A. The hanger cables on both sides were modeled in 30 elements each, while the clamps were modeled in 3 elements.

3.3. Extraction of the Natural Frequency. As shown in Figure 5(b) the ambient vibration signals of the normal hanger cables are difficult to define due to the indistinctness of the measured vibration mode in many cases. Also in this study, only 1 instrument to measure acceleration at each hanger cable was installed. Therefore, it was not possible to extract the vibration mode through experiment. Therefore, the natural frequencies and the vibration mode were determined by comparing the results with measurements presented in the research by Kim et al. [6, 7]. The natural frequencies extracted in this way for the hanger cables are as shown in Table 2. In this case, the natural frequency is determined as the average

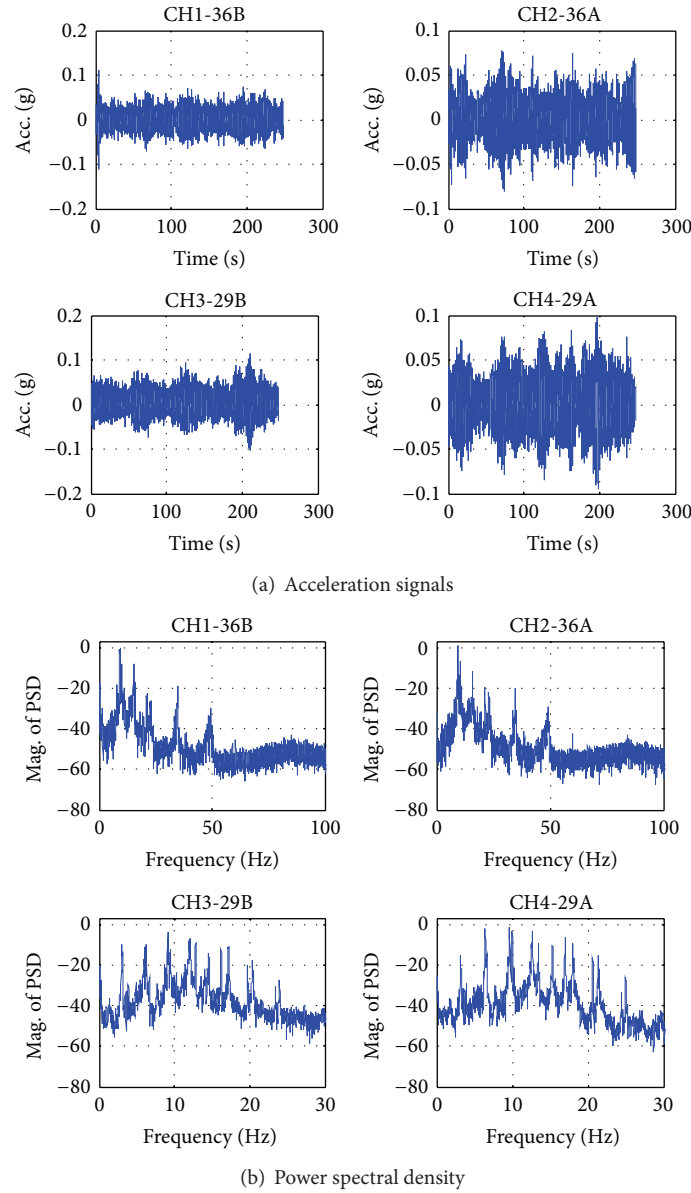


FIGURE 5: Measured accelerations and PSD data of hanger cables: (a) acceleration signals and (b) power spectral density.

TABLE 1: Geometrical and material properties of the hanger cables.

Cable number	Length (m)	Diameter (mm)	Young's modulus (kN/mm ²)	Weight (kN/mm ³)	Design tension (kN)
29A	25.3234	49.52	1.3734×10^2	8.0×10^{-8}	377.685
29B	24.9986				
36A	9.0173				
36B	8.8329				

of the two experiments to measure the natural frequencies that correspond to the symmetric mode of the hanger cables.

4. Results of Tension Estimation

In this study, the procedure for tension estimation using the FE model-based system identification method considered is

shown in Figure 7. Further details can be found in Park et al. [5]. The identification variables in the FE model-based system identification method were the tensile force, axial stiffness, bending stiffness, and torsion stiffness of the cable and the clamp. A total of 9 variables were assumed.

Figure 8 shows the symmetrical mode of the final finite element model of the 36B hanger cable in the FE model-based

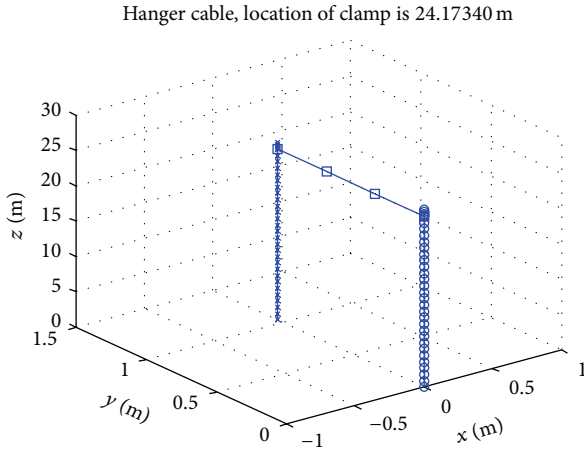


FIGURE 6: The finite element model of the hanger cable (29A).

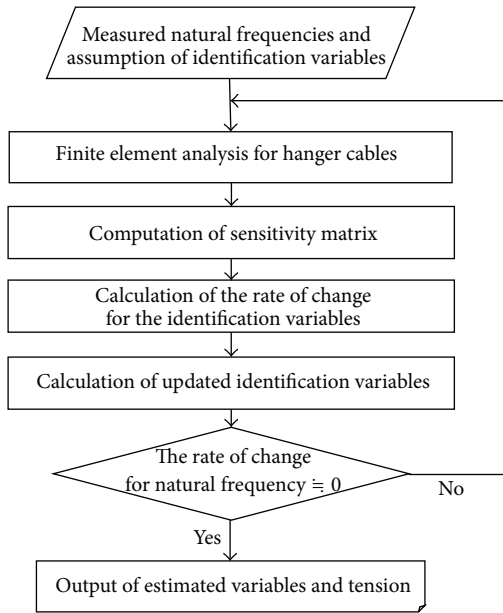


FIGURE 7: The procedure for tension estimation using the FE model-based system identification method.

TABLE 2: The natural frequencies of symmetric modes of the hanger cables.

Symmetrical mode	Measured frequency (Hz)			
	29A	29B	36A	36B
1st	3.20	3.05	9.38	9.20
2nd	6.42	6.10	15.91	15.46
3rd	9.60	9.11	23.15	22.90
4th	12.63	12.05	34.82	34.78
5th	15.32	14.54	49.14	48.28

system identification method. Table 3 shows the tension of each cable according to the estimation methods. Here, the methods by Kim et al. [6, 7] assumed the boundary conditions fixed at both sides and conducted formula-based inverse

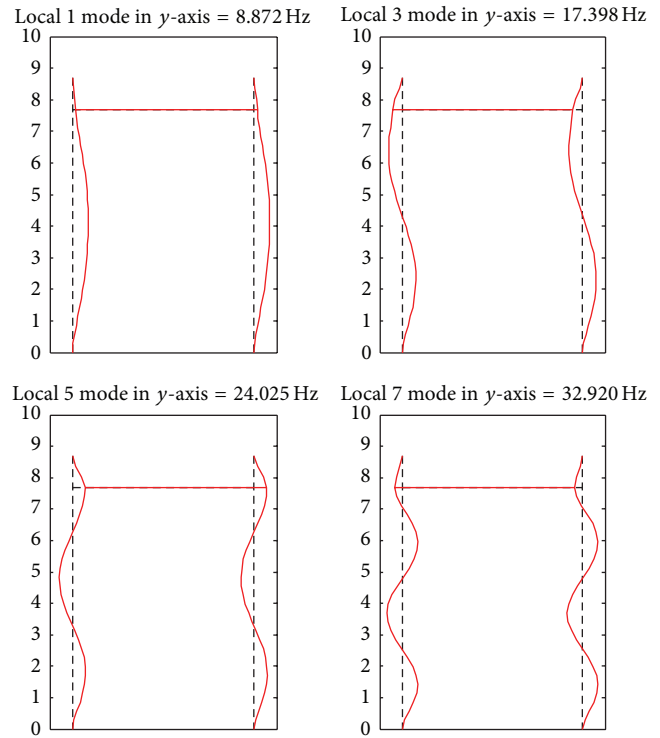


FIGURE 8: Symmetrical mode shapes of the final finite element model.

analysis in consideration of the mode participation factor, while, for the estimation of the tension using the FE model-based system identification method, the boundary condition was defined as fixed at both sides. The 5 symmetrical modes' natural frequencies were used as the input measurement values as well. The taut string theory and linear regression method showed the estimation results of the tension force using (1) and (2), respectively. In this case, the taut string theory used the first symmetrical mode.

As shown in Figure 8, in the case of 36B cable, the 1st, 3rd, 5th, and 7th vibration modes in the perpendicular direction are the 1st, 2nd, 3rd, and 4th symmetrical vibration modes, respectively. When estimating tension using the FE model-based system identification method, as shown in (4) not only the tension of the cable but also other variables, such as the axial, flexural, and torsional rigidities, could be estimated. However, for the hanger cables, variations in the tension force are the main cause of changes to the natural frequency. The influences from other variables are not significant. This was confirmed by the sensitivity analysis of each variable by Park et al. [5]. Estimation of variables other than the tension using the cables of Gwang-An Bridge shows a similar result, too. Therefore, in this paper, the results of the tension estimation other than the other variables are only presented. In Table 3, for the four hanger cables, the estimated tension by the FE model-based system identification method is smaller than those estimated by other methods. This phenomenon is even more significant with the shorter 36B cable. As the length of the cable gets shorter, the estimated tension also appears to be smaller. On the other hand, the formula-based inverse

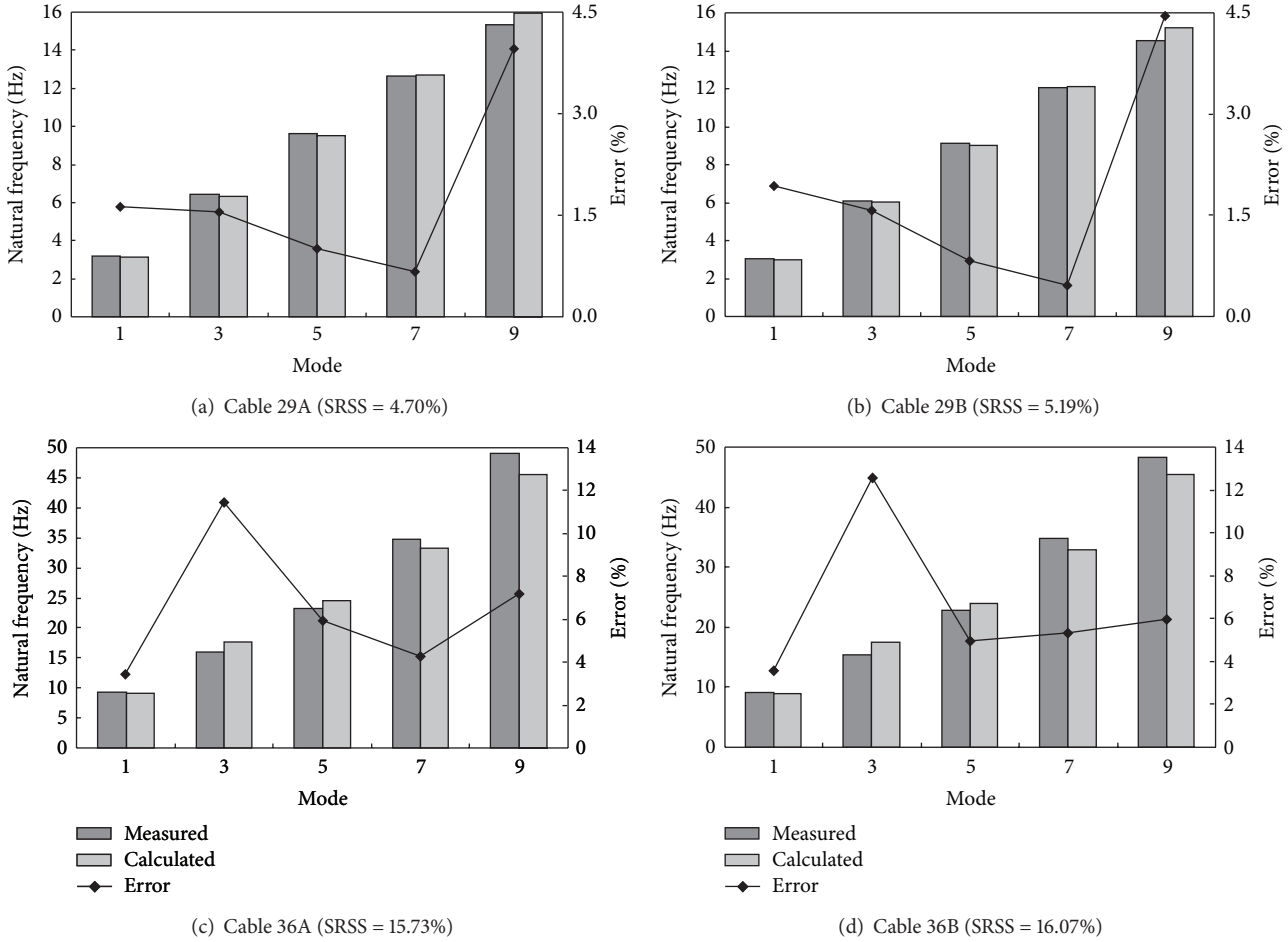


FIGURE 9: Errors in the natural frequencies for the tension estimation using the FE model-based system identification method: (a) cable 29A (SRSS = 4.70%); (b) cable 29B (SRSS = 5.19%); (c) cable 36A (SRSS = 15.73%); and (d) cable 36B (SRSS = 16.07%).

TABLE 3: The tensions (kN) of each hanger cable according to the estimation methods.

Tension estimation methods	Cable number			
	29A	29B	36A	36B
Design tension	377.685			
FE model-based system identification method	355.82	309.92	287.79	256.58
Formula-based inverse analysis method	393.45	342.75	384.45	349.86
Taut string theory	402.35	355.54	412.60	382.73
Linear regression method	397.75	348.68	321.70	294.74

analysis method estimates the tension consistently regardless of the length of the cable. However, the cable tension of A group is estimated to be bigger than that of B group. The taut string theory method shows a similar pattern with the formula-based inverse analysis method but the deviations of the estimated tension between A and B group are significant. The linear regression method shows a reduction in the estimated tension as the cable became shorter as was the case with the FE model-based system identification method.

To check the reliability of the tension force measured by each of these methods, it would be necessary to use load cells to take actual measurements, which would then be compared to the estimations. However, since there are no load cells installed on the hanger cables numbers 29 and 36, it was not possible to determine the exact tension values at the time of the experiment. However, for methods of estimating the tension using inverse analysis and system identification techniques, the accuracy of estimated tension could be checked

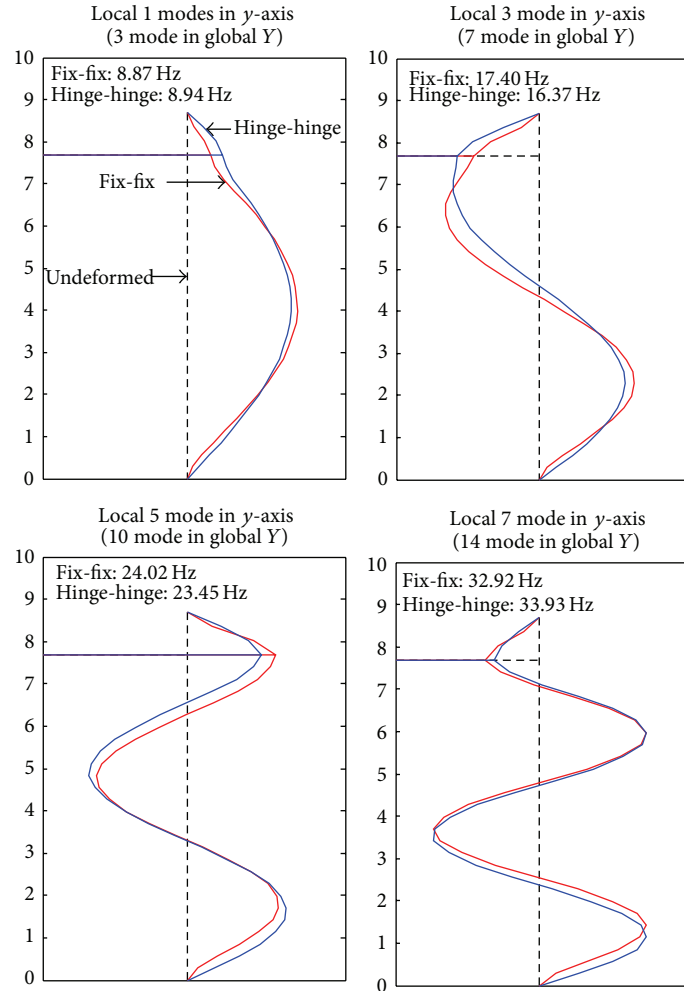


FIGURE 10: Symmetrical mode shapes according to the boundary conditions.

indirectly by means of the SRSS errors of the natural frequencies.

Figure 9 shows the errors in the natural frequencies for the tension estimation using the FE model-based system identification method for each of the hanger cables. As seen in the figure, hanger cable number 29 shows a relatively small error between the measured and calculated natural frequencies. However, the deviation for hanger cable number 36 appears to be significant. Therefore, the tension estimation results for the hanger cable number 36, where the error of the natural frequency is greater, are less reliable. This is because of the lower reliability of the measured natural frequencies, or the finite element model and the boundary conditions of the hanger cables are different from the actual conditions. However, measurement of the natural frequency can be relatively accurate compared to the results of Kim et al. [6, 7]. The only physical difference between cables numbers 29 and 36 is the length, which causes the natural frequency to change. The change here is sensitive to the boundary conditions. Therefore, the influence from the boundary conditions should be assumed to be the cause of the relatively bigger error with

cable number 36, and the influence of the boundary conditions should be analyzed.

5. Sensitivity Analysis of the FE Model-Based System Identification Method Depending on the Input Conditions

When estimating the tension force using the FE model-based system identification method, basically, the errors in the natural frequency are minimized using the measured natural frequency and the calculated natural frequency from the finite element model. Therefore, it is exposed to the influence from the boundary conditions of the finite element model. In fact, to identify the boundary conditions of the hanger cables, it is necessary to extract the vibration modes experimentally. However, in this study, there were several limitations that forced us to install only one instrument to measure the acceleration on the hanger cable. Therefore, it was not possible to extract the forms of the vibration modes through experiments.

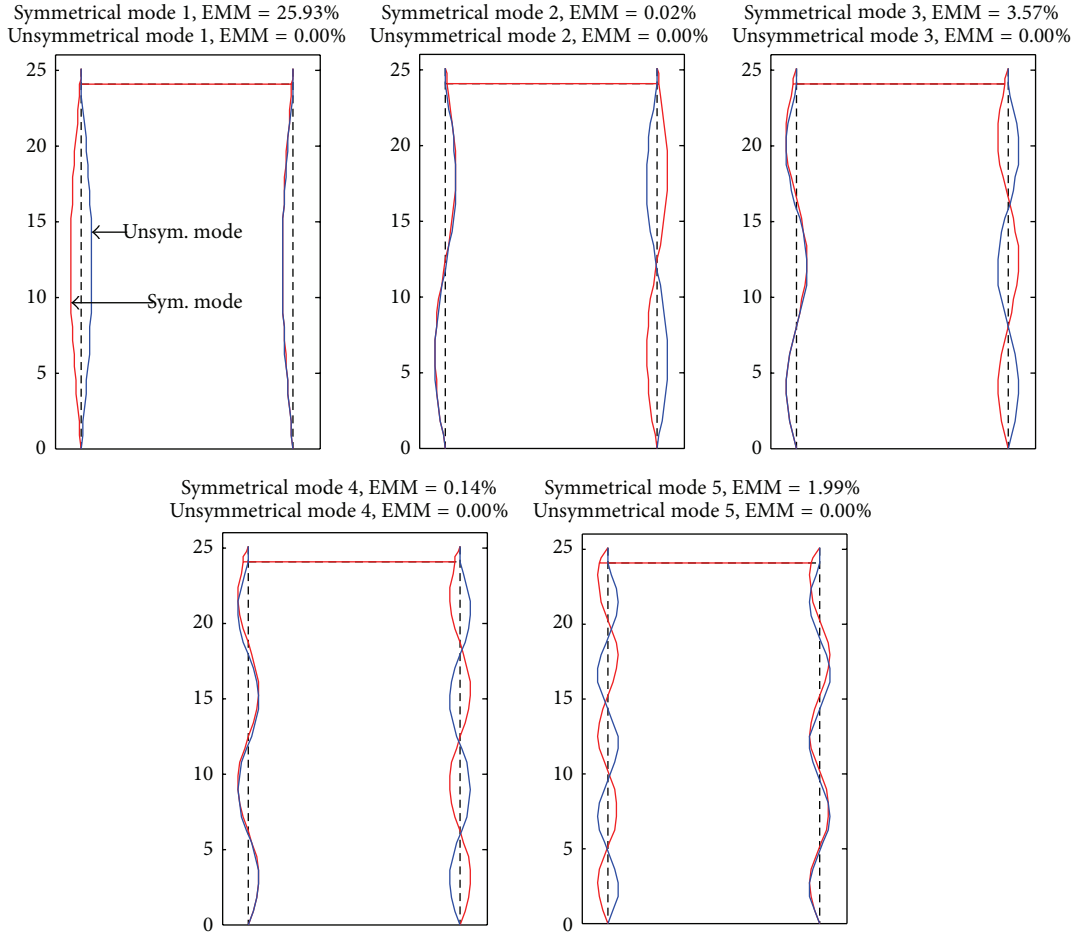


FIGURE 11: Mode shapes according to the boundary conditions.

TABLE 4: Results of the tension estimation using the FE model-based system identification method (hinges at both sides).

Cable number	Frequency	1	2	3	4	5	SRSS (%)	Tension (kN)
29A	Measured (Hz)	3.20	6.42	9.60	12.63	15.32	2.73	381.96
	Calculated (Hz)	3.18	6.36	9.53	12.66	15.68		
	Error (%)	0.79	0.91	0.73	0.25	2.33		
29B	Measured (Hz)	3.05	6.10	9.11	12.05	15.54	3.03	334.38
	Calculated (Hz)	3.02	6.04	9.06	12.05	14.93		
	Error (%)	1.04	0.87	0.52	0.00	2.66		
36A	Measured (Hz)	9.38	15.91	23.15	34.82	49.14	8.31	363.89
	Calculated (Hz)	9.12	16.77	23.90	24.28	47.00		
	Error (%)	2.82	5.40	3.27	1.53	4.35		
36B	Measured (Hz)	9.20	15.46	22.90	34.78	48.28	7.96	331.92
	Calculated (Hz)	8.94	16.37	23.45	33.93	46.83		
	Error (%)	2.83	5.87	2.42	2.44	3.00		

Table 4 shows the results of the tension estimation using the FE model-based system identification method when the boundary condition of the hanger cable was assumed as hinges at both sides.

As seen in the table, compared to the cases of fixed condition at both sides, errors in the natural frequency and

SRSS are reduced, while the estimated tension force is similar to that of the formula-based inverse analysis method. In particular, errors are reduced significantly with the number 36 hanger cable, which is shorter. This results in a subsequent larger change in the estimated tension force because the shorter cable is more sensitive to the boundary conditions

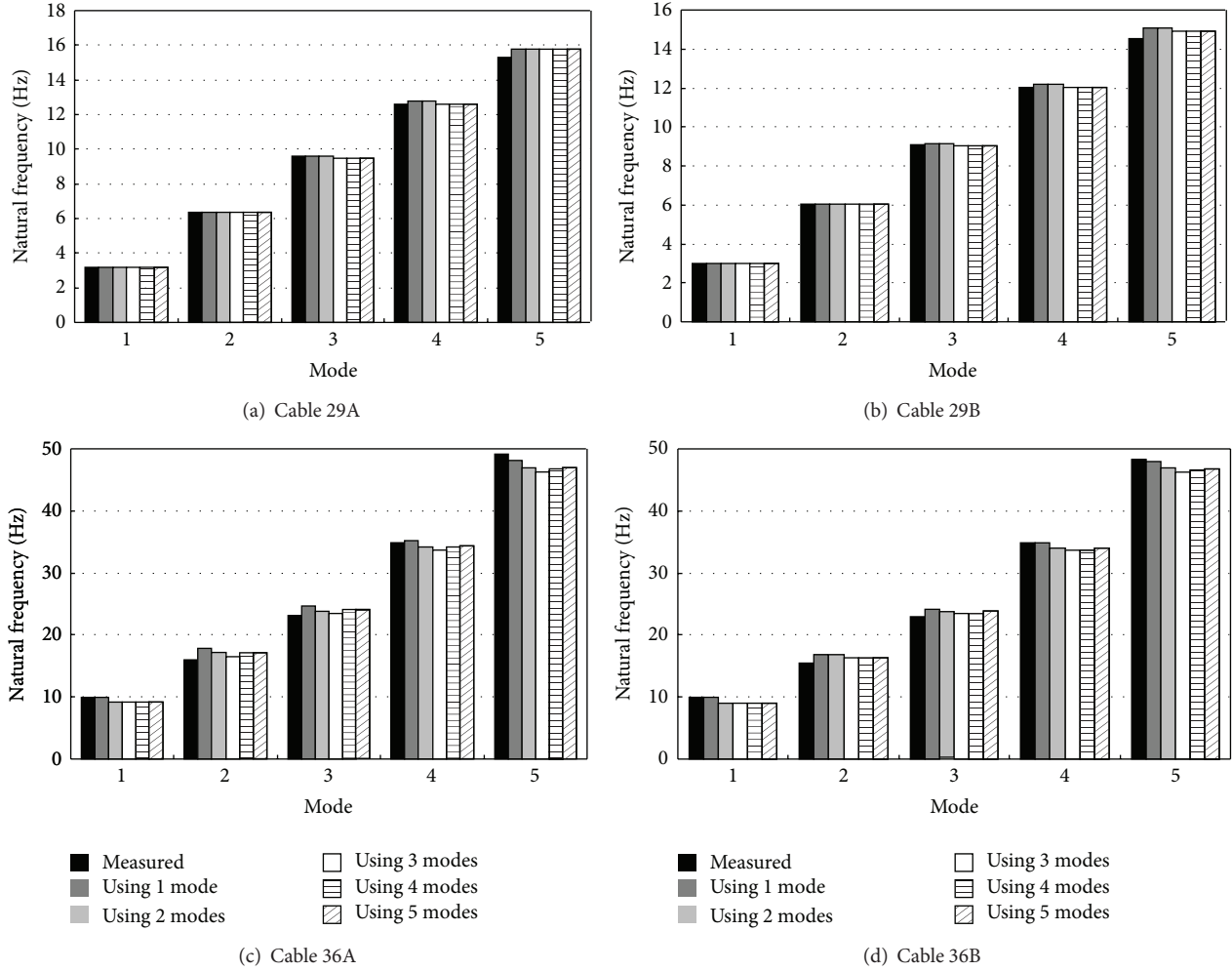


FIGURE 12: Changes of the natural frequencies according to the number of the input natural frequency.

compared to longer cables. Figure 10 shows the symmetrical mode shapes and natural frequency by the boundary conditions of 36B cable.

As seen in the figure, the boundary condition influences the vibration mode and natural frequency significantly. Therefore, from the results of the tension estimation using the FE model-based system identification method, it is rationally assumed that the boundary conditions for this study with the hanger cables of Gwang-An Bridge should be hinges at both sides. This is different from the boundary condition of the inverse analysis, which was fixed at both sides. The reason for this difference is believed to be the differences in the finite element model, the input natural frequency value, and their numbers. Therefore, to identify the boundary conditions of the hanger cables more precisely, a number of acceleration measurement instruments to extract the vibration mode should be used and the boundary conditions be identified experimentally.

The tension estimation method using the FE model-based system identification method is affected not only by the accuracy of the finite element model, but also by the input natural frequency. Therefore, to consider natural frequency

influence, the following method shown in the following is considered:

$$\text{EMM} (\%) = \frac{(\phi_i^T M \{1\} / \phi_i^T M \phi_i)}{M_{\text{total}}} \times 100, \quad (12)$$

where each of the natural frequencies and effective modal mass (EMM) are calculated to use the natural frequency of the modes with higher effective modal mass in a sequential order. Then, the estimated tension force and the calculated natural frequency are analyzed.

Figure 11 shows the 10 natural vibration modes and their effective modal masses with cable 29A under the boundary condition of hinges at both sides and the design tension. As seen in the figure, the effective modal mass of the unsymmetrical mode was close to 0. Therefore, the effective modal mass of each mode is considered and the results after applying 1, 2, 3, 4, and 5 natural frequencies starting from the one with the largest effective modal mass are compared. Table 5 shows the effective modal masses of vibration modes under hinges at both sides as the boundary condition and the design tension.

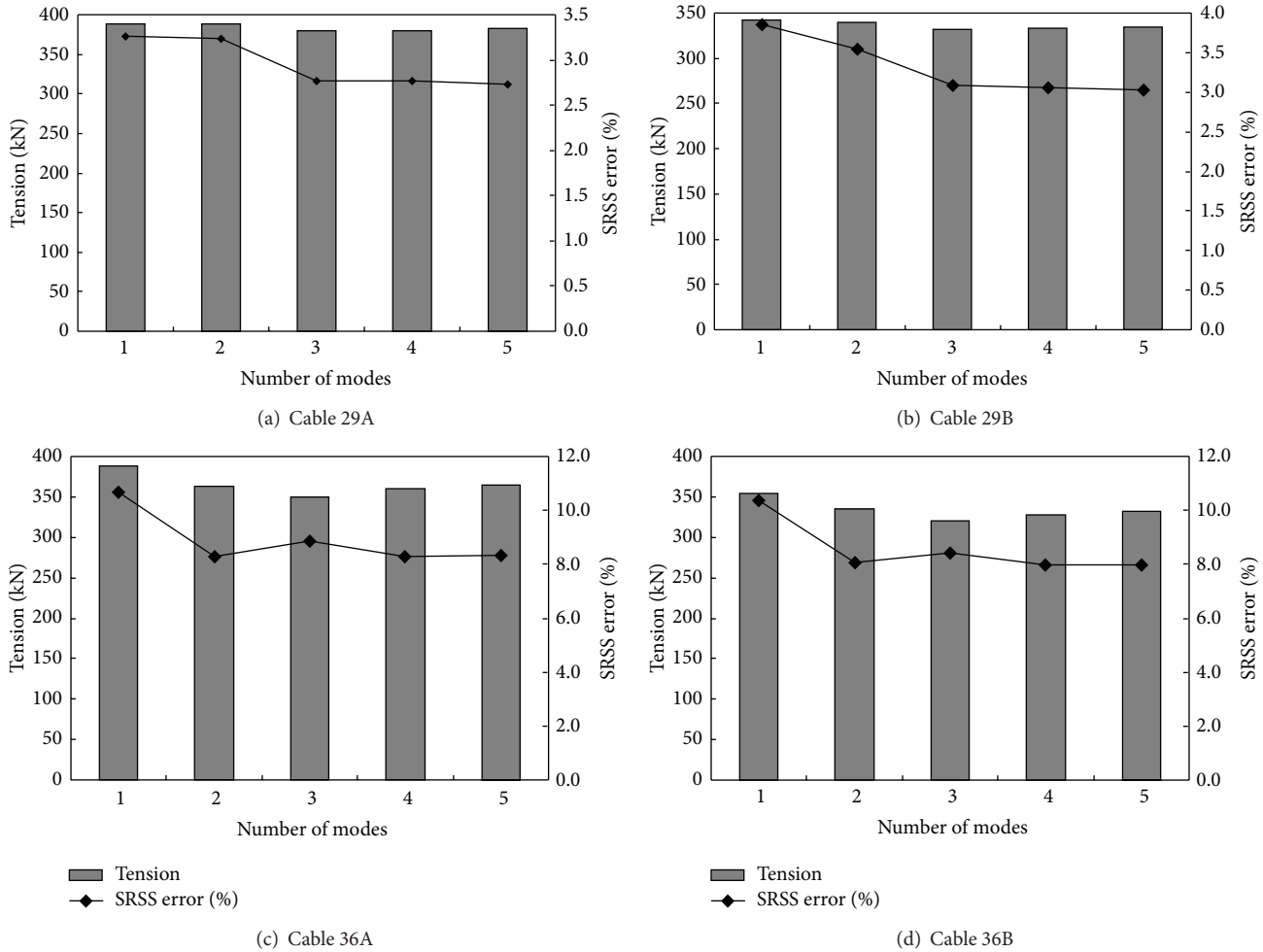


FIGURE 13: Changes of the SRSS errors in the natural frequency and the estimated tension according to the number of the input natural frequency.

As seen in Table 5, shorter cables have greater effective modal masses under the unsymmetrical mode, though the increase is not significantly large. For the symmetric mode, cable number 29 is bigger in the effective modal mass by the order of 1st, 3rd, 5th, 4th, and 2nd modes. However, for cable number 36, the effective modal mass is the largest in the order of 1st, 3rd, 2nd, 5th, and 4th. That is, the longer and shorter cables are generally similar in terms of overall effective modal masses. However, there are tiny differences depending on the influence from the unsymmetrical mode or the order of size of the effective modal masses.

Figures 12 and 13 show the natural frequencies, the SRSS errors in the natural frequency, and the estimated tension of the 5 symmetric modes of the final finite element model according to the input natural frequency for the FE model-based system identification method. As seen in the figure, the changes in terms of the natural frequency of the final finite element model by the number of input natural frequencies in the FE model-based system identification method are not significant. In this case, as for cables 29A, 29B, 36A, and 36B, they show about 10% deviations for the design tension, which are 8.08, 9.34, 38.94, and 34.24 kN, respectively. Therefore, if

the tension is estimated using the FE model-based system identification method, it is possible to reliably estimate the tension using only the natural frequency of the small number of vibration modes with higher effective modal masses, which could be an advantage to using this method.

6. Conclusion

In this paper, the finite element model based method was applied to estimate the tension of hanger cables on Gwang-An Bridge, and its reliability and applicability are investigated. The conclusion is as follows.

The taut string theory and the linear regression method, which are used to estimate the tension of normal cables, could render similar estimation results like the formula-based inverse analysis method and the system identification method based on the finite element models for cable number 29. However, for cable number 36, the results from these two methods differed significantly. Also, the existing methods could not be applied to various boundary conditions of cables, and it was not possible to verify the reliability unless the tensions were measured directly using load cells. On

TABLE 5: Effective modal masses (%) of each vibration mode.

Mode	29A	29B	36A	36B
1 (1st symmetrical mode)	25.9265	25.9176	27.1070	27.2265
2 (1st unsymmetrical mode)	0.0000	0.0000	0.0000	0.0000
3 (2nd symmetrical mode)	0.0237	0.0250	1.2822	1.2983
4 (2nd unsymmetrical mode)	0.0000	0.0000	0.0000	0.0000
5 (3rd symmetrical mode)	3.5729	3.5950	3.5551	3.4151
6 (3rd unsymmetrical mode)	0.0000	0.0000	0.0001	0.0001
7 (4th symmetrical mode)	0.1392	0.1473	0.1101	0.1227
8 (4th unsymmetrical mode)	0.0000	0.0000	0.0002	0.0002
9 (5th symmetrical mode)	1.9872	2.008	0.4461	0.4355
10 (5th unsymmetrical mode)	0.0000	0.0000	0.0003	0.0004

the other hand, the system identification technique allowed the boundary conditions to be taken into consideration easily, and the reliability of the tension estimation could indirectly be assessed by means of errors in the calculated natural frequency from actual measurements of the natural frequency. In addition to the tension, estimates could be made for variables such as the rigidities for cables and clamps. Since it is not sensitive to the number of the natural frequency inputs, the utility of this method is high.

The key to creating a finite element model is to introduce an appropriate boundary condition. Shapes of the vibration mode due to the change of the boundary condition are the same, but the size of the relative vibration mode at each node is different. Therefore, the vibration mode varies depending on the boundary conditions, and this difference becomes larger as it approaches the support. However, changes in the frequencies caused by the boundary conditions did not have a fixed tendency and varied in accordance with the order of the natural frequency. As the cable becomes shorter, it is influenced more by the boundary conditions. Therefore, it is necessary to extract the vibration mode to judge the boundary conditions experimentally.

For this reason, when the length of the cable was longer, not only the existing methods, but also the methods based on the finite element models for the hanger cables could be used. However, as the length decreased, the increase in errors in the existing method is inevitable, and the reliability of the tension estimation based on the finite element model is higher. However, the model-based tension estimation method is seriously influenced by the accuracy of the finite element model that includes the boundary conditions. Therefore, it is important to create an appropriate finite element model.

Conflict of Interests

The authors declare that there is no conflict of interests regarding the publication of this paper.

Acknowledgments

This research was supported by the Construction Core Technology Program funded by the Ministry of Construction & Transportation of the Korean government (Grant no. 2006-D20). The financial support is gratefully acknowledged.

References

- [1] H. M. Irvine, *Cable Structures*, The MIT Press, Cambridge, Mass, USA, 1981.
- [2] T. Shimada, *A study on the maintenance and management of tension measurement for the cable of bridge [Ph.D. dissertation]*, Kobe University, 1995.
- [3] J. K. Yun, J. Son, and S. P. Chang, "A study on tension measurement for cable-supported bridge," in *Proceedings of the Annual Conference of The Korean Society of Civil Engineers*, pp. 117–120, 1999.
- [4] S. S. Ahn, I. K. Lee, I. H. Bae, and H. K. Choi, "Static test method for estimating tensile force of hanger cable," in *Proceedings of Annual Conference of The Korean Society of Civil Engineers*, pp. 1418–1423, 2003.
- [5] T. Park, S. Moon, H. J. Joo, and B. H. Kim, "Estimating tensile force of hangers in suspension bridges using frequency based SI technique: I. Theory," *Journal of The Korean Society of Civil Engineers*, vol. 27, no. 2, pp. 165–172, 2007.
- [6] B. H. Kim, S. Moon, I. H. Bae, and T. Park, "Estimating tensile force of hangers in suspension bridges using frequency based SI technique: II. field application," *Journal of the Korean Society of Civil Engineers*, vol. 27, pp. 173–179, 2007.
- [7] N. S. Kim, D. W. Park, Y. M. Park, and J. H. Jeong, "Back analysis technique for the estimation of tension force on hanger cables," *Jorunal of the Earthquake Engineering Society of Korea*, vol. 21, no. 3, pp. 1–10, 2007.
- [8] H. T. Jang, B. H. Kim, and T. Park, "Estimating tensile force of hangers in suspension bridges using frequency based SI technique: III. Experimental Verification," *Journal of the Korean Society of Civil Engineers*, vol. 28, no. 2A, pp. 215–222, 2008.
- [9] M. S. Triantafyllou and L. Grinfolgel, "Natural frequencies and modes of inclined cables," *Journal of Structural Engineering New York*, vol. 112, no. 1, pp. 139–148, 1986.
- [10] J. C. Russell and T. J. Lardner, "Experimental determination of frequencies and tension for elastic cables," *Journal of Engineering Mechanics*, vol. 124, no. 10, pp. 1067–1072, 1998.
- [11] T. Shimada, K. Kimoto, and S. Narui, "Study on estimating tension of tied hanger rope of suspension bridge by vibration method," *Proceedings of JSCE*, vol. 404, no. 11, pp. 455–458, 1989.
- [12] H. Zui, T. Shinke, and Y. Namita, "Practical formulas for estimation of cable tension by vibration method," *Journal of Structural Engineering*, vol. 122, no. 6, pp. 651–656, 1996.

Research Article

Derivation Method for the Foundation Boundaries of Hydraulic Numerical Simulation Models Based on the Elastic Boussinesq Solution

Jintao Song,^{1,2,3} Chongshi Gu,^{1,2,3} Hao Gu,^{1,2,3} and Shaowei Wang^{1,2,3}

¹State Key Laboratory of Hydrology-Water Resources and Hydraulic Engineering, Hohai University, Nanjing 210098, China

²National Engineering Research Center of Water Resources Efficient Utilization and Engineering Safety, Hohai University, Nanjing 210098, China

³College of Water Conservancy and Hydropower, Hohai University, Nanjing 210098, China

Correspondence should be addressed to Chongshi Gu; zibet998@126.com

Received 25 September 2014; Revised 9 February 2015; Accepted 20 March 2015

Academic Editor: Rafael J. Villanueva

Copyright © 2015 Jintao Song et al. This is an open access article distributed under the Creative Commons Attribution License, which permits unrestricted use, distribution, and reproduction in any medium, provided the original work is properly cited.

The foundation boundaries of numerical simulation models of hydraulic structures dominated by a vertical load are investigated. The method used is based on the stress formula for fundamental solutions to semi-infinite space body elastic mechanics under a vertical concentrated force. The limit method is introduced into the original formula, which is then partitioned and analyzed according to the direction of the depth extension of the foundation. The point load will be changed to a linear load with a length of $2a$. Inverse proportion function assumptions are proposed at parameter a and depth l of the calculation points to solve the singularity questions of elastic stress in a semi-infinite space near the ground. Compared with the original formula, changing the point load to a linear load with a length of $2a$ is more reasonable. Finally, the boundary depth criterion of a hydraulic numerical simulation model is derived and applied to determine the depth boundary formula for gravity dam numerical simulations.

1. Introduction

In hydraulic engineering, numerical simulation models are widely used in structural analysis [1], such as in infinite and discrete element methods. The finite element method (FEM) is the most widely used technique in hydraulic numerical simulation [2]. Selecting the foundation boundaries affects the number of finite element mesh size, calculation accuracy, and computation time [3]. Many scholars have proposed selection methods for foundation boundaries based on the finite element simulation model. Foundation boundaries are generally selected based on engineering experience [4] or by comparing the accuracy of stress results using FEM for different boundary conditions [5]. However, these selection methods are still not applied in engineering design because of different issues in analyzed objects and calculation accuracy [6]. At present, comprehensive qualitative studies remain

inadequate in both China and abroad; for example, selecting calculation boundaries has not been studied based on elasticity theory [7]. According to Saint-Venant's principle [8], hydraulic structure load has more influence on the stress of a point near the load and minimal influence on the stress of a point far from the load; hence, conducting a partition discussion is necessary. Research on foundation boundaries under dam structure load can analyze foundation stress under loads and search for the minimum impact areas to function as boundaries [9]. Many hydraulic structure loads are produced under vertical force such as in gravity dams, water locks, and docks. The current study focuses on hydraulic structures dominated by a vertical force. The Boussinesq stress solution to a semi-infinite elastic mechanics space body under a vertical concentrated load is widely used in soil mechanics calculation [10]. This study combines

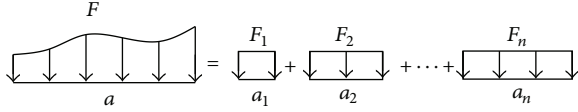


FIGURE 1: Decomposing the structure of a load.

L'Hospital's rule and the Boussinesq equation to derive the formula for the selection principle of foundation boundaries.

2. Methodology

This study investigates the problem of selecting a finite element numerical model and a foundation boundary scope for hydraulic structures under a vertical load such as gravity dams and sluices. The load of hydraulic structures on the foundation consists of nonlinear vertical distributed loads resulting from a nonlinear structure shape, nonlinear materials, and construction factors [11]. It can be decomposed into numerous distributed loads with different sizes (Figure 1). The uneven distribution of loads has different effects on foundation depth. The Boussinesq stress solution to semi-infinite elastic mechanics space body under a vertical concentrated load is widely used in soil mechanics calculation, particularly when the calculation point stress of the foundation is approximately zero. The coordinate of the point can determine the foundation boundaries of a hydraulic numerical simulation model. The formula, however, suffers from a singular point problem [12] near the ground. In this chapter, formula derivation is presented in three parts. Section 2.1 introduces the Boussinesq foundation stress formula for vertical concentrated loads. Section 2.2 describes the singular point problem near the ground and proposes solutions to this problem. Section 2.3 derives the stress formula under distributed loads with a parameter width of a and determines the coordinates of a point in which stress is approximately zero to obtain the foundation boundaries for an elastic numerical simulation model of a hydraulic structure.

2.1. Introduction to Common Formulas. A hydraulic structure load on a semi-infinite elastic foundation consists of different continuous vertical distributed forces, which are decomposed into concentrated forces. Stress equations based on the half-space problem and the plane elastic mechanics problem provided by Boussinesq satisfy the objective of the aforementioned analysis problem.

Suppose that a half-space has no body force and the normal concentrated force P on the plane boundary has a value of F . Figure 2 shows the distribution map of a load. This problem is axisymmetric, and the coordinate origin point is the center of P . The stress boundary condition is $(\sigma_z)_{z=0, y \neq 0} = 0$, $(\tau_{zr})_{z=0, r \neq 0} = 0$. The solution is described as follows:

$$\sigma_x = \frac{3F}{2\pi} \left\{ \frac{x^2 z}{R^5} + \frac{1-2\mu}{3} \left[\frac{1}{R(R+z)} - \frac{(2R+z)x^2}{(R+z)R^5} - \frac{z}{R^3} \right] \right\}, \quad (1)$$

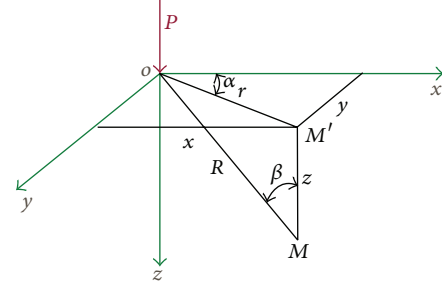


FIGURE 2: Distribution map of a load.

$$\sigma_y = \frac{3F}{2\pi} \left\{ \frac{y^2 z}{R^5} + \frac{1-2\mu}{3} \left[\frac{1}{R(R+z)} - \frac{(2R+z)y^2}{(R+z)R^5} - \frac{z}{R^3} \right] \right\}, \quad (2)$$

$$\sigma_z = \frac{3F}{2\pi} \frac{z^3}{R^5}. \quad (3)$$

In (1), (2), and (3), σ_x is the stress in the direction of x , σ_y is the stress in the direction of y , σ_z is the stress in the direction of z , μ is Poisson's ratio of the foundation, and F is the amount of the force.

The Boussinesq solution focuses on axisymmetric problems. The stress of hydraulic structure load on a foundation is an axisymmetric problem, wherein axes x and y are replaceable when studying finite element boundaries. Equations (1), (2), and (3) show that 3D stresses are proportional to the square root of length factors. The vertical stress (σ_z) on the foundation is critical because it is the main factor that results in the settlement of buildings [13]. Therefore, additional research on vertical stress (σ_z) to derive the foundation boundary of the finite element model is reasonable.

2.2. Singular Point of Common Formulas. Saint-Venant's principle in elastic mechanics states that if a force system acting on a small elastic surface is replaced by another equivalent static force, then the effects on the stress and strain of this region are significant, whereas the effect on distance is negligible. The accuracy of the Boussinesq formula is high when the calculation point is far from the ground. By contrast, the vertical force increases rapidly when the calculation point is near load areas, which contradicts actual situations. Thus, the point load formula is no longer applicable near the dam and requires correction. The vertical stress concentration problem near the dam area under a point load [14, 15] can be proven as follows:

$$\begin{aligned} \lim_{z \rightarrow 0} \sigma_z \Big|_{z=0} &= \lim_{z \rightarrow 0} \frac{3F}{2\pi z^2 [1 + (r/z)^2]^{5/2}} \\ &= \lim_{z \rightarrow 0} \frac{3F}{2\pi} \frac{1/z^2}{[1 + (r^2/z^2)]^{5/2}}, \quad \text{when} \quad (4) \end{aligned}$$

$$u = \frac{1}{z^2}, \quad \lim_{z \rightarrow 0} \sigma_z \Big|_{z=0} = \lim_{u \rightarrow \infty} \frac{u}{(1 + r^2 u)^{5/2}}.$$

Given the randomness of x , y , and z when they satisfy the function of

$$x^2 + y^2 = r^2 = \frac{1}{u^2}, \text{ then} \quad (5)$$

$$\lim \sigma_z|_{z \rightarrow 0} = \lim_{u \rightarrow \infty} \frac{u}{(1 + (1/u^3))^{5/2}} = \infty.$$

In the elastomeric hypothesis, the existence of stress concentration indicates the presence of a plastic expansion area. If such area exists, then the elastomeric hypothesis is contradicted. Newton solved the gravity concentration problem of two close particles by considering each particle as a sphere with a radius. To avoid stress concentration, the point load is changed to a line load with a certain length.

In *Mathematical Principles and Natural Philosophy*, Newton explained the law of gravitation of objects as follows. When the distance between two particles tends to be "infinitely small," the particles are regarded as a sphere with a radius [16], and consequently, the range of the integral of the force between two objects in space can be calculated. When the particles are close to each other, the Boussinesq point stress formula presents the same problem; that is, $G(Mm/r^2) \rightarrow \infty$. Thus, particle assumption is no longer true. Based on the definition of a particle provided in Newton's law of universal gravitation, the concept of a point load is relative and can be calculated based on the particle formula when two objects are far from each other. Based on this principle, the span of a load is regarded as zero when the load is far from the dam. Newton used calculus to solve problems of increasing gravity in two particles with a small distance between them. The Boussinesq vertical stress $\sigma_z \rightarrow \infty$ when the calculation point is near the load. Consequently, the point load near the dam should be changed to a line load with a certain length.

2.3. Deriving the New Equation. To avoid the problem of stress concentration near the ground, the aforementioned method of changing the point load to a distributed load is used to derive the correction formula for the plane and space problems. The modified formula is then used to analyze the influence of the foundation scope. When the calculation point is far from the load areas, its correction width can be ignored based on Saint-Venant's principle. By contrast, when the calculation point is close to the load areas, its correction width cannot be ignored. The following sections discuss the plane and space problems. The vertical stress formula for different depths under the effect of a point load is corrected and the function of load width parameter a and depth l is proposed. The relative error between the original and the corrected formula, as well as the influence of the foundation scope, is then analyzed.

2.3.1. The Plane Problem. Figure 3 shows the diagram of the plane problem. The point of the load is stipulated as the original point. Based on (3), for each point on line $z = z_0$, the vertical stress of point M that is strictly under the original point is maximal. When the vertical stress of point M $\sigma_z \rightarrow$

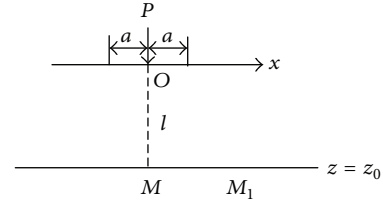


FIGURE 3: Load distribution map of the plane problem.

0, the vertical stress of all points on line $z = z_0$ tends to be zero. In this research, the vertical stress (σ_z) of point M whose distance from the original point is l is studied. The loads of hydraulic structures that are acting on the foundation are superposed by successive point loads of different sizes. The influence scope of an arbitrary point load can then be analyzed. Based on the preceding analysis, the point load is changed to a distributed load with a width of $2a$. The following section provides the hypothetical function of width parameter a and the depth of calculated point l .

(1) Determining the Physical Parameters. According to Saint-Venant's principle, the farther the calculated point from the load areas, the less the error caused by the correction width parameter $2a$ of the distributed load and the original point load. Meanwhile, the closer the calculated point is from the load areas, the larger the width parameter $2a$ should be.

Assuming that the existence of critical depth l_0 satisfies $l \geq l_0$, parameter a approximates zero and the load can be considered as a point load. By contrast, when $l < l_0$, the load should be considered as a distributed load. Observed through continuity, a tapering function between l and a exists.

Assuming that parameter a is inversely proportional to l , then

$$a = \frac{k}{l}. \quad (6)$$

The three situations of the calculated point depth l are as follows.

- ① The calculation point is far from the surface with $l_1/a \rightarrow \infty$.
- ② The calculation point is close to the surface with $a \neq 0$, $a/l_2 \rightarrow \infty$.
- ③ The moderate area is $l_2 < l < l_1$. A constant $\varepsilon > 0$ exists, which ensures that $0 < |l/a - N| < \varepsilon$, where N is a positive integer.

(2) Correction Formula and Comparison. The following formulas correct the vertical stress formula for the three situations of the calculation point depth l , respectively, and compare precision before and after correction.

(1) l is extremely large; thus, $l/a \rightarrow \infty$:

$$\begin{aligned} d\sigma_z &= \frac{3\sigma z^3 dx}{2\pi(x^2 + z^2)^{5/2}}, \\ \sigma_z &= \int_{-a}^a d\sigma_z = \frac{3\sigma l^3}{2\pi} \int_{-a}^a \frac{dx}{(x^2 + l^2)^{5/2}}, \end{aligned} \quad (7)$$

with $x = l \tan \alpha$,

$$\begin{aligned} \sigma_z &= \frac{3\sigma}{2\pi l} \int_{-\arctan(a/l)}^{\arctan(a/l)} \cos^3 \alpha d\alpha \\ &= \frac{3\sigma}{\pi l} \left(\sin \alpha - \frac{1}{3} \sin^3 \alpha \right) \Big|_0^{\arctan(a/l)}, \\ \sigma_z &= \frac{3\sigma}{\pi l} \left(\operatorname{sinarctan} \frac{a}{l} - \frac{1}{3} \sin^3 \arctan \frac{a}{l} \right), \end{aligned} \quad (8)$$

where $\sigma = F/2a$,

$$\sigma_z = \frac{3F}{2\pi la} \left(\operatorname{sinarctan} \frac{a}{l} - \frac{1}{3} \sin^3 \arctan \frac{a}{l} \right). \quad (9)$$

The result of the original formula is $\sigma_{z1} = 3F/2\pi l^2$.
The relative error is

$$\begin{aligned} &\left| \frac{\sigma_z - \sigma_{z1}}{\sigma_{z1}} \right| \\ &= \left| \left((3F/2\pi la) \left(\operatorname{sinarctan} (a/l) - (1/3) \sin^3 \arctan (a/l) \right) \right. \right. \\ &\quad \left. \left. - 3F/2\pi l^2 \right) \right| \cdot (3F/2\pi l^2)^{-1} \\ &= \lim_{a/l \rightarrow 0} \left| \frac{(3F/2\pi la) (a/l - a^3/3l^3) - 3F/2\pi l^2}{3F/2\pi l^2} \right| \\ &= \lim_{a/l \rightarrow 0} \left| \frac{(3F/2\pi) (1/l^2 - a^2/3l^4) - 3F/2\pi l^2}{3F/2\pi l^2} \right| \\ &= \lim_{a/l \rightarrow 0} \left| \left(1 - \frac{a^2}{3l^2} \right) - 1 \right| = 0. \end{aligned} \quad (10)$$

The error is merely $a^2/3l^2$. Given that $l/a \rightarrow \infty$, the error is approximately zero, which illustrates that the Boussinesq solution has good applicability. Hence, the error caused by the width of the distributed load can be ignored.

(2) l is very small; thus, $a \neq 0$, $a/l \rightarrow \infty$. The following statements prove that the stress concentration problem can be solved using (6).

The integration results of the distributed load are as follows:

$$\begin{aligned} \sigma_z &= \frac{3F}{2\pi la} \left(\operatorname{sinarctan} \frac{a}{l} - \frac{1}{3} \sin^3 \arctan \frac{a}{l} \right), \text{ with} \\ \frac{a}{l} \rightarrow \infty, \quad \lim \sigma_z &= \frac{3F}{2\pi la} \left(1 - \frac{1}{3} \right) = \frac{F}{\pi k}. \end{aligned} \quad (11)$$

Thus, σ_z is bounded. In fact, as long as $l \times a$ is bounded, no singular point will exist.

Apply the Taylor series at $x = 0$; then

$$\begin{aligned} \sin(x) &= x - \frac{x^3}{6} + o(x^3), \\ \arctan(x) &= x - \frac{x^3}{3} + o(x^3), \end{aligned} \quad (12)$$

$$\sigma_z = \frac{3F}{2\pi la} \left(\frac{a}{l} - \frac{5a^3}{6l^3} \right) + o\left(\frac{a}{l}\right)^3 = \frac{3F}{2\pi l^2} - \frac{5Fa^2}{4\pi l^4}.$$

The result of the original formula is $\sigma_{z1} = 3F/2\pi l^2$.

The relative error is

$$\begin{aligned} \left| \frac{\sigma_z - \sigma_{z1}}{\sigma_{z1}} \right| &= \left| \frac{3F/2\pi l^2 - 3F/2\pi l^2 - 5Fa^2/4\pi l^4}{3F/2\pi l^2} \right| \\ &= \lim_{a/l \rightarrow \infty} \left| \frac{5a^2}{6l^2} \right|. \end{aligned} \quad (13)$$

Given that a/l is extremely large when the calculation point is near the ground, the error caused by the width of the distributed load cannot be ignored. The stress concentration problem can be solved in this area, which demonstrates that the width of the distributed load cannot be ignored.

(3) l is moderate, which corresponds to depth situation ③:

$$\begin{aligned} &\left| \frac{\sigma_z - \sigma_{z1}}{\sigma_{z1}} \right| \\ &= \left| \left((3F/2\pi la) \left(\operatorname{sinarctan} (a/l) - (1/3) \sin^3 \arctan (a/l) \right) \right. \right. \\ &\quad \left. \left. - 3F/2\pi l^2 \right) \right| \cdot (3F/2\pi l^2)^{-1}, \\ &\left| \frac{\sigma_z - \sigma_{z1}}{\sigma_{z1}} \right| = \left| \frac{l}{a} \left(\operatorname{sinarctan} \frac{a}{l} - \frac{1}{3} \sin^3 \arctan \frac{a}{l} \right) - 1 \right|. \end{aligned} \quad (14)$$

Let

$$\frac{a}{l} = u,$$

$$\left| \frac{\sigma_z - \sigma_{z1}}{\sigma_{z1}} \right| = \left| \left(\frac{1}{u} \right) \left(\operatorname{sinarctan} u - \left(\frac{1}{3} \right) \sin^3 \arctan u \right) - 1 \right|. \quad (15)$$

When searching for the intersection of $y_1 = \operatorname{sinarctan} u - (1/3)\sin^3 \arctan u$ and $y_2 = u$ using the software MATLAB, the result is

$$u = 0.106. \quad (16)$$

When $u < 0.106$, the relative error and the width of the distributed load can be ignored. By contrast, when $u > 0.106$, the relative error cannot be ignored and the point load must be changed to a distributed load. Therefore, for a plane problem, the error caused by the width of the distributed load can be ignored only if $a/l < 0.106$, and the Boussinesq point stress solution can still be used.

2.3.2. *Space Problem.* In a space problem, the point load is changed to a distributed load with a radius of a .

(1) a is the radius of the distributed load. When l is extremely large, $l/a \rightarrow \infty$:

$$d\sigma_z = \frac{3\sigma z^3 dx}{2\pi(x^2 + z^2)^{5/2}} = \frac{3\sigma z^3 r dr d\theta}{2\pi(r^2 + z^2)^{5/2}}, \quad (17)$$

$$\sigma_z = \int d\sigma_z = \frac{3\sigma l^3}{2\pi} \int_0^{2\pi} d\theta \int_0^a \frac{r dr}{(r^2 + z^2)^{5/2}}.$$

The result of the original formula is

$$\sigma_{z1} = \frac{3F}{2\pi l^2},$$

$$\frac{\sigma_z}{\sigma_{z1}} = -\frac{2}{3} \cdot \frac{(a^2/l^2 + 1)^{-3/2} - 1}{(a/l)^2}, \quad (18)$$

$$\lim_{a/l \rightarrow 0} \frac{\sigma_z}{\sigma_{z1}} = \lim_{a/l \rightarrow 0} -\frac{2}{3} \cdot \frac{(a^2/l^2 + 1)^{-3/2} - 1}{(a/l)^2}$$

$$= \lim_{a/l \rightarrow 0} -\frac{2}{3} \cdot \frac{-(3/2) \cdot (a/l)^2}{(a/l)^2} = 1.$$

The preceding equations show that when l is extremely large, the error caused by the radius of the distributed load can be ignored.

(2) l is extremely small, and thus $a \neq 0$, $a/l \rightarrow \infty$. Following the same analysis method,

$$y = \frac{\sigma_z}{\sigma_{z1}} = -\frac{2}{3} \frac{(a^2/l^2 + 1)^{-3/2} - 1}{a^2/l^2}. \quad (19)$$

Let

$$\frac{a^2}{l^2} = x, \quad y = -\frac{2}{3} \frac{(x+1)^{-3/2} - 1}{x}. \quad (20)$$

Following (20), when l is extremely small, the error caused by the radius of the distributed load is large.

When $a/l = 0.106$, $y = 0.986$, and the relative error is small.

3. Applications

The Three Gorges Dam located in Hubei Province, China, is the largest hydropower project in the world. The dam has two parts: the main building and the diversion. Three Gorges is a concrete gravity dam that is 3035 m long, 185 m high, 15 m wide at its crest, and 124 m wide at its bottom. Its installed capacity of 22.5 million kW ranks first in the world. In this section, the method proposed in Section 2 is first used to analyze the boundary range of the Three Gorges Dam through a numerical model. Then, the finite element numerical model of the Three Gorges Dam is established to illustrate the validity and efficiency of the proposed formulas.

3.1. *Deriving Foundation Size.* Hydraulic structure loads such as in gravity dams, water locks, and docks are dominated by a continuous vertical concentration. Based on the conclusions for the plane and space problems, one issue arises, that is, the calculated value of the vertical stress (σ_z) at point M is small when width parameter a and calculation point depth value l satisfy the condition of $a/l < 0.106$.

The objective of the present study is to explore the boundaries of the finite element model selection problem for vertical concentration loads, which is equivalent to finding the coordinates of the points when the base stress is small. In the following section, the base boundary depth of the finite element model is analyzed using the preceding conclusions.

Because of the limit of influenced scope based on the hydraulic structure loads, so the foundation boundary belongs to the result of (11). Equation (11) shows the stress results of the definite integral as follows:

$$\sigma_z = \frac{3F}{2\pi k} \left(\text{sinarctan} \frac{a}{l} - \frac{1}{3} \sin^3 \arctan \frac{a}{l} \right). \quad (21)$$

For this formula, various hydraulic structures have different values of $3F/2\pi k$ because of structure size and material properties. When depth l of the calculation point satisfies the condition

$$a/l = 0.106, \quad (22)$$

σ_z tends to be equal to zero. Parameter a is restricted by the size of the structures. Assume that width L and height H of hydraulic structures satisfy the equation $L = mH$. Then, the deeper l is, the smaller parameter a is, which results in a smaller calculation error of the Boussinesq equation. The maximum value of load length $2a$ is the width L of the structure, which corresponds to the maximum depth as follows:

$$l_{\max} = \frac{a_{\max}}{0.106} = \frac{L}{2 * 0.106} = 4.717L = 4.717mH. \quad (23)$$

When depth l of the calculation point satisfies (23), vertical stress (σ_z) tends to be zero, and l is equivalent to the depth boundary of the finite element calculation model. Various hydraulic structures have different values for parameter m . The value of m should be calculated for each project, and then the base depth boundary of the finite element numerical simulation model can be calculated.

The preceding conclusions can be applied to a specific project. The Three Gorges Water Conservancy Project is the largest gravity dam project in China. In this study, the depth boundary of the finite element numerical simulation model of the aforementioned project is analyzed. The Three Gorges Dam Project is 185 m high and 124 m wide. The parameter m of Three Gorges is

$$m = \frac{L}{H} = \frac{124}{185} = 0.670. \quad (24)$$

Its depth boundary is $l_{\max} = 4.717mH = 3.16H$.

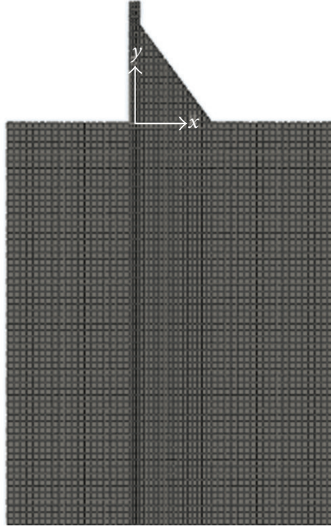


FIGURE 4: Finite element model.

TABLE 1: FEM material parameters.

Area	Parameter		
	Deformation modulus (GPa)	Poisson's ratio (μ)	Density (kg/m^3)
Dam concrete	21	0.167	2400
Foundation	26	0.2	2450

TABLE 2: FEM dimensions of the dam body.

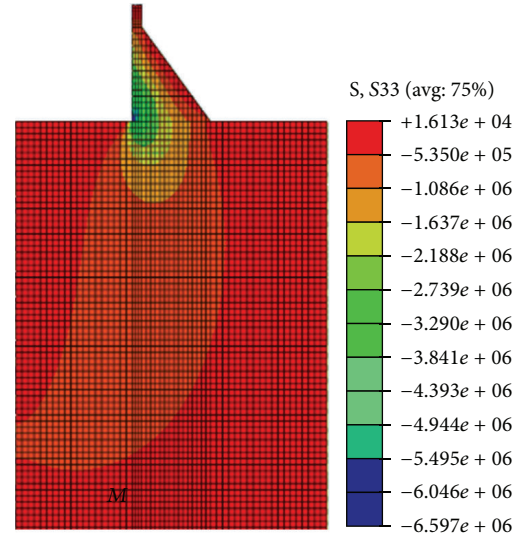
Area	Dimensions			
	Width of dam crest	Width of dam bottom	Height of dam	Slope of downstream surface
Dam body	15 m	124 m	185 m	0.75

TABLE 3: FEM dimensions of the foundation.

Area	Dimensions		
	Width of upstream	Width of upstream	Depth of foundation
Foundation	185 m	185 m	740 m

3.2. Finite Element Numerical Simulation. The establishment of the finite element model of the Three Gorges Dam illustrates the effectiveness and accuracy of the model analysis used in this study. Figure 4 shows the finite element model of the Three Gorges Dam with the following specifications: the x -axis along the downstream direction, the y -axis along the dam axis, and the z -axis along the vertical direction. The finite element model is divided into 5393 units and 11102 nodes. The FEM material parameters are presented in Table 1. The actual dimensions of the finite element model of the Three Gorges Dam are provided in Tables 2 and 3.

Based on the aforementioned calculation principle and parameter, the specific calculation results and analyses are as follows.

FIGURE 5: FEM vertical stress σ_z .

Given that the foundation and dam body have the same size and material along the y -axis direction, the stress results of the plane and space problems along the y -axis section are also the same. The following finite element model is focused on plane problems. Figure 5 illustrates the vertical stress (σ_z) calculation results of the finite element model of the Three Gorges Dam. All size parameters of the finite element method are chosen for the international system of units: meters. The legend of Figure 5 is the size range of σ_z (in Pascal). This figure can indicate that the foundation vertical stress (σ_z) is approximately zero when the depth is deeper than the depth of point M . The depth of point M is the furthest depth of the load effect. Figure 5 shows the depth of point M ; that is, $Z_m = 556$ m. Dam height is 185 m; that is, $Z_M = 556/185H = 3.01H$.

The boundary range acquisition method is based on the Boussinesq formula. This formula is suitable for a semi-infinite body problem under a concentrated load stress. The finite element model of the Three Gorges Dam selected $1H$ to be the foundation range upstream and downstream and $4H$ to be the foundation depth range. According to the finite element calculation results, the foundation influence scope is limited on the loads of hydraulic structures and expanding the scope of the foundation boundary has minimal effect on calculation precision. The Boussinesq formula accurately derives the elastic mechanics formula based on a differential equation, but FEM is the solution to a partial differential equation. Moreover, numerical solution techniques are approximated through the variation method, and the error function is set to minimum values to generate a stable solution. FEM is an approximate method for solving the Boussinesq half-space problem. The two methods, which have different principles, produce slightly different results; however, they exhibit the same trend. The depth boundary defined in Section 3.1 is $Z = 3.16H$. Its relative error is less than 5%; therefore, the model exhibits high precision. Furthermore, the model proves that (23) can be used as

a guideline for depth boundary in the numerical simulation of gravity dams.

4. Conclusions

The following conclusions can be drawn from this study.

- (1) Drawing lessons from the small distance correction method of Newton's law of gravity, the point load is changed to a line load to solve the singular point problem near the face area. Through correct results, (23) can function as a guideline for depth boundary in establishing finite element numerical simulation models of hydraulic structures.
- (2) The formula of parameter a and l should be researched thoroughly. In this study, dam bottom width L is set to a maximum value of $2a$. By using this method, maximum depth boundary l_{\max} is achieved. If a certain magnitude for vertical stress (σ_z) is set, then depth boundary can be reduced.
- (3) This study only investigated the boundary of direction z . The boundaries of directions x and y should be studied further.

Conflict of Interests

The authors declare that there is no conflict of interests regarding the publication of this paper.

Acknowledgments

This work was supported by the National Natural Science Foundation of China (Grant nos. 41323001, 51139001, 51379068, 51179066, 51279052, and 51209077), the Jiangsu Natural Science Foundation (Grant nos. BK20140039 and BK2012036), and the Research Fund for the Doctoral Program of Higher Education of China (Grant nos. 20120094110005, 20120094130003, and 20130094110010).

References

- [1] L. Eisenlohr, L. Király, M. Bouzelboudjen, and Y. Rossier, "Numerical simulation as a tool for checking the interpretation of karst spring hydrographs," *Journal of Hydrology*, vol. 193, no. 1–4, pp. 306–315, 1997.
- [2] N. Moës, J. Dolbow, and T. Belytschko, "A finite element method for crack growth without remeshing," *International Journal for Numerical Methods in Engineering*, vol. 46, no. 1, pp. 131–150, 1999.
- [3] D. V. Griffiths and P. A. Lane, "Slope stability analysis by finite elements," *Geotechnique*, vol. 49, no. 3, pp. 387–403, 1999.
- [4] L. Simoni and B. A. Schrefler, "An accelerated algorithm for parameter identification in a hierarchical plasticity model accounting for material constraints," *International Journal for Numerical and Analytical Methods in Geomechanics*, vol. 25, no. 3, pp. 263–272, 2001.
- [5] G. Chongshi, "Precision analysis on simulational finite element model of dam and batholith," *Hydroelectric Energy*, vol. 20, no. 2, pp. 13–16, 2002.
- [6] D.-Y. Shi, S.-P. Mao, and S.-C. Chen, "On the anisotropic accuracy analysis of ACM's nonconforming finite element," *Journal of Computational Mathematics*, vol. 23, no. 6, pp. 635–646, 2005.
- [7] T. H. Vu and A. J. Deeks, "Using fundamental solutions in the scaled boundary finite element method to solve problems with concentrated loads," *Computational Mechanics*, vol. 53, no. 4, pp. 641–657, 2014.
- [8] S. Chirită and R. Quintanilla, "On Saint-Venant's principle in linear elastodynamics," *Journal of Elasticity*, vol. 42, no. 3, pp. 201–215, 1996.
- [9] L.-C. Huang, Z.-S. Xu, and L.-C. Wang, "Constitutive equations and finite element implementation of strain localization in sand deformation," *Journal of Central South University of Technology (English Edition)*, vol. 16, no. 3, pp. 482–487, 2009.
- [10] Q. Feng, "Traveling wave solutions for the variant Boussinesq equation and the (2+1)-dimensional Nizhnik-Novikov-Veselov (NNV) system by (G'/G)-expansion method," *WSEAS Transactions on Mathematics*, vol. 9, no. 1–3, pp. 191–200, 2010.
- [11] S. R. Lan and J. S. Yang, "Nonlinear finite element analysis of arch dam. I. Constitutive relationship," *Advances in Engineering Software*, vol. 28, no. 7, pp. 403–408, 1997.
- [12] Z. Y. Yan and H. Q. Zhang, "New explicit and exact travelling wave solutions for a system of variant Boussinesq equations in mathematical physics," *Physics Letters A*, vol. 252, no. 6, pp. 291–296, 1999.
- [13] O. Enkhtur, T. D. Nguyen, J. M. Kim, and S. R. Kim, "Evaluation of the settlement influence factors of shallow foundation by numerical analyses," *KSCE Journal of Civil Engineering*, vol. 17, no. 1, pp. 85–95, 2013.
- [14] H. G. Georgiadis and D. S. Anagnostou, "Problems of the flamant-boussinesq and kelvin type in dipolar gradient elasticity," *Journal of Elasticity*, vol. 90, no. 1, pp. 71–98, 2008.
- [15] A. M. Malek, H. Saadatmanesh, and M. R. Ehsani, "Prediction of failure load of R/C beams strengthened with FRP plate due to stress concentration at the plate end," *ACI Structural Journal*, vol. 95, no. 2, pp. 142–152, 1998.
- [16] P. Fara, "Philosophiae naturalis principia mathematica (Mathematical Principles of Natural Philosophy)," *Nature*, vol. 499, no. 7457, p. 153, 2013.

Research Article

An Advanced Coupled Genetic Algorithm for Identifying Unknown Moving Loads on Bridge Decks

Sang-Youl Lee

Department of Civil Engineering, Andong National University, Andong-Si, Gyeongsangbuk-Do 760-749, Republic of Korea

Correspondence should be addressed to Sang-Youl Lee; lsy@anu.ac.kr

Received 10 June 2014; Accepted 24 August 2014; Published 15 September 2014

Academic Editor: Wooyoung Jung

Copyright © 2014 Sang-Youl Lee. This is an open access article distributed under the Creative Commons Attribution License, which permits unrestricted use, distribution, and reproduction in any medium, provided the original work is properly cited.

This study deals with an inverse method to identify moving loads on bridge decks using the finite element method (FEM) and a coupled genetic algorithm (c-GA). We developed the inverse technique using a coupled genetic algorithm that can make global solution searches possible as opposed to classical gradient-based optimization techniques. The technique described in this paper allows us to not only detect the weight of moving vehicles but also find their moving velocities. To demonstrate the feasibility of the method, the algorithm is applied to a bridge deck model with beam elements. In addition, 1D and 3D finite element models are simulated to study the influence of measurement errors and model uncertainty between numerical and real structures. The results demonstrate the excellence of the method from the standpoints of computation efficiency and avoidance of premature convergence.

1. Introduction

Recently, moving loads detection technologies have been developed to assess the bridge condition with limited information related to moving loads. In these studies, the measurement of the weight and velocity of the moving vehicle is significant for the design of bridges and pavements, performance assessment, better maintenance, and the control of illegal vehicles on bridges and highways.

A variety of methods have been carried out to identify the weight and velocity of moving vehicles on bridge structures. These methods are called system identification (SI) methods based on the inverse problem because it uses the static or dynamic responses of structures such as natural frequency, mode shape, and time histories of acceleration of the vehicles. At an early stage of the development of the moving load identification method, only static axle loads are measured. Improved methods capable of identifying both the static and dynamic moving loads were developed from the latter half of the 1980s. Hoshiya and Maruyama [1] identified a moving load on a simply supported beam by applying an extended Kalman filter. O'Connor and Chan [2, 3] developed a method that measured both static and dynamic loads using

strain responses obtained from bridge decks modeled as an assembly of lumped masses with the massless elastic beam element. Considering the interaction forces between vehicle and bridge with the viscous damping on the Euler-Bernoulli beam model, Law et al. [4] identified moving loads using modal superposition principle in time domain. Moreover, Law et al. [5] proposed a frequency time domain method by performing Fourier transformation of the load-response relationship to identify the moving load directly using least squares. Chan et al. [6] applied a moving loads identification method based on Euler's beam theory together with modal analysis. In addition to these methods, Steffen Jr. and Rade [7] used a Fourier series to identify moving loads on a simply supported beam. To obtain a good quality of moving loads, Chan et al. [8] developed a method applicable to the prestressed concrete bridges considering the effect of the prestress on the structure. Chan and Ashebo [9] identified moving loads on a continuous bridge using only a target span. Also, they found that the accuracy of the identified value of moving loads based on bending moment response is better than acceleration response. The effect of the interaction between the bridge and the vehicle, such as the dynamic properties of the bridge and vehicle, made the road surface

roughness an important criterion for the identification of the moving load and many studies have been proposed to confirm the results. Cantieni [10] performed the field test regarding the vehicle-bridge interaction. Hwang and Nowak [11] contributed to the development of a reliability-based design code by developing a process for the calculation of the dynamic load. Wang et al. [12] studied the dynamic response of a single span multigirder bridge deck under single and two vehicle loads with different velocities by adopting grillage beam theory and Huang et al. [13] extended this method to multigirder bridges. Chatterjee et al. [14] performed a simulation with a quarter truck model by simplifying the continuous bridge deck as a continuous Euler-Bernoulli beam subjected to torsional vibration. In addition, the effect of the speed parameter, the vehicle/bridge frequency ratio, and damping of the bridge and road roughness was reported by Yang et al. [15].

To solve these inverse problems, direct search methods based on metaheuristics techniques and artificial intelligence, such as genetic algorithms (GAs), simulated annealing (SA) methods, and neural networks (NN), have been introduced and promisingly applied to the field of structural identification [16]. Among them, GAs attract our attention because they do not require a considerable amount of data in advance in dealing with complex problems and make global solution search possible as opposed to classical gradient-based optimization techniques. Suh et al. [17] presented a coupled neurogenetic technique that is able to identify the region and extent of damage in a beam or frame structure using only frequency information. Mares and Surace [18] demonstrated the ability of a GA to identify damage in elastic structures. Friswell et al. [19] combined the genetic and eigen sensitivity algorithms for locating damage. Chou and Ghaboussi [20] proposed a GA-based method to determine the region and extent of damage in truss structures from the measured static displacements. Krawczuk [21] presented a wave propagation approach to detect damage in beam structures based on GA and the gradient technique. However, conventional GAs have a limit in solving inverse problems using GA because of the high computational cost of a large number of iterations: it is necessary to perform iterative forward computations for each chromosome. Thus, the total time spent in solving the forward problem could be extremely long, usually on the order of magnitude of several thousand or more depending on the complexity of the problem. Unlike these, a uniform microgenetic algorithm (μ GA) can avoid premature convergence and deliver faster convergence to the near optimal region than a simple GA. Carroll [22] found that a uniform μ GA is more robust in handling an order-3 deceptive function than the traditional GA methods. Au et al. [23] developed a natural-frequency-based μ GA for detecting damage in a one-dimensional beam. Lee and Wooh [24] applied a μ GA for detecting damage in plate structures subjected to dynamic loading. However, the numerical examples used in the studies are not practical in that they regard damage as a predetermined rectangular element. Rus et al. [25] examined the identification of defects in laminated composite structures subjected to in-plane static loads using the boundary element method (BEM). They used an elliptic function with five

unknown parameters to represent an arbitrary damage shape. However, this approach has several limitations such as the use of static loads, limitation to in-plane behaviors, and lack of capability to detect the extent of damage. Lee et al. [26] presented a method to detect stiffness degradations using a modified bivariate Gaussian function, with which it is possible to consider an arbitrary damage shape. The method has been applied to concrete plates subjected to impact loads using the finite element method (FEM) and μ GA. Lately, Park et al. [27] proposed a damage-detection technique to determinate damage distribution, which is a modified form of the bivariate Gaussian distribution function. This method uses a combination of the combined finite element method (FEM) and the advanced μ GA and moving loads as input excitation. However, it is required to know the position and velocity of the moving load in advance [28].

In this study, an advanced coupled GA (c-GA) is developed for solving the inverse problem. The c-GA can avoid premature convergence like μ GA and provide faster convergence to the near optimal solution than μ GA by introducing a conventional gradient-based technique for which local searching power is sufficient due to fast convergence. In this study, we use a three-dimensional (3D) beam model for obtaining the measurement data. The approach of the present study is more similar to reality than using the same model for generating the simulated experiment and using the inverse procedure. This is because the difference of measured data due to modeling error between real bridges and numerical models can be accounted for. A one-dimensional (1D) beam model is used to run an inverse procedure to obtain better computational efficiency. In this study, the model uncertainty is significantly considered as a realistic circumstance.

2. Forward Procedure

For the transient analysis of a bridge deck subjected to the effects of moving loads, an implicit time integration method, called the Newmark integration technique, is adopted with the integration parameters $\beta = 1/4$ and $\gamma = 1/2$, which lead to constant-average acceleration approximation. Considering a moving load with a velocity v on a plate element, the total moving distance (${}^{t+\Delta t}D_t$) of the load at time $t + \Delta t$ is given by

$${}^{t+\Delta t}D_t = \frac{v\Delta t}{3.6} + C_{x_1}, \quad (1)$$

where C_{x_1} denotes the initial coordinate of the moving load in the longitudinal direction. The location number \bar{I}_d of the element that the moving load passes through at time $t + \Delta t$ can be expressed as

$${}^{t+\Delta t}\bar{I}_d = N_{x_2}^d I_l + I_s + 1, \quad (2)$$

where

$$I_l = \text{INT} \left(\frac{{}^{t+\Delta t}D_t N_{x_1}^d}{L_{x_1}} \right), \quad I_s = \text{INT} \left(\frac{C_{x_2} N_{x_2}^d}{L_{x_2}} \right), \quad (3)$$

and $N_{x_1}^d$ and $N_{x_2}^d$ are the number of division elements in the longitudinal (x_1) and transverse direction (x_2), C_{x_2} is

the initial coordinate of the moving load in the transverse direction, L_{x_1} and L_{x_2} are the lengths of the plate in the x_1 and x_2 directions, respectively, and $\text{INT}()$ means the integer part of the value in parentheses.

The moving load vectors $\mathbf{F}_k(t)$ at an arbitrary location on the N_k^d th element of the plate should be inevitably distributed into the nodal loads $\bar{\mathbf{F}}_{N_k}(t)$ using the zero-order Hermite (Lagrange) interpolation function Φ . The natural coordinates (ξ_k, η_k) of the element for the moving load at time $t + \Delta t$ can be derived as

$$\begin{aligned} {}^{t+\Delta t}\xi_k &= 2 \left(\frac{[C_{x_1} + {}^{t+\Delta t}D_t] N_{x_1}^d}{L_{x_1}} - I_l \right) - 1, \\ {}^{t+\Delta t}\eta_k &= 2 \left(\frac{C_{x_2} N_{x_2}^d}{L_{x_2}} - I_s \right) - 1. \end{aligned} \quad (4)$$

In a four-node element with three degrees of freedom per node, the moving load distribution into four neighborhood nodes not considering distribution of moment can be expressed as

$${}^{t+\Delta t}\bar{\mathbf{F}}_{N_k} = \Phi^T ({}^{t+\Delta t}\xi_k, {}^{t+\Delta t}\eta_k) \mathbf{F}_k(t + \Delta t). \quad (5)$$

The total external force vectors $\bar{\mathbf{F}}$ applied on the plate at $t + \Delta t$ can be obtained by summing the distributed n loads as given by

$${}^{t+\Delta t}\bar{\mathbf{F}} = {}^{t+\Delta t}\bar{\mathbf{F}}_{N_1} + {}^{t+\Delta t}\bar{\mathbf{F}}_{N_2} + \dots + {}^{t+\Delta t}\bar{\mathbf{F}}_{N_n}. \quad (6)$$

In the Newmark integration scheme, the effective loads at time $t + \Delta t$ can be calculated as

$${}^{t+\Delta t}\hat{\mathbf{F}} = {}^{t+\Delta t}\bar{\mathbf{F}} + \mathbf{M} (\lambda_0^t \mathbf{U} + \lambda_2^t \dot{\mathbf{U}} + \lambda_3^t \ddot{\mathbf{U}}). \quad (7)$$

The dynamic displacements \mathbf{U} , accelerometers $\ddot{\mathbf{U}}$, and velocities $\dot{\mathbf{U}}$ at time $t + \Delta t$ can be solved as

$$\begin{aligned} {}^{t+\Delta t}\mathbf{U} &= \hat{\mathbf{K}}^{-1} {}^{t+\Delta t}\hat{\mathbf{F}}, \\ {}^{t+\Delta t}\ddot{\mathbf{U}} &= \lambda_0 ({}^{t+\Delta t}\mathbf{U} - {}^t\mathbf{U}) - \lambda_2^t \dot{\mathbf{U}} + \lambda_3^t \ddot{\mathbf{U}}, \\ {}^{t+\Delta t}\dot{\mathbf{U}} &= {}^t\dot{\mathbf{U}} - \lambda_6^t \ddot{\mathbf{U}} - \lambda_7^{t+\Delta t} \ddot{\mathbf{U}}, \end{aligned} \quad (8)$$

where the triangularized effective stiffness matrix is $\hat{\mathbf{K}} = \bar{\mathbf{K}} + \lambda_0 \mathbf{M}$ and $\lambda_0, \lambda_2, \lambda_3, \lambda_6$, and λ_7 are integration constants in the Newmark integration method, respectively.

The governing equation of motion of the system is written in the form

$$\mathbf{M}\ddot{\mathbf{U}} + \bar{\mathbf{K}}\mathbf{U} = \bar{\mathbf{F}}(t), \quad (9)$$

where \mathbf{U} and $\ddot{\mathbf{U}}$ are the displacement and acceleration vectors, respectively; \mathbf{M} is the mass matrix without loss before and after damage; $\bar{\mathbf{K}}$ is the stiffness reduction matrix; $\bar{\mathbf{F}}(t)$ is the time history of the applied moving load.

3. Coupled Genetic Algorithm

The accuracy of a system identification method applying a conventional gradient-based technique may be influenced by the insufficient initial information. That is, the trap of minima due to the incomplete initial values often occurs and this problem should be dealt with. In this study, to resolve the earlier trouble of a gradient-based technique in estimating system parameters, the advanced system identification technique applying the c-GA is employed. In general, GAs are good at global searching but slow at converging because they are necessary to perform iterative forward computations for each chromosome. On the other hand, a conventional gradient-based technique is good at local searching but lacks a global search power; thus, to enhance searching capability and improve convergence performance, the incorporation of a GA with a conventional gradient-based optimization technique is enough to attract attention. The introduced c-GA is such an algorithm. In addition, the c-GA can overcome limitations in solving inverse problems using a conventional GA because the high computational cost of a large number of iterations can be reduced dramatically by operating on a very small population size. The small population size very often leads to the phenomenon of genetic drift in chromosomes over a few generations. To maintain the genetic diversity in the population, the c-GA enhances the genetic operation and search strategy. To identify the unknown parameters, the c-GA should be combined with the FEM that can reflect the change of structural properties and loading condition in bridges in the present state. In other words, the FE model parameters that can explain the change of stiffness due to damage under moving loads sensitively should be utilized as identification parameters in an inverse procedure. In terms of the genetic algorithm, the unknown parameter vector \mathbf{q}^s is represented by the selected individuals in each iteration. Meanwhile, dynamic analysis using the combination of FEM and c-GA can be considered the following vector function:

$$\mathbf{U} : \Omega \subset \mathfrak{R}^s \longrightarrow \Gamma \subset \mathfrak{R}^N \quad (10)$$

$$\mathbf{U}(\mathbf{q}^s) = [{}^1U \ {}^2U \ \dots \ {}^N U]^T; \quad \mathbf{q}^s \in \Omega,$$

where Ω is the vector space of identification variables; s is the number of identification variables; Γ is the vector space of dynamic response such as displacements or acceleration data; N is the number of measured data used to identify a system; ${}^1U, \dots, {}^N U$ are dynamic responses calculated by using the dynamic analysis combining the FEM with the c-GA from an arbitrary \mathbf{q}^s . The function \mathbf{U} reflects the distribution of stiffness reductions in structures transformed equivalently from dynamic responses changed from damages. Thus, the system identification for computing a distribution of stiffness reduction is described as the following optimization problem set:

$$\text{minimize} \left(\Xi = \sum_{i=1}^N [{}^i\Psi - {}^iU(\mathbf{q}^s)]^2 \right), \quad (11)$$

where ${}^1\Psi, \dots, {}^N\Psi$ are the measured data and ${}^iU : \mathfrak{R}^s \rightarrow \mathfrak{R}$ ($i = 1, \dots, N$) is the function satisfying $\mathbf{U} = [{}^1U, \dots, {}^N U]^T$.

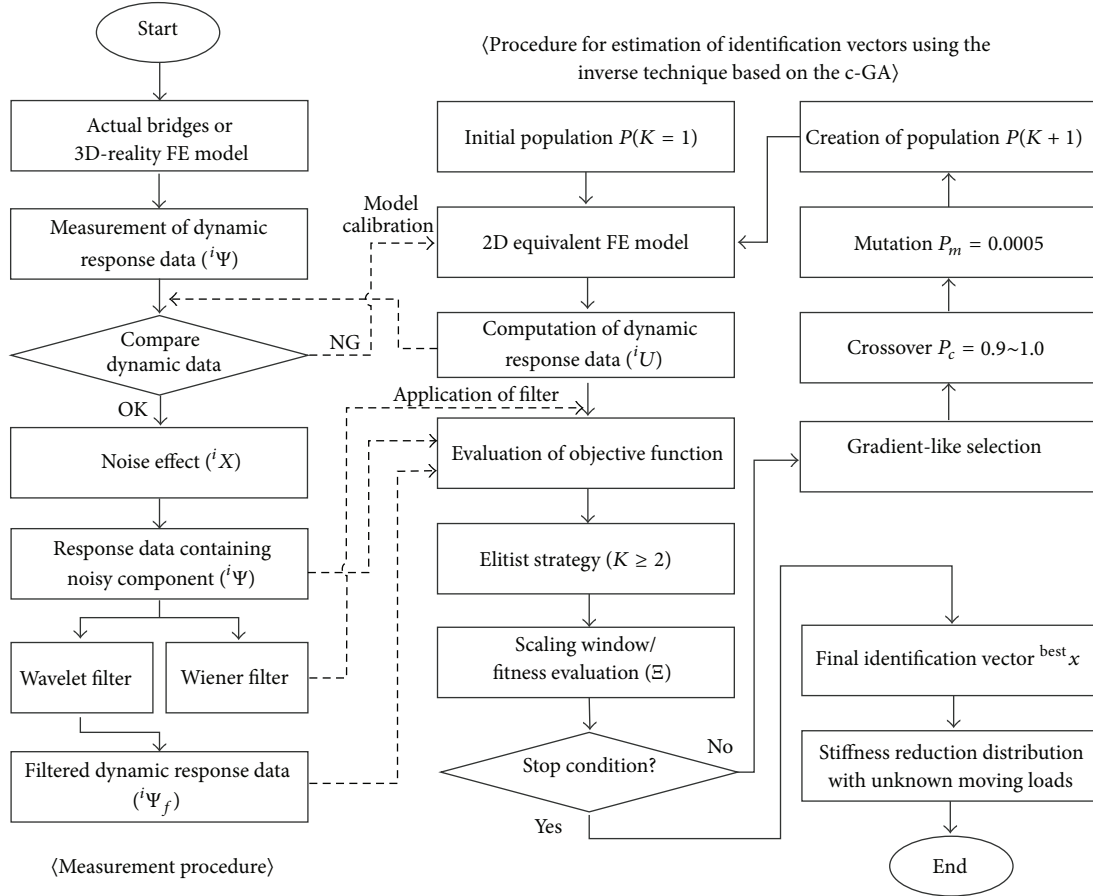


FIGURE 1: A flow chart for identifying the region of damage and the distribution of stiffness change using the combination of FEM and c-GA.

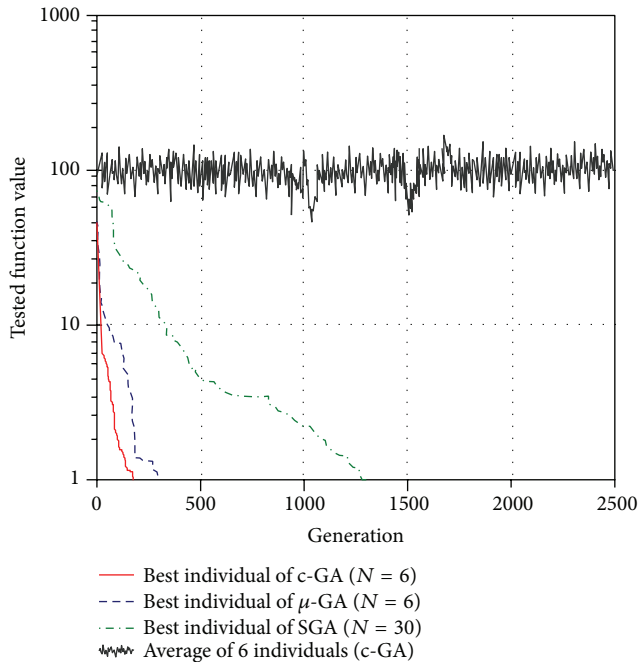


FIGURE 2: Convergence rates obtained through the SGA, the μ GA, and the proposed c-GA.

Figure 1 illustrates a flow chart for identifying the parameters \mathbf{q}^s computed by the combination of FEM and c-GA, as applied in this study. Using the combined finite element analysis and coupled genetic algorithm, the location of a damaged region as well as the distribution of deteriorated stiffness finally can be determined by investigating the unknown parameters \mathbf{q}^s .

4. Numerical Examples

4.1. Comparison with Other Algorithms. The performance of the coupled genetic algorithm (c-GA) proposed in this study is compared with that of the well-known simple genetic algorithm (SGA) and the microgenetic algorithm (μ GA). The test function used is called the foxhole function and the form is as follows:

$$f(\mathbf{x}) = \left(0.002 + \sum_{j=1}^{25} \left(j + \sum_{i=1}^2 (x_i - a_{ij})^6 \right)^{-1} \right)^{-1}, \quad (12)$$

in which the coefficient a_{ij} is continuous, nonconvex, non-quadratic, and multimodal, has low-dimensional detection property, and, especially, has 25 local solutions. The global solution exists at $\mathbf{x} = [-32 \ -32]^T$ and the function value

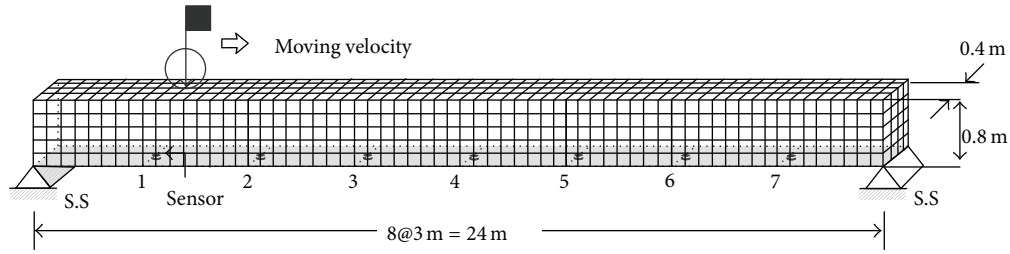


FIGURE 3: 3D-reality concrete beam model [29, 30].

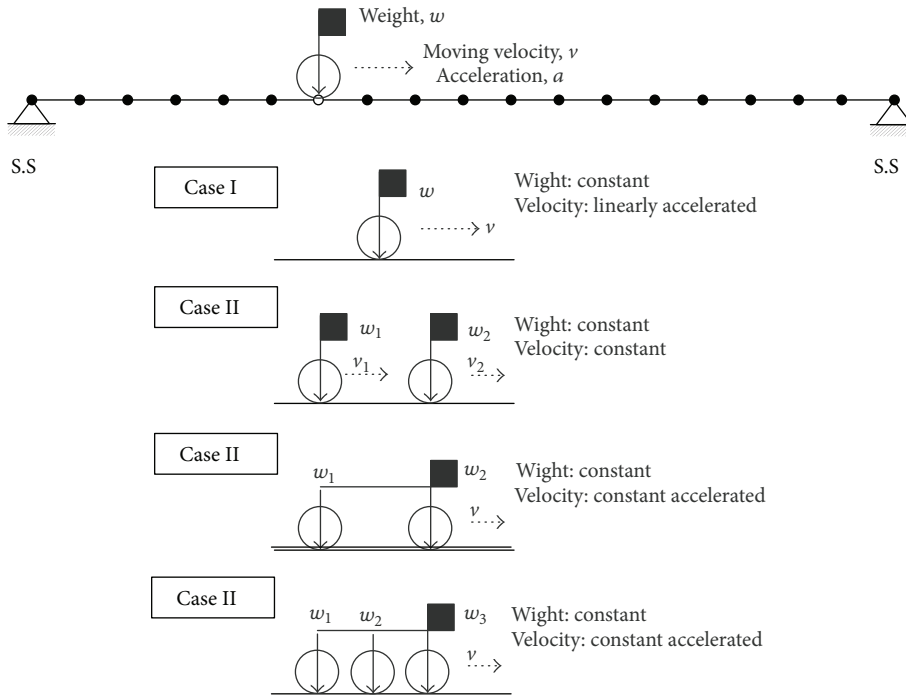


FIGURE 4: Numerical model and four moving load excitation cases of a beam used in the finite element model.

at the point is unity. In Figure 2, convergence rates obtained through the SGA, the μ GA, and the proposed c-GA are represented. The figures indicate that the convergence rate of the c-GA is faster than the others. The reason is that the c-GA decreases the size of the population by 1/5 compared with the SGA; thus, the computation amount in a forward procedure is reduced, which increases the power for detecting the optimal global solution by introducing the gradient-like selection technique in reproduction operation and adopting enhanced strategies such as the elitist strategy and the scaling windows scheme compared with the μ GA.

4.2. Moving Force Detection

4.2.1. Numerical Model. To consider the uncertainties between 2D model and 3D reality, the measurement data obtained from the actual bridge modeled by a three-dimensional FE model [29, 30] shown in Figure 3 are used in the inverse procedure for detecting the characteristics of moving loads. Because of the uncertainties that occurred

from the different models, attention is needed to the selection of the measurement range and location for the moving load excitation. In this study, the dynamic responses such as acceleration, velocity, and displacement are measured at the bottom of the 3D solid model and moving loads are excited at the center line on the top of it as depicted in Figure 3. The geometrical and material properties of the beam are the same as those of the numerical model. For the verification of the ability to identify moving loads using the proposed technique combined with the FEM and the c-GA, in this study, three cases of numerical tests are carried out. To focus on the identification of moving loads, we consider an undamaged concrete beam's 20 divided elements ($N1 = 20$) subjected to the moving load of unknown velocity and weight, as shown in Figure 4. The length, height, width, and density of the beams are 24.0 m, 0.8 m, 0.4 m, and $2,400 \text{ kg/m}^3$, respectively. In implementation using the coupled genetic algorithm, we examine 4~5 individuals due to moving load excitation cases and the probability of uniform crossover was set as 1.0. The combination of given possibilities ($211 = 2048$)

TABLE 1: Estimated parameters values of the final run for the different examples for each case (Ψ : measured value, Ψ^* : estimated value).

Model	Parameter	Measured and estimated values					
		EX1		EX2		EX3	
		Ψ	Ψ^*	Ψ	Ψ^*	Ψ	Ψ^*
Case I	v_0^1	36.00	36.08	36.90	39.45	64.80	64.57
	c_1^1	1.50	1.64	0.90	1.03	-1.50	-1.30
	c_2^1	1.50	1.33	1.10	1.06	-1.50	-1.59
	w_1^1	100.00	101.85	100.00	101.85	100.00	101.85
Case II	v_0^1	50.40	50.84	57.60	55.78	57.60	57.34
	v_0^2	39.60	39.23	36.00	35.85	46.80	47.00
	w_1^1	70.00	75.02	70.00	73.16	70.00	69.26
	w_1^2	100.00	98.68	100.00	97.99	100.00	103.27
Case III	v_0^1	39.60	38.82	64.80	63.45	54.00	51.76
	c_1^1	3.50	3.73	-3.50	-3.15	-2.00	-1.63
	w_1^1	80.00	83.92	80.00	88.221	80.00	88.22
	w_2^1	120.00	119.89	120.00	114.91	120.00	111.19
Case IV	v_0^1	39.60	39.62	57.60	57.60	61.20	61.34
	c_1^1	2.00	1.99	-2.50	-2.49	-2.50	-2.55
	w_1^1	70.00	68.77	70.00	69.75	70.00	75.32
	w_2^1	130.00	129.76	130.00	128.79	130.00	125.07
	w_3^1	130.00	123.99	120.00	128.88	130.00	142.76

can be encoded in binary digits to form each individual. In our case, we use an individual containing 68 chromosomes.

The main goal of this study is to identify the weight and velocity of the moving load passing on a bridge by adopting the quadratic function. In this study, the weight (w) of the moving load will be considered as a constant and a quadratic function is applied to describe the characteristic on the velocity of moving loads because the actual velocity of the moving load may take shape in a smooth curve and will be changed continuously. Thus, the moving velocity of the i vehicle is expressed as

$$v^i = v_0^i + c_1^i t + c_2^i t^2, \quad (13)$$

where v_0^i denotes the initial velocity of the i th vehicle (or axle); c_1^i and c_2^i denote the coefficients of the i vehicle with respect to time. Therefore, general identification variables for detecting moving load properties are given by

$$\mathbf{q}^s = [v_0^i \ c_j^i \ w_k^i]^T \quad (14)$$

$(i = 1, \dots, n_v; \ j = 1, 2; \ k = 1, \dots, n_w),$

where i denotes the number of vehicles considered; j denotes the number of the coefficients used to present the characteristic of velocities; k denotes the number of the axle weights considered. With different moving load parameters in (13), three examples (EX1~EX3) for four moving load excitation cases (Case I~IV) are given in Table 1.

To quantitatively represent the accuracy of the known parameters identified, the relative percentage errors (RPE)

are calculated with respect to the estimated values using the following equation:

$$\text{RPE} = \frac{|\hat{q}^i - q_0^i|}{q_0^i} \times 100 (\%), \quad (15)$$

where \hat{q}^i and q_0^i denote the identified and the original values of the known parameters, respectively.

4.2.2. Detection of Parameters. The estimated values of identification variables of several examples (EX1, EX2, and EX3) for Cases I, II, III, and IV based on the c-GA are represented in Table 1 with RPE in parentheses. Figure 5 shows the comparison of the measured velocity and estimated velocity of the vehicle for EX2 in Case I. As the loading time of a moving load increases, the difference in velocities becomes more or less increased but the overall values are found to not be significantly different. The measured and estimated vertical displacements at the midpoint about the same example and case are plotted in Figure 6. The best fitness function values for EX2 in Case I are shown in Figure 7. It is confirmed from this figure that the estimated values of the parameters would be close to real values when the number of generations is increased. The other examples for EX1 and EX2 in Case I showed a similar tendency.

Case II, representing bridges subjected to moving loads of multivehicles, is to describe a more realistic situation about a moving load excitation. Unlike Case I, all moving loads are assumed to move with constant velocities. In addition, two velocities and two weights of the moving loads are estimated. Figure 8 shows a comparison of the measured and estimated

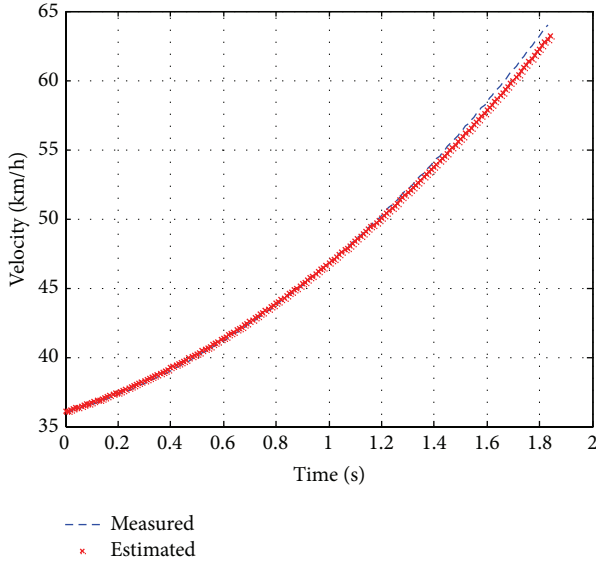


FIGURE 5: Measured and estimated velocities of the moving load for EX2 in Case I.

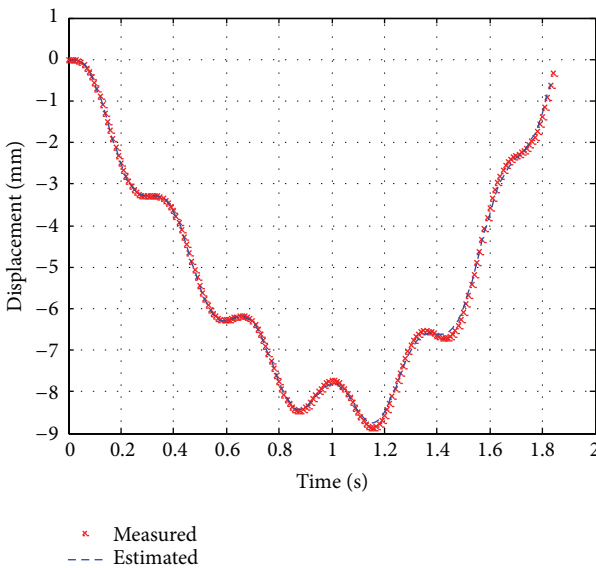


FIGURE 6: Measured and estimated displacements at the middle sensor for EX2 in Case I.

velocities of the vehicles for EX1 in Case II. The difference between the measured and estimated velocities is found to be very small. The estimated vertical displacements at the midpoint about the same example and case agree well with the measured ones as depicted in Figure 9. The best fitness function values are plotted in Figure 10. The convergence rate of unknown parameters for Case II is relatively slow compared to Case I since the number of moving loads is double and the moving load properties contained in the dynamic response are superposed and, thus, each property of the moving load is not easily identified. However, it can be observed from the figure that the value of the fitness function converges after approximately the 3,000th generation. The

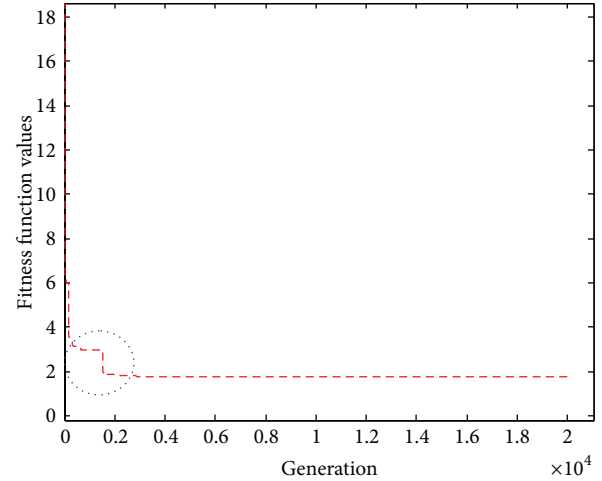


FIGURE 7: Best fitness function values for EX1 in Case II.

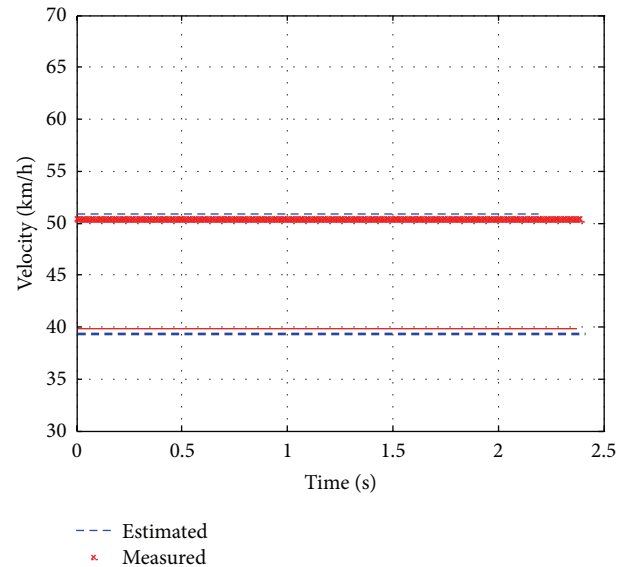


FIGURE 8: Measured and estimated velocities of the moving load for EX1 in Case II.

other examples for EX2 and EX3 in Case II showed a similar tendency. In Case III, two axle loads are considered to describe midsize vehicles such as a car. Unlike Cases I and II, in this case, a moving load is assumed to move with constant acceleration. Two axle weights distributed into the front and rear wheels in a vehicle are estimated. Figure 11 shows a comparison of the measured and estimated velocities of the vehicle for EX1 in Case II. The initial velocity of the vehicle shows a slight difference but the overall values are found to not differ significantly. In this case, a vertical velocity is used as the dynamic response data for identifying the unknown parameters. The vertical velocities at the midpoint of the 3D-reality model and the equivalent model are plotted in Figure 12. The behavior between the two models is shown to be identical from the figure. It is seen from Figure 13 that the estimated values of the parameters would be close to

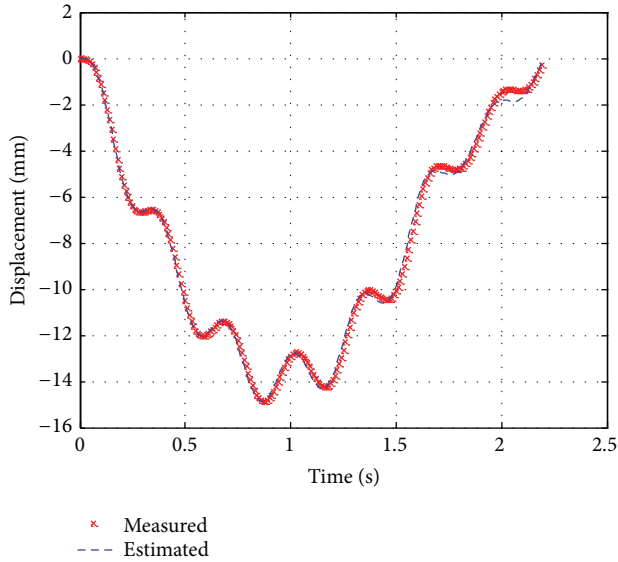


FIGURE 9: Measured and estimated displacements at the middle sensor for EX1 in Case II.

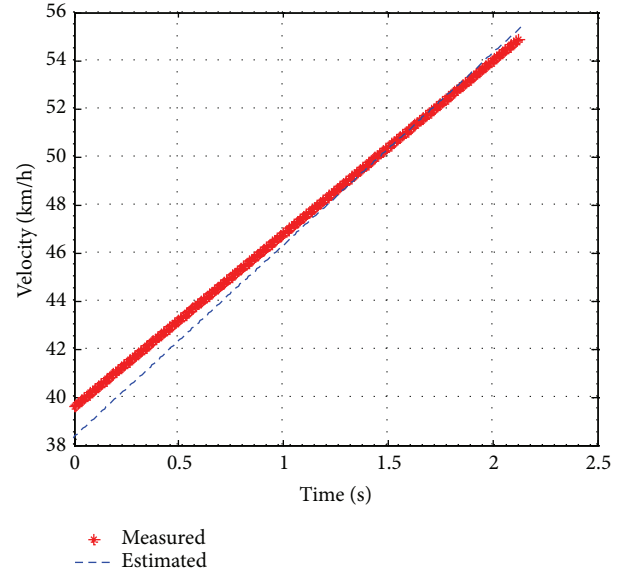


FIGURE 11: Measured and estimated velocities of the moving load for EX1 in Case III.

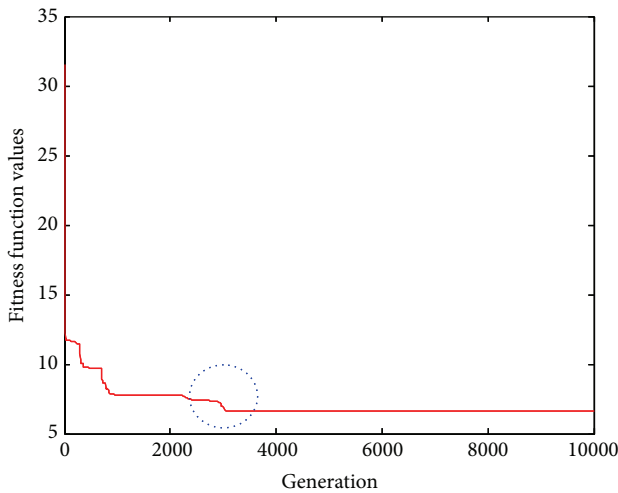


FIGURE 10: Best fitness function values for EX1 in Case II.

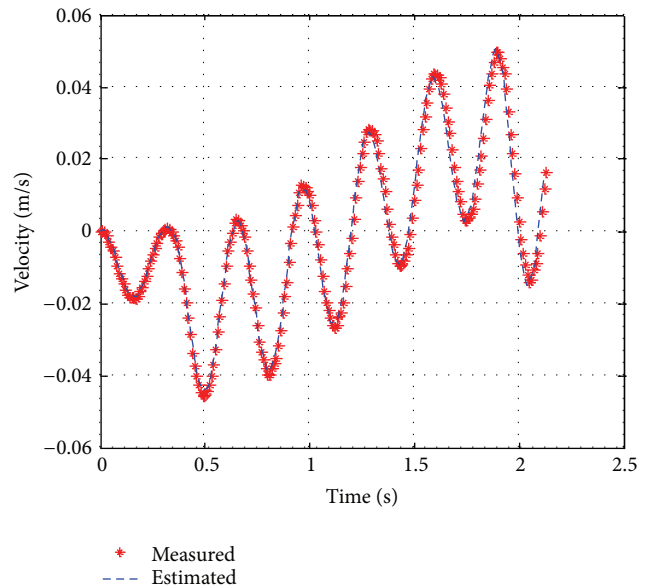


FIGURE 12: Measured and estimated velocities at the middle sensor for EX1 in Case III.

real values if the number of generations is increased. The other examples for EX2 and EX3 in Case III showed a similar tendency.

In Case IV, three axle loads are considered to represent large vehicles such as a truck. Like Case III, in this case, the moving load is assumed to move with constant acceleration as well. Figure 14 shows a comparison of the measured velocity and estimated velocity of EX3. As depicted in the figure, the velocity of the vehicle is detected exactly. The quantitative properties of the moving load are also present in Table 1. Initial velocity v_0^1 and constant acceleration c_1^1 are relatively exactly evaluated as 0.224% and 2.120%, respectively, in RPE. The accuracy of estimation results of axle loads is unsteady in this example but, in the remaining examples (EX1 and EX2), for the most, part axle loads are exactly evaluated with the relative percentage errors being less than 5%, as expected.

In this case, accelerations are used as the dynamic response data for identifying unknown parameters. The accelerations at the midpoint of the 3D-reality model and the equivalent model are plotted in Figure 15. From the figure, we see that the behavior between the two models is shown to be similar. The best fitness function values are plotted in Figure 16, and it is seen that the estimated values of the parameters would be close to real values if the number of generations is increased.

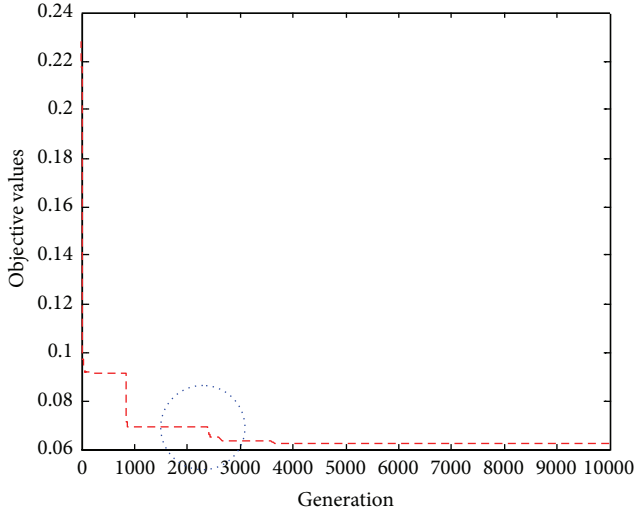


FIGURE 13: Best fitness function values for E1 in Case III.

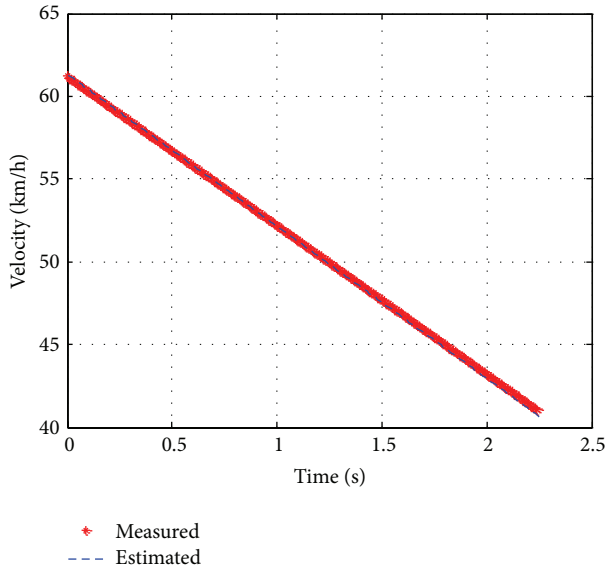


FIGURE 14: Measured and estimated velocities of the moving load for EX3 in Case IV.

5. Summary and Conclusions

In this study, unknown moving loads parameters in a beam-type structure are estimated by using the *c*-GA, which has a superior computational efficiency. The damage characteristics are not considered to investigate only properties of moving loads. A quadratic function is applied to describe the characteristic of the velocity of moving loads. In addition, to consider modeling error in this study, dynamic responses obtained from a three-dimensional FE model under a moving load are used to obtain measurement data. Parametric case studies showed that the proposed technique combining the FEM and the *c*-GA is adequate to detect the properties of moving loads. Based on the present computational results, the following conclusions may be derived.

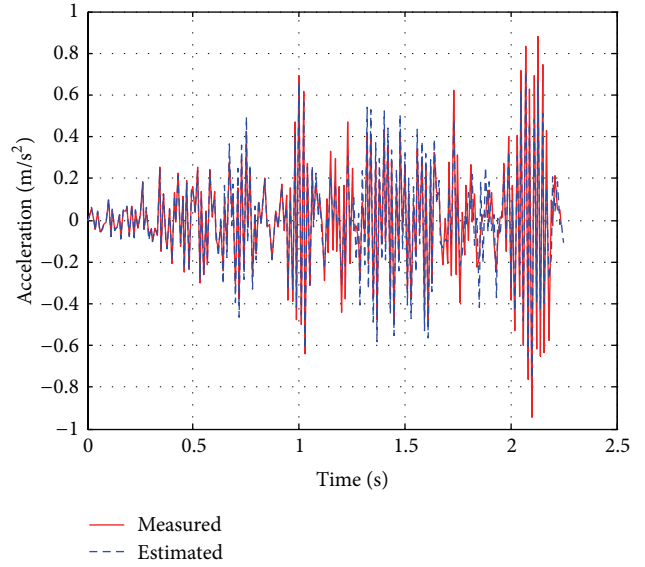


FIGURE 15: Measured and estimated velocities at the middle sensor for EX3 in Case IV.

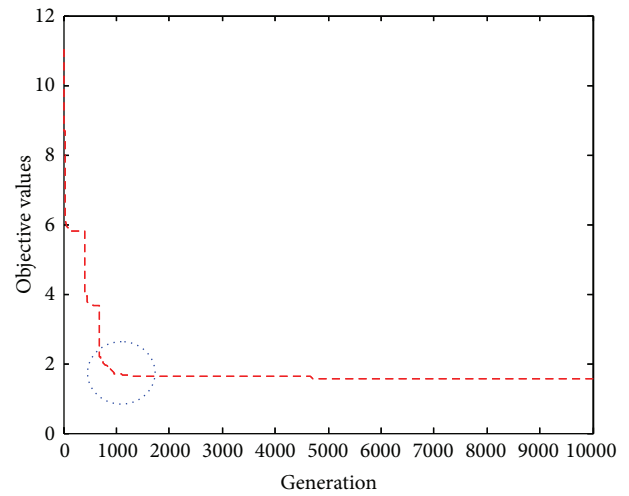


FIGURE 16: 16 best fitness function values for EX3 in Case IV.

- (1) The *c*-GA, in comparison with its predecessor (SGA) or other conventional searching techniques, is more attractive not only because it can avoid premature convergence but also because it converges faster.
- (2) The weight and velocity of the moving load are estimated with small error for examples in Cases I, II, III, and IV considered in this study.
- (3) The velocity properties of moving loads are relatively evaluated by using a quadratic function for representing continuous moving velocity.
- (4) The detections based on the dynamic response such as displacement, velocity, and acceleration are all effective in the inverse procedure.

It is concluded from numerical examples that the proposed method works well for the numerical experiments

that were tested. However, our moving load characterization using two-dimensional modeling is a limited example for solving the inverse problem of complex structures with large degrees of freedom; hence, more advanced studies should be carried out for more realistic bridge models such as a slab or continuous bridge. In addition, for the application of an uncertain measurement system, it is necessary to develop filtering techniques that are capable of canceling noise signals that may be contained in the measured data. Furthermore, for more complicated situations like damaged bridges subjected to unknown moving loads, more advanced studies that can simultaneously detect the characteristics of the damage and the moving load are needed.

Conflict of Interests

The author declares that there is no conflict of interests regarding the publication of this paper.

Acknowledgment

This research was supported by a basic Science Research Program through the National Research Foundation of Korea (NRF) funded by the Ministry of Education, Science and Technology (no. 2012R1A1A1014722).

References

- [1] M. Hoshiya and O. Maruyama, "Identification of running load and beam system," *Journal of Engineering Mechanics*, vol. 113, no. 6, pp. 813–824, 1987.
- [2] C. O'Connor and T. H. T. Chan, "Dynamic wheel loads from bridge strains," *Journal of Structural Engineering*, vol. 114, no. 8, pp. 1703–1723, 1988.
- [3] C. O'Connor and T. H. T. Chan, "Wheel loads from bridge strains: laboratory studies," *Journal of Structural Engineering*, vol. 114, no. 8, pp. 1724–1740, 1988.
- [4] S. S. Law, T. H. T. Chan, and Q. H. Zeng, "Moving force identification: a time domain method," *Journal of Sound and Vibration*, vol. 201, no. 1, pp. 1–22, 1997.
- [5] S. S. Law, T. H. T. Chan, and Q. H. Zeng, "Moving force identification—a frequency and time domains analysis," *Journal of Dynamic Systems, Measurement and Control*, vol. 121, no. 3, pp. 394–401, 1999.
- [6] T. H. T. Chan, S. S. Law, T. H. Yung, and X. R. Yuan, "An interpretive method for moving force identification," *Journal of Sound and Vibration*, vol. 219, no. 3, pp. 503–524, 1999.
- [7] V. Steffen Jr. and D. A. Rade, "Identification method of multi-degree-of-freedom systems based on fourier series," *The International Journal of Analytical and Experimental Modal Analysis*, vol. 6, no. 4, pp. 271–278, 1991.
- [8] T. H. T. Chan, S. S. Law, and T. H. Yung, "Moving force identification using an existing prestressed concrete bridge," *Engineering Structures*, vol. 22, no. 10, pp. 1261–1270, 2000.
- [9] T. H. T. Chan and D. B. Ashebo, "Moving axle load from multi-span continuous bridge: laboratory study," *Transactions of the ASME: Journal of Vibration and Acoustics*, vol. 128, no. 4, pp. 521–526, 2006.
- [10] R. Cantieni, "Vehicle/bridge dynamic interaction for highway bridges," in *Proceedings of the 2nd European Conference on Structural Dynamics (Eurodyn '93)*, vol. 2, pp. 961–968, Trondheim, Norway, 1993.
- [11] E.-S. Hwang and A. S. Nowak, "Simulation of dynamic load for bridges," *Journal of Structural Engineering*, vol. 117, no. 5, pp. 1413–1434, 1991.
- [12] T.-L. Wang, D. Z. Huang, and M. Shahawy, "Dynamic response of multigirder bridges," *Journal of Structural Engineering*, vol. 118, no. 8, pp. 2222–2238, 1992.
- [13] D. Huang, T.-L. Wang, and M. Shahawy, "Impact analysis of continuous multigirder bridges due to moving vehicles," *Journal of Structural Engineering*, vol. 118, no. 12, pp. 3427–3443, 1992.
- [14] P. K. Chatterjee, T. K. Datta, and C. S. Surana, "Vibration of continuous bridges under moving vehicles," *Journal of Sound and Vibration*, vol. 169, no. 5, pp. 619–632, 1994.
- [15] Y.-B. Yang, C.-H. Chang, and J.-D. Yau, "An element for analysing vehicle-bridge systems considering vehicle's pitching effect," *International Journal for Numerical Methods in Engineering*, vol. 46, no. 7, pp. 1031–1047, 1999.
- [16] T. Marwala, "Damage identification using committee of neural networks," *Journal of Engineering Mechanics*, vol. 126, no. 1, pp. 43–50, 2000.
- [17] M.-W. Suh, M.-B. Shim, and M.-Y. Kim, "Crack identification using hybrid neuro-genetic technique," *Journal of Sound and Vibration*, vol. 238, no. 4, pp. 617–635, 2000.
- [18] C. Mares and C. Surace, "An application of genetic algorithms to identify damage in elastic structures," *Journal of Sound and Vibration*, vol. 195, no. 2, pp. 195–215, 1996.
- [19] M. I. Friswell, J. E. T. Penny, and S. D. Garvey, "A combined genetic and eigensensitivity algorithm for the location of damage in structures," *Computers and Structures*, vol. 69, no. 5, pp. 547–556, 1998.
- [20] J.-H. Chou and J. Ghaboussi, "Genetic algorithm in structural damage detection," *Computers and Structures*, vol. 79, no. 14, pp. 1335–1353, 2001.
- [21] M. Krawczuk, "Application of spectral beam finite element with a crack and iterative search technique for damage detection," *Finite Elements in Analysis and Design*, vol. 38, no. 6, pp. 537–548, 2002.
- [22] D. L. Carroll, "Chemical laser modeling with genetic algorithms," *AIAA Journal*, vol. 34, no. 2, pp. 338–346, 1996.
- [23] F. T. K. Au, Y. S. Cheng, L. G. Tham, and Z. Z. Bai, "Structural damage detection based on a micro-genetic algorithm using incomplete and noisy modal test data," *Journal of Sound and Vibration*, vol. 259, no. 5, pp. 1081–1094, 2003.
- [24] S.-Y. Lee and S.-C. Wooh, "Waveform-based identification of structural damage using the combined finite element method and microgenetic algorithms," *Journal of Structural Engineering*, vol. 131, no. 9, pp. 1464–1472, 2005.
- [25] G. Rus, S.-Y. Le, and R. Gallego, "Defect identification in laminated composite structures by BEM from incomplete static data," *International Journal of Solids and Structures*, vol. 42, no. 5–6, pp. 1743–1758, 2005.
- [26] S.-Y. Lee, T. Park, and G. Z. Voyiadjis, "Detection of stiffness reductions in concrete decks with arbitrary damage shapes using incomplete dynamic measurements," *ASCE Journal of Engineering Mechanics*, vol. 134, no. 7, pp. 567–577, 2008.
- [27] T. Park, M.-H. Noh, S.-Y. Lee, and G. Z. Voyiadjis, "Identification of a distribution of stiffness reduction in reinforced concrete slab bridges subjected to moving loads," *Journal of Bridge Engineering*, vol. 14, no. 5, pp. 355–365, 2009.

- [28] M.-H. Noh and S.-Y. Lee, "A bivariate Gaussian function approach for inverse cracks identification of forced-vibrating bridge decks," *Inverse Problems in Science and Engineering*, vol. 21, no. 6, pp. 1047–1073, 2013.
- [29] ABAQUS, "Defining a model in Abaqus," Online manual, Version 6.9, 2009, <http://abaqusdoc.ucalgary.ca/v6.9/books/usb/default.htm?startat=pt01ch01s03aus03.html#usb-int-imodel>.
- [30] ABAQUS, *Abaqus Analysis User's Manual, Online Manual, Version 6.9*, 2009, <http://abaqusdoc.ucalgary.ca/v6.9/books/usb/default.htm>.